Plasma Physics Reports, Vol. 30, No. 10, 2004, pp. 807–815. Translated from Fizika Plazmy, Vol. 30, No. 10, 2004, pp. 867–876.

TOKAMAKS

Spectra of Enhanced Scattering by Spontaneous Density Fluctuations in a Tokamak

A. D. Gurchenko, E. Z. Gusakov, M. M. Larionov, K. M. Novik, A. N. Savel'ev, V. L. Selenin, and A. Yu. Stepanov

Ioffe Physicotechnical Institute, Russian Academy of Sciences, Politekhnicheskaya ul. 26, St. Petersburg, 194021 Russia

Received September 10, 2003; in final form, December 9, 2003

Abstract—The wavenumber-resolved radar backscattering diagnostics in the upper hybrid resonance (UHR) region was used to study low-frequency short-scale turbulence in the FT-1 tokamak. The scattered spectra were measured for different delay times of the scattered signals. It is shown that the width of the spectrum of enhanced scattering by spontaneous fluctuations is proportional to the delay time. Possible mechanisms for the formation of the scattered spectra are proposed and discussed. The results of simulations and additional experiments were used to determine the dominant mechanisms governing the formation of the scattered spectra in the FT-1 tokamak. These mechanisms are related to the effect of multiple small-angle scattering of both the probing wave and the waves backscattered in the UHR region by long-scale density fluctuations and to the Doppler effect caused by the entrainment of short-scale fluctuations by the long-scale turbulent flow. *© 2004 MAIK "Nauka/Interperiodica".*

1. INTRODUCTION

The problem of anomalous heat and particle transport in tokamaks has stimulated great interest in developing new methods for local measurements of plasma turbulence. An advanced method for local measurements of short-scale density fluctuations is microwave scattering diagnostics in the upper hybrid resonance (UHR) region [1–3]. With this method, it is possible to study lower hybrid, ion Bernstein, and ion-acoustic waves, as well as electron-temperature-gradient (ETG) driven drift modes and the short-scale component of the ion-temperature-gradient (ITG) driven turbulence and trapped-electron-mode (TEM) turbulence. In UHR scattering diagnostics, the probing extraordinary wave is launched from the high-field side and detectors receive the radiation backscattered by low-frequency electron density fluctuations in the UHR region. The position R_{UH} of the UHR region in the equatorial plane is defined by the relation

$$\omega_i^2 = \omega_{ce}^2(R_{UH}) + \omega_{pe}^2(R_{UH}), \qquad (1)$$

where ω_i is the probing frequency and ω_{ce} and ω_{pe} are the electron cyclotron and electron plasma frequencies, respectively. In the UHR region, the projection of the wave vector of the probing wave onto the gradient of the plasma permittivity $\varepsilon = 1 - \omega_{pe}^2/(\omega_i^2 - \omega_{ce}^2)$ sharply increases to values far exceeding its vacuum value $k_0 = \omega_i/c$. This makes it possible to measure small-scale fluctuations. The amplitudes of the probing and backscattered waves also increase as the UHR region is approached; as a result, the backscattered signal is considerably enhanced. Since the effect of enhanced scattering takes place in the narrow UHR region, the diagnostics provides high spatial resolution. An important advantage of this method is that the same antenna can be used both to launch the probing wave and to receive the scattered radiation. The scanning of the plasma volume is performed by shifting the UHR region through varying the probing frequency or the magnetic field.

Since the wavenumbers of the probing and scattered waves (k_{iR} and k_{sR}, respectively) vary strongly in the vicinity of the resonance point R_{UH}, the Bragg condition for backscattering by the low-frequency fluctuations, $k_{iR}(R_s) - k_{sR}(R_s) \approx 2k_{iR}(R_s) = -q_R$, is satisfied over a wide range of fluctuation wavenumbers q_R. As a result, all of these fluctuations contribute to the scattered signal; this significantly simplifies the diagnostics, since, in this case, a smaller amount of prior information about the turbulence under study is needed. On the other hand, because of the poor resolution in wavenumbers caused by the integral contribution from fluctuations with different spatial scales to the scattered signal in the UHR region, information on density fluctuations in the plasmas of linear devices or high-temperature tokamak plasmas [3] has long remained only qualitative.

In [4], it was pointed out that this drawback of enhanced-scattering diagnostics can be overcome by employing the effect of the slowing down of extraordinary waves in the UHR region. It was shown in [4, 5] that the delay time of the backscattered signal in the UHR region depends on the wavenumber q_R of the scattering fluctuations:

$$t_d = 2q_R\omega_i/\left|\frac{\partial\omega_{pe}^2}{\partial R} + \frac{\partial\omega_{ce}^2}{\partial R}\right|_{UHR} + t_w, \qquad (2)$$

[1] This article was submitted by the authors in English.

1063-780X/04/3010-0807$26.00 © 2004 MAIK "Nauka/Interperiodica"

where t_w is the delay time related to the propagation of the probing wave through the waveguide transmission lines and through the plasma far from the UHR region. Expression (2) was derived under the assumption $\varepsilon \sim (R - R_{UH})$, which is valid in the immediate vicinity of the UHR point for fluctuations satisfying the condition $2k_0 \ll q_R \ll \rho_{ce}^{-1}$, where ρ_{ce} is the electron cyclotron radius. For fluctuations satisfying the condition $2k_{conv} \ll q_R \leq \rho_{ce}^{-1}$ (where $k_{conv} \equiv k_0\sqrt{c/V_{Te}}$ is the wavenumber corresponding to the point of linear conversion of the probing wave into a slow electron Bernstein wave), linear dependence (2) breaks down. The reason is that, under the latter condition, the scattering point gradually shifts away from the UHR point. We took this effect into consideration by numerically calculating the delay time with allowance for thermal corrections to the dispersion relation for extraordinary waves. Dependence (2) was verified in model experiments [6–8], and the time-of-flight modification of the enhanced-scattering diagnostics was used to study short-wavelength ion-acoustic oscillations and lower hybrid waves in linear plasma devices [9] and to investigate the propagation of lower hybrid waves in the plasma of the FT-1 tokamak [10]. In this paper, we present the results from experimental studies of the short-scale component of spontaneous turbulence in the FT-1 tokamak with the use of the above diagnostics.

2. EXPERIMENTS ON ENHANCED RADAR SCATTERING

The experiments were carried out in the FT-1 tokamak [11] with a major radius of $R_0 = 62.5$ cm and minor radius of $a = 15$ cm. The operating parameters in the quasisteady phase of a discharge were as follows: the toroidal magnetic field at the chamber axis was $B_T \approx 1$ T, the plasma current was $I_P \approx 30$ kA, the electron density was $n_e(0) \approx 10^{13}$ cm^{-3}, and the central electron temperature was $T_e(0) \approx 400$ eV.

In measurements, we used the radar scheme [12–14], which allowed us to determine the fluctuation wavenumber q_R from the delay time of the scattered pulse relative to the probing pulse. The probing wave at a frequency of 28 GHz was amplitude-modulated by a sequence of short pulses with a full width at half-maximum of 3.5 ns and a repetition period of up to 70 ns. The probing wave was launched into the plasma through a horn antenna. When the modulation was switched off, the output power of the antenna was no higher than 20 W. The component corresponding to a certain delay time could be separated from the scattered signal by gating the received radiation by a similar sequence of pulses. The delay time was determined from the shift between the modulation and gate pulses; this shift was set at zero when the scheme was calibrated in the absence of a plasma in order to compensate for the delay time t_w, related to the propagation of the probing wave far from the UHR region. After superheterodyne reception and amplification, we studied the frequency spectra of the separated spectral component with the help of a spectrum analyzer with an analyzing time of 2 ms.

The probing wave was launched and the scattered radiation was received with identical horns placed alongside each other on the high-field side in the equatorial plane of the tokamak. The fraction of ordinary-polarized waves in the emitted and received extraordinary radiation was less than 1%. The antenna beam width at a level of 3 dB in the vertical direction was 16° (±8°).

The noise level in our experiments was determined by electron cyclotron radiation.

When the scheme was calibrated in the absence of a plasma, the frequency of the received signal, which was reflected from the tokamak wall, was equal to the probing frequency. The difference-frequency spectrum of the received signal contained one narrow line at the frequency $f_s - f_i = 0$, where f_i and f_s are the frequencies of the probing and scattered waves, respectively. In the presence of a plasma, the spectrum of the received signal was broadened due to scattering by low-frequency plasma fluctuations.

Curve *1* in Fig. 1a shows the spectrum of a backscattered signal received without resolution in wavenumbers (continuous reception) at $B_T = 1$ T ($r_{UH} = R_{UH} - R_0 \approx 13$ cm). The central narrow line at a frequency of $f_s - f_i = 0$ corresponds to the direct coupling of the launching and receiving antennas. The scattered spectrum itself consists of wide wings extending from 0.3 to 4 MHz on both sides. When studying the spectrum with the delay-time resolution method, it turned out that the wings were very narrow at $t_d = 0$ ns (Fig. 1a, curve *2*). At $t_d = 5$ ns (curve *3*), the wings became broader, while the amplitude of the central line decreased substantially. The central line, which remained unsuppressed at $t_d > 5$ ns, corresponds to the continuous incident radiation attenuated by 20 dB by the gating modulator. For a delay time of $t_d = 10$ ns (Fig. 1b, curve *4*), the spectrum width increased and the intensity of the wings grew to a maximal level. Here, by the spectrum width we mean the full width of its wings at a certain fixed level (e.g., at –3 dB) relative to the peak of the scattered spectrum. Note that the peak of the spectrum is usually masked by the central line at the probing frequency; the maximum spectral intensity of the scattered signal can be found by extrapolating the wings of the spectrum to their intersection at the probing frequency. It can be seen from curve *5*, which corresponds to $t_d = 20$ ns, that, at longer delay times, the scattered signal decreases. In this case, the central part of the spectrum is substantially lowered, so its width increases even more.

From the measured frequency spectra, we deduced the dependence of the intensity of the signal backscattered in the UHR region on the delay time (or, accord-

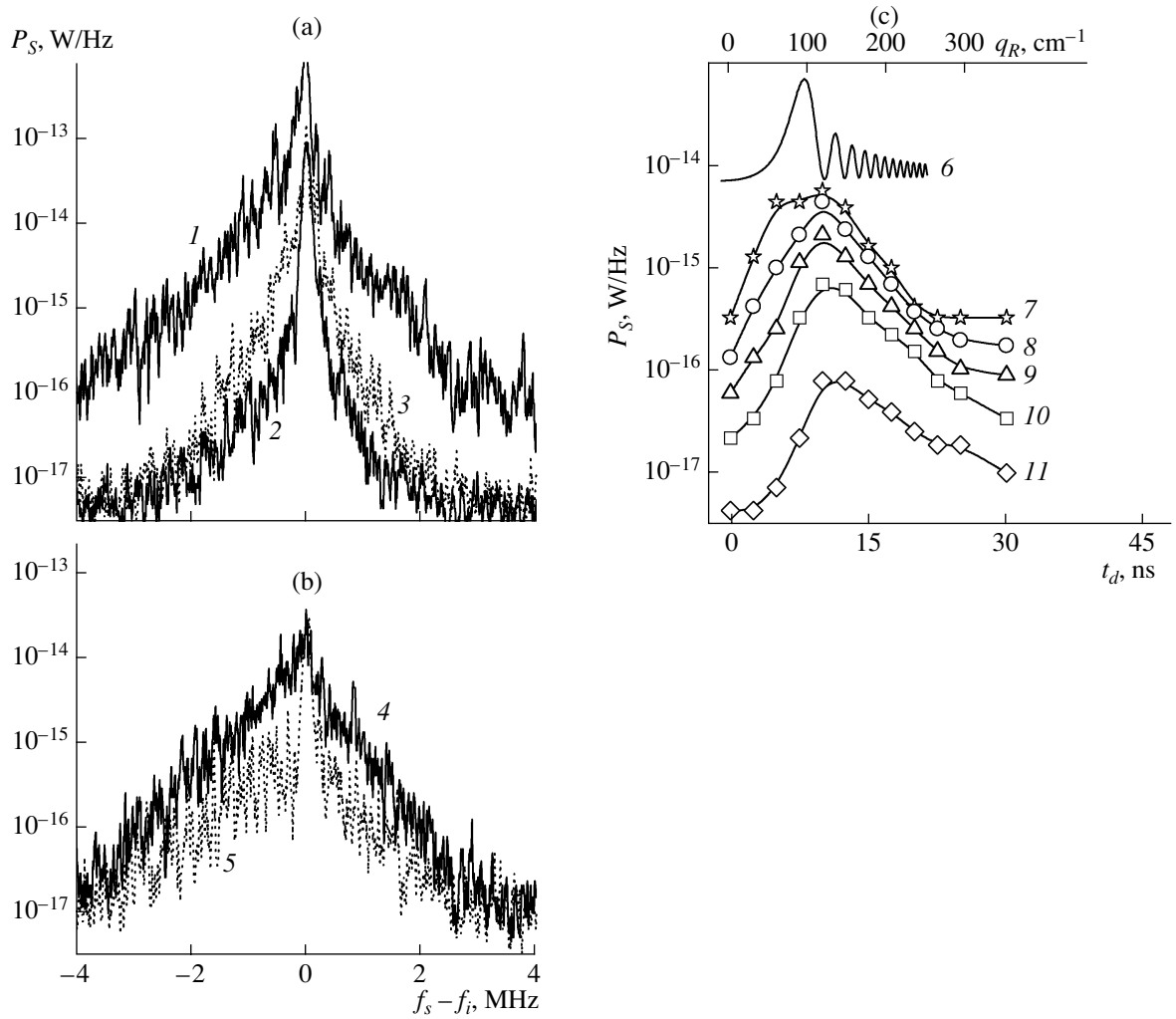

Fig. 1. (a, b) Spectra of enhanced radar scattering (*1*) at continuous reception and with gating at (*2*) 0, (*3*) 5, (*4*) 10, and (*5*) 20 ns; (c) the scattering efficiency (in arbitrary units) vs. wavenumber of scattering fluctuations (curve *6*) and the time dependences of the spectral components of the scattered signal: (*7*) 330 kHz, (*8*) 600 kHz, (*9*) 1 MHz, (*10*) 1.5 MHz, and (*11*) 3 MHz.

ing to formula (2), on the radial wavenumber of the scattering fluctuations). This dependence is shown in Fig. 1c for different frequencies $f_s - f_i$ within the range from 0.3 (curve *7*) to 3.0 MHz (curve *11*). For wavenumbers of up to $q_R \approx 100$ cm^{-1}, the signal amplitude rapidly increases by more than 10 dB. For larger wavenumbers, the intensity of the scattered signal gradually decreases. The presence of the maximum in the intensity of the scattered signal as a function of the fluctuation wavenumber can be explained by the theoretically predicted dependence of the scattering efficiency $\rho_{BS}(q_R)$ on the radial wavenumber [3] (Fig. 1c, curve *6*). This dependence has a maximum at $q_R = 2k_{conv}$; in this case, the backscattering occurs near the point of linear conversion, where a slow "warm" mode is generated [3]. For the measured value of the electron temperature $T_e(r_{UH}) = 70$ eV, we easily find the wavenumber corresponding to linear conversion, $2k_{conv} = 96$ cm^{-1}; this value is in good agreement with the wavenumber $q_R = 104$ cm^{-1}, corresponding to the maximum intensity of the scattered signal at $t_d = 10$ ns. Hence, to determine the wavenumber spectrum of short-wavelength fluctuations by the data from Fig. 1c, it is necessary to make a correction for the wavenumber dependence of the scattering efficiency $\rho_{BS}(q_R)$. Note that there is no need to do this when determining the frequency spectra of fluctuations with a given wavenumber q_R from Fig. 1a, because, for the observed small frequency shifts, the frequency dependence of the scattering cross section can be ignored [3]. Note that the spectra in Fig. 1a differ substantially from the backscattered spectra observed previously with the time-of-flight technique in linear devices [6]: they do not demonstrate any appreciable dispersion. Thus, as the delay time increases and, according to formula (2), the radial wavenumber of fluctuations also increases, the frequency shift of the scattered spectrum varies insignificantly. This shift

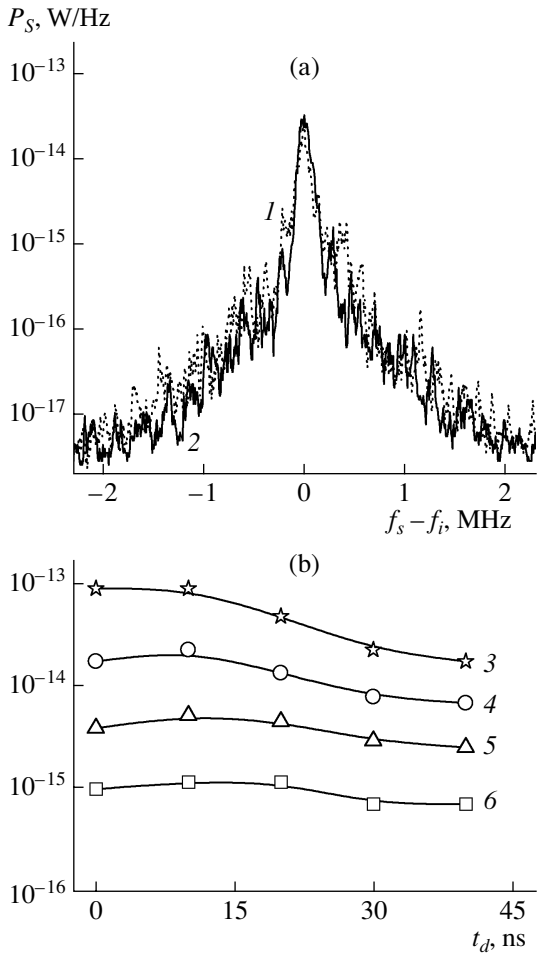

Fig. 2. (a) Reflectometic spectra at delay times of (*1*) 20 and (*2*) 30 ns and (b) the time dependences of the spectral components of the scattered signal: (*3*) 330 kHz, (*4*) 600 kHz, (*5*) 1 MHz, and (*6*) 1.5 MHz.

always remains much less than the spectrum width, which increases with wavenumber. Possible mechanisms for such behavior of the scattered spectrum with increasing fluctuation wavenumber are discussed below in Section 3.

At a lower magnetic field (B_T = 0.69 T), the UHR region ($r_{UH} \approx -13.9$ cm) is screened by the cutoff surface ($r_c \approx -14.9$ cm) and is inaccessible to the probing wave. In this case, the observed signal is caused by the reflectometric backscattering by density fluctuations. A specific feature of this experiment is that the cutoff surface is located very close to the antenna. The intensity of the scattered signal in this case was higher by 10 dB than for the UHR scattering. Figure 2a shows the reflectometric spectra for measurement delay times of 20 (curve *1*) and 30 ns (curve *2*). It can be seen that the spectra differ slightly from one another and are considerably narrower than those in Fig. 1. The dependences of the intensity of the scattered signal on the delay time for $f_s - f_i$ from 0.3 (curve *3*) to 1.5 MHz (curve *6*) also differ strongly from the case of backscattering in the UHR region. When the diagnostics operated as a reflectometer, the intensity of the signal gradually decreased with increasing delay time (Fig. 2b). At frequency shifts of $f_s - f_i > 0.3$ MHz, the response from the probing wave was observed for 40 ns, which was more than two orders of magnitude longer than the time required for the wave to propagate once from the antenna to the cutoff surface and back. This means that, in this case, the probing and scattered waves pass multiply between the cutoff and the antenna horn (as is in a high-Q cavity) and the scattered signal is formed over a quite long time.

3. SIMULATIONS OF ENHANCED-SCATTERING SPECTRA

The key feature of the frequency spectra of the signals backscattered from the UHR region is that they are rather broad and that their width increases with wavenumber q_R. In a first approximation, the spectrum width is proportional to q_R; as a result, different spectra become similar to one another after scaling the abscissa by a factor equal to the ratio of the corresponding delay times or wavenumbers.

To explain the revealed features of the spectra, we performed simulations of the signal backscattered from the UHR region. In accordance with the aforesaid, we assumed that the intensity of the observed signal is proportional to the product of the three factors: $p_{BS} \sim \rho_{BS}(q_R)S(q_R)F(\Omega/q_R)$, where $\rho_{BS}(q_R)$ is the enhanced-scattering efficiency (Fig. 1c, curve *6*); the factor $S(q_R)$ describes the radial-wavenumber spectrum of short-scale fluctuations; and the factor $F(\Omega/q_R)$ (where $\Omega = 2\pi(f_s - f_i)$) describes the observed features of the frequency spectrum of the signal. The wavenumber spectrum of short-scale fluctuations was taken as a power function $S(q_R) = 1/q_R^\alpha$ with an exponent α that is not known a priori and should be found by fitting the measured spectra by a model dependence. Several physical mechanisms were proposed to describe the frequency dependence $F(\Omega/q_R)$.

The first mechanism for the broadening of the frequency spectrum is related to the Doppler shift caused by the motion of short-scale density fluctuations in the poloidal direction in the course of plasma rotation: $\Omega = q_\theta V_\theta$, where q_θ is the poloidal component of the wave vector of the scattering fluctuations and V_θ is the plasma poloidal rotation velocity. Since the antennas oriented along the equator have finite beam widths, the sign of q_θ is different on the different sides from the equatorial plane. The spectrum contains both positive and negative frequencies Ω, and its width depends on the spot size of the antenna beam on the UHR surface. The misalignment of the antenna patterns relative to the equatorial plane should result in a shift of the frequency spectrum as a whole.

The second mechanism is similar to the first but takes into account the poloidal motion of fluctuations (rather than the plasma rotation) with the phase velocity determined by the dispersion of drift waves: $\Omega = q_\theta V_\theta$, where V_θ is the electron diamagnetic drift velocity. A specific feature of the second mechanism is that the measured frequencies are interpreted as the eigenfrequencies of the drift turbulence, which is responsible for scattering.

In both cases, the increase in the spectrum width with increasing q_R can be attributed to the increase in the poloidal component of the wave vector of the probing wave $k_{i\theta}$ in the UHR region [13, 14]. Such an increase is typical of toroidal systems, in which the UHR surface does not coincide with a magnetic surface because the magnetic field is nonuniform along the major radius (Fig. 3a). In these systems, the projection of the wave vector onto the gradient of the permittivity tensor component $\varepsilon = 1 - \omega_{pe}^2/(\omega_i^2 - \omega_{ce}^2)$ increases sharply in the vicinity of the resonance; as a result, the wave vector of the probing wave is oriented almost perpendicular to the UHR surface (Fig. 3a, curve *7*). The projection of the wave vector onto the magnetic surface (curve *8*) also increases considerably. Figure 3b shows the ray trajectories for an extraordinary wave launched from the high-field side in the equatorial plane at different angles θ: from 4° to 20° (curves *1*–*5*) and from –4° to –20° (curves *1*'–*5*'). These trajectories were calculated for an equilibrium configuration of a toroidal discharge (in particular, with allowance for the Shafranov shift of the magnetic surfaces). The positions of the UHR surface and the limiter are shown by curves *7* and *6*, respectively. The angles ±8° for rays *2* and *2*' correspond to a decrease in the antenna directional pattern by 3 dB. Solid lines in Fig. 3c show the dependences $k_{i\theta}(k_{ir})$ calculated by ray tracing for the same launching angles. Far from the UHR region, the absolute value of the radial wavenumber does not exceed its vacuum value $k_0 \approx 6$ cm^{-1} and the poloidal wavenumber increases toward the discharge axis to a value of about k_0 and then decreases. The poloidal wavenumber increases again near the UHR surface; simultaneously, the radial wavenumber k_{ir} increases sharply. It can be seen from Fig. 3c that the dependence $k_{i\theta}(k_{ir})$ is almost linear for different initial values of $k_{i\theta 0}$ and is described by the following analytic expression for the projection of the resonance component of the wavenumber on the normal to the UHR surface:

$$\frac{k_{i\theta}}{k_{ir}} \approx \frac{(\nabla\varepsilon)_\theta}{(\nabla\varepsilon)_r} = \left.\frac{y}{x - rR(\omega_{pe}^2)_r'/(2\omega_{ce}^2)}\right|_{UHR}, \qquad (3)$$

where x and y are the coordinates of the intersection point of the ray trajectory with the UHR surface, $R = x + R_0$, $r^2 = x^2 + y^2$, and $(\omega_{pe}^2)_r' = \partial\omega_{pe}^2/\partial r$. The dependences calculated by expression (3) (dashed lines) and by ray tracing (solid lines) coincide not only qualita-

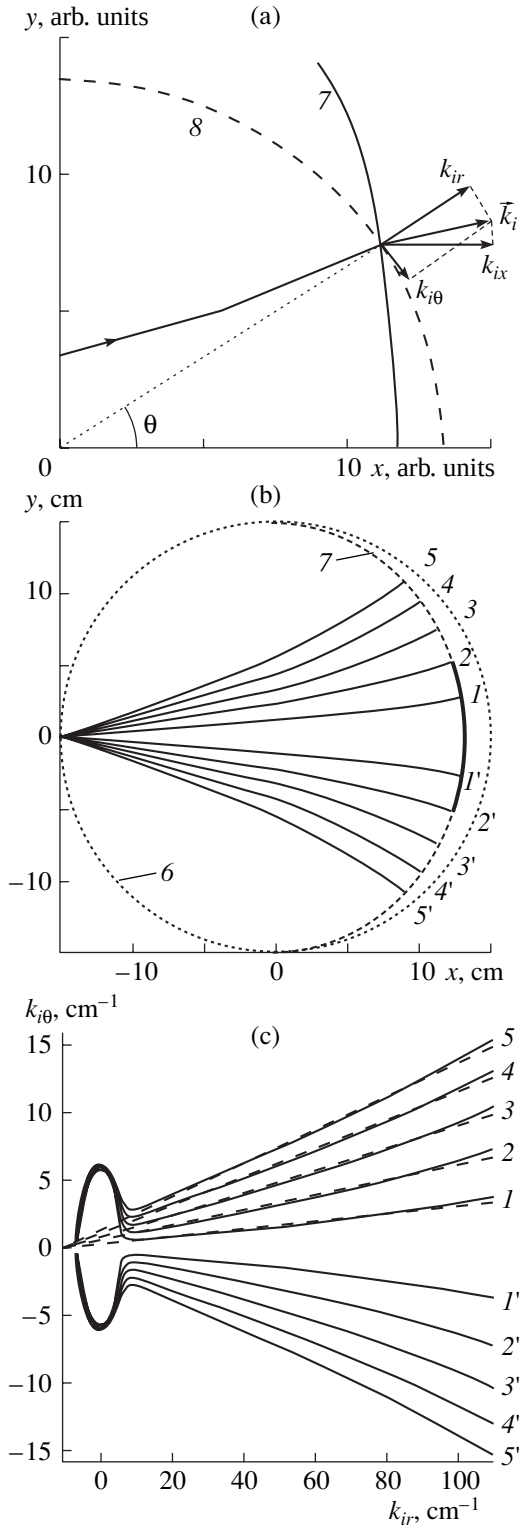

Fig. 3. (a) Scheme of projecting the wave vector of the probing wave in the UHR region on the poloidal direction; curves *7* and *8* show the positions of the UHR region and magnetic surface, respectively. (b) Ray trajectories for launching angles of (*1*, *1*') ±4°, (*2*, *2*') ±8°, (*3*, *3*') ±12°, (*4*, *4*') ±16°, and (*5*, *5*') ±20°; curve *6* shows the position of the limiter. (c) The poloidal wavenumber as a function of the radial wavenumber for the same launching angles; the solid lines show the ray tracing trajectories, and the dashed lines correspond to calculations by formula (3).

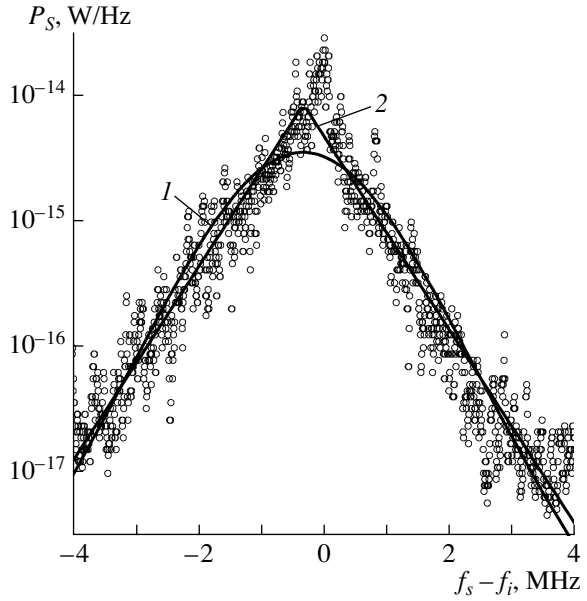

Fig. 4. Approximation of the measured spectrum for a delay time of 10 ns (circles) by the (*1*) poloidal and (*2*) radial models.

tively, but also quantitatively. The ordinate of the intersection point of the UHR surface with a ray launched from the equatorial plane at a small angle is a linear function of the launching angle; as a result, according to formula (3), the poloidal wavenumber of the probing wave in the UHR region is proportional to both the radial wavenumber and this angle, $k_{i\theta} \sim \beta k_{iR}\theta$. Since the Bragg scattering conditions $q_R = -2k_{iR}$ and $q_\theta = -2k_{i\theta}$ are satisfied, one can expect that the spectrum of the scattered signal with allowance for the Doppler broadening will be determined by the directional patterns $p_i(\theta)$ of the launching and receiving antennas, which are assumed to be identical, and the backscattered signal will be proportional to

$$p_{BS} \sim \frac{\rho_{BS}(q_R)}{q_R^\alpha} p_i^2\left(\frac{\Omega}{\beta q_R V_\theta}\right). \quad (4)$$

Using this expression and taking into account the actual antenna directional pattern, we approximated the spectra measured for different magnetic fields (for x_{UH} from 12.0 to 14.8 cm). The approximation procedure consisted of choosing the parameters V_θ and α at which model dependence (4) best fitted the measured spectra (Figs. 1a, 1b). The approximation quality can be judged from Fig. 4, in which one of the measured spectra (for t_d = 10 ns) is shown by circles and the dependence calculated by expression (4) is shown by curve *1*. The values of the poloidal velocities required to adequately describe the spectra lie within the range from $V_\theta = (2.2 \pm 0.5) \times 10^6$ cm/s (at x = 12 cm) to $V_\theta = (4.5 \pm 0.5) \times 10^6$ cm/s (at x = 14.8 cm). These values are substantially larger than the plasma poloidal rotation velocity $V_{rot} \approx$ (1–2) $\times 10^5$ cm/s, which was measured previously by the spectroscopy of impurities in the FT-1 tokamak under similar discharge conditions [15]. This might seem an important argument in favor of the assumption that the observed frequencies are the fluctuation eigenfrequencies. However, the velocity V_θ also exceeds the electron diamagnetic drift velocity $|\mathbf{V}_{dr}| = |cT_e[\nabla n_e \times B_T]/(n_e e B_T^2)|_{UHR}$, which varies from 3×10^5 (for x = 12 cm) to 3×10^6 cm/s (for x = 14.8 cm) under the FT-1 conditions. Of course, short-scale density fluctuations propagating in the radial direction (it is these fluctuations to which the enhanced-scattering diagnostics is sensitive) do not necessarily satisfy the simple linear dispersion relation $\Omega = q_\theta V_\theta$, which holds for large-scale drift fluctuations. In particular, the dispersion relation for small-scale fluctuations can be modified due to the presence of instabilities related to the electron and ion temperature gradients [16]: these instabilities can increase the poloidal phase velocity of fluctuations. On the other hand, such abnormally high poloidal velocities can be evidence of an additional mechanism for spectrum broadening.

The third mechanism for the formation of the observed frequency spectrum [17] is related to the fact that the scattering occurs in a layer with developed turbulence. The signal backscattered from the UHR region is caused by the short-scale turbulent component with a wavelength of ~0.05 cm, whereas the tokamak turbulence primarily consists of intense large-scale perturbations with typical wavenumbers of $q_\theta \sim 0.3\rho_{ci}$, corresponding to centimeter wavelengths (here, ρ_{ci} is the ion cyclotron radius). Plasma motion caused by these large-scale perturbations results in the Doppler broadening of the signal scattered by small-scale fluctuations that are entrained by the long-scale turbulent flow: $\Omega = q_R V_R$, where V_R is the equatorial projection of the turbulent flow velocity in the UHR region. The velocity V_R is a random quantity; this allows us invoke the concept of the velocity distribution function of the turbulent flow $f(V_R)$. The fact that, in this model, the spectrum width increases with increasing measurement delay time follows naturally from the proportionality between the frequency shift and the wavenumber q_R, whereas the shape of the spectrum is determined by the distribution function of the turbulent flow over radial velocities, $f(V_R) = f(\Omega/q_R)$. In this case, we used an approximation procedure similar to that described above. In particular, the following expression for the enhanced-scattering signal was used:

$$p_{BS} \sim \frac{\rho_{BS}(q_R)}{q_R^\alpha} f(\Omega/q_R). \quad (5)$$

In simulations, we considered different types of distribution functions. An example of the best fit of the spectrum (for t_d = 10 ns) with the use of an exponentially decaying (on the linear scale) function $f(\Omega/q_R)$ is illus-

trated in Fig. 4 (curve *2*). The r.m.s. velocity that provided the required broadening of the spectra increased from $\sqrt{\langle V_R^2 \rangle} = (1.5 \pm 0.5) \times 10^4$ cm/s to $\sqrt{\langle V_R^2 \rangle} = (3 \pm 0.5) \times 10^4$ cm/s as the magnetic field B_T was increased so that the UHR region shifted to the plasma periphery. Unfortunately, it was impossible to perform direct measurements (say, with probes) of the radial-velocity distribution function of the turbulent flow at the plasma periphery in this experiment. A comparison of the quantity $\sqrt{\langle V_R^2 \rangle}$ at the plasma periphery with the deviation of the velocity V_{turb} from its mean value measured with the help of probes located behind the limiter edge in an ohmically heated plasma in the FT-2 tokamak [18], which is similar to the FT-1 in many parameters, shows that the former quantity exceeds the latter by a factor of 2 to 3: $\sqrt{\langle V_R^2 \rangle} \approx 2.5 V_{turb}$.

The fourth mechanism for the formation of backscattered spectra is related to the broadening of the frequency spectrum due to the multiple small-angle scattering of the probing and backscattered waves by long-scale fluctuations before and after scattering by short-scale fluctuations in the UHR region. In [19, 20], it was shown that small-angle scattering, as well as backscattering, is enhanced in the UHR region. For this reason, small-angle scattering switches to the regime of multiple scattering first of all in the vicinity of the UHR surface, where long-scale plasma density fluctuations causing the slow motion of the UHR surface and the distortion of its shape result in the deep phase modulation of the probing and backscattered waves; in the broadening of their spectra; and, eventually, in the broadening of the backscattered spectrum. It is worth noting that, as for the mechanisms discussed above, the broadening of the signal backscattered from the UHR region turns out to be proportional to the wavenumber of the short-scale scattering fluctuations:

$$p_{BS} \sim \frac{\rho_{BS}(q_R)}{q_R^{\alpha}} \exp\left(-\frac{(\omega_s - \omega_i)^2}{\frac{\delta n^2}{n_{UH}^2} \langle \Omega^2 \rangle l^2 q_R^2} \right), \qquad (6)$$

where the quantities $\rho_{BS}(q_R)$ and α were defined previously, δn^2 is the mean square of density perturbations, $\sqrt{\langle \Omega^2 \rangle}$ is the spectral width of turbulent density perturbations at a level of –3 dB, and l is the scale of plasma inhomogeneity in the UHR region. The physical reason for the width of the scattered spectrum depending linearly on the wavenumber of backscattering fluctuations is that the residence time of the probing and backscattered waves in the UHR region increases linearly with wavenumber. A comparison of formula (6) with the experimental data shows that, for $\sqrt{\langle \Omega^2 \rangle} \approx 200$ kHz (an estimate for the spectral width of long-scale turbulence obtained from the results of reflectometric measurements; see Fig. 2a), relative density perturbations of $\delta n/n_{UH} \approx 4 \times 10^{-2}$ are sufficient to explain the observed spectral width of the signal backscattered from the UHR region. This level of turbulent density perturbations is typical of the core plasma in tokamak discharges [21]. An argument in favor of this mechanism is also that the measured spectral width of the backscattered signal increases substantially (almost twofold) when the UHR region shifts to the plasma periphery, where the level of long-scale turbulence is usually higher [22] and reaches a value of $\delta n/n_{UH} = 10^{-1}$.

As the UHR region shifts outward, the second approximation parameter decreases (irrespective of the model used) from $\alpha = 3 \pm 0.5$ (at $x = 12$ cm) to $\alpha = 2 \pm 0.5$ (at $x = 14.8$ cm). This can be interpreted as an increase in the fraction of short-scale fluctuations in the edge plasma. Such behavior can be explained by a decrease in the temperature toward the plasma periphery and by the related decrease in the characteristic spatial scales (say, the Larmor radius). Extrapolating the dependence $1/q_R^3$ to large scales and assuming that the turbulence is isotropic in a plane perpendicular to the magnetic field, we obtain a rough estimate for the relative level of density fluctuations, $\delta n/n_{UH} \geq 10^{-2}$, which is appropriate for explaining the characteristic features of the backscattered spectrum by the action of the above mechanism of multiple small-angle scattering.

Another interesting feature of the measured spectra (Figs. 1a, 1b) is their slight asymmetry. The left wing of the spectrum is always higher than the right wing; this can be interpreted as a leftward shift of the spectrum as a whole. This feature can be explained in different ways, depending on the adopted mechanism for the formation of the backscattered spectrum.

In the frameworks of the first and second models, the small shift of the spectrum toward negative difference frequencies $f_s - f_i$ can be explained by the misalignment of the antenna directional pattern relative to the equatorial plane. The misalignment angle of $\varphi \approx 1.5° \pm 1°$, which was determined from the measured spectra, turned out to be less than the error in the positioning of the antennas in the tokamak chamber; i.e., this misalignment is quite realistic.

When explaining the asymmetry of the spectra by invoking the third mechanism, it is necessary to assume that the turbulent flux has a nonzero average velocity $V_{0R} = (1.5 \pm 0.5) \times 10^4$ cm/s. In our case, the velocity V_{0R} is directed from the center to the edge of the plasma column; this gives a small red frequency shift of the spectrum.

It follows from the results of our simulations that the first and second mechanisms for the formation of the backscattered spectrum, which are related to the poloidal rotation of fluctuations, lead to more problems in interpreting the characteristic features of the scattered

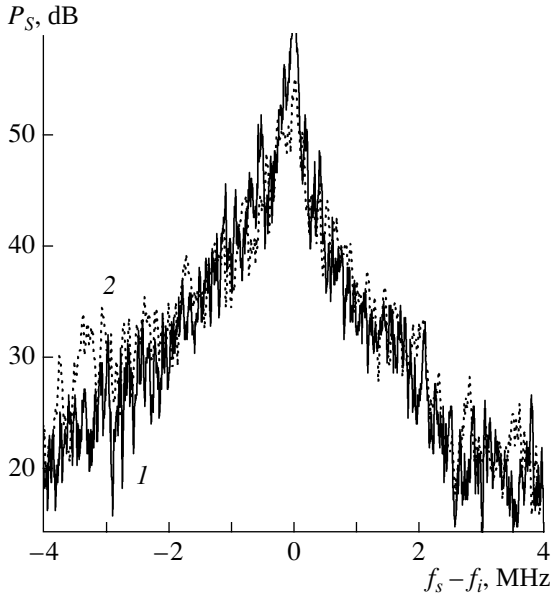

Fig. 5. Enhanced-scattering spectra for opposite minor cross sections of the tokamak for two antenna beam widths: (*1*) ±8° and (*2*) ±15°.

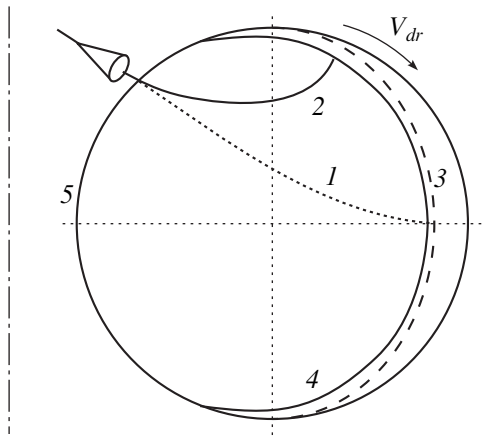

Fig. 6. Scheme of an experiment with the off-equatorial launching of the probing wave: (*1*) the central ray trajectory and (*3*) the position of the UHR region for $B_T \approx 1$ T and $n_e(0) \approx 10^{13}$ cm^{-3} and (*2*) the central ray trajectory and (*4*) the position of the UHR region for $B_T \approx 0.85$ T and $n_e(0) \approx 2 \times 10^{13}$ cm^{-3}.

spectra observed in the FT-1 tokamak; hence, it is unlikely that these mechanisms are dominant. This is also confirmed by observing backscattered spectra with the help of horns positioned in the opposite (along the torus) minor cross section and having a twice as wide directional patterns. The operating conditions were chosen such that they were very similar to those in the first cross section. Figure 5 shows the spectra (unresolved in q_R) obtained in these two cross sections. The spectrum for antennas with wide directional patterns are shown by the dashed line (curve *2*), and the spectrum for antennas with a half as wide patterns is shown by the solid line (curve *1*). It can be seen that the spectra are very similar to one another; this allows us to conclude that the mechanisms related to the poloidal rotation do not play a governing role in the broadening of the backscattered spectrum in the FT-1 tokamak.

At the same time, these mechanisms can be used to interpret the asymmetry of the backscattered spectra, as was shown by an additional experiment in which the same antenna was used to both launch the probing wave and receive the scattered radiation. The antenna was displaced by 45° in the poloidal direction relative to the equatorial plane (Fig. 6). For the parameters typical of our experiments, the central ray of the directional pattern reached the UHR region (surface *3*) in the equatorial plane (trajectory *1*). In a sense, this is equivalent to the conventional scheme of equatorial probing. At a lower magnetic field ($B_T = 0.85$ T) and a higher density ($n_e(0) = 2 \times 10^{13}$ cm^{-3}), a stronger refraction resulted in the displacement of the central ray upward from the equatorial plane (trajectory *2*). In these experiments, the scattered spectra unresolved in wavenumbers q_R (i.e., with continuous probing and reception) were measured. For probing, we used a standard 20-mW oscillator; for this reason, the valid-signal range in the spectral intensity at $|f_s - f_i| > 0.3$ MHz was only two orders of magnitude (Fig. 7). For typical experimental parameters, the scattered spectrum (curve *1*) was similar to that for the case of equatorial probing. Since a ferrite circulator was used for reception and the signal was received by the same antenna, the received signal at the probing frequency was much higher (in comparison to that in Fig. 1). For this reason, the spectra in Fig. 7 contain a high line at $-0.3 < f_s - f_i < 0.3$ MHz, which is cut by the upper frame of the figure at a level of –30 dB. In experiments with a higher density, the left wing of the spectrum grew substantially, whereas the right wing shrank somewhat (curve *2*).

If the formation of the spectrum were governed by first two mechanisms considered in the previous section, then, in view of such a high skewness of the directional pattern, one could expect a substantial frequency shift of the scattered spectrum. In the presence of an intense line at $-0.3 < f_s - f_i < 0.3$ MHz, it difficult to identify the maximum of the scattered spectrum; however, the strong transformation of its wings can be interpreted as a frequency shift. The direction of the shift should depend on the direction of the poloidal velocity V_θ. Taking into account the direction of the toroidal magnetic field, we can conclude that, in our case, the directions of the diamagnetic drift velocity V_{dr} (Fig. 5) and velocity V_θ coincide, which results in a red frequency shift.

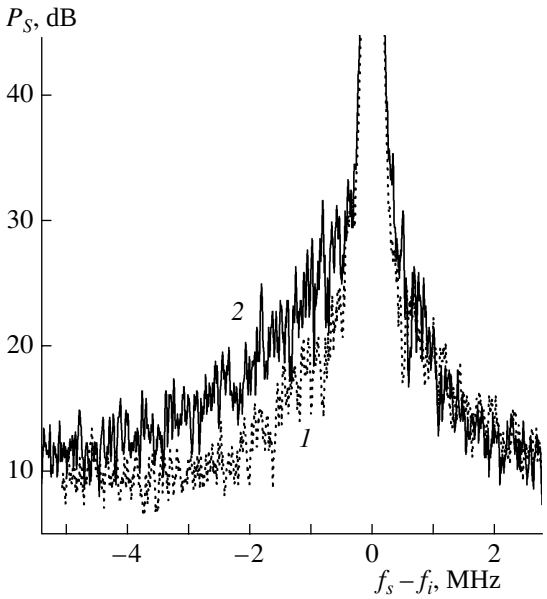

Fig. 7. Enhanced-scattering spectra measured in an experiment with the off-equatorial launching of the probing wave for (*1*) $B_T \approx 1$ T and $n_e(0) \approx 10^{13}$ cm^{-3} and (*2*) $B_T \approx 0.85$ T and $n_e(0) \approx 2 \times 10^{13}$ cm^{-3}.

4. CONCLUSIONS

Time-of-flight enhanced-scattering wavenumber-resolved radar diagnostics has been used to perform local measurements of low-frequency short-scale turbulence in the FT-1 tokamak. It has been shown that the width of the scattered spectrum increases with increasing radial wavenumber of the scattering fluctuations. Several possible mechanisms for the formation of such spectra have been proposed. The results of numerical simulations of the scattered signals and the data from additional experiments have been used to reveal the dominant mechanisms for the spectral broadening under the FT-1 experimental conditions. These mechanisms are related to the effect of multiple small-angle scattering of both the probing wave and the waves backscattered in the UHR region by long-scale density fluctuations and to the Doppler effect caused by the entrainment of short-scale fluctuations by the long-scale turbulent flow. The analysis of these two mechanisms makes it possible to obtain information about the amplitude of long-scale turbulent density fluctuations and to estimate the velocity distribution function of this turbulence, which is one of the most important problems of plasma turbulence diagnostics.

ACKNOWLEDGMENTS

This work was supported in part by the Russian Foundation for Basic Research (project nos. 01-02-17926, 03-02-06788, and 04-02-16534), the RF Program for State Support of Leading Scientific Schools (project no. NSh-2159.2003.2), INTAS (grant nos. YSF2002-104 and 01-2056), and the Netherlands Organization for Scientific Research (NWO) (grant nos. 0.47.009.009 and 047.016.015).

REFERENCES

1. A. D. Piliya, Zh. Tekh. Fiz. **36**, 2195 (1966) [Sov. Phys. Tech. Phys. **11**, 1639 (1967)].
2. I. Fidone, Phys. Fluids **16**, 1680 (1973).
3. K. M. Novik and A. D. Piliya, Plasma Phys. Controlled Fusion **35**, 357 (1994).
4. E. Z. Gusakov and A. D. Piliya, Pis'ma Zh. Tekh. Fiz. **18** (10), 63 (1992) [Sov. Tech. Phys. Lett. **18**, 325 (1992)].
5. B. Brusehaber, E. Z. Gusakov, M. Kramer, *et al.*, Plasma Phys. Controlled Fusion **36**, 997 (1994).
6. V. I. Arkhipenko, B. Brusehaber, V. N. Budnikov, *et al.*, Plasma Phys. Controlled Fusion **37**, 347 (1995).
7. V. I. Arkhipenko, V. N. Budnikov, E. Z. Gusakov, *et al.*, in *Proceedings of the 19th EPS Conference on Controlled Fusion and Plasma Physics, Innsbruck, 1992*, ECA **16C** (II), p. 1203.
8. V. I. Arkhipenko, V. N. Budnikov, E. Z. Gusakov, *et al.*, Pis'ma Zh. Éksp. Teor. Fiz. **59**, 393 (1994) [JETP Lett. **59**, 420 (1994)].
9. B. Brusehaber, E. Z. Gusakov, N. M. Kaganskaya, *et al.*, Pis'ma Zh. Tekh. Fiz. **22** (22), 21 (1996) [Tech. Phys. Lett. **22**, 913 (1996)].
10. A. D. Gurchenko, E. Z. Gusakov, V. V. Korkin, *et al.*, Fiz. Plazmy **28**, 532 (2002) [Plasma Phys. Rep. **28**, 489 (2002)].
11. I. P. Gladkovskiĭ, V. E. Golant, V. V. D'yachenko, *et al.*, Zh. Tekh. Fiz. **43**, 1632 (1973) [Sov. Phys. Tech. Phys. **18**, 1029 (1973)].
12. E. Z. Gusakov, N. M. Kaganskaya, K. M. Novik, and V. L. Selemir, Pis'ma Zh. Tekh. Fiz. **21** (14), 11 (1995) [Tech. Phys. Lett. **21**, 541 (1995)].
13. A. D. Gurchenko, E. Z. Gusakov, M. M. Larionov, *et al.*, in *Proceedings of the 26th EPS Conference on Controlled Fusion and Plasma Physics, Maastricht, 1999*, ECA **23J**, p. 37.
14. D. G. Bulyiginskiy, A. D. Gurchenko, E. Z. Gusakov, *et al.*, Phys. Plasmas **8**, 2224 (2001).
15. S. I. Lashkul and A. D. Lebedev, in *Proceedings of the 13th Chechoslovakian Seminar on Plasma Physics and Technology, Liblice, 1985.*
16. W. Horton, Rev. Mod. Phys. **71**, 735 (1999).
17. C. Hanuise, J. P. Villain, D. Gresillon, *et al.*, Ann. Geophys. **11**, 29 (1993).
18. L. A. Esipov, I. E. Sakharov, E. O. Chechik, *et al.*, Zh. Tekh. Fiz. **67** (4), 48 (1997) [Tech. Phys. **42**, 367 (1997)].
19. E. Z. Gusakov and A. V. Surkov, Fiz. Plazmy **27**, 1027 (2001) [Plasma Phys. Rep. **27**, 971 (2001)].
20. E. Z. Gusakov and A. V. Surkov, Fiz. Plazmy **28**, 898 (2002) [Plasma Phys. Rep. **28**, 827 (2002)].
21. F. C. Schuller, Transactions of Fusion Technology **25**, 125 (1994).
22. R. Nazikian and E. Mazzucato, Rev. Sci. Instrum. **66**, 392 (1995).

Translated by N.F. Larionova

Plasma Physics Reports, Vol. 30, No. 10, 2004, pp. 816–864. From Fizika Plazmy, Vol. 30, No. 10, 2004, pp. 877–929.

DUSTY PLASMA

Complex Plasmas IV: Theoretical Approaches to Complex Plasmas and Their Application[1]

V. N. Tsytovich*, G. E. Morfill, and H. Thomas****

**Prokhorov Institute of General Physics, Russian Academy of Sciences, ul. Vavilova 38, Moscow, 119991 Russia*
e-mail: tsytov@tp.lpi.ac.ru
*** Max Planck Institut für Extraterrestrische Physik, 85740 Garching, Postfach 1312, Germany*
e-mail: gem@mpe.mpg.de, thomas@mpe.mpg.de

Received September 26, 2002; in final form, December 23, 2003

Abstract—This paper completes a series of reviews devoted to the physics of complex plasmas, in which one of the components (dust) is in a crystalline or liquid state, while the others (electron, ions, and neutral atoms) are in a gaseous state. This review is devoted to the theoretical approaches used to describe complex plasmas so far. The main theoretical developments have been concentrated in the gaseous and weakly nonideal states of complex plasmas. Here, we describe the achievements in the new kinetic and new hydrodynamic approaches to complex plasmas. At present, only generalizations of the van der Waals approach for complex plasmas have been used to describe phase transitions and plasma condensation in complex plasmas. Here, criteria for transitions are described and compared with the existing experimental observations. Theoretical and numerical results for nonlinear structures, such as dust layers, dust voids, dust sheaths, and dust convective vortices, obtained by solving the stationary balance equations, are also discussed and compared with state-of-the-art experiments. At present, experiments in this field are progressing very fast, while theory is not advancing at the same rate of development. To further develop new theoretical models, one can use the elementary physical processes in complex plasmas described in the previous parts of the review. However, the detailed comparison of theory and experiments also needs more detailed experimental diagnostics of the phenomena observed. In the concluding part of our review, the trends in experiment and theory, as well as some existing applications, including industrial, environmental, and astrophysical ones, are described. © *2004 MAIK "Nauka/Interperiodica".*

1. THEORETICAL APPROACHES IN COMPLEX PLASMAS

1.1. Introduction

In the previous parts of our review, we described in detail the processes of dust charging in complex plasmas [1]; the elementary processes in complex plasmas [2], including the external forces that act on dust grains and dust–dust interactions; and state-of-the-art experiments [3].

We recall here the notation used in the previous parts of our review and used in this part as well. The quantity $P = n_d Z_d/n_i$ is the so-called Havnes parameter, showing the relative number of charges on the dust grains (here, n_d is the dust density, n_i is the ion density, and Z_d is the dust charge in units of elementary charge). In state-of-the-art experiments, the parameter P (which is always less than unity) is on the order of unity (the minimum value of P in state-of-the-art experiments is 0.5×10^{-2}. The dimensionless ion and electron densities are denoted as $n = n_i/n_{i,0}$ and $n_e \longrightarrow n_e/n_{i,0}$ ($n_{i,0}$ is a certain characteristic ion density, either the density far from the structures or the density corresponding the basic state, the parameters of which are determined by both the charge and power balance (see [2])). The small parameter $\tau = T_i/T_e$ is on the order of 10^{-2} in state-of-the-art experiments. The sharpness of a dust structure boundary is determined by another (much smaller) parameter $\tau_d = T_d e^2/T_e^2 z a$ (where a is the dust size and T_d is the dust temperature). In state-of-the-art experiments, τ_d is no larger than 2×10^{-3}, but it is usually on the order of 10^{-6}. The ion Debye radius is determined by the expression $\lambda_{Di} = \sqrt{T_i/4\pi n_{i,0} e^2}$.

To estimate the contributions from the various processes, we used in [3] expressions for the elementary processes in complex plasmas given in [2]. For simplicity, these processes were described by some average quantities, such as the electron, ion, and dust densities; the temperatures; and the ion drift velocity. The description of elementary processes in this form is very useful in applications. However, even in such a description, some processes are determined by the particle velocity distributions. For example, this is true for the charging currents [1], the ion drag force, and the dust–dust interactions [2], which depend strongly on the ion velocity distribution. For simplicity and to be able to perform some estimates, we have already given (see [2]) the results for the case of thermal distributions of electrons and ions. More general is a kinetic approach

[1] This article was submitted by the authors in English.

using velocity distribution functions for all of the components. This requires the use of a kinetic description of complex plasmas. A general kinetic theory of complex plasma should be more sophisticated than the standard plasma kinetic theory because of the openness of the system and the dust charge variability (see [4–8]). In general, even the foundations of the kinetic approach should be changed in complex plasmas [4]. We start here with showing the necessity of kinetic description using simple estimates for the thermalization time of the particle distributions, and will show that the kinetic description is indeed dictated by the parameters of the state-of-the-art experiments. We shall then recall briefly how the kinetic description is formulated in ordinary plasmas and emphasize the important role of fluctuations in such a description. It becomes obvious that, to formulate a basic description in the kinetic theory of complex plasmas, it is necessary to develop a more complicated description of fluctuations in complex plasmas as compared to that in ordinary plasmas. In particular, these fluctuations should take into account the variability of dust charges, the openness of the system, and the presence of external sources. The basic kinetic description in ordinary plasma theory is based on deriving equations containing collision integrals. The same needs to be performed for complex plasmas; above all, generalized collision integrals must be found. Thus, the ordinary kinetic approach cannot be used for complex plasmas and *new kinetic equations* must be found as the basic equations for the kinetic description of complex plasmas. This is one of the major problems in the theory of complex plasmas; the solving of this problem will lay the foundation for other methods for describing complex plasmas. If we take the velocity momenta of these equations, a hydrodynamic equation should be found. The *hydrodynamic description* of complex plasma will thus be based on a *new set of equations*. These, in turn, can be used for other theoretical models and for the numerical simulation of dust structures. The first steps toward the foundations of the new kinetic description of complex plasmas with several simplifying assumptions (see below) were made in [4–8], and the first hydrodynamic description with the elementary processes in complex plasmas taken into account was made in [9]. In [9], the new hydrodynamic equations were not derived from the general kinetic equations. This was performed in [8] and led both to the generalization of the coefficients used in [9] and to the description of new effects related to heat transport.

1.2. The Kinetic Approach in Complex Plasmas

1.2.1. Estimates for the thermalization of ion and electron distributions. Before discussing the first results of the theoretical approach to the kinetic description of complex plasmas, let us make some simple estimates of the thermalization processes for the parameters of the existing laboratory experiments and try to answer the following questions:

(i) Is changing the foundations of the kinetic theory only a superficial exercise in which one can use simple considerations for practical applications, or is an appropriate theoretical consideration dictated by the experiments?

(ii) Is it indeed necessary to reformulate the basic kinetic approach?

The first question can be reformulated as follows: Are the plasma particle distributions indeed thermal in state-of-the-art experiments, or can they be nonthermal? Is it possible to answer the question as to whether the particles are able to form a thermal distribution under experimental conditions when direct measurements are not performed? If the distributions are not thermal, then all of the coefficients describing the elementary processes should be modified and their value for the thermal distribution can serve only as a very rough estimate. The need for the development of the kinetic approach in complex plasmas then becomes obvious.

At this point, it should be remembered that complex plasmas have several components: electrons, ions, neutral atoms, and dust. Estimates will be different for different components. We can expect that the dust component should more often be found to be thermal due to strong dust interactions. For Coulomb dust–dust collisions, this is, in a certain sense, unimportant. Generally, however, when screening and collective interactions are taken into account, the theoretical problems of whether the dust can be distributed as thermal and what is the time scale of dust thermalization should be resolved. In some expressions for the processes in complex plasmas, there are integrals over the velocity of the electron and ion distribution functions and these integrals are typically only slightly sensitive to the details of these distribution functions (for example, the numerical coefficients change by a factor on the order of unity). However, we have examples [2] where, in some cases, these integrals can be very sensitive to the ion distribution function (as is the case with the presence of ion drift). If the particle distribution is not thermal, the estimates of the criteria of transition to a strongly coupled state using thermal distributions can be considered only as a rough first approach to get some intuitive conclusions for the processes determining this transition. In principle, the kinetic approach provides not only a detailed description of the transition to a strongly correlated state but can be checked experimentally on the kinetic level, since any dust grain motion can be detected during the transition. Such a full kinetic description that includes the transition to a strongly correlated state of a complex plasma does not as yet exist.

The first steps toward the description of the gaseous states of complex systems were made in [4–8] and in [10, 11]. The gaseous states will have many unusual kinetic features that can precede the conversion into a strongly correlated state. These can be investigated very simply on the kinetic level. The approaches of [4–8]

and [10, 11] are different, and the final equations, while formally similar, are also different. The difference is the starting points of the theory in [4–8] and [10, 11]. The authors of [4–8] use two-step averaging, where the first step deals with averaging with respect to the discreetness of the plasma components (electrons, ions, and neutrals) and the second step deals with averaging with respect to the dust component discreetness. There is no obejection to this two-step averaging; it can be used as a starting point in deriving the averaging kinetic equations describing the change in the distributions of electrons, ions and neutrals in the course of the charging process by introducing the corresponding cross sections for charging. The approach of [10, 11] introduces the charging process into the equations where all of the components are discreet. This is possible in principle, but difficulties are encountered in describing the charging process self-consistently. Therefore, it seems that the results of [10, 11] can be applied to the further theoretical treatments only for the cases where they coincide with the results of [4–8]. This coincidence does not always exist. For example, in both cases, the dust charge enters into the kinetic equations as a new variable, which leads to collision integrals that also describe diffusion with respect to dust charges, but the diffusion coefficients are different. The authors of [4–8] consider the average charge as changing self-consistently over time as the average distribution function varies over time. These equations are similar to quasilinear equations, and only the deviations from the regular change in the dust charge are considered as fluctuations. In the approach of [10, 11], such a division is not made and the equilibrium charge is not varying. It seems that it is not possible to exclude the division of the dust charge variation into the regular part and fluctuations, which is obvious from the approach of [4–8] and is not done in [10, 11]. Therefore, when speaking about fluctuations, the two approaches deal with different values. It is reasonable here to devote our attention primarily to the results obtained in [4–8].

We start with giving some theoretical estimates to help the reader understand whether we can expect the electron and ion distributions in complex plasmas can or will be nonthermal. This estimate is easy to perform using the approach of [4–8]. As was mentioned in the previous parts of this review, complex plasma systems with energy input into the system and with the injection of particles having nonthermal distributions are open systems. In particular, ionization by an RF field always creates nonthermal distributions of electrons and ions. Therefore, the question as to whether the plasma particles are distributed thermally or not is related to the question of the rate of the mechanism making the distributions thermal. It is well known from ordinary plasma treatment that, in plasmas, binary particle collisions can indeed thermalize the particle distributions. In complex plasmas, there are not only binary collisions between charged particles but also their collisions with neutrals and dust grains. We need to estimate the rates of both kinds of collisions to find whether they can thermalize the electron and ion distributions. It is obvious that electrons and ions are created in the ionization process with nonthermal distributions. Indeed, we mentioned that the plasma particle distributions are usually formed under conditions of a balance between ionization (ion–electron pair creation) and the absorption of electrons and ions by the dust grains. When discussing the elementary processes in complex plasmas [2], we wrote the corresponding two terms for ionization and losses in the continuity equation for the ion density. These terms describe an effect integral with respect to the particle distribution in velocities. To describe these effects kinetically, we should write the corresponding term in the equation for the particle distribution function. It will contain cross sections for ionization that are velocity dependent. We should multiply these cross sections by the electron distribution function instead of the electron density, as was done in [2]. Thus, electron–ion pairs with different velocities are created with different efficiencies and, therefore, the source does not create thermal electron and ion distributions. The process of the absorption of electrons and ions by dust is also selective in velocities: the fast electrons are mainly absorbed because the low-energy electrons are reflected by the dust grains. Since the cross section for absorption increases with decreasing ion velocity, the low-energy ions are mainly absorbed. As a result, the distributions of the ions and electrons that remain unabsorbed by the dust turn out to be nonthermal [6, 11]. The question arises as to whether electron–electron, ion–electron, or ion–ion collisions can thermalize the particle distributions. In estimating the effect of the thermalization of electrons and ions by ion–ion and electron–ion collisions, it is necessary to consider in more detail the values of the impact parameters in ion/electron–dust collisions. As in [2], we will consider only singly ionized ions. The electron–ion collision frequency ν_{ei} and the electron–electron collision frequency ν_{ee} are of the same order of magnitude. We give an exact expression for the former and an approximate estimate that follows from elementary considerations:

$$\nu_{ei} = \frac{4\sqrt{\pi}n_e e^4 \Lambda}{3\sqrt{m_e}T_e^{3/2}} \approx n_e v_{Te} \pi r_{\mathrm{col}}^2, \quad r_{\mathrm{col}} = \frac{e^2}{T_e}, \qquad (1)$$

where $\Lambda = \ln(p_{\max}/p_{\min})$ is the so-called "Coulomb logarithm" and $p_{\max}$ and $p_{\min}$ are the maximum and the minimum impact parameters in Coulomb collisions. The exact expression given by the present theory and the approximate result (1) differ by the numerical factor on the order of unity in the expression for the Coulomb Logarithm. For estimates, we will use expression (1) with the Coulomb logarithm in its standard form. In state-of-the-art low-temperature experiments with a complex plasma, the Coulomb logarithm is not large and is on the order of 2–3, and approximate expression (1)

gives a reasonable estimate. The exact and approximate expressions for the ion–ion collision frequency are

$$\nu_{ii} = \frac{2\sqrt{\pi}n_i e^4 \Lambda}{3\sqrt{m_e}T_i^{3/2}} \approx n_e v_{Te}\pi r_{\rm col}^2, \quad r_{\rm col} = \frac{e^2}{T_i}. \qquad (2)$$

The collision frequencies ν_{ee}, ν_{ei}, and ν_{ii} determine the rate at which electrons and ions are thermalized. The ion–dust and electron–dust collisions were considered in [2] by taking into account the dust charge factor Z_d^2 in Coulomb interactions and using the Coulomb logarithm with the maximum impact parameter equal to λ_{Di} (the value of the minimum impact parameter was not specified). In this case, the Coulomb logarithm can differ from the standard one and needs a more detailed consideration. As a first step, we will consider the Coulomb logarithm for electron/ion–dust collisions to be on the same order of magnitude as that for electron/ion–electron/ion collisions. We will then consider in detail the difference between these Coulomb logarithms. Let us compare the elementary expression for the ion–dust collision frequency with the ion–ion collision frequency. Note that it will contain the factor $Z_d^2 n_d$ instead of n_i; thus, we have [2]

$$\nu_{id} \approx PZ_d\nu_{ii}. \qquad (3)$$

Therefore, ion–dust collisions are dominant for

$$P \gg \frac{1}{Z_d}, \qquad (4)$$

which is satisfied in all of the state-of-the-art experiments for the gaseous state of complex plasma and for the transition to a strongly coupled state. Thus, ion–ion collisions are not able to restore the thermal ion distribution. The same is true for the thermalization of the electron distribution. Inequality (4) was first derived in [12] and further used in [4, 13].

We should also consider the difference between Coulomb logarithms in ion/electron–dust collisions and in ion/electron–ion/electron collisions. Note that ion/electron–dust collisions are somewhat more complicated, since one must also determine the smallest value of the impact parameter in the Coulomb logarithm. As was mentioned in [1, 2], in describing the orbit limited (OL) approach, there can be significant (depending on the particle energy) absorption on the grains or elastic Coulomb scattering by the grains. Thus, the smallest impact parameter can be related to absorption on the grains. However, there is also the possibility of small-angle and large-angle (say $\pi/2$) scattering. Usually, large-angle scattering makes the greatest contribution to the scattering process, and the Coulomb logarithm contains a minimum impact parameter corresponding to the scattering by the angle $\pi/2$. The question is whether there is a "space" between the impact parameter for scattering by the angle $\pi/2$ and the impact parameter for absorption. The electron absorption cross section averaged over the thermal distribution (see OL cross sections in [1]) is $\pi a^2\exp(-z) = \pi p_{e,\,\rm abs}^2 = \pi a^2 z/\sqrt{\tau\mu}$ (with $\mu = m_i/m_e$) or $p_{e,\,\rm abs} \approx a\exp(-z/2) \approx a\sqrt{z}/(\tau\mu)^{1/4}$, while for the ion absorption, we have $p_{i,\,\rm abs} \approx a\sqrt{z}/\tau$. The impact parameters corresponding to the scattering by $\pi/2$ can be estimated from the condition that the kinetic particle energy is on the order of the grain electrostatic energy: $p_{e,\,\rm min} = Z_d e^2/T_e = az$, $p_{i,\,\rm min} = Z_d e^2/T_i = az/\tau$. Therefore, for electrons, there is large-angle scattering only when $\sqrt{z} > \mu\tau^{1/4}$ (which is usually not the case), while there is large-angle scattering for ions when $\sqrt{z}/\tau < p < z/\tau$. Thus, we need be concerned with the problem of large-angle scattering only for ions. The ion–dust collision frequency for scattering by the angle $\pi/2$ is $\nu_{id} = n_d\pi Z_d^2 v_{Ti}/2T_i^2$ and can be found from the frequency of multiple scattering by substituting $9\sqrt{\pi}/8$ for $\ln\Lambda$. The effect of charging on electron scattering by grains can be considered as scattering by the enhanced ion density in the vicinity of a grain (this effect should be classified as a nonlinear effect related to the influence of nonlinear screening on collisions). One may consider the electron scattering as being caused by the excess of ions in the Debye cloud. The excess of the ion density can be estimated as $\delta n_i \approx 3Z_d/4\pi\lambda_{Di}^3$, and the mean size of the Debye cloud is $\sqrt{\pi}\lambda_{Di}$. The collision frequency related to the multiple Coulomb scattering during the passage of an electron through many such Debye clouds is $\nu_{ei,\,d} \approx 3\pi^{3/2}n_d v_{Te}Z_d e^4/T_e^2 = (8/9\pi\sqrt{2}P)\nu_{ei}$; therefore, these additional nonlinear ion–electron collisions can exceed the usual ones only for $P > 8/9\pi\sqrt{2} \approx 0.2$. Since $P < 1$ and since, for P on the order of unity, condition (4) is satisfied with a large margin, ion–dust collisions are dominant under the conditions of state-of-the-art experiments.

Thus, neither large-angle scattering nor nonlinear scattering can change the important estimate (4), showing that, for P on the order of unity, ion–ion collisions cannot provide sufficiently fast thermalization and the ions must be nonthermal in complex plasmas.

We can worry that ion–neutral collisions can probably serve as a mechanism for the restoration of the ion thermal distribution since the neutral atoms come into contact with the walls and, therefore, have a thermal distribution with a temperature close to the wall (chamber) temperature. We write the condition for the ion–

dust collision frequency to be larger than the ion–neutral collision frequency:

$$\frac{a}{\lambda_{Di}^2\tau}P\lambda_{in} \gg 1. \quad (5)$$

Let us recall that, in comparing the friction force due to ion–dust collisions with the friction force due to ion–neutral conditions, one should use λ_{Di}/τ as the effective collision length, not because the real collision length in ion–neutral collisions is larger by τ but because the real length in ion–dust collisions have an additional factor, z/τ. For the existing experimental data and P on the order of unity, ion–dust collisions are dominant at $a >$ 0.003 μm, which is also satisfied in experiments on strong correlation in which larger dust grains usually have a larger dust charge and stronger dust–dust interactions. Thus, there are no efficient mechanisms that restore the thermal distributions of electrons and ions. The kinetic description can also be important for describing in a more exact way the conditions for the conversion of the system to a strongly coupled state.

1.2.2. Role of fluctuations in the general kinetic approach. Before starting to outline the kinetic description of processes in complex plasmas, we must recall the description of kinetic processes on ordinary plasmas. Let us briefly describe the derivation of collision integrals in ordinary plasmas and point out the important role of fluctuations. Several aspects of the procedure often used to obtain the kinetic description of various systems are important. The general approach in plasmas is to start from the Klimontovich approach [14], which in fact is to use a microscopic description of each particle moving along the trajectories changed by the fields produced by all other particles. Here, we will illustrate the role of fluctuations using a simpler but equivalent approach [15]. The evolution of the microscopic distribution, which depends on the momenta and coordinates of all the particles of the system, is determined by the Liouville theorem. Integration of the microscopic distribution over the momenta and coordinates of all particles except for one yields an equation for the one-particle distribution $f^{\alpha}_{\mathbf{r},\mathbf{p},t}$ (each plasma component is marked by the superscript α):

$$\frac{\partial f^{\alpha}}{\partial t} + \mathbf{v}_{\alpha}\cdot\frac{\partial f^{\alpha}}{\partial \mathbf{r}_{\alpha}} + e_{\alpha}\mathbf{E}\cdot\frac{\partial f^{\alpha}}{\partial \mathbf{p}_{\alpha}} = 0. \quad (6)$$

This equation is not very informative, since the electric field depends on all of the other particles and a great deal of information is lost after integration with respect to other particles. Nevertheless, at relatively low collision frequencies (in fact, the collision frequency should be much less than the corresponding plasma frequency), we can consider the influence of the other particles as fluctuations and can prove that the fluctuations are weak. We then introduce the averaged distribution $\langle f^{\alpha}\rangle$ and the fluctuating part of the distribution δf^{α}

$$f^{\alpha} = \langle f^{\alpha}\rangle + \delta f^{\alpha}. \quad (7)$$

By averaging Eq. (6) in the absence of an averaged field (the generalization for the case in which the latter is present is unimportant), we get the equation for the averaged distribution, which we write in the form

$$\frac{\partial\langle f^{\alpha}\rangle}{\partial t} + \mathbf{v}_{\alpha}\cdot\frac{\partial\langle f^{\alpha}\rangle}{\partial \mathbf{r}_{\alpha}} = -e_{\alpha}\left\langle \delta\mathbf{E}\cdot\frac{\partial\delta f^{\alpha}}{\partial \mathbf{p}_{\alpha}}\right\rangle = I^{\mathrm{col}}_{\alpha}. \quad (8)$$

The right-hand side can be expressed through the averaged particle distribution using the first linear approximation for fluctuations. The linear approximations for these are proven to be the first approximations in $1/N_D$, where $N_D = (4\pi n\lambda_D^3)/3$ is the total number of particles in the Debye sphere. The equation for fluctuations is obtained by substituting Eq. (8) into Eq. (6), and the fluctuating part of the distribution is assumed to consist of the independent particle fluctuations $\delta f^{\alpha,(0)}$ and the induced part $\delta f^{\alpha,\mathrm{ind}}$. For the independent particle fluctuations, standard averaging is used:

$$\langle \delta f^{\alpha(0)}_{\mathbf{p},\mathbf{k},\omega}\delta f^{\beta(0)}_{\mathbf{p}',\mathbf{k}',\omega'}\rangle = \Phi^{\alpha}_{\mathbf{p}}\delta_{\alpha,\beta}\delta(\mathbf{p}-\mathbf{p}')\delta(\omega-\mathbf{k}\cdot\mathbf{v})\delta(\omega+\omega')\delta(\mathbf{k}+\mathbf{k}'), \quad (9)$$

and the field-induced part is given by a simple expression

$$\delta f^{\alpha,\mathrm{ind}}_{\mathbf{p},\mathbf{k},\omega} = -i\frac{e_{\alpha}}{\omega-\mathbf{k}\cdot\mathbf{v}}\frac{\mathbf{k}}{k}\cdot\frac{\partial\Phi^{\alpha}_{\mathbf{p}}}{\partial\mathbf{p}}\delta E_{\mathbf{k},\omega}. \quad (10)$$

The independent particle fluctuations were discussed in [2] in connection with dust charge fluctuations, and the fluctuations induced by the electric field created by the independent particle fluctuations (see [15]) are determined by the fluctuating electrostatic field and the electrostatic dielectric function $\epsilon_{\mathbf{k},\omega}$. The right-hand side of Eq. (8), $I^{\mathrm{col}}_{\alpha}$, is called the Landau–Balescu collision integral. This integral describes the particle collisions and leads to the exact expressions for the electron–electron, ion–electron, and ion–ion collision frequencies. The most important properties of this integral is that, for thermal distributions, the collision integral is exactly zero and that the deviations from the thermal distributions relax to thermal distributions with rates equal to the above frequencies. We here recall all of these moments (which are well known in general plasma theory) to demonstrate the fundamental role of fluctuations, and to describe the role of the new effects that appear in complex plasmas as compared to ordinary plasmas.

For completeness, we write out the Landau–Balescu collision integral:

$$I_\alpha^{\mathrm{col}} = \frac{\partial}{\partial p_{\alpha,i}} \int \sum_{\alpha'} I_{i,j}^{\alpha,\alpha'}(\mathbf{v}_\alpha - \mathbf{v}_{\alpha'}) \times \left(\langle f^{\alpha'} \rangle \frac{\partial}{\partial p_{\alpha,j}} < \langle f^{\alpha} \rangle - \langle f^{\alpha} \rangle \frac{\partial}{\partial p_{\alpha',j}} \langle f^{\alpha'} \rangle \right) d\mathbf{v}_{\alpha'}, \quad (11)$$

where

$$I_{i,j}^{\alpha,\alpha'} = 2e_\alpha^2 e_{\alpha'}^2 \int \frac{d\mathbf{k} k_i k_j}{k^4 \left| \epsilon_{\mathbf{k},(\mathbf{k}\cdot\mathbf{v})} \right|^2} \delta(\mathbf{k}\cdot(\mathbf{v}_\alpha - \mathbf{v}_{\alpha'})) \approx 2\pi\Lambda \frac{1}{|\mathbf{v}_\alpha - \mathbf{v}_{\alpha'}|} \left(\delta_{i,j} - \frac{(v_{\alpha,i} - v_{\alpha',i})(v_{\alpha,j} - v_{\alpha',j})}{|\mathbf{v}_\alpha - \mathbf{v}_{\alpha'}|^2} \right), \quad (12)$$

Λ is the Coulomb logarithm, and $\epsilon_{\mathbf{k},\omega}$ is the plasma dielectric constant describing the response to electrostatic perturbations. After averaging over the fluctuations, kinetic equation (8) contains only the average distribution function. This equation is used to describe the evolution of the averaged distribution function (it is this function that is usually detected); the price of this simplification is the appearance of collision integrals in the right-hand side of the equations. Averaging over fluctuations is sometimes called averaging over the discreetness of the correspondent component.

Note that kinetic equations (8) with collision integral (11) is the foundation of the *present theoretical description of ordinary plasmas.* Taking the momenta of these equations with respect to velocities leads to the *present hydrodynamic equations of ordinary plasmas.* Thus, to develop a basis for describing complex plasmas, one must not only generalize this approach for all of the components, but also consider the new effects related to the openness of complex plasmas and the charging process [1] and take into account the estimates of the new elementary processes in complex plasmas [2].

1.2.3. New effects in collision integrals in complex plasmas. To generalize the above averaging procedure to complex plasmas, it is necessary to focus on several specific aspects of the problem. We will list several new physical points that are important for the procedure of averaging used in obtaining collision integrals in complex plasmas [4–8]:

(i) In general, the starting equations should take into account the discreteness of all of the components, and the averaged equation obtained should describe the system in terms of continuous functions (as was mentioned above, the averaging can be considered as averaging with respect to the discreetness of each component).

(ii) The discreetness of the dust component is the largest. This circumstance can be used to construct a simplified kinetic approach [4] in which dust discreetness is taken into account, while the other components are described by continuous distribution functions. In fact, this procedure uses a two-step averaging, the first step being the averaging over the electron and ion discreetnesses (leaving dust to be treated dynamically), with the second step being the averaging over the dust discreetness.

(iii) The complete averaging procedure has not been performed so far because of complications related to the need for a detailed description of the dust charging, which ultimately turns out to be more sophisticated than in the simplified models discussed in [1].

(iv) In the first stage, averaging should lead to some equations for electrons and ions with collision integrals describing the charging process. A constructive approach to the averaging procedure is to use in these equations the charging models described in [1], namely, the OL, radial drift (RD), or diffusion limited (DL) models, and, in the second stage, to perform averaging only over the dust discreetness.

(v) Fluctuations caused by dust discreetness will play a major part in the consideration of collision integrals, and the averaged description of all of the components of a complex plasma will contain the collision integral modified by the charging processes [4].

(vi) This procedure of averaging over dust discreetness has been performed so far only for the OL model for a gaseous state. It resulted in a *new type of collision integrals for complex plasmas* [4–8]. We will describe only the main new qualitative features of these:

(vii) Up to now, an experimental check of the first stage of the averaging procedure for ordinary plasmas has not been performed because of the very small scales on which the discreetness of electrons and ions is important.

(viii) In complex plasmas, the discreteness of the dust component can be directly measured (one can observe each single dust grain); hence, any averaging procedure for the dust component can be checked experimentally.

(ix) In the dust component, not only the fluctuations of the positions and momenta of particles but also the fluctuations of dust charge are important; they can induce fluctuations of the electric field and, therefore, can lead to additional fluctuations of electrons and ions.

(x) Fluctuations related to dust discreetness have much lower frequencies than fluctuations related to electrons or ions; therefore, two-stage averaging can be justified by the presence of a physically simple small parameter: the ratio of the two characteristic time scales of fluctuations.

1.2.4. A new type of dust distribution function. For dust grains, it is useful to introduce new kinetic variables such as the dust charge Q, the dust angular momentum $\mathbf{\Omega}$, and the dust surface temperature T_{ds}. These new kinetic variables describe the "inner" degree of freedom of the dust grains which, in other aspects, behave like point charges (if, as is usual, the dust size a is much less than the screening length λ_{scr}). The dust

distribution function should depend not only on the translational variables (such as the position and momentum of the dust grain), but also on the inner degrees of freedom. The angular momentum of dust spinning plays an important role in the kinetic description of complex plasmas in a strong magnetic field, and the dust surface temperature plays an important role in the case of an inhomogeneous plasma flux onto the dust particles and in the case where thermophoretic forces are important. There are also certain cases where the variables related to the inner degrees of freedom are not so important. However, one of these—the dust charge Q—is always important. For simplicity, we restrict our consideration by introducing only one new variable into the distribution function for dust grains, namely, the dust charge. The microscopic distribution function of dust grains will then be the function $f^d_{Q,\mathbf{r}_d,\mathbf{p}_d,t}$, where the dust charge Q should be treated as a new independent variable. The equation for the total (not averaged) distribution function should take into account the charging process

$$\frac{\partial f^d}{\partial t} + \mathbf{v}_d \cdot \frac{\partial f^d}{\partial \mathbf{r}_d} + Q\mathbf{E} \cdot \frac{\partial f^d}{\partial \mathbf{p}_d} + \frac{\partial}{\partial Q} I f^d = 0, \qquad (13)$$

where $I = I_e + I_i$ is the total current on a dust grain (which can include the photoeffect current, secondary emission current, etc.). In averaging this equation, the fluctuations of the charges are important. In the approach of [4–8], only the dust discreteness was taken into account, while the electrons and ions were described by the average distribution function $\Phi_{e,i}(\mathbf{v}, \mathbf{r}, t)$. In this case, the interaction with dust grains was taken into account by the collision integral related to the OL charging process, and the binary electron–electron, ion-ion, and electron–ion collision integrals were ignored in accordance with relation (4). The dust discreteness creates dust fluctuations that, in turn, create fluctuations in the electron and ion distributions. In the first approximation, these induced fluctuations are proportional to the dust density. All of these fluctuations contribute to the effects averaged over the fluctuations, and their influence is described by collision integrals on the right-hand sides of the equations for electrons, ions, and dust. These collision integrals, found in [4–8], serve as one basis of the kinetic theory of complex plasmas. Only the gaseous state of complex plasma was treated in [4–8]. In deriving collision integrals, an additional small parameter $1/Z_d \ll 1$ (apart of other parameters already mentioned above) was used.

1.2.5. Main features and results of the new kinetic theory of complex plasmas. Here, we list the main results of such a kinetic approach [4–8]:

(i) The free particle fluctuations in the presence of charging are described by expressions more complicated than Eq. (9). They contain singular functions that, in some cases, are not simple to treat; however, in all cases, the values averaged over charges can be found explicitly [4].

(ii) The fluctuations and the collision integral are determined not only by the plasma dielectric response function, which is proportional to e_α^2 for each species, but also by other response functions containing the particle charge e_α and either the cross section of charging $\sigma_\alpha^{\mathrm{ch}}(Q)$ or its derivatives with respect to the dust charge. This result seems to be natural since the change in the dust charge influences the electric fields in complex plasmas [4]. This effect was noticed for the first time in [12]. In the simplest case, this means that collisions depend not only on the screening length (such as the Debye length) but also on the charging length, which is shown in [2] to be longer than the screening length by approximately λ_{Di}/a.

(iii) The collision integrals for electrons and ions with dust are changed due to the inelasticity of collisions and the possible transfer of energy and momentum to the dust grains [4, 6]. Along with the averaged charging equation, they present a self-consistent system of equations for the spatiotemporal evolution of the dust charge and the electron and ion distribution functions. This system of equations is similar to the known quasilinear equations in ordinary plasmas, which describe the excitation of waves and their inverse effect on the particle distribution. In the equations of [4, 6], the dust charge is considered instead of waves and, simultaneously, the particle distribution is changes due to the charging process. The numerical solution of these equations [6] shows how the charging process reduces the low-energy part of the ion distribution and the high-energy part of the electron distribution, which, in turn, changes the rate of charging.

(iv) The ion/electron–dust collision integral describes the influence of the charging process on electron–electron, electron–ion and ion–ion collisions. It is found that the charging frequency (as well as the Coulomb logarithm, which is important for elastic collisions) is "renormalized" (modified). These values start to be dependent on the dust size, the dust charge, and the frequencies related to dust charging ion–dust collisions [4]. The equation for the distribution function averaged over fluctuations, $\Phi^\alpha_{\mathbf{p}} = \langle f^\alpha_{\mathbf{p}} \rangle$ ($\alpha = e, i$), is

$$\left(\frac{\partial}{\partial t} + \mathbf{v}_\alpha \cdot \frac{\partial}{\partial \mathbf{r}}\right)\Phi^\alpha_{\mathbf{p}} = S^i - \nu_{d,\alpha}\Phi^\alpha_{\mathbf{p}} + I^{\alpha,\mathrm{col}}_{\mathbf{p}}, \qquad (14)$$

where $\nu_{d,\alpha} = \int v\sigma_\alpha(Q)\Phi_d(Q, \mathbf{p}_d)dQd\mathbf{p}_d/(2\pi)^3$ is the electron/ion–dust collision frequency without allowance for collective effects and $I^{\alpha,\mathrm{col}}_{\mathbf{p}}$ is the electron/ion–dust collision integral, which accounts not only for diffusion in momentum space but also for the collective

renormalization of the electron/ion absorption rate [4] and can be symbolically written as

$$I_{\mathbf{p}}^{\alpha,\,\mathrm{col}} = \frac{\partial}{\partial p_i} D_{i,\,j}^{\alpha,\,d} \frac{\partial \Phi_{\mathbf{p}}^{\alpha}}{\partial p_j} + \frac{\partial}{\partial p_i} F_{\mathbf{p},\,i}^{\alpha,\,d} \Phi_{\mathbf{p}}^{\alpha} + \nu_{d,\,\alpha}^{\mathrm{fl}} \Phi_{\mathbf{p}}^{\alpha}. \quad (15)$$

The renormalized frequency of electron/ion absorption is $\nu_{d,\,\alpha}^{\mathrm{ren}} = \nu_{d,\,\alpha} - \nu_{d,\,\alpha}^{\mathrm{fl}}$. The renormalization of the Coulomb logarithm is described by the part of the diffusion coefficient (the first term of the right-hand side of Eq. (15)) that corresponds to elastic electron/ions–dust collisions. The table for the changes in the Coulomb logarithm is given in [5].

(v) In the kinetic theory [4–8] for electrons/ions, the terms describing absorption on dust and ionization are present but separate from the collision integrals. Consideration of these effects together with collisions proves the statement that electron and ion distributions in complex plasmas should be nonthermal.

(vi) The dust charge distribution has a sharp maximum close the average dust charge Z_d, and the fluctuations around this value, as was mentioned in [7] (see also [2]), are determined by the dust density (in the experiments performed so far, they have exceeded the fluctuations due to electron/ion discreteness).

(vii) The equation for the average dust charge found in [4] contains the averaged distribution functions of electrons and ions, for which equations with collision integrals taking into account the charging process are derived [6].

(viii) The dust–dust collision integrals obtained depend on the average distribution containing the charge variable and describe diffusion not only in velocity (momentum) space but also in charge space. These dust–dust collision integrals contain all of the collective attraction effects described qualitatively in [2]. The symbolical form of the dust–dust collision integral for $\langle f_d(Q, \mathbf{p})\rangle = \Phi_d(Q, \mathbf{p})$ is [4]

$$I_d^{\mathrm{col}}(\mathbf{p}_d, Q) = \frac{\partial}{\partial p_{d,\,i}} D_{i,\,j}^{p,\,p} \frac{\partial}{\partial p_{d,\,j}} \Phi_d(\mathbf{p}, Q) + \frac{\partial}{\partial p_{d,\,i}} F_{d,\,i}^{pp} \Phi_d(\mathbf{p}, Q) + \frac{\partial}{\partial p_{d,\,i}} D_i^{p,\,Q} \frac{\partial}{\partial Q} \Phi_d(\mathbf{p}, Q) \quad (16)$$
$$+ \frac{\partial}{\partial Q} D_j^{Q,\,p} \frac{\partial}{\partial p_{d,\,j}} \Phi_d(\mathbf{p}, Q) + \frac{\partial}{\partial Q} D^{Q,\,Q} \frac{\partial}{\partial Q} \Phi_d(\mathbf{p}, Q).$$

(ix) It follows from Eq. (16) that the distribution functions diffuses not only in momentum space but also in charge space. This is due to the change of the dust charge in each dust–dust collision event. In principle, this effect is natural, since the dust charge is not fixed and, as was mentioned in [2], its value changes when two dust grains approach one another. Therefore, after their interaction, the grain charges can differ from their values before the interaction. They can even gain or lose their kinetic energy, taking the difference from the energy of interaction during the collisions. This means that dust grains can be accelerated or decelerated during collisions. On a qualitative level, this effect was first mentioned in [16]. It is described by Eq. (16) and, in particular, by the terms that have derivatives with respect to both momentum and dust charge. This new qualitative effect needs further investigation. It seems obvious that, in the case of deceleration or acceleration during collisions, the dust distribution function cannot be a product of two distributions, one in the dust charges only and another in the momenta of dust grains only.

(x) One can find equations for the distribution function integrated over dust charges

$$\Phi_d(\mathbf{p}) = \int \Phi_d(\mathbf{p}, Q) dQ. \quad (17)$$

The result obtained in [7] is that, in the equation for this distribution function, the collision integral on the right-hand side describes diffusion and friction in momentum space. In the first approximation in $1/\nu_{\mathrm{ch}}$, this integral contains $\delta(\mathbf{k} \cdot (\mathbf{v}_d - \mathbf{v}_d'))$ as in the usual expression (12). As in Eq. (12), this δ function describes energy conservation in the course of a collision event between two dust grains. This is natural since, after we integrate over all of the possibilities of changes in charges for given changes of momenta, the dust particles exchange only energy. In the next approximation in $1/\nu_{\mathrm{ch}}$, there appear terms describing variations in the kinetic energy caused by the change of the grain charge due to collisions.

(xi) The most important point is that the effective dielectric constant entering in the collision integrals describes the *full complex plasma response, taking into account all of the charging processes, i.e., all of the responses, including the charging cross sections and their derivatives.* These responses lead to collective dust–dust interactions and to the collective dust attraction discussed in [2, 17].

(xii) In the model used in [4], the ionization source was assumed to be independent of the electron distribution. The difference between [7] and [2, 17] is that, in [2, 17], a case where the ionization rate is proportional to the electron density was considered, while in [7], the ionization rate was assumed to be independent of the electron distribution. The case considered in [2, 17] is closer to the experimental conditions. It should be emphasized that collective attraction was first derived in [7]. The collective attraction found in [17] is greater than that found in [5]; therefore, the dependence of the ionization rate on the electron density is rather important. As was mentioned above, the model of [17] is closer to the state-of-the-art experiments than the model of [7]; however, both of them illustrate the presence of similar cosinusoidal terms in the collective attraction potential. Undoubtedly, if the ionization term in the model of [4–8] is taken to be proportional to the electron density, it will lead to a more detailed descrip-

tion of the effect found in [17]. This is left to future research.

(xiii) *An important point is that the collective attraction is included in the dust–dust collision integrals.*

(xiv) Another important point is that *the dust–dust collision integral is zero for thermal dust distributions.* This result includes collective interactions (attraction) and the nonthermal electron and ion distributions, which, after integrating over ion/electron velocities, enter into the coefficients in front of this integral. This means that, *even starting from a nonthermal distribution, the dust distribution will relax to a thermal one, independently of whether the ion/electron distributions are thermal or not.* Only *the characteristic time of relaxation to a thermal distribution will depend on the electron and ion distributions*; this dependence is not strong, however, since these distributions are integrated over the electron/ion velocities.

(xv) The kinetic treatment depends strongly on the type of source existing in an open complex plasma system and on the charging model used.

(xvi) The kinetic theory was developed only for a gaseous state. A great deal of research remains to be done in the rest of the field, particularly on fluctuations and dust pair correlations in transitions to strongly correlated states.

1.3. The New Hydrodynamics and Thermodynamics of Complex Plasmas

1.3.1. Hydrodynamic equations derived from kinetic equations. The usual procedure for deriving hydrodynamic equations from kinetic ones is to consider the values averaged over particle velocities (or momenta), i.e., to integrate the kinetic equation over particle momenta with certain weights. For complex plasmas, this procedure is modified since a new variable—the dust charge—is present in the kinetic description. On the other hand, the electrons and ions usually have nonthermal distributions. Therefore, this integration over particle momenta should be performed for distributions satisfying the initial balance of ionization and absorption on dust grains, as was described in detail in [1, 2]. The new hydrodynamic equations for complex plasmas with allowance for elementary processes in complex plasmas described in [2] were first obtained in [9]. They can serve as the first approximation [18] to a self-consistent description of complex plasmas, since they use thermal distributions for all of the components of a complex plasma. In particular, it was shown in [18] that the boundary between the dust region and the dust-free region should be sharp with a jump in the dust density. The first kinetic proof that sharp boundaries can be present in complex plasma was made in [19]. However, it was not clear from [19] whether this is a general phenomenon in complex plasma, since in [19] a particular particle distribution was used. In a certain sense, the hydrodynamic proof of the presence of sharp boundaries made in [18] is more general, since it is independent of the distribution and uses only the continuity equations and Poisson's equation. We will return to this problem when discussing the problems of dust voids.

In complex plasmas, the deviation of the equilibrium distribution from a thermal one does not in fact create many complications if the hydrodynamic equations have the form of a closed set of equations containing only the values integrated over the particle momenta. For plasma particles (electrons and ions), the usual weights should be used: 1, $\mathbf{p}$, and $(\delta p)^2 = (\mathbf{p} - \bar{\mathbf{p}})^2$; i.e., the number density (the factor $(2\pi)^3$ determines the normalization of the distribution functions) is

$$n_{e,i} = \int \Phi^{e,i} d\mathbf{p}/(2\pi)^3, \tag{18}$$

the hydrodynamic velocity is

$$u_{e,i} = \frac{1}{m_{e,i} n_{e,i}} \int \mathbf{p}_{e,i} \Phi^{e,i} d\mathbf{p}/(2\pi)^3, \tag{19}$$

and the internal energy is

$$U^{e,i} = (1/m_{e,i}) \int (\delta p)^2_{e,i} \Phi^{e,i} d\mathbf{p}/(2\pi)^3.$$

Note that all of these quantities contain the distribution functions Φ averaged over the fluctuations; i.e., they are described by equations with the collision integral on the right-hand sides. The kinetic equations for electrons and ions contain terms in their right-hand sides (see Eqs. (14), (15)) that describe ionization and absorption on dust grains due to the charging process [4]. For average distributions, collision integrals appear. For the electron/ion density (see Eq. (18)), we obtain a continuity equation with two terms on the right-hand side: the ionization rate averaged over the distribution and the effective absorption on dust grains, which is reduced due to the collective effects (the first two terms in Eq. (15) do not contribute to the continuity equation, since they contain the derivative with respect the momentum and because they conserve the number of particles). The equation for the directed electron/ion velocity will have the standard form of a force balance equation in which the term on the left-hand side describes the dust inertia with the so-called ram pressure term $(\mathbf{u} \cdot \nabla)\mathbf{u}$ and, on the right-hand side, the electric field force and the force related to friction on dust with the renormalized Coulomb logarithm appear (in [18], a simple estimate of the Coulomb logarithm as $\ln(\lambda_D/a)$ was used). In the equation for the internal energy (the equation for heat transfer), the contribution from inelastic electron/ion collisions is important.

The distribution function of the dust grains contains new variable Q, over which moments must also be taken. Besides the already mentioned integral $\int f^d_Q dQ$, it is necessary to calculate the moment containing the

additional factor Q. The dust density is defined by the relationship

$$n_d = \int \Phi^d d\mathbf{p} dQ/(2\pi)^3, \quad (20)$$

which contains the integration of the distribution function over charges. The dust continuity equation has the standard form, since the number of dust grains is conserved in collisions. Besides this equation, the hydrodynamic equation for the dust average charge

$$-eZ_d = \frac{1}{n_d}\int Q\Phi^d(\mathbf{p}, Q)d\mathbf{p}dQ/(2\pi)^3, \quad (21)$$

appears thus:

$$\frac{\partial Z_d}{\partial t} + \mathbf{v}_d \cdot \frac{\partial Z_d}{\partial \mathbf{r}} = I_e^{\text{ren}} - I_i^{\text{ren}}, \quad (22)$$

where I_α^{ren} is the renormalized values of the electron/ion currents on the dust grain in units of the electron charge (being negative) per unit time. The equation for the dust averaged velocity

$$\mathbf{u}_d = \frac{1}{n_d m_d}\int \mathbf{p}_d \Phi^d(\mathbf{p}, Q)d\mathbf{p}dQ/(2\pi)^3 \quad (23)$$

contains the usual convective dust inertia term on the left-hand side (in most cases, it is small) and the electric force, the ion drag force, the thermophoretic force (in the presence of temperature gradients), and the force due to friction on neutrals on the right-hand side. When the friction on neutrals is much larger than the dust inertia term, the right-hand side describes the force balance equation for dust grains [2].

The next averaging momenta, apart from $(\mathbf{v}_d - \mathbf{u}_d)^2$, enter into the heat transfer equations, but in complex plasmas, there exist two additional equations. The first of these describes the transfer of fluctuations of the dust charge, $\int (Q + eZ_d)^2 f^d(\mathbf{p}_d, Q)dQ$ (in experiments, Q is usually negative and Z_d is positive). Moreover, in complex plasmas, there is a *new average quantity containing the dust charge fluctuations and the velocity fluctuations,* such as $\int (Q + eZ_d)(\mathbf{v}_d - \mathbf{u}_d)dQd\mathbf{p}_d/(2\pi)^3$. It should be emphasized that, in most cases, the dust distribution can be thermal, which simplifies the averaging procedure. Thus, in a certain approximation, some sort of "thermodynamics" can be introduced for the dust component, but it cannot be introduced for the electron and ion components, which are, as a rule, nonthermal.

The kinetic and hydrodynamic descriptions also depend strongly on the source. The new hydrodynamics not only operates with new renormalized coefficients, it operates with new averaged quantities such as the averaged product of dust and velocity fluctuations. In a rough approximation, the new hydrodynamic equation in complex plasmas (without heat and fluctuation transfer taken into account) was first found in [9].

1.3.2. Hydrodynamic equation for the case where the ion–dust collisions dominate and heat transfer is ignored. It is useful to write the hydrodynamic equations in the dimensionless units [18]:

$$n \equiv \frac{n}{n_0}, \quad n_e \equiv \frac{n_e}{n_0}, \quad P \equiv \frac{n_d Z_d}{n_0}. \quad (24)$$

The ion–dust mean free path is λ_{Di}^2/aP; therefore the electric field strength $\mathbf{E}$ and the distance $\mathbf{r}$ will be normalized as follows:

$$\mathbf{r} \equiv \frac{\mathbf{r}a}{\lambda_{Di}^2}, \quad \mathbf{E} \equiv \frac{\mathbf{E}e\lambda_{Di}^2}{aT_e}, \quad (25)$$

where a is the size of the dust grains, which are assumed to be spherical; $\lambda_{Di}^2 \equiv T_i/4\pi n_0 e^2$ is the ion Debye length for a homogeneous system in the absence of hydrodynamic motions; and T_e and T_i are the electron and ion temperatures, respectively (in energy units). The reason for the normalization of the distance and electric field is that the nonlinear equations in these units will not have any free parameters except for

$$\tau \equiv \frac{T_i}{T_e}, \quad u \equiv \frac{u_i}{\sqrt{2}v_{Ti}}, \quad (26)$$

where $v_{Ti} \equiv \sqrt{T_i/m_i}$ is the ion thermal velocity. The normalization of the electric field has a simple meaning: the electric field unit corresponds to a constant field in which an electron acquires the energy T_e over a distance determined by the unit of distance given by the first expression in Eqs. (24). The electron and ion temperatures will be considered constant in the plasma volume, and the heat transfer effect will be ignored.

We also introduce the quantity z as a dimensionless characteristic of the dust charge

$$z \equiv \frac{Z_d e^2}{aT_e}. \quad (27)$$

We start with the hydrodynamic equation for the dust component. Ignoring the terms with the dust pressure and dust inertia (which can easily be restored), we obtain the force balance equation for the dust grains (here, $u_i \gg u_d$):

$$P(\mathbf{E} - \alpha_{\text{dr}} zn\mathbf{u}) = 0, \quad (28)$$

where α_{dr} is the renormalized drag coefficient (see [2] and the discussion in the previous section). The force balance $\mathbf{E} - \alpha_{\text{dr}} zn\mathbf{u} = 0$ takes place only in the regions where the dust exists $P \neq 0$. The condition for ignoring the dust pressure is $Z_d \gg T_d/T_e$.

The force balance equation for electrons contains only the electric field force and electron pressure force,

$$\mathbf{E} = -\frac{1}{n_e}\frac{\partial n_e}{\partial \mathbf{r}}. \tag{29}$$

In the ion force balance equation, the ion inertia and ion pressure forces are relatively small because they have the additional factor $\tau \ll 1$. Ignoring them and, as well, the friction on neutrals, we obtain another simple equation (we used Eq. (29) to exclude the electric field):

$$\frac{1}{n_e}\frac{\partial n_e}{\partial \mathbf{r}} + P\mathbf{u}z\alpha_{\rm dr} = 0. \tag{30}$$

Assuming that the ionization is proportional to the electron density, we find the ion continuity equation in the form

$$\frac{\partial n}{\partial t} + \frac{\partial n\mathbf{u}}{\partial \mathbf{r}} = n_e\frac{1}{\tau_i} - \alpha_{\rm ch}Pn, \tag{31}$$

where $\alpha_{\rm ch}$ is the renormalized charging coefficient (see [1, 2] and the discussion in the previous section).

The charging time is usually very small compared to the hydrodynamic times, so that we can use the local charging equation containing the same charging coefficient as in Eq. (31). In the OL approach, we have

$$\exp(-z) = z\alpha_{\rm ch}2\sqrt{\pi}\frac{n_e}{n\sqrt{\tau\mu}}. \tag{32}$$

In solving the hydrodynamic equations, it is useful to find the dust charge at a certain point and differentiate Eq. (32) to follow the charge evolution in time and space using this equation. Finally, Poisson's equation closes the whole system (no quasineutrality is assumed ad hoc):

$$\frac{\partial \mathbf{E}}{\partial \mathbf{r}} = \frac{\tau\lambda_{Di}^2}{a^2}(n - n_e - P). \tag{33}$$

We will use this set of equations to describe the dust structures with sizes much less than the ion–neutral mean free path λ_{in}.

1.3.3. Hydrodynamic equation for the case where the ion–neutral collisions dominate and heat transfer is ignored. Here, the distance will be normalized to the ion–neutral mean free path λ_n divided by τ and, accordingly, the electric field will be normalized to the value at which an ion acquires the energy T_i over the distance equal to the ion–neutral mean free path:

$$\mathbf{r} \equiv \frac{\mathbf{r}\tau}{\lambda_n}, \quad \mathbf{E} \equiv \frac{e\mathbf{E}\lambda_n}{T_i}. \tag{34}$$

The drift velocity will be normalized in the same way as in the previous section, but the densities n and n_e and the parameter P will be normalized to the quantity n_*, which differs from n_0 by a factor equal to the ratio of the ion–dust mean free path to the ion–neutral mean free path:

$$n_e \equiv \frac{n_e}{n_*}, \quad n \equiv \frac{n}{n_*}, \quad P \equiv \frac{n_d Z_d}{n_*}, \tag{35}$$

where

$$n_*\ [\mathrm{cm}^{-3}] \equiv \frac{\tau^2 T_e}{4\pi e^2\lambda_n a} = 0.4416 \times 10^9\left(\frac{\tau}{0.02}\right)^2\left(\frac{T_e\ [\mathrm{eV}]}{2}\right)\left(\frac{0.01}{\lambda_n\ [\mathrm{cm}]}\right)\left(\frac{1}{a\ [\mu\mathrm{m}]}\right). \tag{36}$$

The second equality is written in units often used in state-of-the-art experiments. In these units, the equation of force balance for dust can be written in the same form as in the previous section (see Eq. (28)), but also including for a more general description the thermophoretic force $\mathbf{F}^T$:

$$\mathbf{E} = \alpha_{\rm dr}(u)n\mathbf{u}z + \tau\mathbf{F}^T. \tag{37}$$

The small parameter τ is intentionally introduced in Eq. (37) to illustrate that, for $\mathbf{F}^T$ on the order of unity, the thermophoretic force can be ignored. For the thermoforetic force, we have the equation (for simplicity, it is written here in one-dimensional form) [20]

$$\frac{d(zF^T)}{dx} = q_i + q_d. \tag{38}$$

This equation represents a simple neutral temperature conduction and depends on the boundary conditions (for example, different temperatures of the electrodes in the experimental setup). The right-hand side of the equation contains internal sources of heat related to ion drift, q_i, and a heat source related to the absorption of energy by dust grains and its transfer to neutrals via dust–neutral collisions, q_d:

$$q_i \approx n\mathbf{u}\cdot\mathbf{F}^{\rm fr}/4\sqrt{2}\pi, \quad q_d = Pn(z+2)/2\sqrt{\pi}\alpha_{\rm ch}, \tag{39}$$

where $\mathbf{F}^{\rm fr}$ is the force describing the friction of ions by neutral gas. As was mentioned above, the thermophoretic force created by the sources q_i and q_d in the absence of external temperature gradients is relatively weak. The friction force arising due to ion–neutral collisions has the form [20]

$$\mathbf{F}^{\rm fr} = \mathbf{u}(2 + \alpha_{\rm fr}|\mathbf{u}|), \tag{40}$$

where the coefficient $\alpha_{\rm fr}$ is on the order of unity and depends weakly on the sort of gas and other complex-plasma parameters.

The force balance equation for electrons survives in the same form as Eq. (29), but the force balance for ions takes the form

$$\mathbf{E} = \mathbf{u}(2 + \alpha_{fr}|\mathbf{u}|) + Puz\alpha_{dr}\mathbf{u}. \quad (41)$$

As before, the ion continuity equation will contain the ionization and absorption on dust, but the total particle flux $\mathbf{\Psi}$ consists of the convection flux $n\mathbf{u}$ and the diffusion flux, which is proportional to the density gradient:

$$\frac{\partial n}{\partial t} + \frac{\partial \mathbf{\Psi}}{\partial \mathbf{r}} = \frac{n_e}{x_i} - \alpha_{ch}(u)Pn, \quad (42)$$

$$\mathbf{\Psi} = n\mathbf{u} - \tau\alpha_{dif}\frac{\partial n}{\partial \mathbf{r}}, \quad (43)$$

where α_{dif} is related to the diffusion coefficient and is on the order of unity.

Poisson's equation takes the form

$$\frac{\partial \mathbf{E}}{\partial \mathbf{r}} = \frac{\lambda_{in}}{a}(n - n_e - P). \quad (44)$$

This set of equations is used below to construct the theory of dust structures.

1.3.4. Role of heat transfer. Heat transfer can play an important role in the formation of dust structures and can serve as a force acting together with the gravity force or substituting for the gravity force [21]. The thermophoretic force can play an important role at high ion drift velocities even in the absence of temperature gradients in the neutral gas. An important point is that, in the presence of a temperature gradient, the fluxes of energy and momentum onto a dust grain are different on opposite sides of the grain [22, 23]. The heating of the dust surface by the heat flux was investigated in [24, 25], where it was shown that the difference between the temperatures of the neutral gas and the dust surface temperature is rather small (the relative difference is 10^{-3}–10^{-2}. The difference in the temperatures at the opposite sides of a dust grain caused by the anisotropy of the heat flux is on the same order of magnitude. It was proved in [22, 23] that this anisotropy, as well as the difference in the absorbed momentum, can increase in the case of large dust charges. This can lead to an additional force acting on dust grains. This effect was first treated in [22, 23]. On the whole, the problem of heat transfer in a complex plasma is still far from being resolved from the theoretical point of view because, as was mentioned above, the corresponding heat transfer equations should be found explicitly for all of the components interacting with one another. The equations for the transfer of dust charge fluctuations and the equations for the mixed product of the velocity and charge fluctuations have not yet been investigated (approaches to this problem were discussed above). Moreover, as was mentioned in [22], the heating of the dust surface can lead to secondary electron emission. Also, the ultraviolet radiation present in some gas-discharge experiments can influence the type of structures that can be created in complex plasmas [26]. This radiation can also heat the dust surface and take part in heat transfer.

1.4. Theory of Dust Structures

1.4.1. General remarks on structures in complex plasmas. The formation of structures is one of the most general phenomena in complex plasmas. Ordinary plasmas are very unstable in many experiments, due to the low rate of binary collisions. Long-term investigations of ordinary plasmas have shown that, as a rule, only binary particle collisions lead to the thermalization of particle distributions (if contacts with certain thermal surfaces are not important). In ordinary plasmas, even small deviations in the particle distributions from the thermal ones result in instabilities. A complex plasma is a very dissipative system that, however, needs a constant supply of energy and particles, which opens the door for universal instability related to the formation of structures and self-organization processes [27]. One of the puzzling observations in a complex plasma is that not only different structures are formed quite often, but also that the boundary between the dust-containing region and the dust-free region is very sharp. The regions where the dust is completely absent are referred to as dust voids. At the void surface (where the dust density changes abruptly), all of the other plasma parameters (such as the electron and ion densities and temperatures) are continuous. Therefore, the virtual dust charge is also continuous at the void boundary. By the term virtual dust charge, we mean the charge that a dust grain acquires when one puts this grain onto the surface separating the dust-containing region and the dust-free region. These surfaces can exist only for certain distributions of the electric field and the degree of ionization and are really *virtual surfaces for dust grains.* On these surfaces, the force balance equations for a single grain should be satisfied independently of whether this grain exists on this surface or does not exist. This virtual balance depends on the virtual charge of a virtual grain. This means that, if we put only one or several grains onto these surface, then they will stay on these surfaces, because the force balance for the grains is satisfied at this surface. We note that the force balance is satisfied for a single grain, and this is enough for it to stay at this surface. This is a general statement that has been verified experimentally. Such surfaces often arise in the presence of ionization, and their appearance in complex plasma systems was first confirmed by numerical computations [18]. One usually finds that a finite plasma flux created by ionization is present on these surfaces. Thus, for such surfaces to exist in a discharge, one does not need many grains be present on each side of the surface. Let us consider now a case where there are many grains on, say, the right side of this surface and no grains on the left side of this surface. The distribution of the grains to the right of this surface will be determined by the equations that describe vari-

ations in the plasma flux, dust charge and density, plasma particle densities, and other parameters of a complex plasma. If the parameters at the surface are known, then the stationary distributions in the structure are determined by the balance equation. If there are no dust grains on the other side of this surface, we call this structure *a virtual dust void structure*. The distribution of dust on the dust side of the surface can be different and depends on the boundary conditions far from the virtual surface. For free boundary conditions and plain geometry, we call this structure *a dust layer*. In the case of a spherical geometry, when natural conditions at the center of a dust cloud (such as the absence of fluxes, an electric field, and drift velocities) are satisfied, we call this structure *a spherical dust cloud* or, for astrophysical purposes, *a dust star*. In the case where the surfaces are plane and the dust-free region is surrounded by two dust layers, the structure is called *a plain void*, and, in the case of a spherical dust-free region, it is called *a spherical void*. In cases where the dust is in contact with a wall and the boundary conditions at the wall can be satisfied, we call this structure *a dust sheath* (plane or spherical, respectively). The structures can also be classified in terms of the ratio of the structure size to the mean free paths. When the size of the structure is on the order of or less than the ion–dust mean free path and is less than the ion–neutral mean free path, we call it a collisionless structure (although dust–ion collisions are important). When the size of the structure is larger than the ion–neutral mean free path, we call it a collision-dominated structure. This terminology was taken from the theory of plasma sheaths, which are referred to as collisionless sheaths when the sheath size is less than the ion–neutral mean free path and are called collision-dominated plasma sheaths when the size of the plasma sheath is larger than the ion–neutral mean free path. The above structures were investigated by numerically solving the set of balance equations for the electron and ion densities, the ion drift velocity, the dust density, and the dust charge. Obviously, the surface separating the dust-containing region and the dust free-region can be more complicated than a simple spherical or plane surface; however, simple numerical solutions for rather complicated balance equations are available only for the 1D case. These solutions can, nevertheless, be used to demonstrate the possible types of structures.

1.4.2. Sharpness of the void boundary. Before dust voids were discovered experimentally, first in [28] and then under microgravity conditions in [29] (these experiments were discussed in the previous part of this review [3]), one important feature was predicted in [18, 19]: In the case of 1D geometry (plane or spherical), it is possible to find an exact solution to Poisson's equation inside the dust-containing region. This was already mentioned in [1, 2], but we can now show this explicitly by using the hydrodynamic equations written in the previous section. In a steady-state case, the above balance equations allow one to obtain expressions for the spatial derivatives of the density, the drift velocity, the charge, etc. On other hand, the ion balance equation expresses the electric field through these quantities. Formally, substituting the derivatives of the mentioned quantities into Poisson's equation, we obtain an algebraic equation relating the parameter P in the dust region to the charge density, the drift velocity, etc. If these quantities are known on the above surface, the parameter P can be calculated to the right of this surface. The balance equation are also satisfied at $P = 0$. This solution should be valid to the left of the surface, while to the right of the surface, P is nonzero. Thus, a jump in the parameter P should occur at this surface. Poisson's equation does not allow any other solutions without such a jump. Since the dust charge is continuous at this virtual surface, the jump in the dust density should be present. Thus, *the boundaries of the structures should be very sharp*. This conclusion was made in [18] before sharp dust surfaces were discovered experimentally, just as a general consequence of solutions to Poisson's equation in complex plasmas.

The conclusion about the sharpness of the surface was drawn only for stationary structures. Only stationary structures were investigated numerically with the dust pressure effect ignored, because estimates showed the smallness of the latter. Nevertheless, further investigation of the role of the dust pressure has shown that it determines the thickness of the boundary and that the relative thickness $\delta x/x_{\rm str}$ (the ratio of the surface thickness to the size of the structure) is on the order of (see [30, 31])

$$\frac{\delta x}{x_{\rm str}} \approx \frac{T_d}{T_e Z_d}. \tag{45}$$

In state-of-the-art experiments, the right-hand side of Eq. (45) is indeed very small and the observed thickness of the boundary should be very sharp.

Another important finding in investigations of the structures is that, in many cases, the parameters at the boundary can be found with the help of the integrals of motion in the dust-free region by expressing the electron density through the ion density from the balance equation and representing the first integral of Poisson's equation as the sum of the electron and ion pressures, the ram pressure of the ion flux, and the electric stress pressure. One needs to define certain parameters far from the boundary, for example, the value of the ion flux velocity, which is usually directed either to the region occupied by the dust or to the boundary surface. Having found the parameter values at the surface from the conditions of the electric-field and dust-charge continuity at the surface, one can then numerically find the distance from the surface at which the required value of the plasma drift velocity is reached. The answer is unusual: it is reached at rather short distances as compared to the size of the structure. The conclusion is that the structures are always surrounded by voids of finite and rather small size.

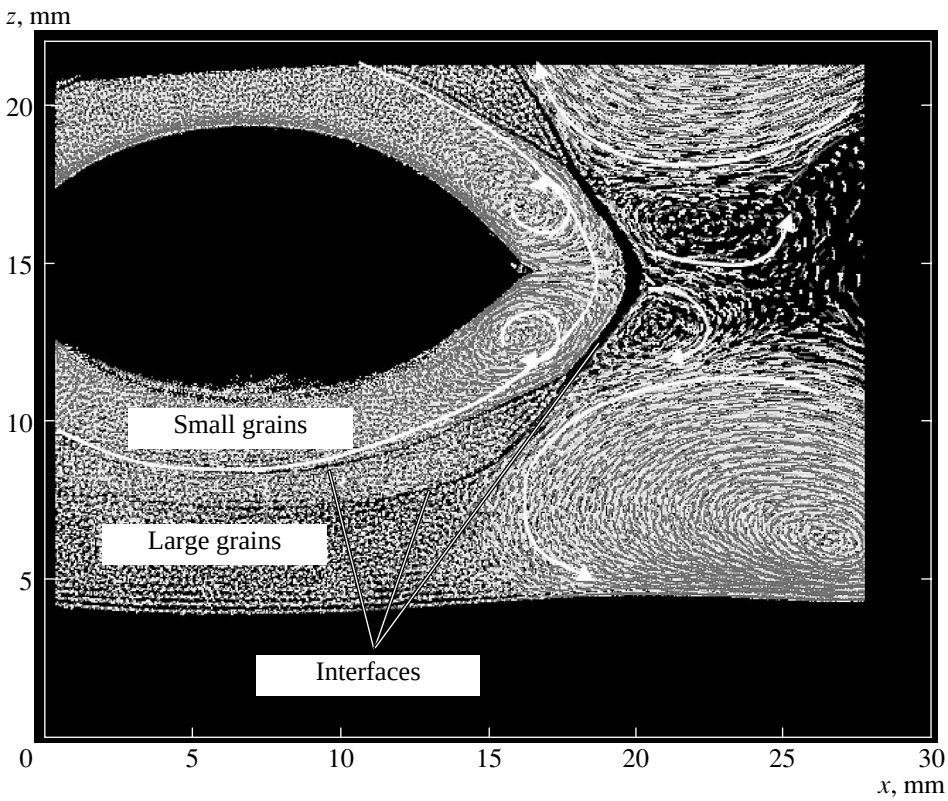

Fig. 1. Structures observed in the PKE–Nefedov experiment.

After these introductory comments, we show in Fig. 1 an actual complicated structure with void layers and vortices that was observed in the recent PKE–Nefedov experiment on board the International Space Station [32].

All of the structures that can be seen in Fig. 1 were obtained when dust grains with two sizes were injected into the discharge, one with a size of $a = 9.6$ μm and another one with a size twice smaller, $a = 4.8$ μm. One can see the central void with a sharp boundary, a sharp boundary between the regions occupied by grains with different sizes, thin void regions between these regions, a plasma crystal at the bottom (see also Fig. 62 given in [3], where this part is enlarged), and dust vortices at the side edges. Dust convection creating dust vortices on both sides of the observed structure is clearly seen. We note that the formation of structures is the main property of complex plasmas and that the first microgravity experiments fully confirm this statement. Dust convection in the structures also seems to be a general phenomenon, as was pointed out in [33] (the threshold for convection will be discussed below). We will also discuss 1D numerical solutions to the set of the above hydrodynamic equations that describe these structures in the collisionless and collision-dominated cases. We will present only several examples of such numerical calculations (for more details, see the literature cited below).

1.4.3. Dust plasma layers. Flat dust layers were previously investigated numerically both in the collisionless case [18] and the collision-dominated case [34]. In general, in the absence of ionization, any structure of grains should create a plasma flux toward the structure. This is a simple consequence of plasma particle (electron and ion) absorption on each dust grain [1, 2]. The collection of grains in a certain domain of space will, therefore, form a collective plasma flux toward it. In fact, it does not matter how this flux is produced far from the structure. The simplest model is the presence far from the structure of a localized ionization source creating the necessary number of electrons and ions that further will be absorbed by the collection of grains. However, a plasma flux far from the structure can be created in any other manner. The simplest possibility for a dust structure to be created is ionization at large distances from the structure, but there could also exist more complicated conditions such that the ionization exists close to the structure or is homogeneous and operates inside the structure. Different virtual boundaries of structures have been found. Investigations into the collision-dominated case include ion–neutral and neutral–dust collisions. We will consider here only the case of stationary structures, when the all of the electron/ion pairs created in a given volume are absorbed by the grains in the structure [18, 30].

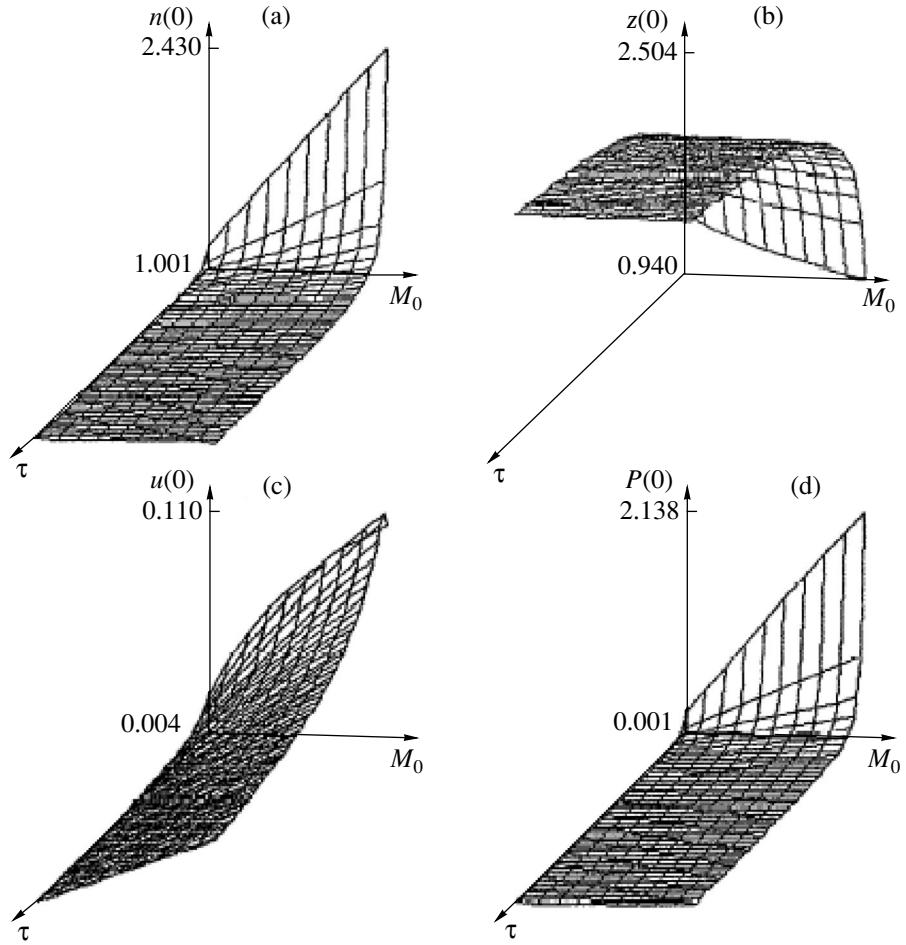

Fig. 2. Dependence of the parameters at the surface of a collisionless dust layer on the temperature ratio τ ($0.02 < \tau < 1$) and on the Mach number M_0 ($0.005 < M_0 < 0.03$) for $a/\lambda_{Di} = 0.1$: (a) the ion density $n(0)$, (b) the dust charge z_0, (c) the ion drift velocity $u(0)$, and (d) the jump in $P(0)$.

In the absence of ionization inside the structure, the drift velocity $u_0 = M_0\sqrt{2\tau}$ far from the structure determines the flux toward the structure (in the collisionless case, M_0 is equal to the Mach number of the ion flow far from the structure) [18]. This flux is not dissipated in the collisionless case, where ion–neutral collisions are absent. The plasma parameters at the virtual boundaries (the electron and the ion densities, the virtual dust charge, and the ion drift velocities) can be found using only the conservation laws and the boundary conditions at the virtual boundaries (the continuity of the electric field and the dust virtual charge). Generally [8, 18], all of the structures have sharp boundaries with the dust density jump depending on M_0. The flux at the surface produces ram pressure, so that the structure can self-confine dust grains. The number of dust grains that can be confined in the structure is finite (for flat structures, it is the number of grains per unit surface area and, for spherical structures or finite-volume structures with other shapes, it is the total number of grains in the structure). In fact, it is possible to invert this statement and say that the number of particles in the structure defines completely the flux and therefore the initial value of M_0. The structures can be almost quasineutral with a small dust jump at the surface or can be charged when this jump is large. Figure 2 shows the dust density $n(0)$, the dust charge $z(0)$, the ion drift velocity $u(0)$, and the jump in the parameter $P(0)$ at the surface of the structure as functions of the parameters M_0 (in the range $0.005 < M_0 < 0.05$) and τ (in the range $0.02 < \tau < 1$). These dependences where found by numerically solving equations obtained from the conservation laws in the dust-free region, namely, the conservation of flux $nu = u_0$ (the ion density is normalized to its value outside the structure, so that $n_0 = 1$) and the conservation of pressure

$$\frac{E^2a^2}{2\tau\lambda_{Di}^2} - n_e - \tau n(1 + 2u^2) = \text{const} = -1 - \tau(1 + 2u_0^2). \quad (46)$$

These equations, together with the solution to the electron density equation in the dust-free region,

$$n_e = \frac{1}{n^\tau}\exp\left(-\tau u_0^2\left(\frac{1}{n^2}-1\right)\right), \quad (47)$$

and the dust force balance equation $E = \alpha_{dr} nuz$, lead to the following two relationships that must be satisfied at the virtual dust boundary:

$$\frac{u_0^2 a^2 z(0)^2 \alpha_{dr,0}^2}{2\tau} = \left[\frac{1}{n(0)^\tau \exp\left(\tau u_0^2\left(\frac{1}{n(0)^2}-1\right)\right)} - 1 + \tau\left(n - 1 + 2u_0^2\left(\frac{1}{n(0)}-1\right)\right)\right] \quad (48)$$

and

$$\exp(-z(0)) = \frac{n(0)^{1+\tau}(z(0)+\tau)}{\sqrt{\mu\tau}\exp\left(-\tau u_0^2\left(\frac{1}{n(0)^2}-1\right)\right)}. \quad (49)$$

The dependences presented in Fig. 2 were found by numerically solving these equations. It can be seen from Fig. 2d that the jump in the parameter P at the surface of the structure can be rather large for certain values of M_0 and τ. The virtual boundary becomes a real boundary of the structure if the solutions in the dust region can be found by numerically solving the set of hydrodynamic equations in the dust-containing region and if the boundary conditions can then be satisfied. It was found in [18] that, in all cases, the distributions are symmetrical about the point at which the drift velocity changes its sign (this point can be called the center of the structure) and can reach the other surface where all of the plasma parameters are the same as those at the initial surface, but the direction of the drift velocity is opposite. If we also assume that, at the other side far from the structure, there exists an equal and oppositely directed plasma flux, then the whole structure will be symmetric. It has been found that such symmetric structures can exist for $u < u_{cr} = 1/\sqrt{2}$. An example of the distribution of the parameters in the structure (where the drop of the potential $\phi \equiv e\phi/T_e$ is also shown) is given for the whole structure in Fig. 3 for a hydrogen plasma for conditions far from critical (Fig. 3a) and for half of the structure for conditions rather close to critical (Fig. 3b). The drop of the potential is seen to be much larger in the second case [18].

In [18], one can find a detailed discussion of symmetric structures, the conditions of their quasineutrality, the influence of ion–neutral collisions, the structures with large jumps in the parameter $P(0)$ at the surface (these structures can be charged and can be both of the soliton type and of the antisoliton type with a decrease in the density toward the center), etc. The symmetry is lost if the plasma flux at one side of the structure is not opposite in direction and is not equal in magnitude to the plasma flux at the other side of the structure. The difference appears on the other side of the structure if there exists a wall that is under the floating potential; in this case, however, the problem converts into the dust sheath problem. This means that the ionization sources far from the structure can be different. The difference is also present when an ionization source operates inside the structure and, especially, when it is inhomogeneous. New void regions can then appear inside the structure. Qualitatively, similar distri-

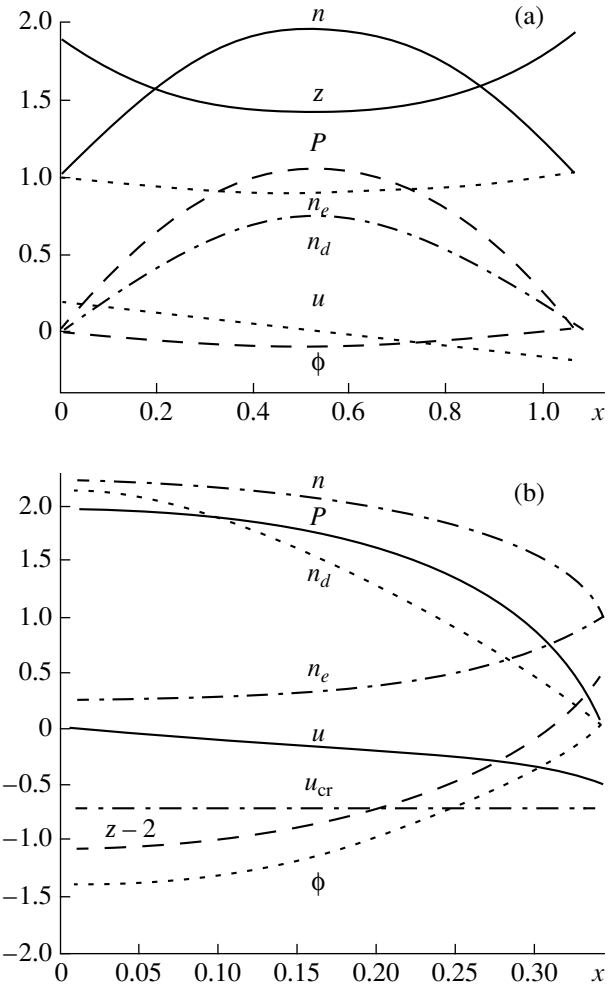

Fig. 3. Spatial distributions of the parameters in collisionless hydrogen structures: (a) the distribution of the parameters in a dust layer located between two dust-free regions ($\tau = 0.1$, $a/\lambda_{Di} = 0.1$, $u_0 = 0.2$, the total number of dust grains per unit surface area is $N_d = 0.493$) and (b) the distribution of the parameters in half of the structure (from the center $x = 0$ up to the surface) for parameters often encountered under astrophysical conditions: the external plasma flux is close to the critical flux, $\tau = 1$, and $a/\lambda_{Di} = 10^{-5}$.

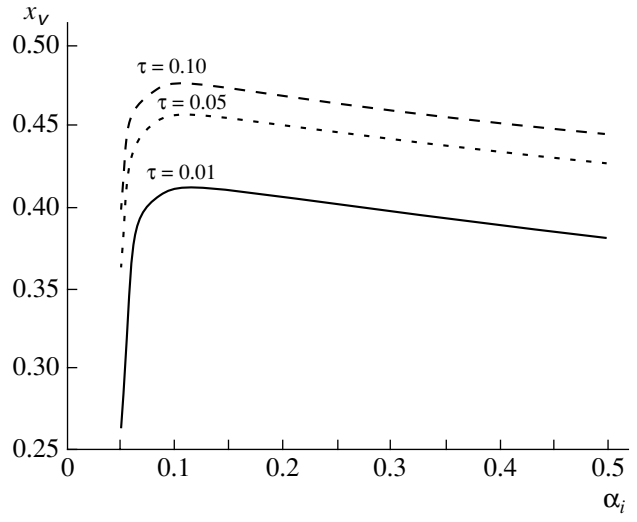

Fig. 4. Size of a collisionless void x_v as a function of the coefficient of ionization $\alpha_i = 1/\tau_i$ for different values of τ.

butions have been found in the collision-dominated case [34] for a single sheath between the electrode and the structure, but again they were a combination of voids and sheaths. We will restrict ourselves here only to some simplest examples.

1.4.4. Dust voids. Dust voids were first observed in laboratory experiments using small-size dust grains [28], then in microgravity short-time experiments in parabolic flights [29], and recently in space station PKE–Nefedov experiments [32]. All of these structures had rather sharp boundaries with an almost 100% absence of dust inside the void (see Fig. 1), and the voids corresponded to the collision-dominated structures in all cases, since the sizes of the observed voids were larger than the ion–neutral mean free paths. The theory of voids was first developed for collisionless voids [35] and then for collision-dominated voids [36]. In both [35, 36], only virtual surfaces were found. In void creation, an important role is played by ionization processes. Let us assume that, in some region, which we shall call the central region, the ionization rate is sufficiently high. The produced ion–electron pairs propagate from this central region and create an ion flux (ions are the most important element for momentum transfer, and the ion drift velocity enters into the equation for the void surface). We assume that there initially exists a dust cloud that is approached by the ion flux. An important feature of the evolution of the dust distribution and void creation is that, in the vicinity of the void surface, the drag force acts mainly on the first dust layer the ion flow meets, and the drag force moves this layer faster than the subsequent layers, where the drag force is depleted due to ion absorption by the first layer. This creates a large dust density gradient, and, due to the steepening of dust density profile with time, rather sharp edges are created, giving rise to the formation of a void in the final stationary stage [18, 35, 36]. Stationary void structures were first observed in experiments [28] and then in microgravity experiments in ballistic flights [29], and in space station experiments [32]. The dynamics of the void formation was not considered experimentally and serves only as a reasonable physical and theoretical model. The theory in [35] is based on a set of hydrodynamic equations in which ion–neutral collisions are ignored, but the ionization rate is assumed to be proportional to the electron density and is homogeneous over the entire volume. In the dust region, the ionization rate is lower because the electron density is reduced by absorption on dust grains. The theory developed in [35, 36] gives not only the size of the voids as a function of the degree of ionization and the ion and electron densities in the void region, but also the dust charge, the jump in the dust density, and the ion drift velocity at the surface of the void. It follows from the form of the ionization term $n_e/\tau_i \equiv n_e\alpha_i$ in the continuity equation for ions (31) that the size of the void in the collisionless case depends on the degree of ionization. In [35], the problem was solved in plane geometry. Figure 4 [35] shows the dependence of the size of the void x_v (in units of λ_{Di}^2/a) on α_i. We note that, according to computational results shown in Fig. 4, voids cannot be formed at a low degree of ionization (small α_i). This is natural from the physical standpoint.

In the collision-dominated case, the size of the void is obtained in units of λ_{in}/τ (see the set of hydrodynamic equations written above for this case). The collision-dominated case corresponds to the experiments in [28, 32]; observations confirm the theoretical results of [31, 36–38], according to which the size of the void increases with increasing ionization rate. Figure 5 shows the dependence of the collision-dominated void size x_v (in units of λ_{in}/τ) as a function of the ion–neutral mean free path ($x_n \equiv \lambda_{in}a/\lambda_{Di}^2$). The theory is in reasonable agreement with the observations.

Dust voids do not exist as separate structures but always surround dust clumps (layers). In the above theory of dust layers, after the parameters of the virtual surface have been found, it is possible to solve the dust-free hydrodynamic equations and to find at which distances from the surface the initial flux values $n = 1$ and $u = u_0$ are reached. The answer is that these distances in the dimensionless units are much less than unity. In turn, this means that finite-size voids exist on each side of the structure (layer) and that the sizes of these voids are much less than the size of the structure. The formation of voids is usually accompanied by dust clumping. A homogeneous dust distribution has been shown to be universally unstable against clumping and the formation of void structures. This instability can also result in the formation of a single void or a set of dust layers separated by dust voids, as was observed in [27]. The presence of sharp boundaries was found directly from the

force balance equation using Poisson's equation [18]. Thus, one can say that this is a direct consequence of the electrostatic balance in complex plasmas. Although the whole time evolution of the complex plasma (starting from the onset of instability to its nonlinear stage) was not fully analyzed, one can suppose that the development of universal structurization instability [36] can result in the complete structurization of complex plasma, i.e., its division into dust structures and voids. The sizes of the structures and voids are determined by the threshold obtained in [20, 32], which is minimal at P_0 and on the order of unity. In the collisionless case, it is on the order of the charging length (more exactly, the charging length divided by $P_0^{3/2}$), while in the collision-dominated case, it is on the order of λ_{in}/τ. For collision-dominated voids, the ion drift velocity at the void surface is larger and is on the order of ion thermal velocity $u(0) \approx 1$–2 (see [36, 38]). This computational result also agrees with observations [28].

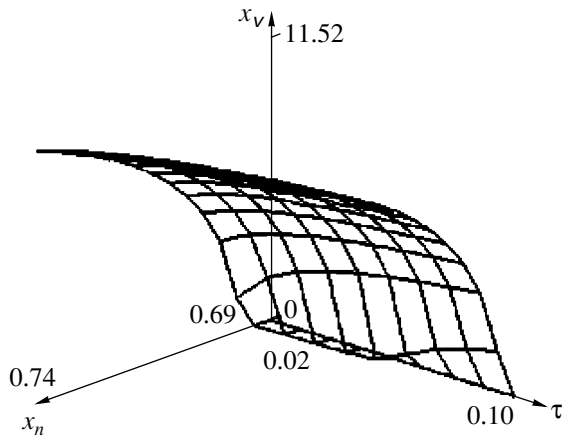

Fig. 5. Size of a collision-dominated void x_v (in units of λ_{in}/τ) as a function of $x_n = \lambda_{in}/\lambda_{id}$ and τ (λ_{in} is the ion–neutral mean free path, λ_{id} is the ion–dust mean free path).

1.4.5. Collision-dominated dust plasma layers. When the size of the region in front of the plasma layer is larger than the mean free path for ion–neutral collisions, the flux created far from the structure will be dissipated without reaching the dust surface. Thus, the ionization should be substantial near the layer. The simplest case is that where ionization is homogeneous, which corresponds to most RF experiments. Let us assume that the level of ionization is sufficient to form a void at the center. As before, we can find the void virtual boundary and then solve the collision-dominated equations written above in the dust region to find the distribution of all of the parameters of the structure and to find whether this distribution corresponds to a dust layer of finite size. This kind of investigations, performed in [34], indeed show the possibility of the existence of a collision-dominated dust layer with a parameter distribution somewhat similar to that discussed above, but the difference is in the scale length: in the collisionless case, it is a distance on the order of the mean free paths for ion–dust collisions $\lambda_{di} = \lambda_{Di}^2/aP$, while in the collision-dominated case, the size is on the order of λ_{in}/τ [34]. We present here only the results for the more complicated case also considered in [34], where the system contains two types of dust grains, one of them twice as large as another, and is bounded by plane electrodes at both sides. This corresponds exactly to the observations shown in Fig. 1, where the central part, in a certain approximation, can be regarded as flat. In the collision-dominated case, the possible structures were investigated both in the presence of mono-disperse dust grains of size a and in the presence of two-size grains with sizes a and $2a$. The main conclusion from the balance equation found in the theoretical model is that, in stationary (time independent) structures, dust grains with different sizes should be separated in space by a thin void that is similar to the interface region observed in experiments [32] (see Fig. 1). The difference between the computational results and the observations is due to the simplifying assumption about plane geometry. This qualitative agreement with the observations of the spatial separation of dust grains of different sizes and the presence of a sharp interface surface between them is quite impressive. Calculations also show that, for certain parameters, the void separating dust grains of different size can be much larger, but its size is always less than the size of each layer. Under certain conditions, such that the flux created in the void region is strongly dissipated by the first layer of smaller dust grains, computations show that the flux can be insufficient to support the next layer of larger grains. It can be seen in Fig. 6 that the distribution of the parameters in the first dust cloud with smaller dust grains differs radically as compared to the case considered above [34]. The simplest types of dust layers and dust voids are schematically drawn in Fig. 7.

1.4.6. Dust sheaths. Dust sheaths are dust structures formed close to a wall. The structure of the electric field in these sheaths is quite different from that in the well-known dust-free plasma sheaths. They also can be collisionless and collision-dominated. Numerically, the hydrodynamic equations for dust sheaths where solved in [30, 39]. Dust voids also appear for dust sheaths, and two voids can be present simultaneously: one void in front of the sheath and another void between the dust region and the wall [30, 39]. A dust sheath is drawn schematically in Fig. 7. Numerical computations were performed by the scheme described above. The parameters of the first surface, as in the case of dust layers, were calculated using the boundary conditions. The difference between the dust sheath and the plasma sheath is that the flux created far from the sheath should be superthermal (in most cases, even supersonic; i.e., its velocity should be higher than not only the ion thermal velocity but also the sound velocity, which is higher by

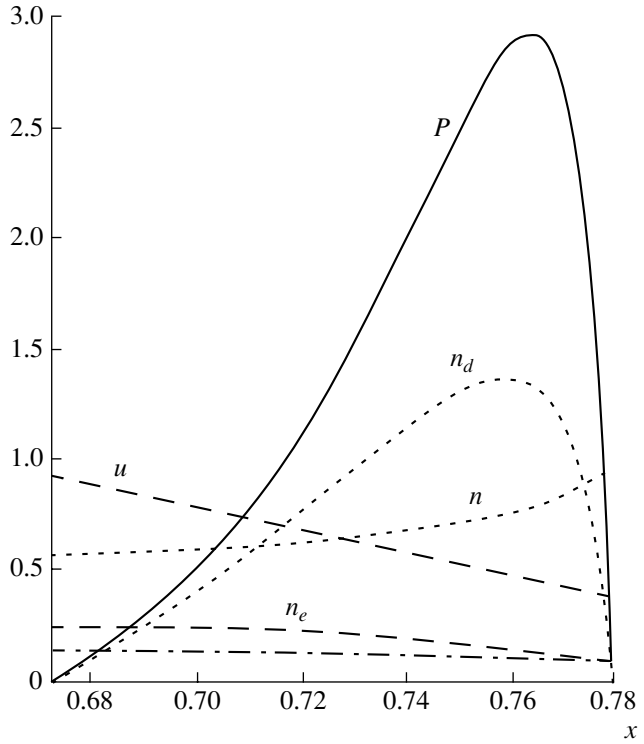

Fig. 6. Spatial distributions of the parameters in the first collision-dominated dust layer, consisting of smaller dust grains. The second layer, consisting of grains 100% larger than those in the first layer, is located at larger distances and is not shown in the figure. The two dust layers are separated by a thin dust void.

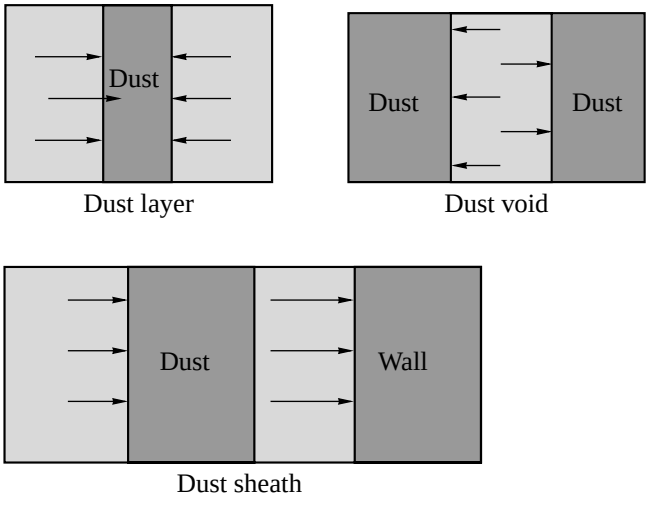

Fig. 7. Sketch of a dust layer, dust void, and dust sheath. The arrows show the direction of the ion flux.

$1/\sqrt{\tau}$). Since in experiments $\tau \approx 0.01$–0.02, the sound velocity exceeds the thermal velocity by one order of magnitude. Therefore, in the boundary conditions, the expression for the drag coefficient should be used for drift velocities substantially exceeding the thermal velocity ($M_0 = \sqrt{2\tau}u_0$, so that, for $M_0 \approx 1$, one usually has $u_0 \gg 1$). After the parameters of the first boundary have been found, the calculations continue to the second boundary and to the void separating the second boundary and the wall. At the wall, the floating potential (zero current) condition was used in [29, 39]. This condition determines the possibility of the void existing. The parameters inside the void in front of the dust sheath should be also calculated. For any sheath structure, the number of grains per unit area $N_d = \int (P/z)dx$ is determined by the value of the initial flux and can be calculated numerically. In dimensionless units, it is on the order of unity. Two conditions were found under which a stationary dust sheath cannot be created for certain initial Mach numbers: (1) the boundary conditions at the first surface are not satisfied and (2) the boundary conditions at the wall are satisfied only inside the dust region, which means that, under these conditions, the dust will come into contact the wall. As a result, they will fall out onto the wall and the number of grains in the sheath will be lower, so that the flux also will be lower, which will correspond to another initial Mach number. The possible Mach number for which the sheath exists can be found using the boundary conditions at the first surface. These Mach numbers are arranged in several bands (two or three), which looks like the "quantization" of Mach numbers. The thickness of a collisionless sheath is on the order of the ion–dust mean free path, and the thickness of a collision-dominated sheath is found to be on the order of ion–neutral mean free path divided by τ. After calculating all of the parameters inside the dust region, it is possible to calculate the ion density virtual curve for which the boundary conditions at the wall are satisfied. When this curve inside the dust region intersects the real curve for the ion density, the dust sheath cannot exist in view of the second mentioned restriction. Figure 8 shows the distribution of the parameters inside a sheath in which the virtual ion density curve inside the dust region does not intersect the real density curve and the sheath exists, and Fig. 9 gives an example where such intersection occurs.

The first restriction gives the bands of the allowed Mach numbers (M_0 is on the order of 1–3). In this case, the Mach number increases continuously in the dust region and in the void regions surrounding the dust sheath and reaches its maximum value (up to $M \approx 5$) at the wall. Another important property of the dust sheath found by numerically solving the hydrodynamic equations is that almost the entire drop of the potential between the plasma and the wall (which is several times the electron temperature T_e) occurs in the dust part of the sheath, and only a small part of the total drop of the potential is left for the surrounding voids. The dimensionless size of the dust voids surrounding the sheath is substantially less than the dimensionless size of the

dust part of the sheath. The value of the drift velocity at the entrance to the sheath in the collision-dominated case is on the order of the thermal ion velocity. In many cases, the Bohm criterion is, therefore, violated.

1.4.7. Dust convection in the structures. In [33, 40], the stability of plain and spherical structures was investigated against the creation of convection vortices and the threshold for the onset of convection was found. The nonlinear stage was analyzed only for plane structures [41] by the method of the maximum unstable mode in the direction perpendicular to the plane of the structure. Computations show the presence of two line vortices rotating in opposite directions and similar to those observed in microgravity experiments [32]. Dust convection in the dust region was observed, which seems to be a general phenomenon for most of the possible combinations of voids and structures. In [40, 41], the linear stage of dust convection was explained by convection instability in which mainly the dust takes part while the other plasma parameters change slightly. It seems that the phenomenon of dust convection is also a new phenomenon, since it differs from the usual convection in gases. The dust charging processes and the noncolinearity of the drag and the flux play a most important role in the formation of dust convection cells. Only one component of complex plasma, namely, the dust, is convected, while the perturbations of other components (such as the electron and ion densities) are small [33, 40, 41]. The further investigation of convection for most structures by numerically solving hydrodynamic equations is quite feasible.

1.4.8. Numerical investigation of the possibility of the formation of strongly coupled dust structures in microgravity experiments. To create a strongly coupled structure in microgravity experiments, it is necessary to form inside the chamber a structure surrounded by a void and a wall (preferably spherical in shape). It is also desirable to obtain a rigid structure in which the dust grains are located in a deep potential well, as was emphasized earlier. The dust crystal found in the last PKE–Nefedov experiment [32] was located close to the wall, where the presence of ion drift does not allow a rigid structure to be created. Therefore, it is necessary to discuss the results of numerical investigations showing the possibility of creating dust crystals at the center of the chamber. The theoretical possibility of the existence of such nonlinear structures was investigated in [20, 34] in 1D spherical geometry. Such a structure is shown schematically in Fig. 10, where a spherical dust cloud (structure) located at the center is surrounded by a spherical void and a spherical wall at the floating potential.

The problem was to prove the possibility of the existence of such a stationary dust structure by numerically solving the collision-dominated hydrodynamic equations and to optimize the number of dust grains that can be confined by the system. The necessary conditions of for the existence of such structures were found. We will not reproduce them here and only note that the ionization rate at the center of the structure should be lower than a certain critical ionization rate, that the ion and electron densities at the center of the

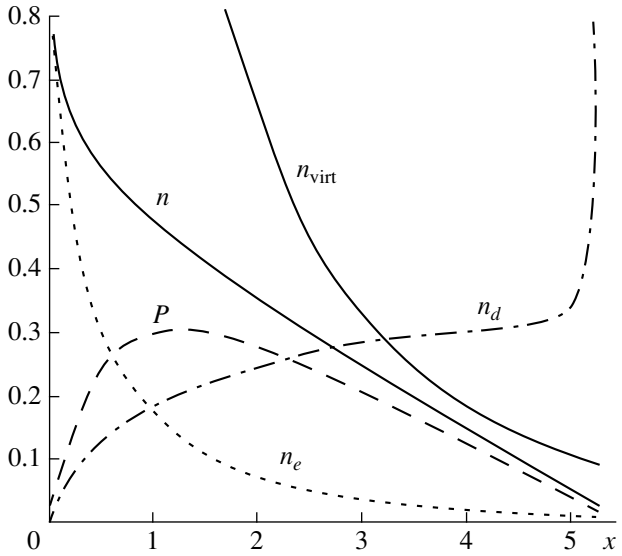

Fig. 8. Examples of the distributions of the parameters in a dust sheath for $M = 1.02$ (only the dust-containing region is shown). The distance x is given in units of λ_{Di}^2/a. The upper solid line for $n_{\rm virt}$ does not cross the curve n; i.e., the dust sheath is surrounded by two voids. The second void lies between the right surface of the sheath (vertical line) and the wall.

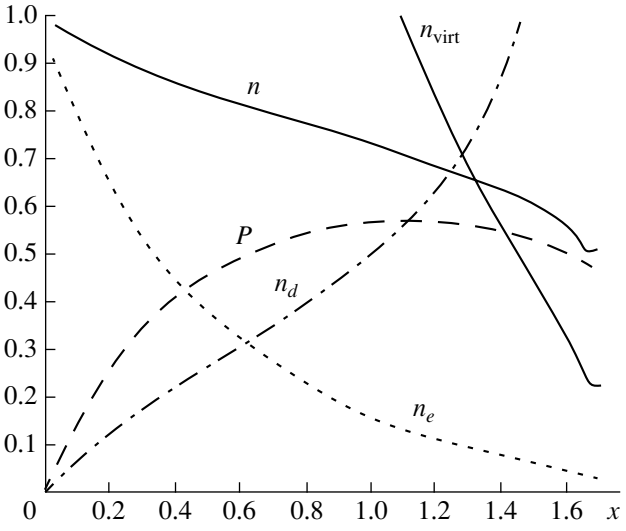

Fig. 9. The same as in Fig. 8 but for another value of the Mach number. The two curves $n_{\rm virt}$ and n intersect inside the sheath, which means that the dust contacts the wall or falls on the wall being translated to the wall by the ion drag force (such a sheath does not exist if the drag is not balanced by other forces).

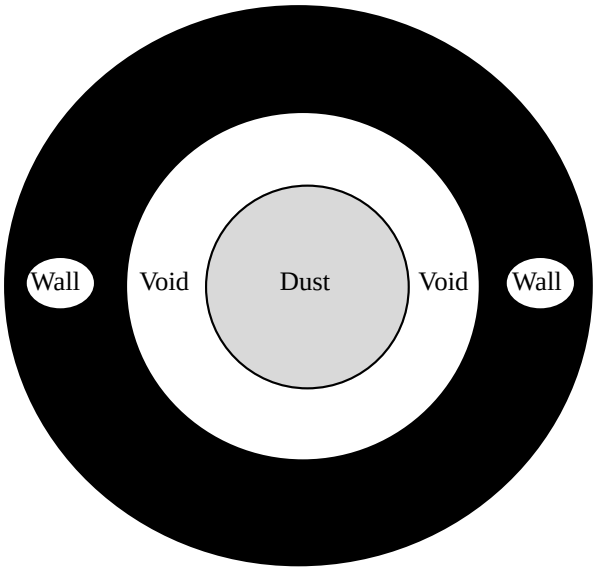

Fig. 10. Sketch of a spherical dust structure in microgravity experiments with spherical walls.

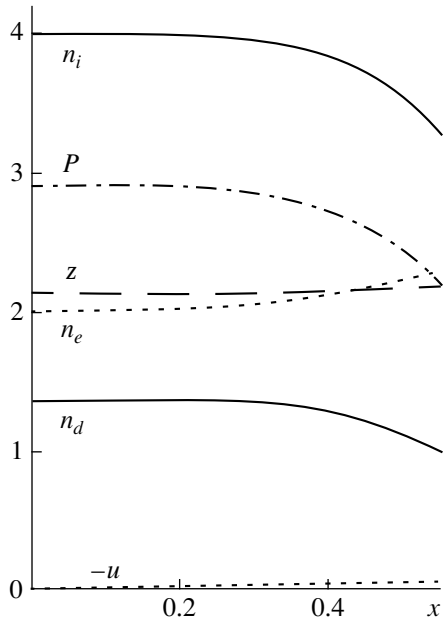

Fig. 11. Distribution of the parameters in the dust component of a spherical structure computed numerically from the balance equations under microgravity conditions. The parameters are optimized so that the main flux at the center of the structure is convective.

structure should be higher than a certain critical value, and that the direction of the ion flux in the void region should be inverted (close to the wall, it should be directed toward the wall and, close to the surface of the structure, it should be directed toward the structure). It was found that the ionization power and the pressure must be chosen so that, at the center of the structure, the diffusion flux is minimal and the convective flux is maximal (both of these vanish exactly at the center of the structure, so these conditions must be satisfied in the vicinity of the center). The maximum possible number of grains that can be confined was found. The restrictions found in [20] are related to the ionization rate, since it is necessary to avoid the formation of a void at the center of the chamber. It was found that the total number of dust grain cannot be larger than several million for the ion–neutral mean free path usually encountered in experiments. The criterion of crystallization is found to be satisfied throughout the entire structure. Thus, if a liquid layer occurs at the surface of the structure, it will be very thin. However, the void between the central structure and the wall cannot be made very thin. The difficulties in obtaining these structures are obvious. To obtain them numerically, it is necessary to tune the parameters very fine, which means experimentally a very accurate adjustment of the ionization rate and the pressure (this, nevertheless, was achieved in [32] in an actual installation with a rather complicated geometry). The alternative—a dust structure or a dust void—is one of the important problems to be resolved in microgravity experiments on dust crystal formation. In Fig. 11, one can see the distribution of the structure parameters inside the optimized dust cloud and, in Fig. 12, the distribution of the parameters of the optimized structure in the void region between the structure and the wall.

Further optimization can be achieved by placing a UV source close to the wall [26].

1.4.9. Further steps in numerical investigations of dust structures. Although the computations show good qualitative agreement with the observations, it is obvious that a deeper collaboration between the theoretical and the experimental work is desirable. From the theoretical standpoint, state-of-the-art experiments do not allow one to determine enough details (such as the spatial distributions of different components, the ion drift velocity, etc.) that can be directly compared with computations. The drift velocity is usually not measured, and one can only guess its value indirectly, not to mention the measurements of the spatial distributions of drift velocities inside the structures and voids. The problem is, of course, with unperturbing measurements. Even the ion velocity distribution in plasma sheaths without dust remained not very well known for a long time. Recent measurements [42] yielded rather unexpected distributions with anisotropic temperatures in the direction of the ion flow. The plasma density distribution is much easier to measure, but inside the structures, such measurements still present problems. Experiments are often aimed at demonstrating new phenomena rather than a deeper understanding of them; this can be achieved only by the complex use of theory, experiments, and numerical computations. From the experimental point of view, a theory should be devel-

oped for geometries closer to the experimental ones rather than for the 1D geometry simply treated in numerical computations. To perform even 2D computations, detailed knowledge of the boundary conditions is required and it is desirable that these conditions be as close to the experimental ones as possible. It seems to be natural to use the heat transfer equation and charge fluctuation transfer equation in future computations, as well as to use a more exact "renormalization" of the drag and charging coefficients. The new hydrodynamics should be developed with the treatment of many discontinuities, including the new one related to sharp dust boundaries. As concerns the "thermodynamics" of complex plasma, the corresponding equations can be used only for the dust component, since its distribution can be often thermal. Therefore, not only the dust "thermodynamics" but also the dust motions should be included in numerical investigations of the dust structures. The new aspects will be related to dust structures in a strong external magnetic field; these experiments, which have now only started, will certainly bring new qualitative unexpected results. Thus, one can foresee the need for numerical investigations of structures in a strong magnetic field.

1.4.10. Self-organization in complex plasmas. Open dissipative systems [43, 44] such as complex plasma structures are most favorable for self-organization. According to [20, 38] self-organization can start with the formation of dust structures surrounded by voids, with a subsequent complication of the structures due to competition between them for the plasma flux as a necessary element of their survival. Further development of these structures can lead to the formation of the simplest crystal states in their centers and the "memorizing" of the result of the best competition for the flux. There is no indication so far that this process can develop either under laboratory or space conditions, even though it is a very interesting problem, since it can allow investigations into some processes similar to those in biological systems. As a start, it is possible to investigate the evolution of two dust structures due to the competition for the external plasma flux [38].

1.5. Theory of Structures with Small Numbers of Grains and the Theory of Dust Clusters

1.5.1. Introductory remarks. The continuum description used in kinetic theory and hydrodynamic theory cannot be used for structures with a small number of grains. Such structures are usually called dust clusters. In the absence of all of the complications related to specific dust behavior, the investigation of clusters formed in ordinary matter is a wide field of research. Clusters have been investigated theoretically for 2D and 3D purely Coulomb systems in ordinary matter. In the 2D case, a parabolic confining potential is usually used to confine the charges in the plane. Detailed theoretical investigations can be found in [45]. It was found that, at a low kinetic energy, the clusters

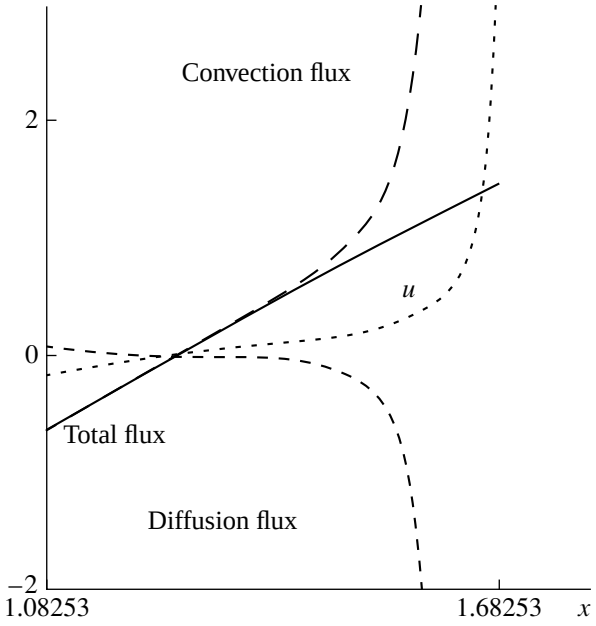

Fig. 12. Distribution of the parameters in the void between the spherical dust structure and the floating-potential wall for the conditions of Fig. 11.

have a shell structure and that, as the kinetic energy increases, instability develops that leads to intershell rotation. A further increase in the number of particles in the shells, as well as an increase in the kinetic energy, results in the increase in the intershell diffusion, which, in the 3D case, leads eventually to the formation of a Wigner lattice. These clusters in ordinary matter are usually confined in certain traps. When the particle interaction is a simple Coulomb interaction, such clusters are called Coulomb clusters. Three-dimensional Coulomb clusters consisting of ions were observed experimentally in Paul and Penning traps [46, 47], and 2D clusters in colloidal suspensions were observed in [48] (for the theory of such clusters, see [49]). Liquid colloid suspensions are not suitable for the investigation of the dynamic processes because of the great overdamping caused by the interaction with the electrolyte.

In ordinary matter, Coulomb interactions in clusters can be considered as the sum of all of the possible binary interactions. In [1, 2], we demonstrated that this is not always true for an ensemble of dust grains; i.e., collective interactions become important for a large-size ensemble of grains when the size of the dust cloud exceeds the mean free part for ion–dust collisions [1, 2], $L > L_{cr} = \lambda_{Di}^2/aP$. For small numbers of grains in the clusters, $L < L_{cr}$, the interactions between the grains can be considered as the sum of binary dust–dust interactions. Of course, the difference is that these binary interactions differ substantially from pure Coulomb interactions because they include noncollective shadow

attraction, long-range repulsion, and nonlinear screening. In [1, 2], the screening was shown to differ from ordinary exponential screening and the interaction to differ from the so-called Yukawa interactions [1, 2]. Dust clusters represent the limits in which the collective interactions do not operate, but the binary interactions should operate. Therefore, dust clusters open up new possibilities for investigating binary dust interactions. Clusters have their own oscillation frequencies, damping rates, and equilibrium conditions. All of these can be used to detect binary dust interactions. The simplest dust cluster is a dust molecule, which was investigated for the first time in [50].

Dust clusters differ from clusters in ordinary matter not only in new types of interactions but also in the presence of dust–neutral collisions. The latter can alter the properties of clusters in two aspects:

(i) The collisional damping of dust motion can stabilize some cluster configurations that are unstable in the absence of dust–neutral collisions.

(ii) The damping can be much weaker than in colloids; therefore, the eigenmodes of clusters can be investigated much more easily, both theoretically and experimentally.

1.5.2. Analytic results for the simplest 2D clusters. In [49], a general theory accounting for arbitrary types of interactions was developed for 2D clusters confined to a plane by an external parabolic potential well. This theory allows one to analyze the experimental data (the global modes of the clusters, their stability, and the oscillation frequencies) for arbitrarily charged particles in clusters in the presence of both attraction and repulsion interactions and to experimentally evaluate the type of the intergrain forces. This opens up better possibilities for investigating binary dust–dust interaction in complex systems than in experiments on the scattering of one grain by another grain (see [1]). The reason is that, in the course of scattering, a test particle has also a nonlinear shielding cloud that can be modified during the collision, while for clusters, the value of the potential of interaction can be measured directly.

Let us consider a 2D cluster consisting of N grains confined by external parabolic potential $V_{\text{conf}} = m_d\omega_0^2 r^2/2$ for an arbitrary pair dust interaction potential $V(r) = f(r^2)$ that defines the function $f(x)$, through which all of the results can be expressed. It is found that, for an equilibrium stationary polygon to exist, the following condition must be satisfied:

$$\omega_{N,0}^2 = -\frac{4}{m_d}\sum_{k=1}^{N-1}\sin^2\left(\frac{\pi k}{N}\right)f'\left[4R^2\sin^2\left(\frac{\pi k}{N}\right)\right] > 0, \quad (50)$$

where $f'(x)$ is the derivative of $f(x)$ with respect to its argument x and $N = 2, 3, 4, \ldots$ is the number of grains in the cluster. Equation (50) can be used to determine the equilibrium size R of the polygon in the given trapping field. For equilibrium to exist, it is necessary that the right-hand side of Eq. (50) be positive. The criterion of the stability of the equilibrium state against small perturbations is described by the equation

$$(A_1 - A_{l+1} + B_{l+1})(A_1 - A_{l-1} + B_{l-1}) \geq (B_1 - B_l)^2, \quad (51)$$

where

$$A_l(N) = -\frac{4}{m_d}\sum_{k=1}^{N-1}\sin^2\left(\frac{\pi kl}{N}\right)f'\left[4R^2\sin^2\left(\frac{\pi k}{N}\right)\right],$$

$$B_l(N) = \frac{4}{m_d}\sum_{k=1}^{N-1}\sin^2\left(\frac{\pi kl}{N}\right)4R^2 \quad (52)$$

$$\times\sin^2\left(\frac{\pi k}{N}\right)f''\left[4R^2\sin^2\left(\frac{\pi k}{N}\right)\right].$$

For a given N, criterion (50) should be met for all possible l ranging from 0 to $N/2$. For example, for the sum of noncollective attraction and Yukawa interaction,

$$V(r) = \frac{Z_d^2e^2}{r}\left[\alpha_{\text{scr}}\exp\left(-\frac{r}{\lambda_{\text{scr}}}\right) - \alpha_{\text{ncoll}}\right], \quad (53)$$

and in the case of a small cluster with $N = 4$, the criterion of the existence of equilibrium $\omega_{N,0}^2 > 0$ takes the form

$$\omega_{4,0}^2 = \frac{1}{\sqrt{2}}(1+\sqrt{2}R)\exp(-\sqrt{2}R)$$
$$+\frac{1}{4}(1+2R)\exp(-2R) - \frac{\alpha_{\text{ncoll}}}{\alpha_{\text{scr}}}\left(\frac{1}{\sqrt{2}}+\frac{1}{4}\right), \quad (54)$$

where R is normalized to λ_{scr} and ω_0^2 is normalized to $Z_d^2e^2\alpha_{\text{scr}}/m_dR^3$. From Eq. (54), one can clearly see that, by changing the confining potential, one can reach a point at which $\omega_0^2 = 0$ and equilibrium is lost. By measuring this point, one can determine the coefficient α_{ncoll} for noncollective attraction. A similar procedure can be used for clusters with other numbers of grains N. If the results for different N coincide, then the type of interaction used is correct. However, if there is no coincidence, one cannot say whether it occurs because the attraction potential is different or because the Yukawa interaction is not applicable. One can also check the above complete nonlinear potential, which includes the influence of charging on the interaction. Figure 13 [49] shows the quantity $Y_N = \omega_0^2/Z_d^2e^2m_dR^3\alpha_{\text{scr}}$ as a function of R (in units of λ_{scr}) for different numbers of grains N in the cluster for the case where the dust grains interact by the pure Yukawa potential and noncollective attraction is ignored (see Eq. (53) with $\alpha_{\text{ncoll}} = 0$), while Fig. 14 shows the square of the equilibrium frequency $Y_{N,\text{ncoll}}(R)$ for the interaction potential, including non-

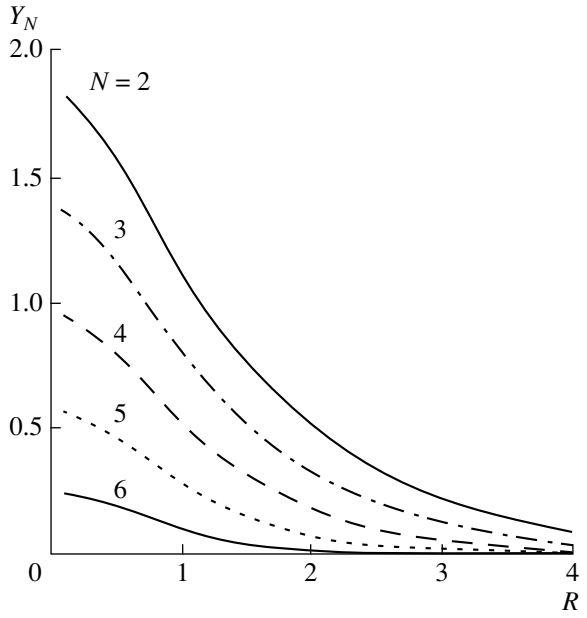

Fig. 13. Square of the normalized equilibrium frequency of a 2D cluster Y_N as a function of the cluster size R for different values of the number N of grains in the cluster. The binary interactions of the grains are assumed to be Yukawa interactions, R is in units of the screening length λ_{scr}.

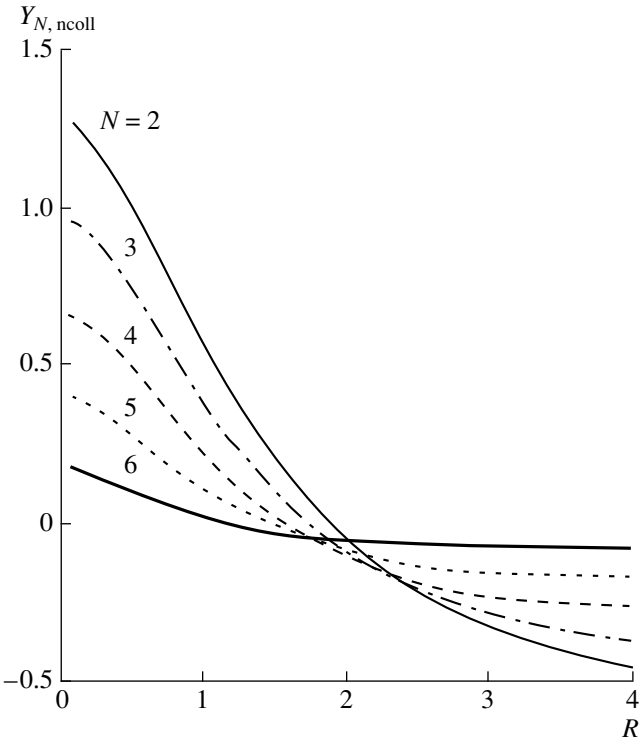

Fig. 14. The same as in Fig. 13 but with the additional noncollective dust–dust attraction for $\alpha_{ncoll}/\alpha_{scr} = 0.3$ taken into account.

collective attraction (normalized in the same way as in Fig. 13) for different numbers of grains in the cluster N and for the ratio $\alpha_{ncoll}/\alpha_{scr} = 0.3$.

Collective interaction does not operate for a small number of grains; however, there exists a condition under which grains with a large size (and a large charge) are embedded in an almost continuous "sea" of small grains that affect the balance between ionization and absorption. This is similar to collective interaction in the sense that the interaction potential of large grains is of the same type as collective interaction, $\propto(1/r)\cos(r/\lambda_{coll})$, where λ_{coll} is the length determining the first minimum of the attraction potential. The corresponding equilibrium frequency $C_N(R) = \omega_0^2/Z_d^2e^2m_dR^3\alpha_{coll}$ as a function of R (in units of λ_{coll}) for N dust grains interacting by the potential $V_C = (Z_d^2e^2/r)\alpha_{coll}\cos(r/\lambda_{coll})$ is shown in Fig. 15 [51].

It can be seen that, in the case of noncollective interaction or collective interaction for each frequency, there exist at least two values of R where the cluster can be in equilibrium, while for the Yukawa potential, there exists only one such value of R.

The noncollective interaction can be measured by finding the condition where the equilibrium will be lost. The presence of several equilibrium values of R opens the possibility of the theoretical treatment of clusters with several shells, as has been observed experimentally. However, a detailed analysis should be first made of the frequencies and the stability of the simple poly-

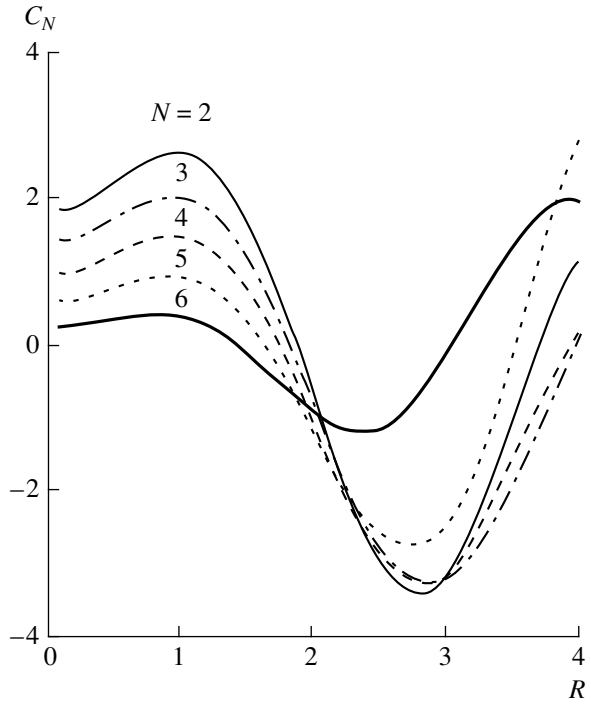

Fig. 15. The same as in Fig. 13 but with collective interaction taken into account; R is in units of the collective length λ_{coll}.

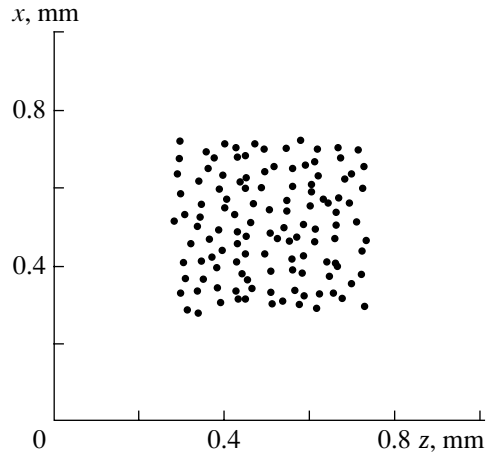

Fig. 16. Initial random dust distribution in the computation box for MD computations with allowance for long-range noncollective attraction and repulsion.

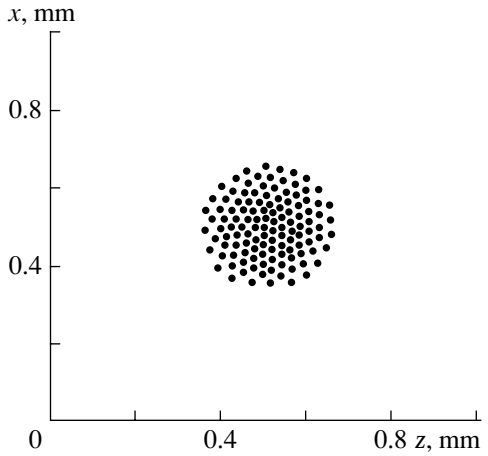

Fig. 17. Final stage corresponding to the 2D boundary-free cluster observed in MD computations.

gon clusters described by dispersion relation (51). Also, the problem of frequencies and the stability of the shell clusters should be examined. To compare theory with experiments, it is necessary to include the damping due to ion–neutral collisions, which can not only lead to the damping of oscillations of clusters but can also change the criteria of their stability.

1.5.3. Molecular-dynamics computations of dust clusters. In several numerical simulations already performed, the KARAT code [52] was used to solve problems of charging, attraction interaction, and the formation of plasma clusters. One advantage of the KARAT code is that it takes into account not only electrostatic phenomena but also electromagnetic processes, the presence of beams, nonthermal distributions, and magnetic fields, and is suitable for both particle-in-cell (PIC) and molecular-dynamics (MD) simulations. PIC simulations were used in [52] to check the OL theory for kinetic effects in charging and to check the noncollective attraction forces. One should note that, in the KARAT code, the input and output can be done in physical units, for instance, in μm for the dust size.

Table

	2D	3D
T_i, eV	0.03	0.03
T_e, eV	3	3
n, cm^{-3}	3×10^9	3×10^9
a, μm	2	1
N	50	200
Z_d	5200	2600
λ_D, μm	23.4	23.4
λ_M, μm	228	228
ν_{nd}, s^{-1}	100	280
m_d, g	5×10^{-11}	6.3×10^{-12}

Note: N is the number of grains in a cluster, n is the plasma density, λ_D is the Debye length, and λ_M is the dust molecule size corresponding to the minimum of the potential for noncollective attraction and Yukawa repulsion.

MD simulations of the transition from a random dust distribution to a plasma cluster were first performed in [53], where the dynamics of electrons and ions was not considered, but it was assumed that they were responsible for the shielding of grains and long-range repulsion and noncollective attraction. Grain friction in neutral gas was also taken into account. Only binary pair dust–dust interactions were taken into account. This excluded collective interactions, although, in principle, MD calculations can be performed with large numbers of grains such that the size of a dust cloud exceeds the length L_{cr}, at which collective interactions start to operate. But any extension to such sizes will be inconsistent under the assumption that only binary pair interactions are taken into account. Computations were performed together with a check that the applicability limit of pair dust interactions was not exceeded. This can be done by controlling the initial size of the dust cloud, the cloud evolution, and the final size of the dust cloud. The interaction coefficients were calculated in dimensional units using the theoretical expressions and parameters often encountered in state-of-the-art experiments. These coefficients were used in the MD code to trace the dynamics of the grains that were initially distributed randomly in the computation box. Two- and three-dimensional MD simulations were performed with about 10^5 grains in the computation box. The parameters of the MD computations are shown in the table.

The grains start to move from their initial random positions (Fig. 16) due to the forces acting between

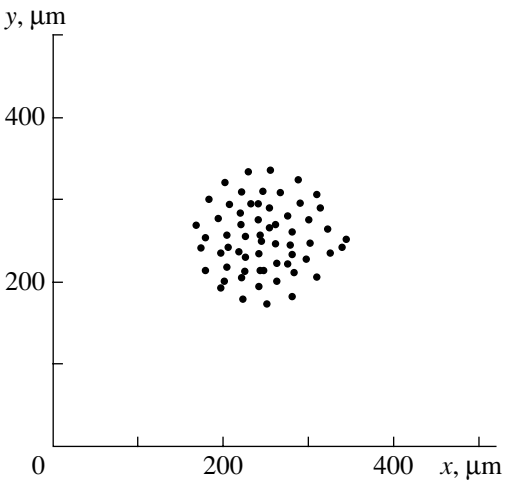

Fig. 18. Final stage corresponding to the 3D boundary-free cluster observed in MD computations. A projection of the distribution onto a plane $z = 260$ μm is shown.

them (including the friction on neutrals) and finally take new positions corresponding to a crystal structure shown for the 2D case in Fig. 17 and for the 3D case in Fig. 18 (in the latter case, the crystal is regular; Fig. 18 presents the projection of the 3D configuration on a plane and, therefore, the observed irregularities are related to the visualization problems).

One can clearly see the hexagonal structure of the plasma cluster lattice obtained numerically. The binary correlation functions (the definition will be given below) found in computations are shown for 2D and 3D simulations in Figs. 19 and 20, respectively. The final size of the dust cluster was 5000 and 3000 μm for 2D and 3D computations, respectively. This satisfies the condition $L < L_{cr}$.

The observed cloud contraction to a cluster is due to only the attraction forces and thus, in contrast to the above case of the presence of an external confinement potential, the clusters obtained in numerical MD simulations are boundary-free clusters. It seems inappropriate to use a larger total number of grains in these MD simulations, since the size of the crystal structure obtained will exceed the distance at which the collective effects will be significant.

So far, no simulations have been reported in the literature that self-consistently treat charged grains and the ion and electron dynamics, i.e., all of the components of a complex plasma [54]. An interesting development in this important field is the NRL dynamically shielded dust (DSD) simulation code, used also for the problem of particle shielding [55, 56]. This code utilizes MD techniques [57], PIC methods [58], the particle–particle/particle–mesh (P^3M) technique [59], and the dresses particle regression (DPR) [59]. The self-contraction of a dust cloud in the initial stage of simulations [53] is satisfactorily described by electrostatic instability, which is similar to gravitational instability and is caused by noncollective attraction [60, 61].

One aspect of the transition to a strongly correlated state should be emphasized: the most important indication of such transition is the behavior of the pair correlation function $g(\mathbf{r})$ obtained by averaging of the product of the dust densities with respect to the discreteness the dust component,

$$g(\mathbf{r}) = \langle \delta n_d(\boldsymbol{\rho}_0)\delta n_d(\mathbf{r} + \boldsymbol{\rho}_0)\rangle. \qquad (55)$$

In this expression, the dust density is assumed to be stationary (time-independent) and the dust cloud to be almost homogeneous, in which case the correlation function depends only on the difference of the coordinates of two positions at which the dust density is con-

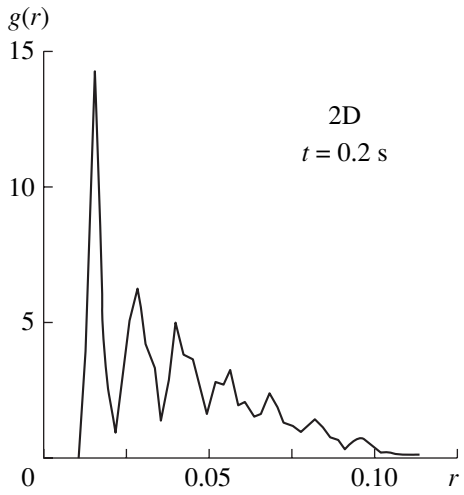

Fig. 19. Pair correlation function $g(r)$ obtained in MD computations of a 2D boundary-free cluster.

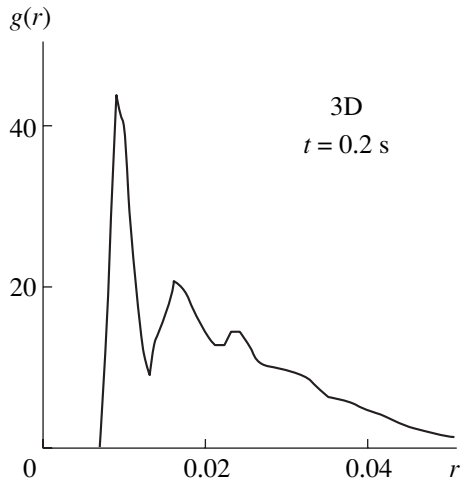

Fig. 20. Pair correlation function $g(r)$ obtained in MD computations of a 3D boundary-free cluster.

sidered. Expression (55) can be used in slightly inhomogeneous systems if the characteristic length of the inhomogeneity is much larger than the correlation length. Correlation function (55) can be measured in the gaseous state of complex plasmas, in transitions to liquid and crystal states, and in a crystal state. The theory of correlations can be developed in the gaseous state, where the correlation function can be expressed through the dielectric function of complex plasma. Such a dielectric constant for a fully homogeneous state assumes that $L \gg L_{cr}$ and, therefore, the expression for the dielectric function should be used with collective effects included (see [2, 7, 62]). For clusters with $L < L_{cr}$, the correlation length should be much smaller that L_{cr} for expression (55) can be used to describe pair correlations. When this requirement is satisfied, the correlation function is determined by noncollective attraction in binary dust interactions. The general theory of dust correlations in the gaseous complex plasma state was developed in [4–8], where the correlation function was described in terms of electrostatic plasma responses (see also [62]).

In [62], the dielectric function for noncollective dust pair interactions found in [60] was used to theoretically describe the pair correlations for noncollective dust–dust attraction. The applicability of expression (55) is related to the smallness of the ratio of the dust size to the Debye length ($a^2/\lambda_{Di}^2 \ll \sqrt{\tau}$, as follows from the condition $L_{corr} \ll L_{cr}$ with allowance for the estimate of the correlation length found from MD simulations [53] and theoretical analysis [62]). The pair correlation function for collective interaction has not yet been investigated. The investigations in [62] indicate that the correlation function can be oscillatory in character even in the gaseous state. As the dust temperature decreases, the amplitude of oscillations increases. The theory of correlations for phase transitions is still not developed. One can expect that the appearance of deep oscillations in **r** decaying on short scales is an indication of the conversion into the liquid state, and the appearance of deep spatial oscillations on large scales is an indication of the conversion into a crystal state. In ordinary matter, the criteria for conversion into the liquid and crystal states are found experimentally: the second minimum should be at least about two-thirds of the first one. In the gaseous state, the correlation function in ordinary matter has no oscillations. It is a very surprising and interesting result of the theory of correlations in complex plasma for the cases of both noncollective and collective interactions of the dust grains that these correlations show the presence of oscillations, i.e., that the complex plasma in its gaseous state is, in a certain sense, "prepared" for the phenomenon of plasma condensation. The latter can occur when the dust temperature is lowered.

There are many problems of the behavior of dust correlations in the gaseous state that remain to be analyzed theoretically and compared with experiments. The kinetic consideration of the correlations, including the change in the electron and the ion distributions in the charging process, has not yet been considered.

Developing the theory of correlations should be done in several stages: a more detailed theoretical investigation of (1) the collective correlation function in the gaseous state, (2) correlations in phase transitions, and (3) correlations in a strongly correlated crystal state. All of these developments should studied in future theoretical investigations of complex plasmas.

1.6. Theoretical Approach for Phase Transitions in Complex Plasmas

1.6.1. Transitions in systems with large and small numbers of grains. There are many problems related to phase transitions in complex plasmas. Among these, the most important are the following two:

(i) The openness of the complex plasma system and the possibility of using the thermodynamic approach to describe such transitions. One can hope only to describe the dust component thermodynamically.

(ii) If under certain conditions the thermodynamic description can be applied to the dust component, the problem is that the number of grains is usually not very large and, for the number of grains less than a certain critical one, the thermodynamics of small finite number of particles should be used. The latter problem remains to be developed (see, nevertheless, [63]), and, in general, further development of the thermodynamics of systems consisting of a finite number of particles is needed.

One may hope that 3D crystals can be described in terms of the existing thermodynamics applicable to systems consisting of a large number of particles, but there is no hope of describing 2D monolayer crystals or 3D clusters consisting of a few dust grains. Obviously, for a small number of grains, noncollective interactions operate, including the noncollective attraction described above, while for 3D crystals, collective interaction should operate.

The theoretical criterion for the collective interaction to dominate is

$$L \gg L_{cr} = \frac{\lambda_{Di}^2}{aP_0}. \tag{56}$$

For existing observations [64–69] of plasma condensation, L is on the order of one centimeter, while λ_{Di} is about 30–50 μm, a is about 10 μm, and P_0 is about 0.3–0.5. In this case, L_{cr} is about 0.01–0.1 cm, which means that the theory should be based on the collective interaction of dust grains. Such interaction has been investigated only for large distances; for short distances, it is known that the screening is nonlinear. Hence, we should operate with a certain screening length that does not coincide with the linear Debye length. In state-of-the-art experiments, the collective

parameter is neither large nor small: $1 < \eta_{coll} < 4$, if there is no ion drift present. But some experiments are performed in plasma sheaths in the presence of an ion flow, which substantially decreases the ion drag and the ion charging coefficients to the product of which η_{coll} is proportional. Therefore, for some 3D systems, collective interaction can be weak; i.e., $\eta_{coll} \ll 1$. When the experiments are performed not in the plasma sheath but, for example, in the striations of a glow discharge [68], the electric field is also present and this field also creates an ion drift. To reach a large collective effect, it is possible either to exclude the ion drift or to increase the size of dust grains. In ground-based experiments, the grain size cannot be made large since the grains will not levitate in the plasma sheath and can fall onto the lower electrode. Of course, there is the possibility of using hollow bubble-type grains, whose mass is sufficiently small for them to levitate in the plasma sheath. This is a subject for future experiments. Under microgravity conditions, one should be able to produce plasma crystals far from the wall, since the wall, often being at the floating potential, will create an ion flow toward itself and therefore decrease the efficiency of the collective interactions. We note that, at present, crystals under microgravity conditions are created close to the wall. But there still exists the possibility of optimizing the attraction between the grains and creating more rigid crystals far from the wall. There are also two limits of the possible experimental conditions: collisionless and collision-dominated. Experiments can be performed for both cases. In the collision-dominated case, the collective coefficient is less sensitive to the presence of the ion drift but the interaction always corresponds to weak collective interaction, as has already been pointed out. Therefore, in what follows, we focus our attention on the case of weak collective interaction for both collisionless limit and collision-dominated limits. Due to the validity of condition (57), the interactions should be considered as collective interactions. We also leave the case of a small number of grains, where the problem of phase transitions is much more complicated than for large system in which condition (57) is satisfied.

1.6.2. About the equation of state in complex plasmas. It is desirable to describe the complex plasma state and the process of condensation by some form of the van der Waals equation [70], which was very helpful in describing phase transitions in ordinary matter. It has already been emphasized that the complex plasma is an actually an open system and there exists a question of whether it is even possible to define the equation of state for such a system. Obviously, this can only be done with some limitations. First of all, it is desirable to write an equation only for the dust component and, in particular, for the dust pressure p_d (which, in the case where the dust is considered an ideal gas, is determined by the relationship $p_d = n_d T_d$). It has also been emphasized that, in experiments, electrons and ions are not thermal since the characteristic time of ion–ion, ion–electron, and electron–electron collisions, which can only make their distribution thermal, is much larger than the times of ion–dust collisions and ionization–the processes that make the ion and electron distributions nonthermal. The condition that the ion–dust collisions dominate over the ion–ion collisions is

$$Z_d P_0 \gg 1. \tag{57}$$

This condition is satisfied in most of the experiments with complex plasmas performed so far. The electron and ion distributions become nonthermal due to the charging process, which depletes the high-energy part of the electron distribution and the low-energy part of the ion distribution [6]. Ionization also produces nonthermal distributions. Then the question arises about the dust distribution: it is thermal or not? It is possible that this distribution is thermal because of the very high rate of dust–dust collisions due their large charges. The dust charge also depends strongly on the electron and ion distributions. Therefore, strictly speaking, one cannot apply the concepts of thermodynamics and of free energy to the dust component to derive the equation of state. We are speaking here about the problem of finding the equation of state for the dust component exclusively. Nevertheless, we can try to introduce the dust temperature, since the dust distribution itself can be thermal due to the high rate of dust–dust collisions. It was found theoretically in [7] that these collisions indeed thermalize the dust distribution. Also, the measured dust distributions are often found to be close to thermal distributions (see [71]).

Another effect operating in the presence of many grains is the charge reduction of an individual grain by collective effects (the presence of other grains). It can be estimated that this effect is small if the number of grains in the Debye sphere times the ratio of the dust size to the Debye length is small. In most experiments, this factor is indeed not large and is often small. Thus, for simplicity, we will ignore this effect. With all of these uncertainties and ignoring charge variations, one can try to write the van der Waals equation for the dust component in the form already known in statistical physics [70].

In [72], the case most applicable to state-of-the-art experiments, that of collective dust–dust interactions, is considered, and the critical value of the coupling parameter Γ_{cr} is estimated. We then shall consider noncollective interactions and will point out the restrictions for its applicability to the case of a small number of grains and find for this case Γ_{cr}, which depends on the size of the system. Finally, we will show that, for the Yukawa interaction, phase transitions are not possible in the van der Waals approach.

1.6.3. Van der Waals equations in complex plasmas: Collective interactions. Using prescriptions of statistical physics for the dust component only, we write [70, 72]

$$(p_d + p_0)(1 - n_d/n_0) = n_d T_d, \tag{58}$$

where the pressure correction term (containing the new quantity p_0) and the density correction term (containing the new quantity $1/n_0$) are defined in statistical mechanics through the partition function [70]

$$B(T_d) = 2\pi\int_0^\infty\left(1 - \exp\left(-\frac{V_{dd}(r)}{T_d}\right)\right)r^2 dr \approx \frac{1}{n_0} - \frac{p_0}{n_d^2 T_d}. \tag{59}$$

The last two terms in Eq. (59) are due to the approximate division of the integration region with respect to r into the region of strong interaction, $V_{dd}(r)/T_d \gg 1$ (the first term), and the region of weak interaction, $V_{dd}(r)/T_d \ll 1$ (the second term). We simply rewrote the known van der Waals equation, making the subscripts d in expressions for the density and temperature. In Eq. (59), V_{dd} is the dust–dust interaction energy, which depends on the interdust distance r, and integration is performed with respect to interdust distances. The first part of the integral determines the density corrections and appears from integration over the region where the interaction energy is much larger than the temperature and the exponential term can be ignored, while the second term is determined by integration over the region where the dust energy interaction is small as compared to the dust temperature and the exponential term can be expanded. Thus, we have

$$\frac{1}{n_0} \approx \frac{2\pi}{3}\bar{r}^3, \tag{60}$$

where $\bar{r}$ is the distance at which the interaction energy is on the order of the dust temperature (it will be assumed that $\bar{r} > a$, otherwise one must substitute the dust size a for $\bar{r}$ in the density correction term). If $\bar{r} \ll \lambda_{scr}$, we can use the approximate dust Coulomb interaction to obtain the estimate $\bar{r} \approx \Gamma_d/n_d^{1/3}$. It is easy to estimate that, with all of the nonlinearities in the screening taken into account, $\bar{r}$ is larger than the screening length. For both cases $\eta_{coll} \ll 1$ and $\eta_{coll} \gg 1$, we have $\bar{r} \approx r_{lin} Z_d T_i/T_d \gg r_{lin}$ (where r_{lin} is the distance at which the linear approximation used before for collective dust–dust interactions start to be valid). Because of the high number of collisions with neutrals, the dust temperature cannot differ greatly from the ion temperature and Z_d is very large. Even during phase transitions where the dust temperature can increase by one or two orders of magnitude, it cannot reach $Z_d T_i$ for the usual values of $Z_d \approx 10^3$–10^4. Thus, to estimate $\bar{r}$, we can use the collective interactions already found by using the linear dielectric permittivity. This gives for $\eta_{coll} \ll 1$ the density correction term as

$$\bar{r} \approx \frac{Z_d e^2}{T_d}\eta_{coll}; \quad \frac{1}{n_0} = \frac{2\pi}{3}\left(\frac{Z_d^2 e^2}{T_d}\right)^3 \eta_{coll}^3 = \frac{\Gamma_d^3 \eta_{coll}^3}{2n_d} \tag{61}$$

and the pressure correction term as

$$p_0 = n_d^2 \frac{\pi Z_d^2 e^2 \lambda_{Di}^2}{P_0 \tau}. \tag{62}$$

The applicability condition of expression (62) (namely $\bar{r} > a$) can be written as $T_d < T_e \eta_{coll} z$. In state-of-the-art experiments, $3 < z\eta_{coll} < 10$ and the maximum dust temperature during the melting of a plasma crystal does not exceed the electron temperature by an order of magnitude, which means that the finite dust size correction in the density (volume) term can be on the order of the interaction correction only exclusively (probably under conditions close to the melting point). Expressions (61) and (62) were obtained by integrating the collective dust–dust interaction potential $(Z_d^2 e^2 \eta_{coll}/r)\cos(r/\lambda_{coll})$ from $\bar{r}$ up to infinity, assuming that $\bar{r} \ll \lambda_{coll}$ (the distance at which the first collective attraction minimum is located is $\pi\lambda_{coll}$) and that weak damping due to ion–neutral collisions suppresses the interaction at very large distances. The first assumption $\bar{r} \ll \lambda_{coll}$ means that, in the collisionless limit, we have approximately $Z_d \eta_{coll}^{3/2} (a/\lambda_{Di}\sqrt{\tau}) z_0 \sqrt{P_0} (T_i/T_d) \ll 1$. Although the first factor Z_d is large, all other factors are rather small due to the assumption $\eta_{coll} \ll 1$ made in the derivation of this inequality. Therefore, it can easily be satisfied. One usually defines the volume V_d occupied by the dust and the total number of grains N_d in this volume such that the dust density is $n_d = N_d/V_d$. The dependence of the volume correction and the pressure correction on V_d is quite different for complex plasmas and ordinary gas. For example, in ordinary gas, n_0 is independent of V, while in expression (60) $n_0 \propto V_d^6$. The ratio p_0/n_d^2 in ordinary gas is independent of V, while in expression (62) it is inversely proportional to V_d. This makes the van der Waals equation for the dust component in complex plasma quite different from the van der Waals equation in ordinary gas [70].

Note that most laboratory experiments are performed in plasma sheaths in the presence of an ion flow, which changes the collective interactions as described above. Unfortunately, in this case, it is difficult to obtain an analytical expression for the interactions because there is anisotropy, but the above types of integrals, which determine the density and pressure corrections in the van der Waals equations, can be calculated numerically. There remains a great deal of work to be

performed in the future: it is necessary not only to calculate the set of interaction curves at different angles to the flow but also to interpolate between these curves in order to calculate the corresponding integral numerically. A similar situation arises in the of presence of a strong magnetic field. The calculations performed here are given for purposes of illustration and also to point out the remaining problems for the procedure that should be performed in future theoretical efforts (along with experimental efforts to measure the potential of dust–dust interactions and the distributions of ions in velocity space in the ion flow), and even to prove the possibility of using the van der Waals equations for complex plasmas.

1.6.4. Estimates of collective Γ_{cr} for phase transition in complex plasmas. As soon as one finds the dependence of the dust pressure on V_d from Eq. (58), the critical temperature for a phase transition can be found from two relations

$$\frac{\partial p_d}{\partial V_d} = 0, \quad \frac{\partial^2 p_d}{\partial V_d^2} = 0. \tag{63}$$

Since the dependence of the dust pressure on V_d differs from the usual one, the expression for the critical temperature has a slightly different numerical coefficient which, in the collisionless limit, is 15/22 instead of 8/27 in [70]. This coefficient enters into the expression

$$T_{d,\,\mathrm{cr}} = \frac{15}{22}\frac{p_0 n_0}{n_d^2}. \tag{64}$$

After substituting expressions (61) and (62) into Eq. (64), the latter gives a threshold value for Γ for the phase transition

$$\Gamma_{\mathrm{cr}} = \sqrt{\frac{15}{11}}\left(\frac{3}{4\pi}\right)^{1/6}\frac{n_d^{1/3}\lambda_{Di}}{\sqrt{P_0\tau\eta_{\mathrm{coll}}^3}}. \tag{65}$$

Due to the presence of the small quantities $\sqrt{\tau}$ and $\eta_{\mathrm{coll}}^{3/2}$ in the denominator of expression (65), the critical value of the coupling constant Γ_{cr} for phase transitions is rather high. In the collision-dominated case, only the numerical coefficient changes from 15/11 to 2/3, but η_{coll} is different and is determined by expression (75) in [2].

For $\eta_{\mathrm{coll}} \gg 1$, the potential well for collective attraction is rather deep,

$$U_{\mathrm{well}} \approx Z_d T_i z_0 \frac{a}{\lambda_{Di}\sqrt{\tau}}\sqrt{P_0}, \tag{66}$$

and this can be reached in the regions where the ion flow is absent and the coefficients α_{dr} and α_{ch} are on the order of unity; i.e., at $\eta_{\mathrm{coll}} \gg 1$, we have $a/\lambda_{Di}\sqrt{\tau} \gg 1$ and, therefore, $U_{\mathrm{well}} \gg Z_d T_i$, which, in most cases, is much larger than T_d. Hence, the van der Waals approach, assuming the opposite inequality, apparently cannot be applied. Assuming that, in the course of phase transition, the dust separation is on the order of the width of the potential well and the dust temperature is on the order of its deepness, we obtain the rough estimate

$$\Gamma_{\mathrm{cr}} \approx 1, \quad T_{\mathrm{cr}} \approx U_{\mathrm{well}}. \tag{67}$$

Such plasma crystals will be very rigid since, after dust cooling by dust–neutral collisions, each dust grain in the crystal will be sitting in a very deep potential well. Such crystals are unknown in ordinary matter and they can probably be obtained only in microgravity experiments, where the dust cloud that is to be converted to the crystal state is created at the center of the experimental chamber, far from the chamber wall. The melting temperature of such a crystals should be very high. This is the greatest demand for future plasma crystal experiments under microgravity conditions.

1.6.5. Van der Waals equation in complex plasmas: Noncollective interaction. A peculiar aspect of the concept of noncollective dust–dust interaction is that it can be applied only to finite systems (see Eq. (56)). On the other hand, noncollective interaction allows the existence of a single attraction well that is located at

$$r_{\mathrm{well}} \approx \lambda_{Di}^2/a\eta_{\mathrm{st}}. \tag{68}$$

When only the shadow effect of ions is important (see [2]), the sticking coefficient η_{st} is equal to the ion sticking coefficient $\eta_{\mathrm{st},\,i}$, which is on the order of unity, and expression (56) indicates that the range in which the noncollective interactions in the van der Waals equation can be used is determined by the inequality $P_0 \ll 1$. When the neutral flux dominates, the effective sticking coefficient in Eq. (68) is expressed through the neutral sticking coefficient $\eta_{\mathrm{st},\,n}$ by the expression $\eta_{\mathrm{st}} = \eta_{\mathrm{st},\,n} n_n T_n T_i / 4 T_e^2 z^2$ (see [2]) and, for high dust pressures, can be much larger than unity. In this case, condition (56) can be less restrictive, allowing $P_0 \approx 1$. In any case, the size of the system cannot be larger than L_{cr}. We will assume that $L > r_{\mathrm{well}}$. The quantities n_0 and p_0 can be found using the noncollective potential of interaction containing long-range repulsion and attraction terms [2]. The integration over small r gives expression (60) with

$$\bar{r} \approx \min\left\{r_{\mathrm{well}}, \frac{Z_d e^2}{T_d}\eta_{\mathrm{ncoll}}\right\}, \tag{69}$$

where η_{ncoll} is the coefficient of noncollective interaction (see [2]). The integration over large r should be restricted by the size of the system L. This assumes that the inhomogeneity of the distributions inside the system is not great. This is partially supported by numeri-

cal MD computations with noncollective interactions (see Figs. 17, 18). Due to the accepted condition that the size of the system is larger than r_{well}, the integral over large r is determined by the noncollective attraction term. We then obtain

$$p_0 = \eta_{\text{ncoll, attr}} n_d^2 \frac{Q^2 L^2}{2T_d}. \quad (70)$$

The critical parameters for the phase transition are determined by Eqs. (63). We find

$$\eta_{\text{ncoll, attr}} n_d \frac{Q^2 L^2}{T_d} = \frac{3^{7/5}}{27^{2/5}} \approx 1.07. \quad (71)$$

From here, we obtain the dependence of the critical dust temperature on L/L_{cr}:

$$T_{d,\text{cr}} = 0.074 Z_d T_i \frac{\eta_{st}}{P_0} \frac{L^2}{L_{cr}^2}. \quad (72)$$

The two factors entering into this expression, $Z_d \gg 1$ and η_{st}/P_0, are large (see inequality (20)), while the numerical coefficient and the factor $(L/L_{cr})^2$ are small.

1.6.6. Absence of phase transitions for the Yukawa potential. Physically, the absence of phase transitions follows from the fact that $B(T_d)$ is always positive and, as a result, $p_0 < 0$. Calculations similar the above calculations yield all of the coefficients, and the result is that phase transition conditions (63) can be satisfied only if $n_d < 0$, which is obviously impossible.

1.6.7. Comparison of Γ_{cr} with experimental data. It is only possible to make some estimates, since the real value of the ion drift velocity is unknown, at least for the experiments performed so far. For experiments on plasma crystals in RF and glow discharges, we obtain $\Gamma_{cr} \approx 10^3$–10^4 and, for dense plasmas (such as combustion plasma), we have $\Gamma_{cr} \approx 1$, which is in qualitative agreement with observations (see a detailed description of experiments in [3]). Expression (72) can be used in the future when 3D dust clusters are observed. Up to the present, only experiments on 2D clusters have been performed, for which the staring expressions that were used to derive the van der Waals equations are not valid.

2. RESEARCH TRENDS AND APPLICATIONS

2.1. Trends in Experimental Investigations of Complex Plasmas

2.1.1. Charging of dust grains. Two aspects are important for the dust charging problem: the first is direct measurements of the dust charge, and the second is to check the existing theoretical models to be able to estimate dust charges under the conditions where direct measurements of dust charges is impossible. The planned experiments should deal with simple single dust grain charging, which is important for noncollective dust interactions, and with the collective effects in dust charging. It is desirable to clarify many of the aspects of the existing models of dust charging, particularly the dependence of the charges on the grain material and the grain structure. The checking of different charging models such as described in part one of the review [1] for spherical grains, namely, the OL model, the RD model, or the DL model as described in [1], is one of the first steps in this kind of research. The dependence of the charges on the ratio of the grain size to the Debye screening length a/λ_{Di} and the ratio of the latter to the ion–neutral mean free path is also an important subject for investigation. In practice, the attachment coefficient of both electrons and ions can be different for different materials and, therefore, the electron and ion currents can be modified. One of the most important phenomena to be investigated in detail is the dependence of electron and ion attachment on the structure of a grain, especially for the case where the grain surface is rather irregular. This occurs for grains growing up to the cauliflower shape caused by grain agglomeration [73–76]. It is believed (but not yet proven) that such agglomerate structures are fractal. The sticking coefficient for irregular-shape grains is virtually unknown.

Grains of specially designed shapes can be used in experiments, particularly cylindrical grains (microrods) or even fractal-shaped grains. Another important problem is the dependence of the grain charge on the particle distributions; the simplest problem of this kind is the charging in the presence of an ion flow or an electron beam. The process of charging (especially in the presence of beams or flows) can change the surface properties (and, therefore, the attachment coefficients) and raise the secondary electron emission. Unfortunately, the large amount of data from probe measurements cannot be used in solving these problems, since the size of the probes is usually larger than the screening length, while the size of the dust grain is usually smaller than the screening length (only such grains are used in the present experimental research of complex plasmas).

Collective effects in grain charging are another subject for future investigations. The simplest experiment could be the testing of a decrease in the grain charge when two grains become closer to one another. This would be the first step in testing the influence of other grains on the charges of an individual grain. In the presence of many grains, this effect will be enhanced. Also, an insufficient number of plasma particles (for example electrons) in the vicinity of the grain (caused, e.g., by the presence of other grains) can reduce the grain charge. It is important that all of these questions be investigated experimentally.

An important factor is the nonlinear shielding of the grain charges and the presence of the nonscreened part of the potential. This long-range potential could be important in grain interactions. Although the Yukawa model is used in many experiments to compare the

observed results with theoretical findings, this type of screened potential is not predicted by the theory, due to both nonlinearities and the long-range part of the potential. Therefore, experiments to check the screening of dust grains is of great importance. These cannot be performed only as colliding experiments, as was done in the pioneering work of [77, 78], because the problem needs a complex approach. Above all, collisions should be investigated between dust grains of different size where the smaller grain can serve as a test grain. This would allow one to avoid nonlinearity in screening, which can change the screening during a collision. Second, nonintrusive methods of dust grain measurements should be developed; among these are the scattering of radio waves by grains and the experimental use of the properties of grain clusters.

2.1.2. Dust–dust interactions. Among the processes that should be investigated is the influence of the ion drag, dust friction, and thermophoretic force on the interaction of two isolated dust grains. The presence of the noncollective dust attraction forces can be checked by varying the neutral pressure for the known neutral–dust attachment coefficient by using specially designed dust materials with large attachment coefficients. This investigation opens up a whole new field of research on dust agglomeration and has promising future applications for the problems of etching.

The manipulation of dust grains by both gravity and thermophoretic forces under laboratory conditions will be used in future experiments on the investigation of dust–dust interactions. These investigations will have direct applications for dust clusters, in which the dust–dust interaction is usually noncollective. One of the methods for the detection of intergrain interactions is the investigation of small clusters of grains embedded in a parabolic potential well. A cluster of N grains has $2N$ oscillation modes, the frequency of which for a small number of grains depends only on the pair intergrain interactions. Thus, by measuring the frequencies of the cluster normal modes, it is possible to make some conclusions on the pair interdust interactions. By increasing the number of grains in a cluster, one can check whether the binary interactions depend on the number of grains in the cluster and, therefore, detect the critical number of grains at which collective interactions start to operate.

Of most interest for future experiments is the detection of collective dust–dust interactions. The experiments can be performed in 3D dust clouds, dust crystals, dust monolayers, and dust linear chains. The grains chosen for the detection of the interaction can differ from other grains by some parameters such as the grain size or grain shape. The experimental problem is to determine the pair grain interactions as a function of the average density of other grains. Such experiments can provide answers to many problems of collective grain behavior and to the problem of the threshold conditions for plasma condensation. As the number of grains in a 3D cluster increases, the pair interaction between grains changes until the cluster acquires properties similar to those of a crystal and the collective interaction will be similar to that in crystals. This is a long-term experimental program. Three-dimensional clusters can be investigated under microgravity conditions; thus, all of the experiments can be performed using microgravity facilities.

2.1.3. Strong magnetic fields. There are several critical magnetic field strengths that are of importance for the plasma particle motion and for the operation of experimental setups. The first is the ratio of electron and ion gyro-radius to the size of the installation L. When this ratio is small, one can speak about magnetized electrons and ions. There is always friction between ions and dust grains, and even when the ion gyroradius is much less than L, their orbiting on the gyroradius will be interrupted by collisions with dust grains. If the frequency of these collisions is larger than the ion gyrofrequency, the ions will remain unmagnetized, although their motion along curved trajectories between subsequent collisions will result in the transfer of angular momentum to the dust grains, thus causing their rotation. The second restriction is related to the ratio of the gyroradius to the effective size at which the ions and electrons are collected on the grains during the charging process. When the electrons are magnetized in the sense that their gyroradius is less than the electron collection radius, the fast electrons will still reach the grain, while the slow electrons will be reflected. This reduces the electron current by a factor of 4 and decreases the grain charge. Even if the magnetic field is much stronger and the ion gyroradius is much less than the ion collection radius, the ions are magnetized in the charging process and the ion current is reduced, thus leading to an increase in the grain charge. The theoretical predictions about the change of the dust charge with increasing magnetic field are presented in [79]. Experiments in this field are expected to be performed soon.

Another new effect introduced by the magnetic field is dust rotation, which in the simple model is related to the $\mathbf{E} \times \mathbf{B}$ drift.

The rotation of plasma in the magnetic field was experimentally observed in [80, 81].

The condition that the ion gyrofrequency in a magnetic field be higher that the ion–dust collision frequency is [2]

$$B\ [\mathrm{kG}] > 94\frac{a}{\lambda_{Di}}P_0 z_0 \Lambda\left(\frac{0.02}{\tau}\right)\sqrt{\frac{n}{10^9\ \mathrm{cm}^{-3}}}, \qquad (73)$$

where we recall that a is the grain size, λ_{Di} is the ion Debye length, $P_0 = n_d Z_{d,0}/n_{i,0}$, $z_0 = Z_{d,0}e^2/aT_e$, and Λ is the Coulomb logarithm. Note that criterion (73) is derived for continuous dusty plasmas for which the parameter P_0 can be introduced. In the experiments in [80], a dust monolayer was used and the friction force

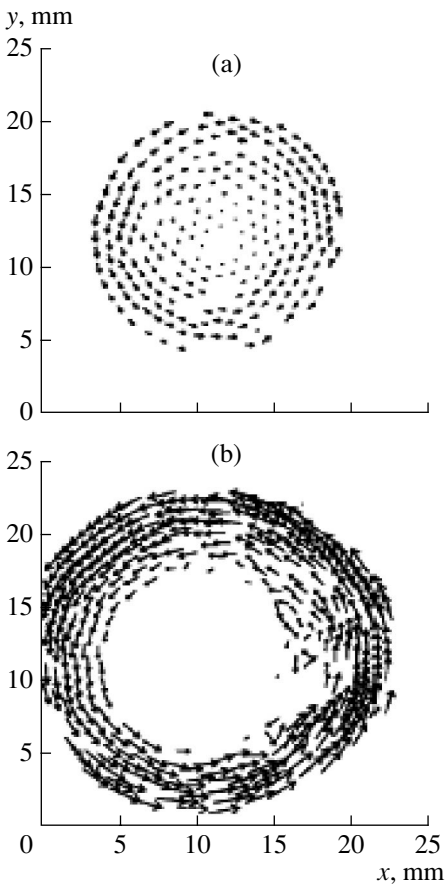

Fig. 21. Typical configuration of a dust cloud rotating in a magnetic field. The vectors indicate the particle displacements in 20 consequent frames, N is the number of grains, p is the pressure, and U_{pp} is the peak-to-peak RF voltage: (a) U_{pp} = 47 V, p = 0.40 mbar, N = 250; (b) U_{pp} = 82 V, p = 0.3 mbar, N = 450.

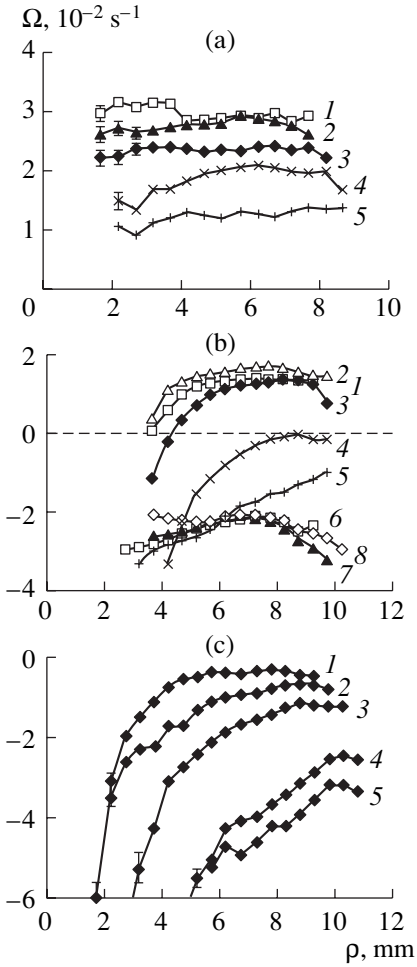

Fig. 22. Angular velocity Ω of a dust grain moving in a magnetic field vs. distance ρ from the center of rotation. Positive values of the angular velocity correspond to counterclockwise rotation. Each figure shows a set of curves taken at a fixed RF voltage and total number of dust grains N and for different pressures p: (a) V_{pp} = 47 V, N = 250 (curves *1*, *2*, *3*, *4*, and *5* are obtained for p = 0.3, 0.4, 0.5, 0.6, and 0.7 mbar, respectively); (b) V_{pp} = 82 V, N = 850 (curves *1*, *2*, *3*, *4*, *5*, *6*, *7*, and *8* are obtained for p = 0.25, 0.3, 0.5, 0.7, 0.8, 0.9, 1.1, and 1.2 mbar, respectively); (c) V_{pp} = 93 V, N = 700 (curves *1*, *2*, *3*, *4*, and *5* are obtained for p = 0.4, 0.6, 0.7, 0.9, and 1.0 mbar, respectively).

was substantially lower than that used in derivation of condition (73). The presence of an inhomogeneous electric field can cause the azimuthal $\mathbf{E} \times \mathbf{B}$ drift and the rotation of the dust cloud in the plane perpendicular to the magnetic field, as was first observed in [82] in dc glow discharge plasmas and in [83] in RF plasmas.

The first experiments on complex plasmas in a magnetic field [80, 81] indicate a direction in which future experiments can be extended. Therefore, we shall briefly describe these results.

The magnetic field strength used in [80] was 140 G but the ratio a/λ_{Di} was about 1/50, which gives a critical field of about 1 kG. The ion friction on dust grains is obviously much less in the case of a dust monolayer and is absent for ions far below the layer. Thus, estimate (73) does not operate well under the conditions of the experiment [80]. In [80], the ions simply drift in the magnetic field and the radial electric field confines the dust layer. The dust rotation velocity is determined by the balance between the ion drag force produced by the ion drift and the dust friction on neutral gas. Thus, the effect of rotation depends strongly on the neutral pressure and on the peak-to-peak voltage U_{pp}, which determines the dc electric field at distances where the grain rotation is observed. Figure 21 illustrates the dependence of the rotation of a dust cloud on U_{pp} and the gas pressure, and Fig. 22 illustrates the dependence of the angular velocity of rotation on the distance from the center of rotation. It was observed that, under certain conditions, the dust clouds contracts to a small size due to dust spiraling toward the center (Fig. 23).

These figures illustrate what kind of new effect one can expect to observe in complex plasma in an external magnetic field. Above all, the contraction of the dust

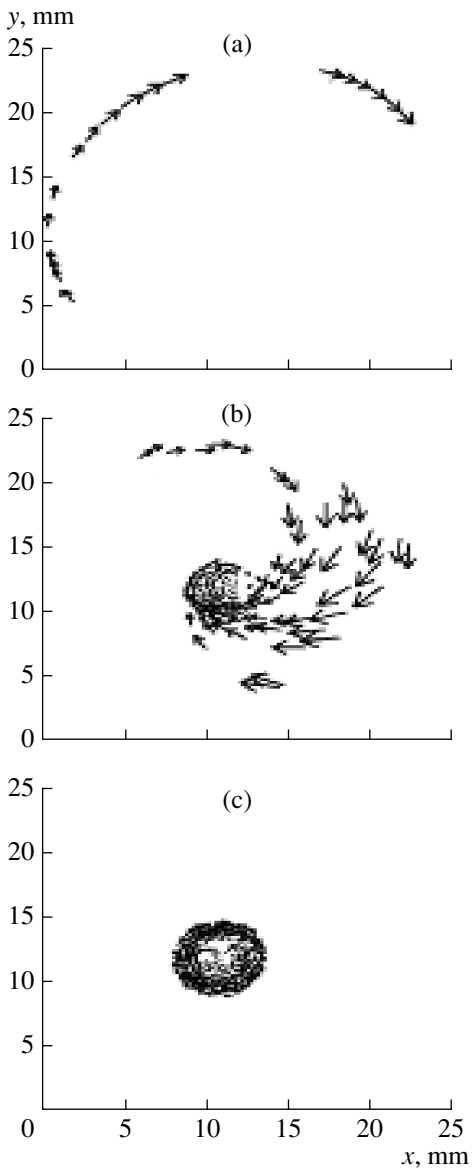

Fig. 23. Three consecutive graphs showing the (a) initial, (b) intermediate, and (c) final stages of contraction of a dust cloud toward the center after a sudden increase in V_{pp} from 100 to 300 V for a pressure $p = 3$ mbar. The vectors indicate the grain displacements in 20 consequent frames. The contraction happens on a time scale of a few seconds.

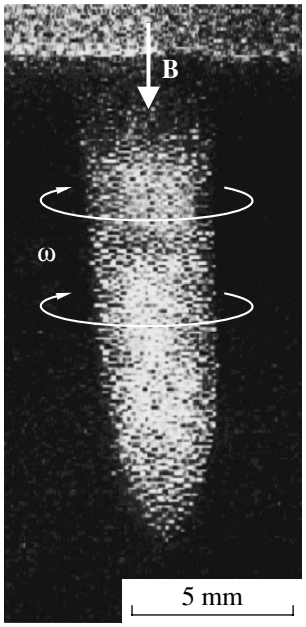

Fig. 24. Typical column-shaped dust cloud in a magnetic field.

cloud perpendicular to the magnetic field is also an effect that is expected from the theory of collective dust–dust interaction in a strong magnetic field described in [2, 30] (see below). It is also expected that the melting temperature of the plasma crystal in a magnetic field will increase with increasing magnetic field strength, since, as was demonstrated in [2, 30], the potential well of the collective attraction increases with magnetic field strength.

In [81], in which a much stronger magnetic field (from 0.4 to 40 kG) was used, the ratio of the dust size to the Debye radius was on the same order of magnitude as in [80]. In this case, the critical field can be estimated using expression (73), since all ions are subject to friction on dust for the dust cloud configuration shown in Fig. 24.

The observed rotation of the cloud was almost a solid body rotation (see Fig. 25). The observations of [81] are interesting because they indicate what new kinds of dust structures can be encountered in future experiments in a magnetic field. In simulations involving only screened grains (charged negatively), the particles exhibit an azimuthal $\mathbf{E} \times \mathbf{B}$ drift (say, in a clockwise direction). In the experiments, it was surprisingly found that sometimes the grains rotate in the opposite direction (anticlockwise). The explanation for this is the interaction with other plasma components. The ions, being charged positively, drift opposite to the negatively charged particles. It is the drag by ions that may finally force the grains to drift in the opposite direction. Obviously, the grains, having a large mass, are not magnetized and, therefore, do not experience the drift force.

Of course, these observations are only the first steps in the direction of investigating the role of strong magnetic fields in complex plasmas.

One important question is the rotation of dust grains produced by charging of nonspherical grains [79]. The particles absorbed by the grain usually should lose their angular momentum before they are attached to the grain, thus forming the accretion disk that is very well known in astrophysical investigations of accretion problems. A similar accretion disk can be formed around a dust grain. The angular momentum will be transformed partially to the grain causing its rotation. A

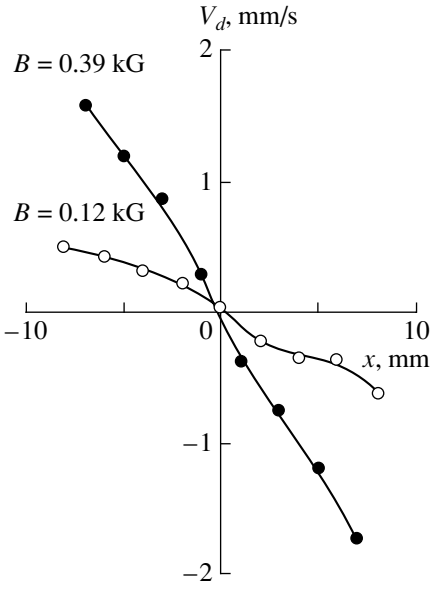

Fig. 25. Rotation speed v_d as a function of the radius r at a vertical magnetic field strength of $B = 0.12$ and 0.39 kG, gas pressure of 220 mtorr, and discharge current of 0.5 mA.

new kinetic approach is necessary to describe the spinning angular magnetic moment and its interaction with an external magnetic field [84]. The consequences of this angular momentum transfer to the dust grain will be very important. It can cause collective grain rotation and, therefore, create regular collective magnetic moments of aligned grains in the magnetic field, which would lead to the creation of a self-consistent magnetic field by the dust clouds. This field of research opens up completely new possibilities for investigating the role of external and self-generated magnetic fields in complex plasmas. One important problem is investigating the change of collective dust–dust interactions in the presence of a strong magnetic field. The examples discussed in [2, 85] show that a strong magnetic field can increase the potential well for dust–dust interaction and can decrease the distance between the grains at which the collective attraction determines their interaction.

Another approach using strong magnetic fields is related to magnetic grains, i.e., grains with an initially large magnetic moment. To describe their interaction with the magnetic field in complex plasmas, both the kinetic and the hydrodynamic approach can be used [84]. Ordinary magnetic materials have a domain structure with different orientations of the magnetic field in different domains. The size of a domain is several μm, and when a single grain represents a single magnetic domain, the magnetic moment of the grain can be rather large, and the magnetic field at the surface of such a grain can also be very large. With these magnetic dust structures, one can perform many experiments including dust plasma condensation, plasma crystals, monolayer crystals, etc., i.e., the entire spectrum of experiments performed so far with dust grains without magnetic moments. Experiments with dust grains having different nonspherical shapes are of special interest. An important problem is the investigation of the alignment of dust grains along a strong external magnetic field, especially in the case of strong dust–dust interactions. Obviously, these grains can produce a large magnetic field themselves and change the external magnetic field.

2.1.4. The boundary between the dust structure and the dust-free plasma. In all structures investigated so far, the surface between the dust-containing region and the dust-free region was rather sharp. Future experiments should be performed to answer the following question: When such a sharp surface can be destroyed, what could the distribution of grains in the surface region be, and what is the value of the surface tension? In the simple description given above, the dust density can have a jump at the surface, and the surface tension is simply determined by the product of the dust density jump and the dust temperature. An interesting problem is to find how the sharp density profile is formed in time and the conditions where this happens. It seems that the sharp surface could be related to the ion drag produced by the ion flow, which acts stronger on the first dust layer it encounters and weaker on the subsequent dust layers; as a result, the first layer moves with a higher velocity and the dust layers at the surface are compressed to form a sharp boundary. The force that acts against these compression forces is the dust pressure. But the dust pressure is rather weak and, therefore, the boundary should be sharp. The thermophoretic forces can work in an opposite way and, therefore, the combination of drag and thermophoretic forces at the dust boundary can create boundaries of different sharpnesses. This effect could be the subject of experimental investigations.

2.1.5. Waves, shocks, solitons, and moving dust structures. The difference between complex plasmas and ordinary matter is the high rate of dissipation. Shocks and solitons in ordinary matter are nonlinear waves without large dissipation: solitons exist in the case of weak dissipation, while in shocks, the dissipation is present only at their front region. In complex plasmas, the dissipation is usually present in the main part of the nonlinear wave; therefore, the general concept of nonlinear waves is cardinally changed: for a nonlinear wave to propagate, it usually must be maintained by an additional external source of energy. Note that this is not surprising, since the complex plasma is an open system and even its ground state needs to be maintained by external ionization. For this reason, it is necessary to carry out more sophisticated experiments. Another important point could be related to the presence of an external magnetic field: The ion and electron gyrofrequencies can often be much less than the charging frequency; therefore, all of the collective magnetic modes known for ordinary plasmas are changed. We definitely need to fix the external sources on which the

linear responses of complex plasma depend, as well as to develop a theory of linear modes for these external sources. Nonlinearities should be determined by nonlinear responses, which also depend on external sources. At present, no advanced theoretical description of linear modes propagating in the background complex plasma in a magnetic field is available. Experiments should be developed together with an appropriate theoretical description of the modes and nonlinearities. The first attempts to investigate experimentally nonlinear structures in a complex plasma were described in [3], and the first efforts to show that nonlinear structures in complex plasma are highly dissipative and need an external source to be supported was made in [3]. In [85], one finds examples of numerical solutions for highly dissipative structure moving with a constant Mach number $M = 1$.

2.2. Trends in Theoretical Investigations

2.2.1. Development of the theory of waves and instabilities. In contrast to ordinary plasmas, in which the waves and instabilities have been investigated in detail and are summarized in textbooks, a proper list of waves and instabilities in complex plasma is still unavailable. This is related first of all to the greater complexity of the ground state in which, in addition to the charge balance condition, the balance of ionization and absorption should also be used [86]; this was realized only recently. Second, it is related to the dependence of the linear dispersion relation for waves and instabilities on the source of ionization. Third, due to universal structurization instability [27], the ground state for waves can be highly inhomogeneous. At present, it is realized fully that the presence of dust in plasma can change the linear dispersion relation in a broad range of frequencies (below, the charging frequency or the charging frequency times $P = n_d Z_d / n_i$) and in a broad range of wavenumbers (below, the inverse charging length or the charging length is divided by P). The work required to prepare a list of waves and instabilities in complex plasmas has not yet been performed. For example, there are several calculations for the damping of Langmuir waves in complex plasmas. But even for such a simple problem, several answers exist in the literature that contradict one another or take into account only part of the effects that can cause damping and do not take into account other effects (which in fact can be larger than those that are taken into account). Even a full hydrodynamic description of waves and instabilities in homogeneous complex plasmas is not yet available. A major effort should be made to systematize the work that has already been performed, in order to clarify the limits of their applicability, etc.

2.2.2. Weakly nonlinear theory in complex plasmas. Here, we have in mind the known quadratic and cubic nonlinearities. To describe quadratic nonlinearities, efforts should be made to find the analogy of $(\mathbf{v} \cdot \nabla)\mathbf{v}$ terms used in the Kordeveg–de Vrees equations for ordinary liquids and plasmas. Obviously, in the presence of the charging damping of ion motions, additional terms of this type can be present in complex plasmas. Their role is still waiting to be analyzed. Both the Kordeveg–de Vrees and the Boussinesq equations will be different in complex plasmas as compared to ordinary plasmas. A full analysis of this problem is still lacking. In ordinary plasmas, cubic nonlinearities describe the modulational interactions. In the future, the full cubic responses in complex plasmas should be found and analyzed. At present, the only fragmentary investigations in this field cannot provide a full understanding of the effects that can be encountered in cubic complex plasma responses.

2.2.3. Development of the theory of complex plasmas in strong magnetic fields. The theory of a complex plasma in a strong magnetic field has only started to be developed. The first major problems are related to the charging and screening of grains in a magnetic field. In [81], only some estimates for the charging cross section in the presence of a magnetic field are given for the limit in which the electron gyroradius is much less than the electron collection radius and for the case in which the ion gyroradius is much less than the ion collection radius. All intermediate cases should be investigated numerically. Further development is related to a more detailed investigation of the collective dust–dust attraction in the presence of a strong magnetic field. This will give an indication of the possible change of crystal structures by the magnetic field and will be one basis for the investigation of collective self-organized structures in a strong magnetic field.

2.2.4. Scaling invariance and phase transitions in complex plasmas. It is well known that, in the transition to the strongly correlated state in ordinary matter, fluctuations increase substantially and the scaling laws describing them can be obtained theoretically and have been confirmed experimentally [87]. One could expect that, for complex plasmas, fluctuations close to the transition will also substantially increase, but the possibility of using scaling lows is questionable since the system is open and the free energy concept is inapplicable. The whole problem must be reconsidered, and this has not yet been done. The lack of a concept of free energy was clearly demonstrated above in calculating the collective attraction forces. Also, the Landau approach for phase transitions using the expansion of the free energy close to the transition point is questionable. If one finds some parameter similar to the parameter of order in the Landau concept, then this parameter in complex plasmas should depend on the type of the source. The new trends can be seen from the universal instability of DAWs found in [86]. The investigations in [86] were made only for the linear stage of instability. This instability has a peculiar property of exciting an almost singular mode. Since the excited "structure" is simply sinusoidal, one can expect that, on the nonlinear stage, it will correspond to a single nonlinear mode.

The amplitude of this mode can probably serve as a Landau parameter for the phase transition. Investigations can then proceed by the scheme of the scale-invariance approach. The final aim of these investigations is to study the pair correlation function.

2.3. Applications

2.3.1. Technological and industrial applications. The treatment of surfaces using plasmas is very much developed in industrial applications. These include the coating of surfaces with thin films and plasma etching for the production of computer chips. The physical processes in these different experiments can be quite similar.

We consider here plasma RF etching, which seems to be one of the processes with the greatest practical importance.

(i) Dust Clouds in Etching Devices

Investigation of the formation of dust clouds in the processes of plasma etching was begun in [74, 88–92] (originally in [89, 90]), where laser scattering from dust in the etching chamber was used to detect dust clouds levitating above the etching wafers. It was soon confirmed that these clouds are an inevitable consequence of the etching procedure, where the etching material forms droplets or dust grains at the surface of the wafer. They become charged at the surface of the etching sample, and the electric force of the sheath then lifts the dust grains above the surface and the grains start to levitate in the electric field of the sheath close to the surface. The density of dust grains in the levitating cloud increase continuously until the interaction between them becomes strong and they often form a dust liquid cloud. The first proof that such a dust cloud can in fact be plasma–dust liquid drops was given in [76]. The cloud levitating above the etching sample can have a rather complicated shape (see Fig. 26).

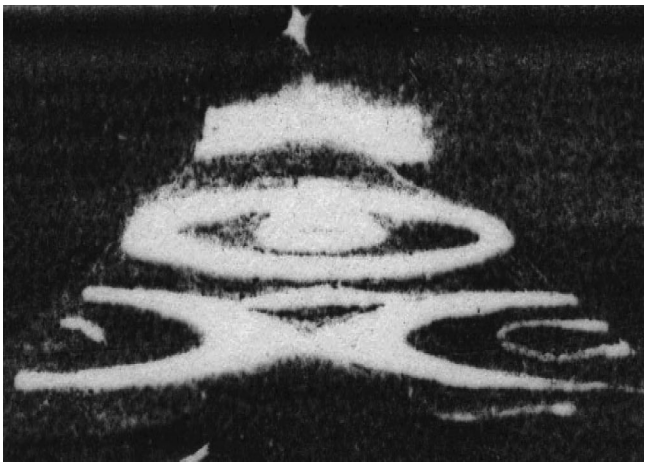

Fig. 26. Dust structure observed in etching experiments.

The size of the grains in the cloud continuously increases during the etching process [91]. It was shown in [92] that the etching products injected into the plasma volume during etching can also form layered structures in which each layer is similar to some kind of a 2D plasma crystal. The structure and the particle separations, however, may vary from one layer to another so that the size of the dust grains decreases with height. The difference between the conditions for etching and dust experiments on plasma crystals is that the dust cloud is composed from grains with different sizes and that the dust density (at least at first stages of etching) is several orders of magnitude larger that in plasma crystal experiments. The dust is formed in etching by natural processes, and, in view of specific practical aspects, there are only a few possibilities for changing devices and performing diagnostics. The dust can finally fall on the etching sample and spoil the product. In [92] it was observed that the fall of the dust grain can be catastrophic in a sense that the dust cloud, after continuously growing, suddenly falls as a whole on the sample. Sometimes the largest grains start to be concentrated on the lowest layer and form a continuous "rain" of dust grains on the sample surface.

The formation of these structures is inevitable and undesirable as natural contamination in the production procedure. We will give only a general description of the problem and briefly discuss some important principal points, not only for etching, but also for many other experimental devices in which low-temperature plasmas come into contact and interact with the surfaces surrounding the discharge volume.

(ii) Formation of Dust Grains in Etching Devices

The formation of dust grains in low-temperature plasmas appears to be a common phenomenon. The discovery of the presence of dust grains in the low-temperature plasmas of gas discharges was made as early as 1924 in the pioneering work by Langmuir [93]. The most detailed and recent investigation on the role of dust grains in the positive columns of gas discharges was performed in [94]. At present, it has been confirmed that most low-pressure plasma discharges contain a relatively large, well confined dust component. This confinement is due to the appearance of negative charges on dust grains having the floating potential, as well as to the presence of negative charges on the wall of the discharge chamber. The appearance of the latter has the same cause. The potential barrier between the volume and the wall for electrons is approximately T_e (in energy units), but for dust grains with a charge $Z_d e$, this potential barrier will be $Z_d T_e$. As a rule, the dust grains quickly lose their kinetic energy in collisions with neutrals, the density of which in a low-temperature

plasma is usually five to six orders of magnitude larger than the density of electrons or ions. The condition for dust confinement, $Z_dT_e > T_n \approx T_i$, is rather well satisfied in gas discharges. The source of dust grains is the evaporation of macroparticles from the surface of the discharge chamber. This serves as a source of dust grains in any discharge, not only those invented for etching, though for etching, this source is much more efficient. Let us describe in a very rough and simple manner the principle of the etching mechanism used in most industrial installations for the formation of computer microcircuits. As was mentioned above, the double layer formed in a gas discharge close to the wall (and also close to the wafer used for etching) repels the electrons and accelerates the ions. The ions traversing the double layer cross the potential difference on the order of the electron temperature, which is much higher than the ion temperature; i.e. the ions receive energy comparable to the electron temperature. The sample for etching has a mask, and the ions (of the naturally appearing ion flux) approaching the sample and bombarding it should create a local temperature on the order of that necessary for melding the material of the sample. This inevitably leads to evaporation and the injection of nonspherical fragments of the etchant into the plasma volume. The physics of the appearance of the ion flux is the same as that leading to the formation of the double layer and the levitation of dust grains. Also, the processes of electrode erosion contribute to the injection of macroparticles into the plasma volume.

This makes a huge difference with ordinary gas discharges. The rate of dust injection depends substantially on the properties of the surface, e.g., on its chemical composition and temperature. These parameters can change during the discharge. In etching, chemical processes and the chemical formation of dust clusters also play an important role [91].

In the process of etching, there exist two sources of dust grains. The first of these is related to the oversaturation of vapors of the materials used for etching within the discharge volume. This results in the creation of microdrops. As a rule, in chemically active mixtures, dust grains may be born by chemical reactions. The other source of dust grains is the process of etching itself.

(iii) Stages of Dust Growth

Laser scattering [95, 96] can be used to detect dust grains from a size of 0.01 μm, but the more practicable and most widely used methods for detecting dust grains start to operate from a size of 0.1 μm. Starting from this size, one can follow the evolution of the dust grains and answer the question of whether they are growing or not. The general answer is that they are almost always growing, but the stage of growth depends on the rate of injection of new dust grains and the agglomeration of smaller grains into larger ones. The etching time is usually much longer than the agglomeration time, and the dust grains can grow during the etching up to a size visible to the naked eye.

The mechanism for the growth of dust grains is not well understood, but obviously consists of several stages. The first is the simple Brownian motion of chemical fragments and the formation of clusters of, say, about 100 molecules. This stage was investigated in detail experimentally [96, 97]. The process then continues as grain agglomeration [97]. As the dust grain size increases, the charging process begins and the Coulomb repulsion prevents further agglomerations [97]. The first stage of agglomeration of small dust grains with small dust charges can be described in terms of noncollective dust attraction [98], although estimates show that the role of collective attraction can be also important [2]. The collective attraction is proportional to the parameter $P = n_dZ_d/n_i$ squared. In the stage of the agglomeration of small grains, it is more convenient to use another parameter, $P' = n_dZ_d/n_e$, which is usually estimated to be 10^3–10^4. Since $P' = P/(1 - P)$, the parameter P in this stage of dust growth is very close to unity; this certainly indicates that collective attraction dominates. It is therefore very probable that the collective attraction of dust grains is responsible for the observed first stage of dust agglomeration. More detailed investigation of this problem still need to be performed. As was mentioned above, an increase in the dust size and, therefore, an increase in the dust charge stops the agglomeration and the dust starts to grow rather slowly due to the recombination of electrons and ions on the grains, which leads to the deposition of the material onto the surfaces of dust grains. This process is an inevitable factor related to the ion and electron fluxes appearing from the adjustment of the potential of a dust grain to that of the floating potential; this leads to the appearance of charge on the dust grains. According to the OL approach, the ion thermal flux is larger than the geometrical ion flux by approximately $2.1T_e/T_i \approx 10^2$, which is sufficient to explain the observed growth rate of dust grains in the stage in which the agglomeration has already become inefficient. The characteristic time of dust growth is on the order of a few seconds, which is rather short compared to the duration of the etching processes. The observations indicate that, at these times from the start of the etching process, the measured dust density is already as high as 10^8 cm^{-3} and the grain size is about 0.1 μm. This value of the dust density is at least four orders of magnitude larger than in the experiments of plasma–dust crystals. Therefore, the ratio of n_dZ_d to n_e is much higher than that in the previously discussed experiments on plasma–dust crystals, $P \approx 10^4$–10^2, so the collective effects introduced by the dust are much stronger. The subsequent growth of dust grains can appear as an interchange between the processes of material deposition and dust particle agglomeration. A detailed physical understanding of these processes is still lacking. It is only known that dust grains always continue to grow

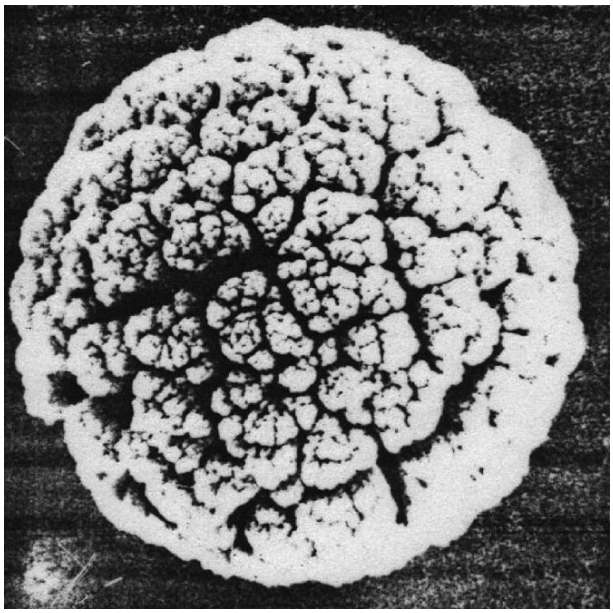

Fig. 27. Cauliflower dust grain observed in etching experiments.

and that they can become, in some stages, perfectly spherical, starting from completely nonspherical shapes, and can, in other stages, form fractal-like structures, probably due to dust agglomeration. After the growth of dust grains due to the deposition of material on their surfaces, another agglomeration stage can often occur. In this stage, the grains often form fractal structures and look like cauliflowers (see Fig. 27).

Most experiments find the appearance of such structures in the final stages of etching. When dust grains are large, both the collective and noncollective attraction of grains can become larger than the Coulomb repulsion. Noncollective attraction was used in [98, 99] to obtain a criterion for dust agglomeration. One of the most important effects in noncollective attraction is that related to the bombardment of dust grains by neutral atoms [100], but collective attraction [85] can also be very efficient. Both effects are proportional to the square of the dust size and, as soon as this size exceeds the threshold value (dust grows for example due to the material deposition process), collective agglomeration can start to operate. Thus, agglomeration can occur either for small dust charges, when the Coulomb repulsion is not able to compete with chemical forces, or for large charges and large sizes, when collective attraction starts to dominate the Coulomb forces.

(iv) The Computer Industry

We should mention one practical aspect of the problem of dust agglomeration: it is the main obstacle to the production of high-quality computer microcircuits. For a long time, this was the main problem hindering the further miniaturization of computers. A review of the results concerning the struggle with this problem until 1994 is given in [101]. In 1999, some progress was made by using the physical properties of dust clouds, namely, the increase in dust–dust interaction with increasing grain size. One could hope that, as soon as this interaction converts the dust cloud into a liquid state and the cloud becomes a liquid drop, the dust cloud can be taken away by inclining the installation, i.e., in the same way as water can be taken off a plate by inclining it. This means the use of the gravity force in an intermediately (not very strongly) coupled state. Another possibility is to use the thermophoretic force, which can be comparable to the gravity force. Finally, a very efficient method is the use of electrostatic cleaners devised in [102]. For microelectronics, the contamination by dust in the etching industry is now under control only for relatively large dust grains ($a > 0.1$ μm) [103]. However, computer technology is developing fast in the ways of miniaturizing computers, and the electronics industry will require in the future that smaller and smaller dust grains be removed from the processing region to avoid the contamination of etching wafers. For dust production and wafer contamination during etching, a crucial role is played by the inhomogeneity of influx from plasma to the substrate, as was pointed out in [104].

2.3.2. Powder production and materials science. Dusty plasma technology allows one to produce powders of very small size grains (in the range of nanometers) that can be rather uniform in size and can have the desired chemical properties [103]. These grains can be used in active surface catalysis. Surface catalysis is a very efficient process because the larger the total surface in the given volume, the larger the catalytic effect. An increase in the surface area can be achieved by dispersing the material into a large amount of small dust grains. This technology is very efficient and promising for industrial applications. Dust grains can also be used in the modern technology of composite materials [105]. The coating of grains with desired materials can have many applications, in the perfume industry among others [103]. Dust grains can be used to produce thin films on the surfaces. The growth of diamonds as dust grains in plasma is a rapidly developing technique [106]. This leads to problems in the surface processing of dust grains [107, 108] and in producing grains with desired surface properties. For these purposes, the industry requires a good understanding of dust–plasma interactions, particularly of the heat exchange between plasma and dust. Ferromagnetic iron dust grains can be used to coat surfaces. Nanostructured composite films can only be produced using dusty plasma technology. Another method for producing nanostructures is the coating of surfaces with plasma monolayer crystals. Carbon nanotubes can be exposed in plasma to implant atoms into nanotubes and form new materials [109]. Thus, the physics of dusty plasmas and complex plasmas has started to play a key role in materials science and surface processing technology [103, 108].

2.3.3. Dust in fusion devices. The wall conditions in fusion devices differ from those in devices for plasma etching; however, near the wall, the temperature can still be sufficiently low for long-term dust survival. The thermal flux onto the wall is rather high, which can lead not only to the evaporation of the thin films coating the wall, but can destroy them and create a flux of flakes from the wall. The temperature at the wall can even be lower than in low-temperature industrial devices due to the radiation cooling of plasma. In particular, this occurs in the so-called detached regions, where the thermal flux onto the wall is almost completely converted into a radiation flux. In these near-wall regions, the temperature can be as low as 0.5 eV. One should expect under these conditions not only survival of the dust produced by the wall but also its levitation in the electric field of the wall sheath. The wall conditions in fusion devices, the temperature profiles, the influence of a thin film covering the wall (the so-called boronization and carbonization of the wall surface) is described in detail in [110] (see also [111]).

Thus, the question arises as to whether dust is really produced at the walls of fusion devices, how long it survives, and what are its characteristics? It was found that dust grains are present in any fusion device and that they can be collected after many discharges. Their size ranges between a few nm to 0.1 μm. For several hundred discharges, their total mass is estimated to be about 100 g [112]. Recent investigations have shown that, in fusion devices, dust is created in every discharge and is produced in especially large amounts in the so-called disruption phases, where the plasma flux onto the wall is rather high—on the order of the flux that is expected in future fusion devices such as the ITER [113]. Dust grains collected after many discharges differ in size, and one can often find dust agglomerates (see Fig. 28). It is unlikely that these agglomerates could be formed in a single discharge since the estimated time of the formation of an agglomerate is much larger than the discharge duration. This indicates that dust grains can grow from discharge to discharge, being attached to the wall between the discharges and levitating in the sheath field during discharges.

In existing fusion devices, dust does not play a major role, although it can influence the start-up phase of a discharge and control the rate of impurities injected into the discharge. Dust can play a more important role close to the limiters and in the detached regions. In future fusion devices such as the ITER, dust can be a major problem because of the much larger flux onto the wall due both to the much longer time of operation to the radioactivity of the dust grains [112]. Wall erosion is well-established phenomenon and is directly related to dust formation. Unipolar arcs at the surface are also well known in fusion devices; in principle, they can produce dust structures of certain complicated shapes, such as the well-known carbon nanotubes. It has been claimed that such nanotubes were observed in tokamaks [114]. It is known that nanotubes are efficiently produced in arc discharges and that unipolar arcs operate in fusion discharges. Thus, the presence of nanotubes as dust grains during a discharge is quite possible. The observations of [114] are indirect, and nanotubes were not collected after discharges; thus, they could somehow be destroyed at the end of a discharge. Observations show that many dust grains collected after a discharge have strong magnetic properties, although no magnetic materials were used to coat or treat the surface. This means that magnetic dust is created during discharges. On the other hand, high-power loading during disruptions or in the edge localized modes leads to the evaporation of wall films, and the dust grains are known to efficiently grow from such oversaturated vapors. These grains can coagulate due to the collective or noncollective attraction described in [2]. The average size of the agglomerates of grains observed in fusion devices after coagulation is about 0.1 μm. The mechanism for the dust growth in the case of high-power loading can be checked by repeatedly exposing a carbon material using high-power electron gun as in [85]. The average power to which the carbon material was exposed was about 1 GW/m^2 and the evidence of the formation of fullerene-like materials was fixed, as well as the formation of dust agglomerates. It is known that fullerenes (at the periphery) and carbon nanotubes (at the center) can be produced in the same arc discharge. Therefore, this observation serves as an independent argument for the possible presence of nanotube dust structures close to the wall of a fusion device [114]. The formation of magnetic dust close to the wall is of special interest both from the general physical point of

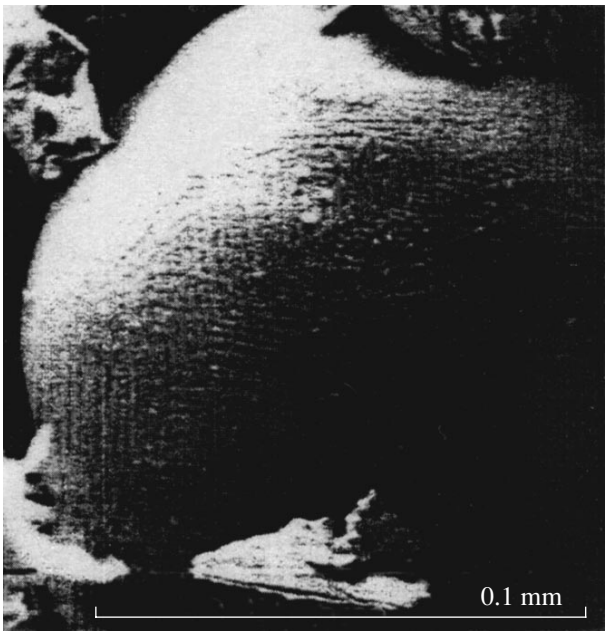

Fig. 28. Dust created by many shots in tokamak fusion devices.

view and for the problem of the start-up phase of fusion discharges, when the magnetic dust collected in minimum-B regions can act as an impurity source raising the emission rates. In future fusion devices, the main concern is the radioactivity of dust [111–113]. This result in many safety problems for future fusion devices. A new technique of dust removal during a discharge should probably be used [108, 113].

2.3.4. Dust cluster laser fusion. After plasma condensation into cluster and grains, the material can be exposed to a very strong laser radiation. The same can be performed for single-layer plasma crystals or dust clusters confined externally in a parabolic potential well [115–118]. After irradiating by a laser, each grain explodes, evaporates, and forms a fast expanding cloud. Electrons heated up to 0.5 MeV act on ions by ambipolar force, thereby increasing their energy above the nuclear reaction threshold. Each expanding cloud, being initially packed closely, has a nuclear density large enough to produce nuclear reactions. The laser absorption rate is larger for the material formed by clusters or plasma crystals than for ordinary dense matter. This method is being considered for the creation of a future fast neutron source and a new table-sized fusion device.

2.4. Environmental Applications

2.4.1. Dust exhausts. Environmental applications for the new field of complex plasmas are related to the possibility of removing dust from industrial exhausts. Most exhausts are dust injected into the atmosphere. Before injection, the dust can be charged by applying a high voltage and initiating a glow discharge at atmospheric pressure. If one succeeds in making this dust interact strongly to form a strongly correlated state, one has the opportunity to use dust cleaners to remove the dust. For industry, it is possible to use the newly found dust properties to cleanse exhausts. Such applications are rapidly developing [119]. However, real success is not yet foreseen in the near future for this to be an efficient industrial technique.

2.4.2. Atmospheric physics. Many physical phenomena in the atmosphere are related to dust. We list only some of them:

(i) The physics of thunderstorms are related to vapor condensation on dust grains.

(ii) Lightning is mainly related to the charges appearing on dust grains.

(iii) Tornados appear as large air vortices with the significant inclusion of dust grains.

(iv) Dust in the upper atmosphere (at altitudes of about 80–90 km) was first observed long ago by radar echoes. This phenomenon, which was named PMSE (Polar Mesopause Summer Echoes) [120], was proven to be related to the reflection of signals by dust clouds [121]. At present, it has been proven by direct rocket measurements that these clouds are dust clouds [122] (referred to as noctilucent clouds). The source of dust can be of meteoric, volcanic, or pollution origin. The most worrying observation is the continuous increase of dust density in these clouds; this could indicate that pollution is the main source of dust in these clouds. The most intensive formation of these dust clouds in summer is related to the appearance of a temperature minimum at these altitudes during the season. In [121], the enhanced scattering by a dust cloud was explained by the formation of an electron cloud shielding dust grains. This mechanism was believed for a long time to be the major mechanism for the enhancement of reflected radar signals. The latest data [122] indicate that an instability related to dust can create a large-scale electron inhomogeneity. A recent approach to treating this instability was made in [123].

(v) Ozone layer physics are closely related to dust in the upper atmosphere because the depletion of heterogenic ozone on the surface of dust grain is much more efficient than the volume depletion. Ozone depletion occurs mainly on the surface of agglomerates of ice with the inclusion of chlorine molecules. The ozone layer is rather wide: its density is maximal at an altitude of 30 km, and it spreads up to 50–80 km, where ionization plays an important role. Physics and chemistry, as well as complex plasma physics, should be applied in a self-consistent manner to treat the problem of ozone layer depletion.

(vi) There are indications that the global warming effect is related to solar cosmic ray activity. Cosmic rays produce the seeds that start chemical chains ending with molecule agglomerates. The latter serve as seeds for water vapor condensation, which determines the level of clouds in the atmosphere and, therefore, the global warming effect.

The above list shows that the complex plasma physics can play an important role in crucial environmental problems.

2.5. Astrophysical Applications

2.5.1. Dust in interstellar media. Dust in space is a very old subject for investigation. The physics of interstellar media are mainly the physics of the emission and scattering of light by dust grains [124, 125]. Very important information about interstellar media can be obtained from the line emission of the solid material of grains. Scattering by grains of different shapes also gives important information about the structure of magnetic fields in interstellar media since it is believed that nonspherical grains are aligned in the direction of the interstellar magnetic field. From the line emission of interstellar dust, it is possible to find the material composition of the dust grains. This also provides information on the chemical processes occurring in the interstellar medium. Not only minerals but also many organic materials have been found to be present in interstellar gas. Interstellar gas is very inhomogeneous

in density and temperature: there are the so-called HII regions with large electron temperatures (5–10 eV) and a gas density of about 0.01–0.1 cm^{-3} and the so-called HI regions with much lower temperatures (about 10^{-5} eV, or 5–10 K). It is believed that the hot regions are related to the remnants of supernova explosions. The many shocks related to these explosions heat the gas. The product of the temperature and the gas density in both regions is almost the same. In the cold regions, so-called dust–molecular clouds exist. In these clouds, hydrogen is in the atomic state (not ionized). It recombines on the dust surfaces, forming molecules, which is why these clouds are called dust–molecular clouds. This recombination is most efficient not in the volume but on the surface of dust grains. The molecules produced as a result of the recombination process either leave the grains or are attached to the grains, thereby increasing their size. Thus, the process of recombination has two important aspects: the growth of dust grains with increasing recombination efficiency and the existence of a source of molecules in the clouds. The conventional view of grain growth in dust–molecular clouds is one based on the effect of accretion: the condensation of nuclei containing a small number of atoms being bound together by the van der Waals and chemical forces. They grow via the sticking of atoms and their attachment to the surface [125]. This first stage of the Brownian motion–driven dust growth has been considered in detail both theoretically and numerically [126–128] and was recently confirmed by microgravity experiments [129]. This model was also used to explain the slow growth of dust grains in dust–molecular clouds to a size of about 0.1 μm on time scales of 10^6–10^9 years. The further growth of dust grains by accretion is hampered by a number of effects, including the decrease in the sticking probability with increasing grain size, the density and temperature of the ambient neutrals and plasma, and the temperature of the dust grains themselves. The high temperature of grains prevents their further growth. This point of view has been accepted by the majority of the astrophysical community and has long been an astrophysical paradigm, ever since the detailed investigation made in [130] on the attachment and detachment probabilities in a low-temperature molecular neutral gas. The concept of slow dust growth has also been accepted for other astrophysical problems, such as the formation of stars [126]. Note that recent astrophysical observations contradict this paradigm.

2.5.2. Dust agglomeration in space. Important recent observations [127] of circumstellar dust shells around long-period variables [131] demonstrate that dust formation takes place on a time scale of tens of years. The winds of these C-stars so efficiently produces dust that the circumstellar dust shell totally obscures the central object (star). Multiple dust shells in the form of circumstellar structures are also observed. Given the rate of production of multiple shell-like structures, one can propose a new process of dust formation, namely, agglomeration in space. An important feature of the light curve from supernova SN1987A is a break at about 500 to 600 days, coincident with an increase in the infrared flux and an increase in the absorption of the red-shifted emission lines [132]. These observations confirm the formation of dust within the supernova ejection after about 500 days. The dust in interstellar space can be studied using telescopes. Small particles of solid matter tend to polarize light reflected and scattered by their surfaces. Particles of about micron size appear brighter in forward-scattered light than in back-scattered light.

Dust agglomeration due attraction shadow forces in neutral gas [2] can be used to explain the observed phenomenon. The conditions for outbursts, stellar winds, and supernova explosions are different than those in molecular clouds; in particular, the charged plasma component can play an important role. In molecular clouds, the collective and noncollective attraction of dust grains [2] can also be important. The main difference between the conditions in outbursts and molecular clouds is the absence of plasma heated to 3×10^4 K (the degree of ionization by cosmic rays or radioactivity is lower than 10^{-7}, except for the boundaries illuminated by UV radiation, resulting in the rapid growth of the plasma density in certain stages). The presence of plasma can considerably change the growth processes. The dust grains in molecular clouds are not highly charged (Z_d is about 2–3), while in outbursts, the dust charges can be large. The shadow attraction force can be estimated in the same manner as in [2, 133]:

$$F = \frac{a^2}{r^2} nT\pi a^2 A, \tag{74}$$

where a^2/r^2 is the solid angle, a is the dust size, r is the distance separating dust grains, nT is the pressure of either neutrals or ions (we can ignore electrons because of their smaller mass), and A is the numerical factor called the sticking coefficient. The value of the latter depends strongly on the dust surface properties and can vary from 10^{-4} to 1 (on average, 10^{-2}). In the calculations, we previously [2] assumed for simplicity that the dust grains have equal sizes. This is not true under astrophysical conditions. The dust distribution over sizes can be estimated as $dn_d(a)da \propto 1/a^\alpha da$; observations indicate that α is about 3. In this case, we should bear in mind that shadow force (74) is determined by the largest size particles (since $F \propto a^4$). Equation (74) is written for equal dust sizes and for the shadow produced by the neutral gas flux. Attraction can occur even when the sticking coefficient is zero but the dust surface temperature differs from the neutral gas temperature. If a neutral atom during its contact with the surface has sufficient time to be thermalized to the dust surface temperature T_{ds} and is emitted with the energy corresponding to the dust surface temperature, the factor A in

Eq. (74) is $1 - \sqrt{T_{ds}/T_n}$, where T_n is the neutral gas temperature. Under the conditions often encountered in space (when the dust is cooled by emission of radiation with a rate $\pi a^2 \sigma_{SB} T_{ds}^4$, where σ_{SB} is the Stefan–Boltzmann constant), the value of A is close to unity. The force given by Eq. (74) operates both in the presence and absence of plasma. In the presence of plasma, the force due to the ion and neutral flux should be compared to the Coulomb force between two dust grains:

$$F_C = \frac{Z_d^2 e^2}{r^2} = \left(\frac{Z_d e^2}{a T_e}\right)^2 \frac{n_i T_e^2 a^2}{e^2 n_i r^2} = z^2 \frac{a^2}{r^2} n_i T_e 4\pi \lambda_{De}^2, \quad (75)$$

where (as before [1–3]) $z = Z_d e^2/aT_e$ is the dimensionless dust charge on the order of 1–2 and $\lambda_{De} = \sqrt{T_e/4\pi n_e e^2}$ is the electron Debye radius. A comparison of Eqs. (74) and (75) demonstrates that, for $r \ll \lambda_{De}$, the bombardment force by ions is lower than the Coulomb repulsive force by a factor of $4\lambda_{De}^2 z^2/a^2$. For $r \gg \lambda_{De}$, the Coulomb force is screened, while the attractive shadow force is not; this can lead to the contraction of the dust cloud until the intergrain distance is comparable to ten Debye radii. For distances larger than the Debye radius, the ion noncollective bombardment attraction [2] can dominate the Coulomb repulsion and should be added to the effect related to gas particle bombardment attraction.

For outbursts of carbon-rich stars, where $n_n \simeq 10^{10}$ cm^{-3}, n_i is on order of n_n, and $T_e \sim 1$ eV (which corresponds to the Debye radius between 100 and 1000 μm, attraction can occur between two equally charged grains. For $r \sim \lambda_{De}$, the repulsive force can overcome the attractive force, thus forming an attractive potential well with a potential given by

$$V \simeq F_C r \approx z^2 n_i \lambda_{De} a^2 T_e. \quad (76)$$

A dust molecule is formed if

$$T_d < T_e n_i \lambda_{De} a^2 z^2, \quad (77)$$

where T_d is the dust kinetic temperature (not the dust surface temperature). In the regions where dust is cooled by emission of radiation, this condition can easily be satisfied. For $n_i \sim 10^{10}$ cm^{-3}, $\lambda_{De} \sim 10^{-2}$ cm (i.e., $r \sim 10^3$ μm and $a \sim 1$ μm), Eq. (77) results in $T_d < T_e z^2 \sim 10 T_e$, which is easily satisfied in carbon-rich star outbursts [131].

In dust molecular clouds, λ_{De} is very large and the degree of ionization is very low; however, cosmic rays produce ionization such that $n_i/n_d \sim 10^{-6}$–10^{-8}. The latter ratio is only about one order of magnitude less than in laboratory experiments. In most laboratory experiments, the neutral and ion shadow forces are of the same order of magnitude and give rise to second and fourth stages of agglomeration. In dust–molecular clouds, if the dust is not radioactive, the main attraction force is determined by the neutral flux, and Eq. (74) can be used when the dust surface temperature is lower than the gas temperature due to radiative cooling. The phenomenon of dust agglomeration caused by dust attraction due to the neutral particle flux (especially, the formation of dust–molecular clouds) has not been much investigated, but it can apparently operate efficiently in the range of temperatures above the critical temperature (10–80 K). For higher temperatures, this serves as the main mechanism for the dust growth. The agglomeration time can be estimated by taking into account the relative number of particles in phase space with energies lower than the attraction potential well:

$$\frac{dm_d}{dt} = 2 m_d v_d n_d^{\frac{1}{3}} \left(\frac{V}{T_d}\right)^{\frac{3}{2}}, \quad v_d = \sqrt{\frac{T_d}{m_d}}. \quad (78)$$

Since the force acting between two dust grains is directed along the straight line connecting this grains, the characteristic agglomeration time can be estimated as the time needed for the dust grain to cover the intergrain distance. Then, as a direct consequence of Eq. (78), we have

$$\frac{1}{\tau_{aggl}} \simeq \sqrt{\frac{T_d}{m_d}} n_d^{\frac{1}{3}} \left(\frac{T_e n_i a^2 \lambda_{De} z^2}{T_d}\right)^{3/2}. \quad (79)$$

For $a \sim 1$ μm, $T_d \sim 100$ K, $n_d \sim 10^{-3}$ cm^{-3}, we find that the time τ_{aggl} is about 10^9 s ≃30 years.

2.5.3. Protostars: Star formation. The regions where stars are formed are usually regions with enhanced gas density in which gravitational collapse can start to form a protostar. Theoretical investigations and observations show that the gas density in galaxies is inhomogeneous and often forms spiral arms with an enhanced gas density [125, 134–137]. However, this enhancement is no larger than 5%. Therefore, at present, the model of star formation in galaxy arms is attributed to shocks propagating in a dust cloud. Stars are formed in dust-reach regions and mainly from the dust material. The primary gas condensation that is important for star formation and for the initiation of gravitational collapse could be due to the attraction shadow forces discussed in the previous section. The shadow force also creates a gravitational-like instability. The dispersion relationship for the agglomeration instability of the dust component can easily be written using the dispersion relationship for the Jean's instability, in which the gravity force is replaced with the shadow force:

$$\omega^2 = k^2 v_s^2 - G_{eff} n_d m_d,$$

where according to Eq. (75),

$$G_{\text{eff}} = \frac{nT_n\pi a^4}{m_d^2} \tag{80}$$

and

$$v_s^2 = \frac{n_d T_d + n_n T_n}{n_d m_d + n_n m_m} \sim \frac{n_n T_n}{n_d m_d + n_n m_n}$$

if $n_n T_n \gg n_d T_d$. Although the attraction forces act only on dust grains, the expression for v_s corresponds to the sound speed at frequencies much lower than the dust–neutral collision frequency [138]. The corresponding Jeans length is determined by the relation

$$L = \frac{2\pi v_s}{\sqrt{G_{\text{eff}} n_d m_d}} \simeq \frac{2\sqrt{\pi}}{n_d a^2 \sqrt{(1 + n_n m_n / n_d m_d)}}. \tag{81}$$

For $a \sim 1$ μm and $n_d \sim 10^{-3}$ cm^{-3}, we have $L \sim 10^{11}$ cm; i.e., dust clumps with a size on the order of 10^{11}–10^{12} cm are formed.

Since these clumps are much smaller than the Jeans length for gravitational collapse, they should precede stellar and planetary formation. It could be envisaged that a clump forming through this mechanism will evolve to larger and larger scales up to the Jeans length, the structures being similar and scale invariant at each stage. These structures are a result of the self-organization found in complex physical systems. They can collapse, forming structures from asteroids to stars, the formation of which still can be related to additional compression produced by shock waves. The characteristic time for a Jeans-like instability to develop is the same as the agglomeration instability time scale [133]

$$\tau_{\text{ag.inst}} \simeq \sqrt{\frac{m_d}{n_n T_n \pi a^4 n_d}}, \tag{82}$$

which, for $n_d \sim 10^{-3}$ cm^{-3}, $n_n \sim 10^3$ cm^{-3}, $T_n \sim 50$ K, and $a \sim 1$–3 μm, is

$$\tau_{\text{ag.inst}} \sim 10\text{–}100 \text{ years}.$$

This time is three orders of magnitude shorter than the Jeans gravitational collapse time, and the Jeans length is larger by 10^3. The result is the a clumpy structure that is often observed in dust–molecular clouds. Investigations similar to those sketched here can be the subject of future, more detailed models of star formation.

2.5.4. Planetary rings. The physics of planetary rings is a broad field of research. The dust grains in the rings have a wide size distribution. The previous theory and the estimates of the elementary processes in dusty plasmas were given for monosize dust grains. Future theoretical investigations in their application to astrophysical problems and especially to the problems of planetary rings should proceed to the generalization of the theory of the elementary complex plasma processes for the case of grains distributed over sizes. The first efforts in this direction were already made in [139, 140], but the whole problem is far from the stage of being applied to astrophysical problems. The problem of planetary rings serves as a rather good illustration of the trends in this field and the investigations that need to be performed (see [119, 140–142]).

The largest rings of Saturn and Jupiter consist of stones with a maximum size on the order of 3 m. From the point of view of complex plasma physics, these stones are dust grains, since their size is much less than the Debye length, which here is on the order of 0.1–1 km. However, the main question is whether these "grains" are ruled by gravity forces or by the self-consistent forces in complex plasmas, such as the drag force, ram flux force, etc. An important point is that each planetary ring consists of grains of different sizes and different rings are characterized by different maximum grain sizes. Thus, for some of the tiny and rather thick outer rings of Saturn, the complex plasma effects could dominate, while for large inner rings, the gravity forces could dominate. Unfortunately, the present-day theory of complex plasma is still not generalized for the case where the complex plasma contains a spectrum of dust grains of different size, which is actually needed for studying the planetary ring problems as well as many other astrophysical problems. The first efforts in this direction were already made in [142]. The role of gravity in the problems of planetary rings is somewhat similar to the problems of the Earth's gravity in laboratory experiments with complex plasmas. However, even in cases where the gravity effects are large, they can be cancelled out due to the balance between the gravity forces and the centrifugal forces acting on a single dust grain in a planetary ring. This balance of forces is analogous to the balance of the gravity and electrical forces in ground-based laboratory experiments with complex plasmas. As in laboratory experiments where the forces in the direction perpendicular to the gravity are not much affected, the forces perpendicular to the ring plane in a planetary ring can be determined by the collective complex plasma effects such as the ram flux pressure, drag force, etc. To investigate these effects in future, it will be necessary to find the forces averaged over the circular Keplerian motion of grains, which to some extent plays a role of an effective magnetic field. Such a program has not yet been started, but only investigations like these can lead to a deeper physical understanding of the reasons why the observed planetary rings are so thin, what the collective waves are that can propagate in the rings, etc. The latter is very important from the point of view of the interpretation of the Mach cones produced by large stones in the rings [119], which are expected to be used as a tool for investigating ring properties. These investigations will be similar to those in laboratory observations of Mach cones [3]; however, one difference could be in the type of modes that will be excited. The conclusions that could be made in the future from these kinds of observations will

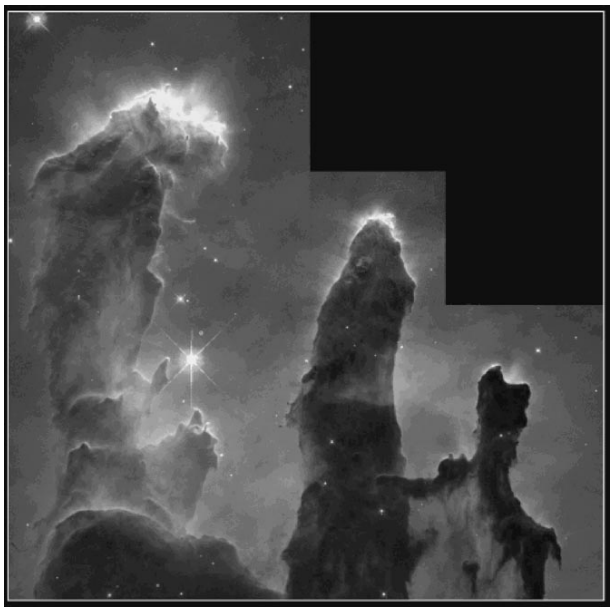

Fig. 29. Sharp dust boundary cloud of the Eagle nebula in space.

depend strongly on the type of the mode excited in a ring. If the wavelength of the excited modes is comparable to the thickness of the planetary ring, these modes will be closer to the surface modes, and their dispersion could be quite different from the dispersion of the DAW modes.

2.5.5. Cometary tails and cometary interactions with the atmospheres of planets. Comets emit large clouds of dust that interacts with the solar wind. At present, it is not clear whether dust drift instabilities are the main subject of interest in this area or if other types of collective instabilities are also important. The penetration of a comet's substance into planetary atmospheres creates dust clouds, which then produce enormous structures that emit and scatter light [143].

2.5.6. Acceleration of grains in space: Relativistic dust grains as cosmic rays of the highest energies. Grain acceleration can be produced by subsequent collisions with shocks in the interstellar media only in cases where the grains do not lose their charge while being accelerated to high velocities [144–149]. The accelerated grain will then propagate in the dilute interstellar plasma (with a density of no higher than 1 cm^{-3}). However, in the course of acceleration, a dust grain should cover a rather large distance. It is easy to solve the charging equation for fast moving grains and find that, for a grain with a size of 2 μm and velocity higher than $0.1c$ (where c is the speed of light), electrons cannot be attached to the grain since the stopping length of these electrons in the frame of the grain is larger than the grain size. A charge balance will be impossible and grains with velocities higher than $0.1c$ will be not charged (see also [150, 151]. Therefore, if one accepts the shock wave acceleration mechanism, one must conclude that the grains cannot be accelerated to relativistic velocities because they will lose their charge before their velocity becomes close to the speed of light, and they will not interact with the magnetic field of the shock, which is necessary to produce further acceleration. The only mechanism that can produce relativistic grains in space is one that is not related to their charges: This is radiative pressure, which can be large in the regions close to supernova explosions. It is known that supernovas occur in dust-rich regions. Therefore, supernovas can produce bursts of relativistic grains. The theory in [145] shows that the γ factor of a grain ($\gamma = 1/\sqrt{1 - v_d^2/c^2}$) can reach a value of 10^2–10^4. When penetrating into a planetary atmosphere (particularly into the Earth's atmosphere) these grains can produce cosmic ray showers. There have been attempts to explain the observation of cosmic ray showers with the highest observed energies on the order of 10^{21} eV as being produced by relativistic grains. The main question raised in [148] is whether such grains can even reach the vicinity of the Earth in view of the influence of solar radiation on their charges. When approaching the Earth, these grains should be neutral. However, solar radiation in the frame of these grains will be X radiation and will efficiently produce photoelectrons. The grains will be charged positively until the charge of the grains disrupts it. The main problem is estimating the distance to which a relativistic grain will be able to approach the Earth from the side opposite the Sun before disruption occurs. The numerical solution of this problem given in [146] shows that grains with γ up to 10^4 will be able to reach the Earth. The spatial distributions of showers produced by such grains will be quite different from those produced by a single proton with the same energy. Specific features of the shower distributions for these two cases can be observed by measuring the showers from above with detectors installed on a system of satellites.

Cosmic rays of the highest energies are the one of the biggest puzzles of the universe because it is quite difficult to find a mechanism for their acceleration in near space (on the other hand, they cannot come from large distances due to the cutoff caused by black-body radiation).

2.5.7. Dust boundaries in space. It is of great importance that dust clouds observed in space have sharp boundaries, as they often have in laboratory experiments. An example is the boundaries of planetary rings or the noctilucent clouds that produce PMSE radar scattering; this is important for ozone layer investigations. Most amazing are the recent observations of the dust clouds that obscure a large part of the sky (Fig. 29); these clouds have very sharp boundaries and there are indications of the process of star formation close to these boundaries. The major theoretical problem is understanding the physics of the formation of sharp boundaries for clouds consisting of grains with the

broad size distribution typical of dust clouds under astrophysical conditions.

3. CONCLUDING REMARKS

In this review, we have tried to give a comprehensive description of the present state of the art of a new, rapidly developing field of science: the physics of complex plasmas. The first part of the review, "Complex Plasmas as Unusual State of Matter" [1], was devoted to the main physical differences of this state of matter from ordinary matter. The aim of the second part, "Elementary Processes in Complex Plasmas" [2], was to give a qualitative description and estimates that could be used both in theory and in experiments and to derive explicit expressions for the fundamental processes that occur in complex plasmas. The third part, "Experiments on Strong Coupling and Long-Range Correlations" [3], described the recent experimental discoveries in this field, while the fourth (present) part, "Theoretical Approaches to Complex Plasmas: Applications," is devoted to the achievements in the theory and applications. We have concentrated mainly on the new physics, with the applications being listed only at the end, although from a practical point of view, the latter are more important. A somewhat formal review of the observed phenomenon in complex plasmas was published recently in [152], where one in fact cannot find a detailed analysis of the main new physical processes in complex plasma (which, as we have explained in the present review, was recently recognized as a quite unusual state of matter). Thus, we have here placed the main stress on the new physics involved.

In this review, we have shown that complex plasma is not only an unusual state of matter with quite different (from ordinary matter) physical properties and a rather large area of application, but also that it is one of the most rapidly developing fields of research in physics. The most important conclusion of this review is that the parameters of state-of-the-art experiments on plasma condensation and the formation of plasma crystals correspond to those at which the new collective interaction between grains operates. This interaction not only provides the attraction potential minima that result in the formation of molecules, but also explains qualitatively the value of the critical parameter Γ for the experimentally observed phase transitions. This classical binding is a completely new phenomenon since, in ordinary matter, the chemical binding that leads to crystal formation has a quantum nature (exchange interactions). Future development of this field promises new and important achievements in physics and applications.

We can also hypothesize that the formation of dust structures with sharp boundaries has long occurred in space and astrophysical plasmas and that these structures, being isolated and self-organized, compete for food (i.e., for plasma). Plasma and dust are everywhere in space. Competition between structures will inevitably occur and become more and more sophisticated, in which case it can be memorized. Plasma crystals are a necessary element for starting the memorizing process. If these structures have a crystal component in the center (which is very probable), then memorizing will lead to the evolution of and mutations in the structure much faster than any biological evolution. In the event this happens, this new "life" could have the "intention" of miniaturizing itself down to the molecular level (as we are at present miniaturizing computers) and should discover a biological life. The first step toward experimentally checking these predictions is to investigate the time dependence of dust structures in microgravity experiments, to form several structures, and to observe their evolution and possible competition when one structure "eats" the other. If such a discovery is really made, it could have great consequences for our future life. The path of research in this direction must be related to the interaction of different self-organized structures in complex plasma and to the search for possible processes that are analogous to the competition in and evolution of biological systems.

REFERENCES

1. V. N. Tsytovich, G. E. Morfill, and H. Thomas, Fiz. Plazmy **28**, 623 (2002) [Plasma Phys. Rep. **28**, 623 (2002)].
2. G. E. Morfill, V. N. Tsytovich, and H. Thomas, Fiz. Plazmy **29**, 3 (2003) [Plasma Phys. Rep. **29**, 1 (2003)].
3. H. Thomas, G. E. Morfill, and V. N. Tsytovich, Fiz. Plazmy **29**, 963 (2003) [Plasma Phys. Rep. **29**, 895 (2003)].
4. V. Tsytovich and U. de Angelis, Phys. Plasmas **6**, 1093 (1999).
5. V. Tsytovich and U. de Angelis, Phys. Plasmas **7**, 554 (2000).
6. P. Ricci, G. Lapenta, U. de Angelis, and V. Tsytovich, Phys. Plasmas **8**, 769 (2001).
7. V. Tsytovich and U. de Angelis, Phys. Plasmas **8**, 1141 (2001).
8. V. Tsytovich and U. de Angelis, Phys. Plasmas **9**, 2497 (2002).
9. S. Benkadda, P. Gabai, V. Tsytovich, and A. Verga, Phys. Rev. E **53**, 2717 (1996).
10. S. Trigger and P. Schram, Contrib. Plasma Phys. **39**, 117 (1999); J. Phys. D **32**, 234 (1999); A. Zagorodny, P. Schram, and S. Trigger, Phys. Rev. Lett. **84**, 3594 (2000); Yu. Chutov, O. Kravchenko, R. Smirnov, and P. Schram, J. Plasma Phys. **63**, 89 (2000).
11. A. Zagorodny, A. Sitenko, O. Bystrenko, *et al.*, Phys. Plasmas **8**, 1893 (2001); A. Ignatov, S. Trigger, W. Ebeling, and P. Schram, Phys. Lett. A **293**, 141 (2002); Yu. Chutov, O. Kravchenko, R. Smirnov, and P. Schram, J. Phys. IV (France) **10**, 395 (2000).
12. V. Tsytovich and O. Havnes, Comments Plasma Phys. Control. Fusion **18**, 267 (1993).
13. V. Tsytovich, Aust. J. Phys. **11**, 1 (1999).

14. Yu. L. Klimontovich, *Kinetic Theory of Nonideal Gas and Nonideal Plasma* (Nauka, Moscow, 1975; Pergamon, Oxford, 1982).
15. V. Tsytovich and D. Ter Haar, *Lectures on Nonlinear Plasma Kinetics* (Springer, Heidelberg, 1995).
16. A. Ivlev, private communication (2001).
17. V. N. Tsytovich and G. E. Morfill, Fiz. Plazmy **28**, 195 (2002) [Plasma Phys. Rep. **28**, 171 (2002)].
18. V. Tsytovich, Comm. Modern Phys. **1**, 1 (2000); Fiz. Plazmy **26**, 712 (2000) [Plasma Phys. Rep. **26**, 668 (2000)].
19. A. M. Ignatov, Fiz. Plazmy **24**, 731 (1998) [Plasma Phys. Rep. **24**, 677 (1998)].
20. G. Morfill and V. Tsytovich, Phys. Plasmas **7**, 235 (2002).
21. H. Rothermel, T. Hagl, G. E. Morfill, *et al.*, Phys. Rev. Lett. **89**, 175001 (2002).
22. A. M. Ignatov, Fiz. Plazmy **28**, 919 (2002) [Plasma Phys. Rep. **28**, 847 (2002)].
23. A. Ignatov, in *Proceedings of the 3rd International Conference on Physics of Dusty Plasmas, Durban, 2002*; AIP Conf. Proc. **649**, 162 (2002).
24. J. Daugerty and D. Graves, J. Vac. Sci. Technol. **113**, 1126 (1993).
25. G. Swinkels, H. Kersten, H. Deutch, and G. Kroesen, J. Appl. Phys. **88**, 1747 (2000).
26. V. Tsytovich, A. Nefedov, V. Fortov, *et al.*, Phys. Plasmas **10**, 2633 (2003).
27. G. E. Morfill and V. N. Tsytovich, Fiz. Plazmy **26**, 1598 (2000) [Plasma Phys. Rep. **26**, 682 (2000)].
28. D. Samsonov and J. Goree, Phys. Rev. E **59**, 1047 (1999).
29. G. Morfill, H. Thomas, U. Konopka, *et al.*, Phys. Rev. Lett. **83**, 1598 (1999).
30. V. Tsytovich, *Problem of Dust Self-Organized Sheath* (Marseille Univ., Marseille, 1998).
31. V. Tsytovich, in *Frontiers in Dusty Plasmas*, Ed. by Y. Nakamura, T. Yakota, and P. Shukla (Elsevier, Amsterdam, 2000), p. 99.
32. A. Nevedov, G. Morfill, V. Fortov, *et al.*, New J. Phys. **5**, 33 (2003).
33. A. Bouchoule, G. Morfill, and V. Tsytovich, Comm. Modern Phys. C **1**, 131 (2000).
34. V. Tsytovich, G. Morfill, U. Konopka, and H. Thomas, New J. Phys. **5**, 1.1 (2003).
35. J. Goree, G. Morfill, V. Tsytovich, and S. Vladimirov, Phys. Rev. E **59**, 7055 (1999).
36. V. Tsytovich, S. Vladimirov, G. Morfill, and J. Goree, Phys. Rev. E **63**, 056609 (2001).
37. S. Benkadda, V. Tsytovich, S. Popel, and S. Vladimirov, in *Frontiers in Dusty Plasmas*, Ed. by Y. Nakamura, T. Yakota, and P. Shukla (Elsevier, Amsterdam, 2000), p. 123.
38. V. Tsytovich, Phys. Scr., T **89**, 89 (2001).
39. S. Benkadda, V. Tsytovich, and S. Vladimirov, Phys. Rev. E **60**, 4708 (1999).
40. S. Benkadda, P. Gabai, V. Tsytovich, and O. Vaulina, Phys. Plasmas **11** (2004) (in press).
41. V. N. Tsytovich, Contrib. Plasma Phys. **44** (2004) (in press).
42. G. Bachet, L. Cherigier, and F. Doveil, Phys. Plasmas **2**, 1782 (1995).
43. A. Hasegawa, Adv. Phys. **34**, 1 (1985).
44. Yu. L. Klimontovich, Usp. Fiz. Nauk **166**, 1231 (1996) [Phys. Usp. **39**, 1169 (1996)].
45. V. Schweigert and F. Peeters, Phys. Rev. B **51**, 7700 (1995).
46. D. J. C. Wineland, J. Bergquist, W. Itano, *et al.*, Phys. Rev. Lett. **59**, 2935 (1987).
47. F. Diedrich, E. Peik, J. Chen, *et al.*, Phys. Rev. Lett. **59**, 2931 (1987).
48. S. Neser, T. Palberg, C. Blechinger, and P. Leiderer, Prog. Colloid Polym. Sci. **104**, 194 (1997).
49. Sh. Amiranashvili, N. Gusein-zade, and V. Tsytovich, Phys. Rev. E **64**, 016407 (2001).
50. V. Tsytovich, Ya. Khodataev, and R. Bingham, Comments Plasma Phys. Control. Fusion **17**, 249 (1996).
51. Sh. Amiranashvili, N. Gusein-zade, and V. Tsytovich, in *Proceedings of the 3rd International Conference on Physics of Dusty Plasmas, Durban, 2002*; AIP Conf. Proc. **649**, 463 (2002).
52. Ya. K. Khodataev, R. Bingham, V. P. Tarakanov, and V. N. Tsytovich, Fiz. Plazmy **22**, 1028 (1996) [Plasma Phys. Rep. **22**, 932 (1996)].
53. Ya. Khodataev, R. Bingham, V. Tarakanov, *et al.*, Phys. Scr. **T89**, 95 (2001).
54. A. A. Samarian, O. S. Vaulina, A. P. Nefedov, and O. F. Petrov, Fiz. Plazmy **26**, 626 (2000) [Plasma Phys. Rep. **26**, 586 (2000)].
55. M. Lampe, G. Joyce, G. Ganguli, and S. Gavrishchaka, Phys. Plasmas **7**, 3851 (2000).
56. G. Joyce, M. Lampe, and G. Ganguli, IEEE Trans. Plasma Sci. **29**, 238 (2001).
57. H. Ohta and S. Hamaguchi, Phys. Plasmas **7**, 4506 (2000).
58. Ch. K. Birdsall and A. B. Langdon, *Plasma Physics via Computer Simulation* (McGraw-Hill, New York, 1985; Énergoatomizdat, Moscow, 1989).
59. R. Hockney and J. Eastwood, *Computer Simulation Using Particles* (McGraw-Hill, New York, 1984; Mir, Moscow, 1987).
60. V. Tsytovich, Ya. Khodataev, R. Bingham, and D. Resendes, Comments Plasma Phys. Control. Fusion **17**, 287 (1996).
61. V. N. Tsytovich and D. Resendes, Fiz. Plazmy **24**, 71 (1998) [Plasma Phys. Rep. **24**, 65 (1998)].
62. V. Tsytovich, U. de Angelis, R. Bingham, and D. Resendes, Phys. Plasmas **4**, 3882 (1997).
63. D. Gross, Lect. Notes Phys. **66** (2001).
64. H. Thomas, G. Morfill, V. Demmel, and J. Goree, Phys. Rev. Lett. **73**, 652 (1994).
65. J. Chu and I. Lin, Physica A (Amsterdam) **205**, 183 (1994).
66. A. Melzer, T. Trottenberg, and A. Piel, Phys. Lett. A **191**, 301 (1994).
67. Y. Hayashi and K. Tachibana, Jpn. J. Appl. Phys. **33**, L804 (1994).
68. V. Fortov, A. Nefedov, O. Petrov, *et al.*, Phys. Lett. A **219**, 89 (1996).

69. S. Nunomura, N. Ohno, and S. Takamura, Jpn. J. Appl. Phys., Part 2 **36**, L949 (1997); Phys. Plasmas **5**, 3517 (1998).
70. L. D. Landau and E. M. Lifshitz, *Statistical Physics* (Nauka, Moscow, 1976; Pergamon, Oxford, 1980), Part 1.
71. G. Morfill, H. Thomas, U. Konopka, and M. Zusic, Phys. Plasmas **6**, 1769 (1999).
72. V. Tsytovich, G. Morfill, and A. Ivlev, Contrib. Plasma Phys. **43**, 439 (2003).
73. G. Selwyn, J. Heidenrich, and K. Haller, Appl. Phys. Lett. **57**, 1867 (1990).
74. A. Bouchoule and L. Bufendi, J. Appl. Phys. **70**, 1991 (1991).
75. A. Garscadden, B. N. Ganguli, P. D. Haaland, and J. Williams, Plasma Sources Sci. Technol. **3**, 239 (1994).
76. L. Boufendi and A. Bouchoule, Plasma Sources Sci. Technol. **3**, 262 (1994).
77. U. Konopka, L. Ratke, and H. Thomas, Phys. Rev. Lett. **79**, 1269 (1997).
78. U. Konopka, G. Morfill, and L. Ratke, Phys. Rev. Lett. **84**, 891 (2000).
79. V. Tsytovich, N. Sato, and G. Morfill, New J. Phys. **1**, 1.1 (2003).
80. U. Konopka, D. Samsonov, A. Ivlev, *et al.*, Phys. Rev. E **61**, 1890 (2000).
81. N. Sato, G. Uchida, Y. Kaneko, *et al.*, Phys. Plasmas **8**, 1786 (2001).
82. G. Ichida, R. Ozaki, S. Iizuka, and N. Sato, in *Proceedings of the 25th EPS Conference on Plasma Physics and Controlled Fusion, Prague, 1998*, p. 2557.
83. D. Law, W. Steel, E. Tomme, *et al.*, in *Proceedings of the 24th International Conference on Phenomena in Ionized Gases, Warsaw, 1999*, p. 142.
84. V. Tsytovich, S. Vladimirov, and G. Morfill, Contrib. Plasma Phys. **44** (2004) (in press).
85. V. Tsytovich and G. Morfill, in *Proceedings of the 3rd International Conference on Physics of Dusty Plasmas, Durban, 2002*; AIP Conf. Proc. **649**, 110 (2002).
86. V. Tsytovich and K. Watanabe, Contrib. Plasma Phys. **43**, 51 (2003).
87. K. Wilson and M. Fisher, Phys. Rev. Lett. **28**, 240 (1972).
88. Y. Watanabe and M. Shratani, Plasma Sources Sci. Technol. **3**, 286 (1994).
89. G. Selwyn, J. Heidenrih, and K. Haller, Appl. Phys. Lett. **57**, 1867 (1990).
90. G. Selwyn, J. McKillop, K. Haller, and J. Wu, J. Vac. Sci. Technol. **18**, 1726 (1990).
91. H. Thieme, M. Quass, H. Kersten, *et al.*, in *Proceedings of the 3rd International Conference on Physics of Dusty Plasmas, Durban, 2002*; AIP Conf. Proc. **649**, 170 (2002).
92. G. Praburam and J. Goree, J. Vac. Sci. Technol. A **12**, 176 (1994).
93. I. Langmuir, G. Found, and A. Ditter, Science **60**, 392 (1924).
94. K. Emelis and A. Breslin, Int. J. Electron. **29**, 1 (1970).
95. G. Selwyn, Plasma Sources Sci. Technol. **3**, 340 (1994).
96. L. Boufendi and A. Bouchoule, Plasma Sources Sci. Technol. **3**, 262 (1994).
97. A. Bouchoule and L. Boufendi, Plasma Sources Sci. Technol. **3**, 292 (1994).
98. V. Tsytovich, Ya. Khodataev, G. Morfill, *et al.*, Comments Plasma Phys. Control. Fusion **18**, 281 (1998).
99. R. Bingham and V. Tsytovich, IEEE Trans. Plasma Sci. **29**, 158 (2001).
100. X. Wang and P. Bhattacharjee, Phys. Plasmas **4**, 3759 (1997).
101. *Proceedings of the NATO Advanced Research Workshop on the Formation, Transport, and Consequences of Particles in Plasmas, Chateau de Bonas, 1994*; Plasma Sources Sci. Technol. **3** (1994).
102. K. Horiuchi, S. Iizuka, and N. Sato, Surf. Coat. Technol. **131**, 243 (2000).
103. A. Bouchoule, *Dusty Plasmas: Physics, Chemistry, and Technological Impacts in Plasma Processing* (Wiley, London, 1999).
104. H. Kersten, E. Stoffels, W. Stoffels, *et al.*, J. Appl. Phys. **87**, 3637 (2000).
105. S. Veprek, S. Reiprich, and L. Shizi, Appl. Phys. Lett. **66**, 2640 (1995).
106. K. Horiuchi, S. Iizuka, and N. Sato, Surf. Coat. Technol. **131**, 243 (2000).
107. E. Stoffels, W. Stoffels, H. Kersten, *et al.*, Phys. Scr. **T89**, 168 (2001).
108. T. Oku, T. Hirata, N. Motegi, *et al.*, J. Mater. Res. **15**, 2182 (2000).
109. A. Bouchoule and L. Boufendi, in *Proceedings of the 25th International Conference on Phenomena in Ionized Gases, Nagoya, 2001*, p. 17.
110. J. Winter, Plasma Phys. Controlled Fusion **38**, 1503 (1996).
111. J. Winter, Plasma Phys. Controlled Fusion **40**, 201 (1998).
112. V. N. Tsytovich and J. Winter, Usp. Fiz. Nauk **168**, 899 (1998) [Phys. Usp. **41**, 815 (1998)].
113. J. Winter, A. Nefedov, and V. Fortov, J. Nucl. Mater. **290–293**, 509 (2001).
114. A. Kukushkin and R. Rantzev-Kartinov, Rev. Sci. Instrum. **72**, 506 (2001).
115. T. Ditmire, T. Donnelly, R. Falcone, and M. Peny, Phys. Rev. Lett. **75**, 3122 (1995).
116. T. Ditmire, T. Donnelly, A. Rubenchik, *et al.*, Phys. Rev. A **53**, 3379 (1996).
117. T. Ditmire, J. Zweiback, V. Yanovsky, *et al.*, Nature **398**, 489 (1999).
118. T. Tajima, Y. Kishimoto, and T. Masaki, Phys. Scr. **T89**, 45 (2001).
119. A. Bratti, O. Havnes, and F. Melanso, Phys. Plasmas **9**, 1 (2001).
120. T. Backnouse, Meteorol. Mag. **20**, 133 (1985).
121. W. Ecklund and B. Basley, J. Geophys. Res. **86**, 7775 (1981).
122. O. Havnes, T. Aslaksen, and A. Brattu, Phys. Scr. **T89**, 133 (2001).
123. V. Tsytovich and O. Havnes, in *Proceedings of the 3rd International Conference on Physics of Dusty Plasmas, Durban, 2002*; AIP Conf. Proc. **649**, 454 (2002).

124. S. A. Kaplan and S. B. Pikel'ner, *Interstellar Medium* (Nauka, Moscow, 1963).
125. L. Spitzer, Jr., *Physical Processes in Interstellar Medium* (Wiley, New York, 1978; Mir, Moscow, 1981).
126. S. Weidenschilling and J. Cuzzi, in *Protostars and Planets III*, Ed. by E. Levy and J. I. Lunine (Univ. Arizona Press, Tucson, 1993), p. 1031.
127. S. Kempf, S. Pfalzner, and T. Henning, Icarus **141**, 388 (1999).
128. P. Meaking, Rev. Geophys. **29**, 317 (1991).
129. J. Blum, G. Wurm, S. Kempf, *et al.*, Phys. Rev. Lett. **85**, 2426 (2000).
130. W. Watson and E. Salpeter, Astrophys. J. **174**, 321 (1972).
131. J. Winters, J. Keady, A. Gauger, and P. Sada, Astron. Astrophys. **359**, 651 (2000).
132. R. Chevalier, Nature **355**, 691 (1992).
133. R. Bingham and V. Tsytovich, Astron. Astrophys. **376**, L43 (2001).
134. E. Sedlmayer, in *Proceedings of the 3rd International Conference on Physics of Dusty Plasmas, Durban, 2002*; AIP Conf. Proc. **649**, 32 (2002).
135. S. Kaplan and S. Pikel'ner, Annu. Rev. Astron. Astrophys. **12**, 113 (1974).
136. G. Morfill and M. Scholer, *Physical Processes in Interstellar Clouds* (Reidel, London, 1992).
137. M. Horany, in *Proceedings of the 3rd International Conference on Physics of Dusty Plasmas, Durban, 2002*; AIP Conf. Proc. **649**, 22 (2002).
138. V. N. Tsytovich, Usp. Fiz. Nauk **167**, 57 (1997) [Phys. Usp. **40**, 53 (1997)].
139. S. Kempf, S. Pfalzner, and T. Henning, Icarus **141**, 388 (1999).
140. J. Winter, J. Keady, A. Gauger, and P. Sada, Astron. Astrophys. **359**, 651 (2000).
141. *Planetary Rings*, Ed. by R. Greeberg and A. Brahic (Univ. Arizona Press, Tucson, 1984).
142. T. Eidhammer and O. Havnes, J. Geophys. Res. **106**, 24831 (2001).
143. V. E. Fortov, Yu. N. Gnedin, M. F. Ivanov, *et al.*, Usp. Fiz. Nauk **166**, 391 (1996) [Phys. Usp. **39**, 363 (1996)].
144. R. Bingham and V. Tsytovich, Astropart. Phys. **7**, 43 (1999).
145. R. Bingham and V. Tsytovich, in *Proceedings of the 3rd International Conference on Physics of Dusty Plasmas, Durban, 2002*; AIP Conf. Proc. **649**, 126 (2002).
146. L. Spitzer, Phys. Rev. **76**, 583 (1949).
147. S. Hayakawa, Astrophys. Space Sci. **16**, 238 (1972).
148. V. Berezinsky and O. Prilutsky, Astrophys. Space Sci. **21**, 475 (1973).
149. *Proceedings of the 2nd International Workshop on Measurements of Highest Energy Cosmic Rays from Space, Maryland, 1997*.
150. Ya. Istomin and S. Barabach, in *Proceedings of the Workshop on Neutral Cosmic Atoms, Kiruna, 1997*, p. 26.
151. F. Hearn, R. Mills, D. Schleicher, *et al.*, Icarus **118**, 223 (1995).
152. P. K. Shukla and A. A. Mamun, *Introduction to Dusty Plasma Physics* (IOP, Bristol, 2002).

Plasma Physics Reports, Vol. 30, No. 10, 2004, pp. 865–871. Translated from Fizika Plazmy, Vol. 30, No. 10, 2004, pp. 930–936.

DUSTY PLASMA

Static Response Function of a Plasma–Wall Sheath

A. M. Ignatov

Prokhorov Institute of General Physics, Russian Academy of Sciences, ul. Vavilova 38, Moscow, 119991 Russia

Received December 25, 2003

Abstract—Results are presented from numerical investigations of the potential of a test charge in a plasma–wall sheath. It is shown that like charges that are at the same distance from a floating electrode can attract one another. © *2004 MAIK "Nauka/Interperiodica".*

1. INTRODUCTION

The interaction between dust grains, which is among the key issues in the physics of dusty plasma, has been studied for many years. This interaction is largely governed by the properties of the surrounding medium. Thus, many laboratory experiments carried out under terrestrial conditions are aimed at studying ensembles of macroparticles (dust grains) levitating above a horizontally positioned, negatively charged electrode. In such experiments, the grains acquire a negative charge, so that the gravity force is counterbalanced by the electric field in the plasma–wall sheath. The details of different experiments and the discussion of theoretical models can be found, e.g., in [1].

The first question that needs to be asked in studying the interaction between the grains in the sheath is how the potential is distributed around a fixed test charge. In a linear approximation, this distribution is determined by the static response function. In most of the models used in the theory of dusty plasma, it is assumed that the electrons in the sheath obey a Boltzmann distribution and the ions form an electrode-directed flow, whose velocity is comparable to or higher than the ion acoustic velocity. The potential of a test charge in an infinite uniform plasma sheath has been studied both analytically and numerically by many authors (see, e.g., [2–8]). This research has resulted in the following picture, which has been confirmed experimentally [6] and is now generally accepted: in the horizontal direction (i.e., across the ion flow) and upstream of the flow, the potential decreases exponentially, whereas, downstream from the test charge, a Mach cone forms, within which the potential oscillates in a complicated manner. It should be noted that, although most of the theoretical papers in this area have been aimed at studying supersonic ion flows, the dispersion law for ion acoustic waves ensures that the Mach cone can also be formed by subsonic flows (as in the case of waves on deep water [9]). For a slightly nonuniform distribution of the plasma parameters, an analogous pattern of the potential distribution has been recently obtained by Hou *et al.* [10], who used the geometrical-optics approximation.

It is clear that models in which the medium is assumed to be infinite and uniform (or a slightly nonuniform) can provide at best only a qualitative description of the plasma–wall sheath. The question about the effect of the metal wall on the interaction between test charges in a semi-infinite plasma was discussed in my earlier paper [11], where the Green's function of a point charge was calculated for a plasma with an ion flow directed perpendicular to the conducting wall. It was shown that, in the case of a subsonic ion flow, the potential of a test charge that is at a certain distance from the wall oscillates in the direction perpendicular to the ion flow. These oscillations can be interpreted as the electrostatic image of the Mach cone. Kourakis and Shukla [12] carried out a more detailed numerical study of the response function obtained in [11] and investigated the influence of the related effect on the oscillations of a dust plasma crystal.

The main drawback of the studies performed in [11, 12] is that, in those papers, the ion flow velocity and the distance from the conducting wall were assumed to be independent of one another. In fact, however, the ion flow velocity at the position of the test charge is a well defined function of its distance from the wall. In the present work, an attempt is made to abandon the uniform medium approximation, thereby making it possible to investigate the potential of a test charge in a nonuniform plasma sheath. The hydrodynamic model used for this purpose is described in Section 2. Section 3 gives a typical example of an unperturbed distribution of the plasma parameters near the wall. Linearized equations for calculating the response function are derived in Section 4, where the method for solving them is also discussed. The results of numerical calculations are presented in Section 5. The analytical and numerical results are compared in the Conclusion.

2. MODEL

Here, a weakly ionized plasma sheath near a conducting wall is described by the following hydrodynamic model, which is widely used in the theory of

1063-780X/04/3010-0865$26.00 © 2004 MAIK "Nauka/Interperiodica"

dusty plasma. The ions are described by the continuity equation

$$\nabla \cdot (n(\mathbf{r})\mathbf{v}(\mathbf{r})) = Zn_e(\mathbf{r}). \quad (1)$$

Here, $n(\mathbf{r})$ is the ion density; $\mathbf{v}(\mathbf{r})$ is the ion flow velocity; $n_e(\mathbf{r})$ is the electron density; and Z is the electron-impact ionization rate, which is assumed to be independent of the coordinates. The ion momentum balance equation has the form

$$\nabla_j(mn(\mathbf{r})v_i(\mathbf{r})v_j(\mathbf{r})) + en(\mathbf{r})\nabla_i\phi(\mathbf{r}) + m\nu n(\mathbf{r})v_i(\mathbf{r}) = 0, \quad (2)$$

where ν is the ion–neutral collision frequency, which is also assumed to be constant, and m is the mass of an ion.

Equations (1) and (2) are supplemented with Poisson's equation

$$\Delta\phi(\mathbf{r}) = -4\pi e[n(\mathbf{r}) - n_e(\mathbf{r})] - 4\pi\rho(\mathbf{r}), \quad (3)$$

where $\rho(\mathbf{r})$ is the external charge density. The electrons are assumed to obey a Boltzmann distribution, $n_e(\mathbf{r}) = N_0\exp(e\phi(\mathbf{r})/T_e)$, where T_e is the electron temperature and N_0 is the electron density at the point at which $\phi(\mathbf{r}) = 0$. Using continuity equation (1), we can readily convert ion momentum balance equation (2) into the time-independent Euler equation

$$(\mathbf{v}(\mathbf{r})\cdot\nabla)\mathbf{v}(\mathbf{r}) + \frac{e}{m}\nabla\phi(\mathbf{r}) + \left(Z\frac{n_e(\mathbf{r})}{n(\mathbf{r})} + \nu\right)\mathbf{v}(\mathbf{r}) = 0. \quad (4)$$

The last term on the left-hand side of this equation shows that, when the ionization in the sheath, where $n_e(\mathbf{r}) \neq n(\mathbf{r})$, is taken into account, the coefficient of friction of the ions against neutrals becomes dependent on the coordinates.

For further analysis, it is convenient to switch to dimensionless variables. Let the spatial scale be the electron Debye length $\lambda_D = \sqrt{T_e/(4\pi e^2 N_0)}$, the velocity scale be the ion acoustic velocity $c_s = \sqrt{T_e/m}$, and the density scale be the plasma density N_0. In explicit form, all the quantities are written as $\mathbf{r} = \lambda_D\mathbf{r}'$, $\mathbf{v} = c_s\mathbf{v}'$, $n = N_0 n'$, $\phi = T_e/e\phi'$, and $\rho = eN_0\rho'$, the collision frequencies being normalized to the ion Langmuir frequency: $Z = \omega_{pi}Z'$ and $\nu = \omega_{pi}\nu'$. Hence, the basic set of equations has the form

$$\nabla\cdot(n\mathbf{v}) = Ze^{\phi},$$

$$(\mathbf{v}\cdot\nabla)\mathbf{v} = -\nabla\phi - \left(\frac{Z}{n}e^{\phi} + \nu\right)\mathbf{v}, \quad (5)$$

$$\Delta\phi = e^{\phi} - n - \rho,$$

where we omit the primes for the dimensionless variables for simplicity.

3. UNPERTURBED PLASMA

We assume that the plasma occupies the half-space $z < 0$ and that the conducting wall, which is held at a floating potential, is in the plane $z = 0$. In the absence of external charges ($\rho = 0$), the dependence of all the quantities with the zero subscript on the z coordinate is described by the set of equations

$$\frac{d(n_0u)}{dz} = Ze^{\phi},$$

$$u\frac{du}{dz} = -\frac{d\phi_0}{dz} - \left(\frac{Z}{n_0}e^{\phi_0} + \nu\right)u, \quad (6)$$

$$\frac{d^2\phi_0}{dz^2} = e^{\phi_0} - n_0,$$

where $u = v_{z0}$ is the z component of the unperturbed ion velocity.

Although the problem of the smooth matching of the equations for the sheath with those for quasineutral plasma has a long history, it is still a subject of discussion in the literature (see, e.g., [13] and the subsequent discussion in [14]). The essence of the problem lies in the fact that the solutions to Eqs. (6) depend on two radically different spatial scales: near the wall ($z \approx 0$), all the quantities vary on a scale of order unity (or on the order of the electron Debye radius), whereas, far from the wall, the characteristic scale of variations is much longer and is determined by collisions as well as by the dimension of the system. This difficulty is aggravated by the fact that, in analyzing perturbed equations (5) numerically, it is necessary to model the processes occurring deep within the quasineutral plasma. In the present paper, the matching problem is overcome in the following way:

First, let us write out the solution to Eqs. (6) in the region where the plasma is quasineutral. Setting $n_0(z) = \exp\phi_0(z)$ yields the following solution to the first two of Eqs. (6):

$$n_0 = \left[(1 + \nu/Z)u^2 + 1\right]^{-\frac{2Z+\nu}{2(Z+\nu)}},$$

$$\phi_0 = \ln n_0, \quad (7)$$

$$E_0 = (2Z + \nu)\frac{u}{1-u^2},$$

where $E_0 = -d\phi/dz - z$ is the z component of the electric field.

Since the coefficients in Eqs. (6) are coordinate-independent, the ion density, potential, and electric field can be assumed to be functions only of the local value of the velocity u, which can thus be treated as a

new independent variable. Replacing the variable, $z \longrightarrow u$, in Eqs. (6) gives

$$u'(u)\frac{d(un_0(u))}{du} = Ze^{\phi_0(u)},$$

$$u'(u)\frac{d\phi_0(u)}{du} = -E_0(u), \quad (8)$$

$$u'(u)\frac{dE_0(u)}{du} = n_0(u) - e^{\phi_0(u)},$$

where

$$u'(u) = \frac{E_0(u)}{u} - \frac{Z}{n_0(u)}e^{\phi_0(u)} - \nu. \quad (9)$$

In the plasma region under consideration, we have $u'(u) > 0$. The above two different spatial scales of the problem are in fact hidden in the dependence of the velocity on the coordinates; this dependence is determined from the solution to a single equation $du(z)/dz = u'(u)$. As functions of u, the solutions to Eqs. (8) turn out to be much smoother.

Equations (8) were solved numerically in the velocity range $u_{\min} < u < u_{\max}$. The velocity $u_{\min}$ should be sufficiently low. In practice, it turned out that the final results are weakly sensitive to the value of the minimum velocity in the range $u_{\min} < 0.1$. The boundary conditions at $u = u_{\min}$ were given by relationships (7). As for the maximum velocity, it can only be determined by invoking some additional conditions. In simulations, the maximum velocity was found from the condition that the electron and ion currents at the wall be the same. In dimensionless variables, this condition has the form

$$un_0(u) = e^{\phi_0(u)}\sqrt{\frac{m}{2\pi m_e}}, \quad (10)$$

where m_e is the mass of an electron. Hence, Eqs. (8) were integrated from $u = u_{\min}$ and the integration procedure was interrupted when condition (10) was satisfied. In the numerical calculations that will be discussed below, the ion-to-electron mass ratio was chosen to correspond to argon.

An example of a numerical solution to Eqs. (8) with $Z = 10^{-4}$, $\nu = 10^{-2}$, and $u_{\min} = 0.1$ is shown in Fig. 1. In this case, the maximum ion flow velocity at the wall is $u_{\max} = 3.08$ and the Bohm boundary of the sheath (i.e., the boundary at which the ion flow velocity is equal to the ion acoustic velocity) is at a distance $|z| = 21.4$ from the wall.

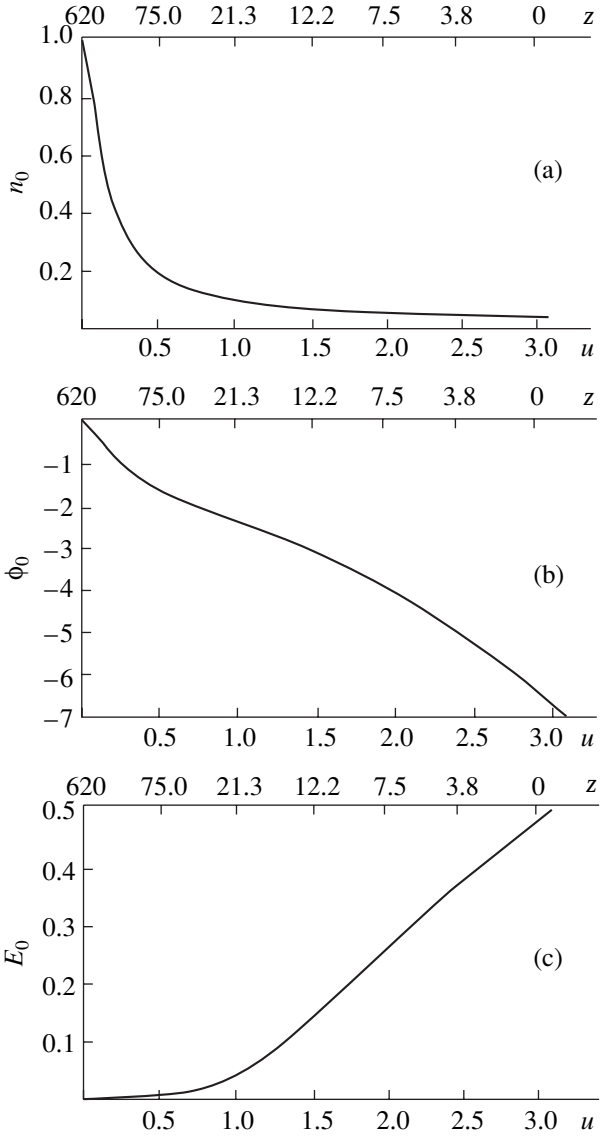

Fig. 1. Example of the dependence of the (a) density, (b) potential, and (c) electric field on u and z.

4. RESPONSE FUNCTION

Let us now consider how an external charge of density $\rho(\mathbf{r})$ perturbs the plasma. In this case, each of the unperturbed quantities in Eqs. (5) contains a correction that is denoted by subscript 1 and is of the same order of magnitude as $\rho(\mathbf{r})$. For example, we have $n(\mathbf{r}) = n_0(z) + n_1(\mathbf{r})$, where $n_1(\mathbf{r}) \sim \rho(\mathbf{r})$. We linearize Eqs. (5) and take the Fourier transformation in transverse coordinates; i.e., we represent all the quantities in the form $\exp(i\mathbf{k}\mathbf{r}_\perp)$, where $\mathbf{r}_\perp = (x, y)$ and $\mathbf{k}$ is the two-dimensional wave vector. As a result, we arrive at a set of linear equations in which the coefficients depend on the z coordinate. However, since the unperturbed quantities n_0, ϕ_0, and E_0 were represented as functions of the velocity u, their perturbations also can be sought as functions of u. Hence, simple but somewhat laborious manipulations yield

$$u'(u)\frac{d}{du}[n_0(u)v_1(u) + un_1(u)]$$

$$-k^2 n_0(u) g_1(u) - Z e^{\phi_0(u)} \phi_1(u) = 0,$$

$$u'(u) \frac{d(u v_1(u))}{du} + \left(\frac{Z}{n_0(u)} e^{\phi_0(u)} + \nu \right) v_1(u)$$

$$+ \frac{Z}{n_0(u)} e^{\phi_0(u)} u \left(\phi_1(u) - \frac{n_1(u)}{n_0(u)} \right) - E_1(u) = 0, \quad (11)$$

$$u u'(u) \frac{dg_1(u)}{du} + \left(\frac{Z}{n_0(u)} e^{\phi_0(u)} + \nu \right) g_1(u) + \phi_1(u) = 0,$$

$$u'(u) \frac{d\phi_1(u)}{du} = -E_1(u),$$

$$u'(u) \frac{dE_1(u)}{du} + (k^2 + e^{\phi_0(u)}) \phi_1(u) - n_1(u) = \rho(u).$$

Here, we have introduced the perturbed longitudinal velocity $v_1(u) = v_{z1}(u)$. It follows from Eq. (4) that the curl of the perturbed transverse velocity is conserved; consequently, it is equal to zero. Accordingly, in Eqs. (11), the transverse velocity components are expressed in terms of the velocity potential, $\mathbf{v}_\perp(u) = i\mathbf{k} g_1(u)$. It should be noted that, in a homogeneous plasma, an ion flow perturbed by an external charge is purely potential; i.e., in the notation adopted here, the relationship $v_1(z) = dg_1(z)/dz$ is satisfied for a homogeneous plasma. In our case, because of the above coordinate dependence of the friction coefficient in Euler equation (4), the ion flow is more complicated and nonpotential. In other words, ionization gives rise to vorticity, as can be readily seen from Eq. (4).

In what follows, we will study the potential of a point charge at the point $\mathbf{r}_0 = (0, 0, z_0)$, in which case the charge density in Eqs. (11) is equal to $\rho = \delta(z - z_0) = u'(u)\delta(u - u_0)$, where u_0 ($u_{\min} < u_0 < u_{\max}$) is the unperturbed ion flow velocity at the position of the charge. For a point charge, it is sufficient to solve Eqs. (11) with zeros on the right-hand sides and then to match the solutions for $u > u_0$ and $u < u_0$ using the continuity conditions for the quantities n_1, v_1, g_1, and ϕ_1 and also the condition $E_1(u_0 + 0) - E_1(u_0 - 0) = 1$.

Equations (11) are supplemented with the following boundary conditions at $u \longrightarrow 0$ ($z \longrightarrow -\infty$). For sufficiently low ion flow velocities, the solution to Eqs. (11) should transform into the relevant solution to the homogeneous (or slightly inhomogeneous) problem. An analysis of the linear dispersion relation for ion acoustic waves without allowance for ionization and collisions, $\varepsilon(\omega, \mathbf{k}) = 1 - \omega_{pi}^2/(\omega + i0 - k_z u)^2 + 1/(k^2 r_{De}^2) = 0$ (see, e.g., [11]), shows that, for $\omega \longrightarrow 0$, there are four roots k_z, two of which are real, $k_{z1,2} = \pm q(k)$, and the other two are complex conjugates, $k_{z3,4} = \pm i\kappa(k)$. When ionization and collisions are taken into account, each of the real roots $k_{z1,2}$ acquires an imaginary correction, which is in the upper half-plane of the complex variable k_z, and the fifth root arises, which corresponds to the vorticity wave and also lies in the upper half-plane of this variable. Consequently, for $z \longrightarrow -\infty$, the only physically reasonable solution is the solution that decreases exponentially according to the law $\exp(\kappa(k)z)$. When collisions are ignored, the undamped solutions $k_{z1,2}$ are excluded from consideration with the help of the emission condition (it can be readily verified that, at $\omega \longrightarrow 0$, the group velocities of the ion acoustic waves are positive).

In order to solve Eqs. (11) numerically, it is convenient to introduce the five-dimensional vector $f = (\phi_1, E_1, n_1, v_1, g_1)$, in terms of which the solutions are written as $f'(u) = A(u)f(u)$, where $A(u)$ is a matrix dependent on u. To single out the solutions that go to zero as $z \longrightarrow -\infty$, the eigenvectors of the matrix $A(u_{\min})$ and its eigenvalues λ are calculated for $u \approx u_{\min}$. Of the five eigenvalues, only one is chosen, namely, that whose real part is positive, $\mathrm{Re}\lambda > 0$. Let the corresponding (arbitrarily normalized) eigenvector be denoted by f_0, and let the solution to Eqs. (11) with the boundary condition $f(u_{\min}) = f_0$ be denoted by $f^{(p)}(u)$. The solution obtained in this way is proportional to the Green's function in the interval between the plasma volume and the test charge, i.e., in the range $u_{\min} < u < u_0$.

In the interval between the test charge and the wall, it is necessary to solve the boundary-value problem. The natural boundary condition at the conducting wall ($u = u_{\max}$) is that the potential of the perturbation vanishes there, $\phi_1(u_{\max}) = 0$. At the other end of the interval ($u = u_0$), the quantities ϕ_1, n_1, v_1, and g_1, whose values are determined by the solution $f^{(p)}(u_0)$, should be continuous. These five boundary conditions in the interval $u_0 < u < u_{\max}$ are used to solve boundary-value problem (11). We denoted the solution so obtained by $f^{(w)}(u)$. Hence, in the interval $u_{\min} < u < u_{\max}$, we have arrived at a solution that consists of two branches, $f^{(p)}(u)$ and $f^{(w)}(u)$, and for which the electric field at the point $u = u_0$ is discontinuous, $E_1^{(w)}(u_0) - E_1^{(p)}(u_0) = \Delta E$, while the other quantities at this point are continuous. In this solution, the value of the jump ΔE in the electric field is arbitrary. However, Eqs. (11) are linear; consequently, in order to calculate Green's function, it is sufficient to divide the solution obtained by ΔE.

The main difficulty in solving the problem by this numerical method is that, in the interval $u_{\min} < u < u_{\max}$, the eigenvalues of the matrix $A(u_{\min})$ can differ considerably (by several orders of magnitude), giving rise to large computational errors. The larger the transverse wavenumber k, the greater the difference between the eigenvalues. This is why the only perturbations that can be investigated by the above algorithm are those with sufficiently long wavelengths, $k \leq 1$. We note that this range of wavenumbers is of primary interest because it is in this range where like charges are expected to

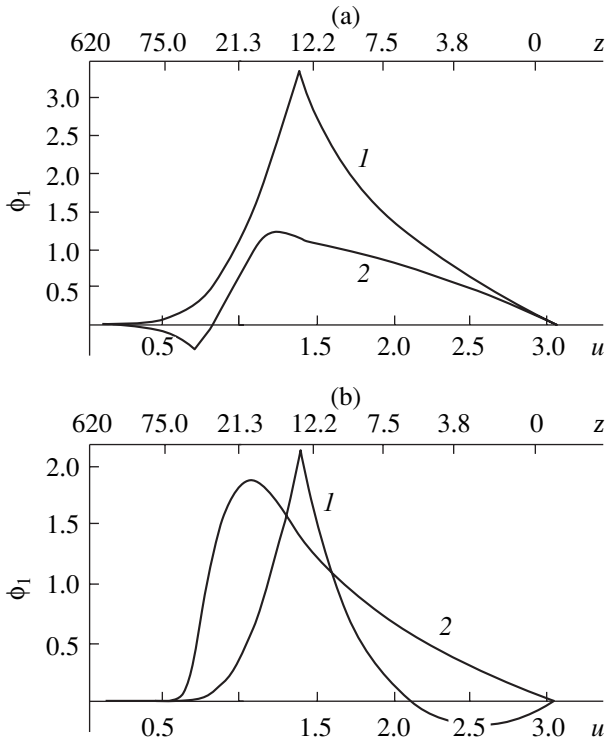

Fig. 2. Dependence of the perturbation potential on the ion flow velocity for u_0 = (*1*) 1.4 and (*2*) 0.71. Figure 2a refers to k = 0.01, and Fig. 2b refers to k = 0.1.

attract one another and the dust layer in a plasma–wall sheath may become unstable (see [11, 12]).

5. RESULTS

Characteristic examples of the dependence of the perturbation potential on u and z are shown in Fig. 2 (the unperturbed distribution of the plasma parameters is illustrated in Fig. 1). For sufficiently small transverse wavenumbers (k = 0.01), the potential of a point charge located in the region where the ion flow is supersonic is always positive (Fig. 2a, curve *1*). At larger transverse wavenumbers ($k \approx 0.1$), a region with a negative potential arises downstream from the point charge (Fig. 2b, curve *1*). In the case of a subsonic ion flow, the potential of a test charge exhibits a qualitatively different behavior: at small k values, it changes sign in the immediate vicinity of the charge (Fig. 2a, curve *2*).

Let us introduce the notation $w(u_0, k) = \phi_1(u)|_{u = u_0}$. If the Green's function for the sheath in coordinate space is equal to $G(z, z_0, \mathbf{r} - \mathbf{r}_0)$, then the function $w(u_0, k)$ is the Fourier transform of $G(z_0, z_0, \mathbf{r})$ in transverse coordinates. The squared frequency of the oscillations of a monolayer of the dust grains levitating in the sheath is proportional to $w(u_0, k)$ [11, 12]; consequently, it is of interest to search for the parameter ranges in which the function $w(u_0, k)$ is negative.

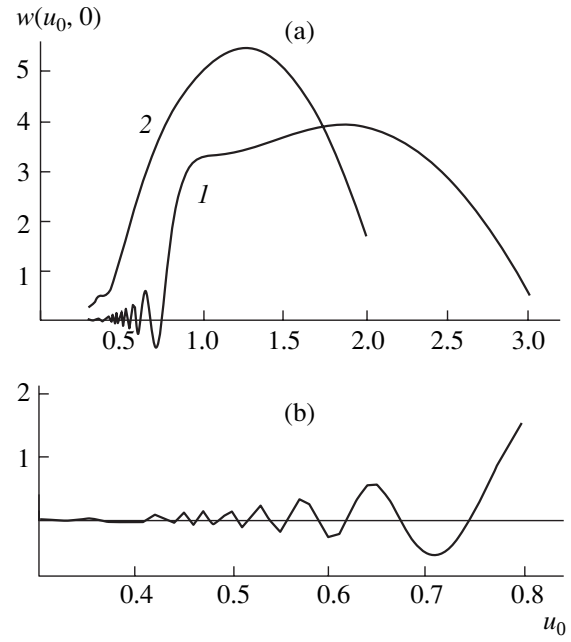

Fig. 3. Dependence of the potential $w(u_0, 0)$ on the velocity u_0 for α = (*1*) 0.01 and (*2*) 0.1. Figure 3b shows a portion of curve *1* in the range of subsonic velocities.

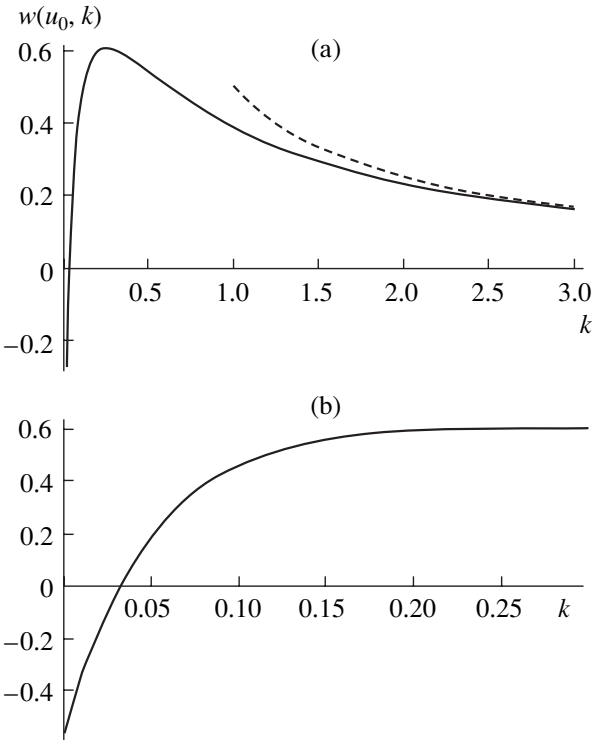

Fig. 4. Dependence of the potential $w(u_0, k)$ with u_0 = 0.71 on the transverse wavenumber. The dashed curve corresponds to the Coulomb potential. Figure 4b shows a portion of the solid curve in the long-wavelength range.

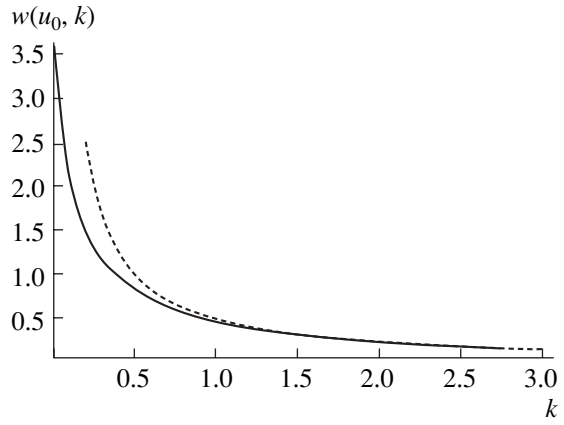

Fig. 5. Dependence of the potential $w(u_0, k)$ with $u_0 = 1.4$ on the transverse wavenumber. The dashed curve corresponds to the Coulomb potential.

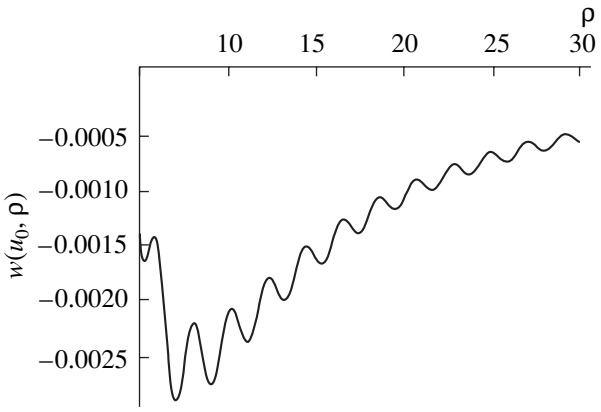

Fig. 6. Bessel transform of the dependence shown in Fig. 4a.

Figure 3 shows how the function $w(u_0, 0)$ (or, as it is virtually identical, the potential of a uniformly charged sheath) depends on the velocity u_0. Both of the curves in Fig. 3 were calculated for the ionization frequency $Z = 10^{-4}$. Curve *1* in Fig. 3a was obtained for the collision frequency $\nu = 0.01$, and curve *2* was obtained for $\nu = 0.1$ (in this case, the maximum flow velocity at the wall is equal to $u_{max} = 2.15$).

We can see from Fig. 3 that, for low collision frequencies in the case of a subsonic ion flow, the function $w(u_0, 0)$ is negative in certain intervals of the flow velocity (and, accordingly, in the corresponding intervals of height z_0). In other words, a dust monolayer at these heights is unstable against long-wavelength perturbations. This instability is suppressed as the collision frequency increases (Fig. 3, curve *2*).

Figure 4 shows the dependence of the potential $w(u_0, k)$ on the transverse wavenumber. This dependence was plotted from several thousand calculated points. The value $u_0 = 0.71$, which was chosen for simulations, corresponds to the minimum in curve *1* in Fig. 3a. In the long-wavelength range (such that $k \le 0.03$), the potential is negative. As was noted above, for $k \ge 1$, the numerical solution of Eqs. (11) may accumulate large errors. Nevertheless, in Fig. 4, the curve in the range of intermediate wavenumbers is surprisingly smooth. In the range of large wavenumbers ($k > 3$), the dependence $w(u_0, k)$ essentially coincides with that of the Bessel transform of the Coulomb potential (see the dashed curve in Fig. 4); under the above normalization conditions, this transform is equal to $1/(2k)$. For a supersonic ion flow, the function $w(u_0, k)$ becomes positive as the distance from the test charge to the wall decreases; moreover, the deviation from the Coulomb potential is substantial only for long wavelengths (see Fig. 5).

Figure 6 shows the dependence of the interaction potential of two test particles that are at the same distance from the wall on the distance between the particles in the case of a subsonic ion flow ($u_0 = 0.71$). The dependence is determined by the Bessel transform $w(u_0, \rho) = \int_0^\infty k\,dk w(u_0, k) J_0(k\rho)$. In the range $k < 3$, the integral was calculated using the dependence shown in Fig. 4a. In the range $k > 3$, it was assumed that $w(u_0, k) = 1/(2k)$. The presence of small-scale oscillations in the interaction potential shown in Fig. 6 seems to be an artifact: they are associated with a slight discontinuity in the integrand at $k = 3$.

6. CONCLUSIONS

In the present paper, some results have been presented from calculations of the static response function of a plasma–wall sheath. It is very difficult to make a comprehensive comparison between the numerical results and the results of analytical theory [11, 12] because this would require a great deal of computation. Qualitatively, however, the numerical analysis developed here is shown to correlate reasonably well with an analytic theory in which the plasma inhomogeneity is ignored. The calculations have confirmed the existence of the parameter range where the potential of a test particle changes its sign; this, in turn, indicates that a gaseous or a crystalline dust monolayer above the Bohm boundary is unstable. This instability can develop only when the collision frequency is sufficiently low to let the ion mean free path be as long as about one hundred electron Debye radii.

At the same time, it worth noting that there is a difference between the analytically obtained (see [11]) and the numerically calculated (see above) dependence of the response function on the transverse wavenumber in the long-wavelength range. The analytical theory implies that, in the limit $k \longrightarrow 0$, the potential $w(k)$ behaves as $w(k) \sim 1/(k^2 + a^2)$, where a is a certain number that depends on the ion velocity. On the other hand,

for the curves shown in Figs. 4 and 5, the derivative $dw(u_0, k)/dk$ does not vanish as $k \longrightarrow 0$, despite the fact that $w(k)$ is an even function of k. Based on the above numerical results, one may conclude that, over a wide range of variation of u_0, the response function behaves according to the law $w(k)|_{k \to 0} \sim a + b|k|$, where a and b are certain numbers. In principle, the appearance of such nonanalytic terms is quite typical in the description of semi-infinite systems; this is exemplified by the dispersion law for waves on deep water, $\sqrt{g|k|}$. This dependence of the response function on the wavenumber can manifest itself in the dispersion relation for dust acoustic waves: in the long-wavelength limit, the dispersion relation should have the form $\omega \sim ak + bk^2$.

ACKNOWLEDGMENTS

This work was supported in part by the Russian Foundation for Basic Research, project no. 02-02-16439.

REFERENCES

1. H. Thomas, G. E. Morfill, and V. N. Tsytovich, Fiz. Plazmy **29**, 963 (2003) [Plasma Phys. Rep. **29**, 895 (2003)].
2. Ya. L. Al'pert, A. V. Gurevich, and L. P. Pitaevskii, *Space Physics with Artificial Satellites* (Nauka, Moscow, 1964; Consultants Bureau, New York, 1965).
3. M. Nambu, S. V. Vladimirov, and P. K. Shukla, Phys. Lett. A **203**, 40 (1995).
4. S. V. Vladimirov and M. Nambu, Phys. Rev. E **52**, R2172 (1995).
5. O. Ishihara and S. V. Vladimirov, Phys. Plasmas **4**, 69 (1997).
6. A. Melzer, V. A. Schweigert, and A. Piel, Phys. Rev. Lett. **83**, 3194 (1999).
7. G. Lapenta, Phys. Rev. E **62**, 1175 (2000).
8. G. Lapenta, Phys. Rev. E **66**, 026409 (2002).
9. B. B. Kadomtsev, *Collective Phenomena in Plasmas* (Nauka, Moscow, 1988).
10. L. J. Hou, Y. N. Wang, and Z. L. Mišković, Phys. Rev. E **68**, 016410 (2003).
11. A. M. Ignatov, Fiz. Plazmy **29**, 325 (2003) [Plasma Phys. Rep. **29**, 296 (2003)].
12. I. Kourakis and P. K. Shukla, Phys. Lett. A **317**, 156 (2003).
13. V. Godyak and N. Sternberg, Phys. Plasmas **9**, 4427 (2002).
14. K.-U. Reimann, Phys. Plasmas **10**, 3432 (2003); V. Godyak and N. Sternberg, Phys. Plasmas **10**, 3435 (2003); D. D. Tskhakaya and P. K. Shukla, Phys. Plasmas **10**, 3437 (2003); V. Godyak and N. Sternberg, Phys. Plasmas **10**, 3439 (2003); M. S. Benilov, Phys. Plasmas **10**, 4584 (2003); V. Godyak and N. Sternberg, Phys. Plasmas **10**, 4587 (2003); R. N. Franklin, Phys. Plasmas **10**, 4589 (2003); V. Godyak and N. Sternberg, Phys. Plasmas **10**, 4590 (2003).

Translated by O.E. Khadin

Plasma Physics Reports, Vol. 30, No. 10, 2004, pp. 872–877. Translated from Fizika Plazmy, Vol. 30, No. 10, 2004, pp. 937–943.

METHODOLOGICAL NOTES

Application of the Lambert *W* Function in Mathematical Problems of Plasma Physics

I. D. Dubinova

All-Russia Research Institute of Experimental Physics, Russian Federal Nuclear Center, Sarov, Nizhni Novgorod oblast, 607188 Russia

Received October 29, 2003

Abstract—Examples of solutions to transcendental equations that arise in mathematical problems of plasma physics are considered. Earlier, such equations were solved only by approximate methods. The use of a new function—the Lambert *W* function—has made it possible to obtain explicit exact solutions that can help to refine the existing relevant theories. As examples, the following problems from different branches of plasma physics are considered: the equilibrium charge of a dust grain in a plasma, the structure of the Bohm sheath, the diameter of the separatrix in a Galathea–Belt system, the transverse structure of an electron beam in a plasma, the energy loss rate of a test charged particle in a plasma, and the structure of the Sagdeev pseudopotential for ion acoustic waves. *© 2004 MAIK "Nauka/Interperiodica".*

1. INTRODUCTION

A function that is convenient for solving transcendental equations of the type $x\exp x = \text{const}$ or $x + \ln x = \text{const}$ was introduced into plasma physics in the late 1980s by Corless *et al.* [1]; they called it Lambert *W* function. Since the Lambert *W* function, which may arise in a wide scope of practical problems in mathematics and mathematical physics, received little attention in Russia, it is expedient to illustrate how to use it in practice. This is the subject of the present paper, in which specific examples will be given of mathematical problems in theoretical plasma physics that can be solved completely and in explicit form only with the help of the Lambert function.

The function is defined by

$$W(x)\exp(W(x)) = x. \quad (1)$$

The fact that the Lambert *W* function is inverse to the function $F = x\exp x$ makes it possible to easily plot it (see Fig. 1) and to determine its simplest properties.

The Lambert *W* function is neither even nor odd. It is defined on the interval $[-1/e, \infty)$, takes on values from $-\infty$ to ∞, and is two-valued for negative x. Point A with the coordinates $(-1/e, -1)$ separates two branches of the function—the upper branch $W_0(x)$ and the lower branch $W_{-1}(x)$. Both branches have a common vertical tangent at point A. The upper branch $W_0(x)$, which is often called the main branch, passes through the coordinate origin and behaves everywhere in a regular manner. As for the lower branch $W_{-1}(x)$, it has an inflection point B with the coordinates $(-2/e^2, -2)$ and a vertical asymptote at $x = 0$.

Other integer values of the index of the function $W_k(k)$, namely, $k \neq 0, -1$, refer to the complex-valued branches [2]. In what follows, the indices of the branches of the function will be omitted when all of them possess common properties and when this can be done without causing confusion.

From definition (1), it is an easy matter to derive the following simple identities:

$$\exp(W(x)) = \frac{x}{W(x)}, \quad \ln W(x) = \ln x - W(x). \quad (2)$$

The rules for differentiation and integration of the Lambert *W* function are as follows: The derivative of

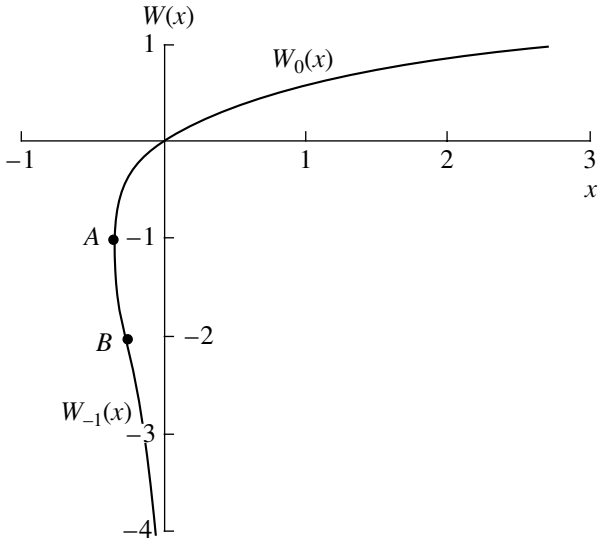

Fig. 1. Plot of the Lambert *W* function.

1063-780X/04/3010-0872$26.00 © 2004 MAIK "Nauka/Interperiodica"

the function can readily be obtained from the rule for differentiating inverse functions:

$$W'(x) = \frac{1}{(1+W(x))\exp(W(x))} = \frac{W(x)}{x(1+W(x))}. \quad (3)$$

The latter equality is valid for $x \neq 0$. At zero, the derivative is defined in the form of the limit

$$\lim_{x\to 0} W_0'(x) = 1. \quad (4)$$

The indefinite integral of the Lambert *W* function can be obtained from the rule for integrating inverse functions [3]:

$$\int_x f(x)dx = xf(x) - \int_{f(x)} g(y)dy. \quad (5)$$

Inserting the Lambert *W* function into this rule yields

$$\int W(x)dx = x\left[W(x) - 1 + \frac{1}{W(x)}\right], \quad (6)$$

where the integration constant is omitted.

Other properties of the Lambert *W* function are described in [1], and the issue of how to use it in the problems of mathematical physics is treated in review [4]. Particularly noteworthy among the problems considered in [4] are the classical problem about the electric potential distribution within a plane capacitor of finite size (the Rogowsky problem) and the accurate derivation of Wien's law from Planck's formula for thermal radiation.

Other examples of successful application of the Lambert *W* function in mathematical physics are also known. Among these are exact solutions to problems such as the distribution of electrons in a storage ring (with allowance for space charge) [5] and the phase boundary in a medium under steady-state heat conduction conditions [6]. The exact solution to the problem of the discharging of a capacitor to a resistor with a temperature-dependent resistance is presented in [7]. This solution describes the initial stage of the current flow in an exploding wire. The number of such successful applications is expected to increase in the future.

An analysis of the familiar examples makes it possible to guess what problems would have solutions containing the Lambert *W* function. First of all, this concerns solutions of the transcendental equations that include exponentials and logarithms, along with algebraic polynomials. These may be differential equations and nonlinear dispersion relations. Such equations can also arise, e.g., in solving boundary-value problems with involved boundary conditions, in analyzing the extremes of complicated functions, in representing implicitly defined functions in explicit form, etc.

In what follows, examples of the use of the Lambert *W* function will be considered for some mathematical problems in plasma physics.[1] The problems in question are taken from well-known papers whose authors arrived at transcendental equations and, without being aware of the Lambert *W* function, solved them either numerically or by approximate methods.

The question arises of whether it is expedient to introduce the Lambert *W* function into plasma physics. The objection is that, in practice, it is often sufficient to know the numerical values of the quantities, which can be calculated to any desired degree of accuracy. In other words, the sought quantity can be obtained without using the new function. This objection can be answered by saying that an explicit exact solution to a particular problem may deepen the understanding of the problem itself and even provide the basis for a new precise theory.

2. ELECTRIC CHARGE OF A TEST BODY IN A MAXWELLIAN PLASMA

The problem about the equilibrium electric charge accumulated by a test body (particle) at a floating potential in a gas-discharge plasma occupies an important place in plasma physics because its solution, on the one hand, is related to the single probe theory and, on the other, serves as a basis for the theory of dusty plasma.

This problem is most simply formulated for a Maxwellian plasma (i.e., for a plasma in which the electrons and ions obey Maxwellian distributions with temperatures T_e and T_i, respectively) in the so-called orbit-limited approach. The formulation of the problem can be found in a great number of papers on probes and dust grains in plasmas.

Here, the problem is formulated using the notation of [10]. The electron and ion currents to a spherical particle of radius *R* have the form

$$I_e(q) = \begin{cases} k'\exp(+\beta_e q) & \text{for} \quad q \le 0 \\ k'(1+\beta_e q) & \text{for} \quad q > 0, \end{cases} \quad (7)$$

$$I_i(q) = \begin{cases} pk'(1-\tau\beta_e q) & \text{for} \quad q \le 0 \\ pk'\exp(-\tau\beta_e q) & \text{for} \quad q > 0, \end{cases} \quad (8)$$

[1] To avoid misunderstanding, it should be stressed that the notation $W(x)$ is also sometimes used for other functions that have found wide applications in mathematical plasma physics: the Dawson function $W(x) = \exp(-x^2)\int_0^x \exp(t^2)dt$ (see, e.g., [8]) and the closely related Kramp function $W(x) = \exp(-x^2)\left[1 + \frac{2i}{\sqrt{\pi}}\int_0^x \exp(t^2)dt\right]$ (see [9]).

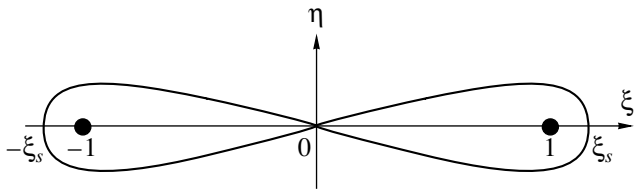

Fig. 2. Shape of the separatrix in a planar model of a Galathea–Belt system. Myxines are shown by closed circles.

where

$$k' = \pi R^2 n_e \left(\frac{8kT_e}{\pi m}\right)^{1/2}, \quad \beta_e = \frac{e^2}{4\pi\varepsilon_0 RkT_e},$$

$$p = \frac{1}{\nu}\left(\frac{\mu}{\tau}\right)^{1/2}, \quad \nu = \frac{n_e}{n_i}, \quad \tau = \frac{T_e}{T_i}, \quad \mu = \frac{m}{M},$$

n_e and n_i are the electron and ion densities, m and M are the masses of an electron and ion, k is Boltzmann's constant, and ε_0 is the permittivity of free space. The equilibrium electric charge accumulated by the particle is determined by an exact balance of the electron and ion currents to the particle's surface:

$$I_e(q) = I_i(q). \tag{9}$$

This is a transcendental equation. Earlier, it was solved either numerically [11] or by approximate methods. Thus, for $q < 0$, Matsoukas and Russel [10] obtained the approximate solution

$$q \approx C\frac{4\pi\varepsilon_0 RkT_e}{e^2}\ln\frac{(\mu\tau)^{1/2}}{\nu}, \tag{10}$$

where C is a constant.

However, it can readily be verified by substitution that Eq. (9) has the following exact solution:

$$q = \begin{cases} -\dfrac{1}{\beta_e}W\left(\dfrac{1}{p\tau}\exp\dfrac{1}{\tau}\right) + \dfrac{1}{\beta_e\tau} & \text{for} \quad q \le 0 \\ \dfrac{1}{\beta_e\tau}W(p\tau\exp\tau) - \dfrac{1}{\beta_e} & \text{for} \quad q > 0. \end{cases} \tag{11}$$

Hence, the solution to the problem about the equilibrium electric charge of a spherical particle in a Maxwellian plasma is given by exact expression (11), which contains the Lambert W function and can be used in probe theories and in the theory of dusty plasma. The example just considered refers to a variety of problems in which the differential equation describing the charging of a particle reduces to a time-independent transcendental equation like Eq. (9).

3. STRUCTURE OF THE ELECTRIC POTENTIAL IN A BOHM SHEATH

In order to determine the profiles of the normalized electric potential $\chi(x) = -eU(x)/kT_e$ and normalized ion kinetic energy $y(x) = Mv_i^2/2kT_e$ in a Bohm sheath in a collision-dominated plasma, Riemann [12] formulated and solved the following problem:

$$\frac{1}{2y}\frac{dy}{dx} - \frac{d\chi}{dx} = 0, \tag{12}$$

$$\frac{dy}{dx} - \frac{d\chi}{dx} = -2y, \tag{13}$$

where $x = z/\lambda$ is the coordinate normalized to the mean free path. He obtained the potential profile in an implicit form:

$$x = \frac{1}{2}\{1 - \exp[-2\chi(x)] - 2\chi(x)\}. \tag{14}$$

With the Lambert W function, however, the potential can be represented explicitly as

$$\chi(x) = \frac{1}{2}W(\exp(2x-1)) - x + \frac{1}{2}. \tag{15}$$

Thus, this example shows that the Lambert W function can be used to convert implicitly defined functions into an explicit form.

4. SIZE OF THE SEPARATRIX IN A GALATHEA–BELT SYSTEM

For the purposes of magnetic plasma confinement, A.I. Morozov proposed devices in which the current-carrying conductors are immersed in the plasma (see [13]). Such devices were named Galatheas, and the conductors were called myxines. One of such devices—the Galathea–Belt system—is a toroidal quadrupole configuration with two myxines. For a planar analogue of this configuration, Morozov and Murzina [14] obtained an analytic solution to the Grad–Shafranov equation for the dimensionless magnetic flux function ψ:

$$\psi = \mu\eta^2 + \lambda(\xi^2 - \eta^2) + \ln\{[(\xi-1)^2 + \eta^2][(\xi+1)^2 + \eta^2]\}, \tag{16}$$

where ξ and η are dimensionless coordinates (see Fig. 2) and μ and λ are constants. In particular, they determined the size ξ_S of the main separatrix in the ξ plane. The equation for the separatrix, $\psi = 0$, reduced to the transcendental equation

$$(\xi_S^2 - 1)^2 = \exp(-2\lambda\xi_S^2). \tag{17}$$

In [14], Eq. (17) was solved exactly for $\lambda = 0$ and numerically for $\lambda = 2$ and $-1/2$. However, using the

Lambert *W* function, it is possible to obtain a solution for any λ value:

$$\xi_{S1} = 0; \quad \xi_{S1,2} = \pm\sqrt{\frac{2}{\lambda}W\left(\frac{\lambda}{2}\exp\left(-\frac{\lambda}{2}\right)\right)+1}. \quad (18)$$

5. EQUILIBRIUM CONFIGURATION OF A NEUTRALIZED ELECTRON BEAM

Different models of equilibrium configurations of neutralized relativistic electron beams were considered by Lawson [15]. The general equilibrium condition that expresses the balance between the centrifugal force experienced by an electron at the radius r_1 and the Lorentz force exerted on the same electron by the self-magnetic field of the beam has the form

$$\frac{\gamma m\beta_\theta^2(r_1)c^2}{r_1} = e\beta_z(r_1)B_\theta(r_1) = \frac{4\pi e^2\beta_z(r_1)}{r_1}\int_0^{r_1} n(r)\beta_z(r)rdr, \quad (19)$$

where γ is the Lorentz factor of the electron and β_0, β_θ, and β_z are its total, azimuthal, and axial relative velocities, which satisfy the equality $\beta_\theta^2 + \beta_z^2 = \beta_0^2 = \text{const}$. In a model in which the electron density is uniform over the beam cross section, $n(r) = \text{const}$, the solution to Eq. (19) reduces to (see [15–17]

$$\frac{4\pi r_1^2 ne^2}{\gamma mc^2} = \frac{\beta_0^2}{\beta_z^2(r_1)} + 2\ln\frac{\beta_0}{\beta_z(r_1)} - 1. \quad (20)$$

In [17], this solution, written in implicit form, was approximated by

$$\beta_z(r_1) \approx \beta_0\left[K\left(\frac{\pi r_1^2 ne^2}{\gamma mc^2}\right)+1\right]^{-\frac{1}{2}}, \quad (21)$$

where $K(x)$ is a monotonically increasing function, which is equal to 2 at $x = 0$ and asymptotically approaches 4 as $x \longrightarrow \infty$. At the same time, solution (20) can be written in the following explicit exact form:

$$\beta_z(r_1) = \beta_0\left\{W\left[\exp\left(\frac{4\pi r_1^2 ne^2}{\gamma mc^2}+1\right)\right]\right\}^{-\frac{1}{2}}. \quad (22)$$

Generally, transcendental equations of the form $x + \ln x = a$ (in particular, Eq. (20)) often arise in a wide variety of problems, such as the plasma density distribution in an RF discharge (see formula (13) in [18]) and the behavior of the parameters of the self-similar motion of a low-density quasineutral plasma (see formula (24) in [19]). With the Lambert function, it is now a simple matter to obtain the explicit exact solution to each of these problems.

6. CRITICAL VELOCITIES IN THE PROCESS OF ENERGY TRANSFER FROM A TEST PARTICLE TO A PLASMA

According to [20], the mean rate of change of the energy of a test charged particle with mass m and charge e in its Coulomb interaction with plasma particles with mass m^* and charge e^* is given by the equation

$$\left\langle\frac{dE}{dt}\right\rangle_* = -\frac{4\pi(ee^*)^2}{v} \times \Lambda n^*\left[\frac{\text{erf}(b^*v)}{m^*} - \frac{2b^*v(m+m^*)}{\sqrt{\pi}mm^*}\exp(-b^{*2}v^2)\right], \quad (23)$$

where v is the velocity of the test particle, Λ is the Coulomb logarithm, n^* is the density of the plasma particles in question, and $1/b^* = \sqrt{2T^*/m^*} = v^*$ is their most probable velocity.

In order to analyze Eq. (23), it is convenient to switch to dimensionless variables. To do this, we consider the function

$$F(x,\beta) = \text{erf}(x) - \frac{2x}{\sqrt{\pi}}(1+\beta)\exp(-x^2), \quad (24)$$

which yields

$$\left\langle\frac{dE}{dt}\right\rangle_* = -\frac{4\pi}{m^*}\Lambda b^*(ee^*)^2 n^*\frac{F(x,\beta)}{x};$$

$$\beta = \frac{m^*}{m}; \quad x = b^*v.$$

The critical velocity at which the energy transfer does not occur is determined by the equation $F(x_{cr}, \beta) = 0$ and the critical velocity at which the energy transfer is most efficient is given by the equation $\partial F_x(x_{max}, \beta) = 0$.

One of the problems considered in [20] is that of the interaction of an electron beam with plasma ions. In this case, the parameter β is very large (for hydrogen ions, it is equal to $\beta = 1836$). In this case, the critical velocities x_{cr} and x_{max} satisfy the transcendental equations

$$Ax_{cr}\exp(-x_{cr}^2) = 1; \quad (25)$$

$$2Ax_{max}^3\exp(-x_{max}^2) = 1, \quad (26)$$

where A denotes a constant equal to

$$A = \frac{2}{\sqrt{\pi}}(1+\beta).$$

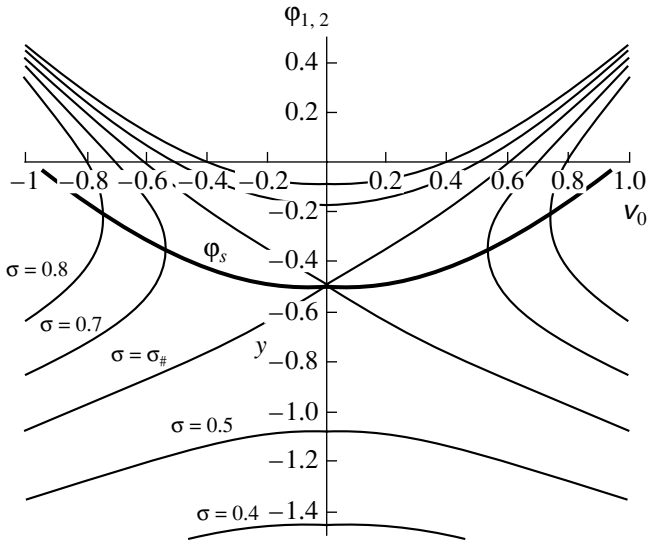

Fig. 3. Contour plot of the roots $\varphi_{1,2}(v_0)$ of Eq. (34) as functions of the parameter σ. The heavy curve separates the (upper) region of the root φ_1, corresponding to the maximum in the pseudopotential, from the (lower) region of the root φ_2, corresponding to the minimum in the pseudopotential.

Zero-, first-, and second-order approximate solutions to Eqs. (25) and (26) are presented in [20]. In the second approximation, the solutions have the form

$$x_{\rm cr}^2 = \ln A + \frac{1}{2}\ln\left(\ln A + \frac{1}{2}\ln\ln A\right); \quad (27)$$

$$x_{\max}^2 = \ln(2A) + \frac{3}{2}\ln\left(\ln(2A) + \frac{3}{2}\ln\ln(2A)\right). \quad (28)$$

However, these approximate formulas are not needed now because exact solutions to Eqs. (25) and (26) can be expressed in terms of the Lambert *W* function:

$$x_{\rm cr} = \frac{1}{A}\exp\left[-\frac{1}{2}W\left(-\frac{2}{A^2}\right)\right]; \quad (29)$$

$$x_{\max} = \frac{1}{2}\sqrt{-6W\left[-\frac{2}{3(4A^2)^{1/3}}\right]}. \quad (30)$$

7. EXTREMES OF THE SAGDEEV PSEUDOPOTENTIAL

In analyzing nonlinear ion acoustic waves, Sagdeev [21] arrived at the following solution to Poisson's equation:

$$\frac{d^2\varphi}{dx^2} = \exp\varphi - \frac{\sigma}{\sqrt{v_0^2 - 2\varphi}}, \quad (31)$$

where σ and v_0 are constants (in the notation of [22]). Equation (31) can be rewritten as a generalized integral of motion for a certain oscillator,

$$\frac{1}{2}\left(\frac{d\varphi}{dx}\right)^2 + V(\varphi) = E \quad (32)$$

with the so-called Sagdeev pseudopotential

$$V(\varphi) = -(\exp\varphi + \sigma\sqrt{v_0^2 - 2\varphi}), \quad (33)$$

where the role of the coordinate is played by the electrostatic potential φ and the role of the time is played by *x*. In order to determine the character of the solution to Eq. (31) and thereby the amplitude of the nonlinear ion acoustic waves, it is necessary to find and classify the extremes of pseudopotential (33). Equating the derivative of expression (33) to zero yields the transcendental equation [22]

$$\frac{dV(\varphi)}{d\varphi} = -\exp\varphi + \frac{\sigma}{\sqrt{v_0^2 - 2\varphi}} = 0. \quad (34)$$

In [22], it was pointed out that, under the inequality

$$\sigma^2\exp(-v_0^2) < \max(-2\gamma\exp(2\gamma)) = \frac{1}{e} \approx 0.37, \quad (35)$$

Eq. (34) has two roots, which correspond to a local maximum of the Sagdeev pseudopotential at $\varphi < (v_0^2 - 1)/2$ and to its local minimum at $\varphi > (v_0^2 - 1)/2$.

At the same time, the exact expressions for the roots of Eq. (34) can easily be obtained in terms of the Lambert *W* function:

$$\varphi_{1,2} = \frac{1}{2}[v_0^2 + W_{-1,0}(-\sigma^2\exp(-v_0^2))], \quad (36)$$

where the first and second roots correspond, respectively, to the maximum and minimum in the pseudopotential. Note that the expressions for the roots contain both real branches of the Lambert *W* function.

In order to illustrate how solutions (36) can be used in practice, let us briefly examine the behavior of the above roots of transcendental equation (32) as functions of the parameter σ. To do this, we turn to Fig. 3, which displays the plots of the functions $\varphi_{1,2}(v_0)$ for different values of σ. An analysis of the plots shows that the roots have the following properties. For $\sigma < \sigma_\#$, the region of the root $\varphi_1(v_0)$, corresponding to the maximum of the pseudopotential, and the region of the root $\varphi_2(v_0)$, corresponding to the minimum of the pseudopotential, do not overlap. For $\sigma > \sigma_\#$, each of the roots $\varphi_{1,2}(v_0)$ splits into branches (a negative and a positive) so that, for certain values of v_0, the branches of the root φ_1 can be conjugate to the branches of the root φ_2. The critical value $\sigma = \sigma_\#$ is a root of the equation

$$W_{-1}(-\sigma_\#^2) = W_0(-\sigma_\#^2). \quad (37)$$

This root is easy to determine: it corresponds to the conjugation point *A* of the real branches of the Lambert *W* function in Fig. 1, $\sigma_{\#} = e^{-1/2} \approx 0.60653$.

To find the locus of the conjugation points, note that each of them corresponds to the conjugation point of the real branches of the Lambert *W* function (point *A* in Fig. 1). Consequently, we must insert $\sigma^2 = \exp(v_0^2 - 1)$ into each of solutions (36). As a result, we obtain

$$\varphi_S = \frac{1}{2}[v_0^2 + W_{-1,0}(-\exp(v_0^2 - 1)\exp(-v_0^2))] = \frac{1}{2}[v_0^2 + W_{-1,0}(-1/e)] = \frac{(v_0^2 - 1)}{2}. \quad (38)$$

In Fig. 3, the locus φ_S is shown by the heavy curve.

8. CONCLUSIONS

To conclude, it is pertinent to recall the arguments given in [6]: "… a newly introduced mathematical function should satisfy certain requirements …. Thus, the function should possess the following features. The first is its applicability to various fields of mathematics, i.e., to different mathematical problems …. The second is its convenience in performing numerical computations. Finally, it should have certain algebraic properties."

The Lambert *W* function satisfies all these requirements well. The above analysis provides convincing evidence that the function is applicable to a wide scope of problems in mathematical physics. As for the convenience of the Lambert *W* function in performing calculations, it should be noted that, several decades ago (before the advent of the computer), use of logarithms, exponentials, and trigonometric functions in calculations was inconvenient, but nowadays the Lambert *W* function is incorporated into such well-known computer software packages as the Maple and Mathematica programs, which make it possible to calculate this function with extremely high accuracy. In addition, the Lambert *W* function exhibits a fairly wide variety of algebraic properties (see [1, 2]): it is closely related to second-order Stirling numbers, second-order Euler numbers, the distribution of primes in the natural number sequence, graph theory, combinatorics, etc.

Use of the Lambert *W* function has made it possible to obtain for the first time explicit exact solutions to the following mathematical problems in different branches of plasma physics: the equilibrium charge of a dust grain in a plasma, the structure of the Bohm sheath, the diameter of the separatrix in a Galathea–Belt system, the transverse structure of an electron beam in a plasma, the critical energy loss rates of a test charged particle in a plasma, and the structure of the Sagdeev pseudopotential for ion acoustic waves.

The number of the above mathematical problems of plasma physics in which the use of the Lambert *W* function leads to exact solutions is far from being exhausted. The examples considered above were essentially randomly chosen from journals published some years previously. It can nevertheless be hoped that these examples have helped to achieve the main goal of the present paper—to convince the reader that the new function can find many useful applications.

Hence, the use of the Lambert *W* function made it possible to obtain explicit exact solutions, which can aid in refining the existing theories in plasma physics.

REFERENCES

1. R. M. Corless, G. H. Gonnet, D. E. J. Hare, *et al.*, Adv. Comput. Math. **5**, 329 (1996).
2. D. J. Jeffrey, D. E. J. Hare, and R. M. Corless, Math. Scientist **21**, 1 (1996).
3. F. D. Parker, Am. Math. Monthly **62**, 439 (1955).
4. S. R. Valluri, D. J. Jeffrey, and R. M. Corless, Can. J. Phys. **78**, 823 (2000).
5. C. Thomas, J. I. M. Botman, R. Bartolini, *et al.*, in *Proceedings of the 8th European Particle Accelerator Conference, Paris, 2002*, p. 1565.
6. S. A. Sergeev and F. F. Spiridonov, Nauchno-Obrazovatel'nyĭ Zh. AltGTU (Altai State Tech. Univ.), No. 4 (2002).
7. V. S. Bulygin, Elektrichestvo, No. 7, 68 (2002).
8. H. Schamel, Plasma Phys. **14**, 905 (1972).
9. A. B. Mikhailovskii, *Theory of Plasma Instabilities* (Atomizdat, Moscow, 1970; Consultants Bureau, New York, 1974), Vol. 1.
10. Th. Matsoukas and M. Russell, J. Appl. Phys. **77**, 4285 (1995).
11. B. S. Xie, Chin. Phys. Lett. **19**, 365 (2002).
12. K.-U. Riemann, J. Phys. D **24**, 493 (1991).
13. A. I. Morozov and V. V. Savel'ev, Usp. Fiz. Nauk **168**, 1153 (1998) [Phys. Usp. **41**, 1049 (1998)].
14. A. I. Morozov and M. V. Murzina, Fiz. Plazmy **22**, 551 (1996) [Plasma Phys. Rep. **22**, 500 (1996)].
15. J. D. Lawson, Phys. Fluids **16**, 1298 (1973).
16. H.-M. Lai, Phys. Fluids **19**, 1068 (1976).
17. V. A. Romanovskiĭ, Fiz. Plazmy **5**, 624 (1979) [Sov. J. Plasma Phys. **5**, 351 (1979)].
18. V. A. Godyak and A. Kh. Ganna, Fiz. Plazmy **5**, 670 (1979) [Sov. J. Plasma Phys. **5**, 376 (1979)].
19. A. V. Gurevich and L. P. Pitaevskii, in *Reviews of Plasma Physics*, Ed. by M. A. Leontovich (Atomizdat, Moscow, 1980; Consultants Bureau, New York, 1986), Vol. 10.
20. D. V. Sivukhin, in *Reviews of Plasma Physics*, Ed. by M. A. Leontovich (Atomizdat, Moscow, 1964; Consultants Bureau, New York, 1968), Vol. 4.
21. R. Z. Sagdeev, in *Reviews of Plasma Physics*, Ed. by M. A. Leontovich (Atomizdat, Moscow, 1964; Consultants Bureau, New York, 1968), Vol. 4.
22. H. L. Pecseli, J. Trulsen, and R. J. Armstrong, Phys. Scr. **29**, 241 (1984).

Translated by O.E. Khadin

Plasma Physics Reports, Vol. 30, No. 10, 2004, pp. 878–881. Translated from Fizika Plazmy, Vol. 30, No. 10, 2004, pp. 944–947.

NONIDEAL PLASMA

Investigation of the Mechanisms for Stark Broadening and Shift of the Spectral Lines in a Nonideal Plasma

O. B. Denisov*, N. Yu. Orlov*, V. E. Fortov*, M. I. Kulish, V. K. Gryaznov**, and V. B. Mintsev****

**Institute for High Energy Densities, Associated Institute for High Temperatures, Russian Academy of Sciences, Izhorskaya ul. 13/19, Moscow, 127412 Russia*

***Institute of Chemical Physics, Russian Academy of Sciences, Chernogolovka, Moscow oblast, 142432 Russia*

Received September 24, 2003; in final form, December 8, 2003

Abstract—A method for calculating the Stark broadening and shift of the spectral lines was developed based on a combination of the ion plasma model and new theoretical and computational methods for taking the Stark effect into account. Theoretical results are compared with experimental data on the broadening and shift of the spectral lines in a strongly nonideal plasma. *© 2004 MAIK "Nauka/Interperiodica".*

1. INTRODUCTION

In recent years, intense investigations of the optical and thermophysical properties of a strongly nonideal plasma have led to substantial progress in this area of research [1]. Experimental measurements of the optical parameters of strongly nonideal plasmas made it possible to observe a number of new physical phenomena [2]. Thus, it was found that some spectral lines are deformed so substantially that, at sufficiently high plasma densities, they may turn out to be practically unresolvable. The mechanism underlying this phenomenon was investigated in our earlier paper [3]. In the present paper, we continue these investigations, with the focus on the processes responsible for the shift of the spectral lines.

It should be noted that recent developments in experimental methods and techniques were accompanied by theoretical studies of the optical properties of a strongly nonideal plasma. An important result of this theoretical work is the elaboration of new analytical and computational methods aimed at incorporating the Stark effect [4]. Another important result is the construction of a theoretical plasma model known as the ion model [5, 6], in which the full statistical ensemble of plasma atoms and ions is described by the solution to the set of equations for a self-consistent field. This approach provides reliable calculations of the quantum-mechanical parameters of the plasma in a broad range of plasma temperatures and densities, including those of a shocked plasma [7]. In the present study, we apply the calculation method based on a combination of the ion plasma model and the method for taking the Stark effect into account [4].

Since experiments in question were carried out at relatively low temperatures (about 3 eV), in which case the multiplet structure of the terms becomes important, we had to apply an approximate approach. Specifically, we calculated the parameters of an ensemble of plasma atoms and ions (in particular, their densities) in the ion model by using the basic wave functions obtained by solving the Schrödinger equations in which the exchange interaction was taken into account only approximately. When solving the Hartree–Fock equations, we took into account the multiplet structure of the terms [8] that determine the parameters of the spectral line studied in experiments. Here, we give only a brief description of the ion plasma model, because it was described in detail in [5–7].

2. ION PLASMA MODEL

We consider an ensemble of interacting plasma atoms and ions in the ground and excited states. As subsystems for Gibbs statistics, we can adopt spherical atomic cells of radius r_0 (with a nucleus of charge Z at the center). The radius of the cell can be defined as

$$r_0 = \left[\frac{3}{4\pi N_A}\right]^{1/3} \frac{1}{a_0}\left[\frac{A}{\rho}\right]^{1/3}, \qquad (1)$$

where A is the atomic weight, ρ [g/cm^3] is the plasma density, $a_0 = 5.292 \times 10^{-9}$ cm is the atomic length unit, and $N_A = 6.02 \times 10^{23}$ is Avogadro's number. Here and below, we use atomic units, in which we denote the temperature by Θ. The subsystems, numbered by the index j, differ from each other by the sets of occupation numbers of the bound (discrete) electronic states, $\{N_{nl}^j\}$, where n and l are the principal and orbital quantum numbers, respectively. Each subsystem also contains unbound (continuum) electrons. The states of subsystems are regarded as the states of plasma atoms and ions.

1063-780X/04/3010-0878$26.00 © 2004 MAIK "Nauka/Interperiodica"

Using the density functional method [7] and approximately taking into account the exchange interaction, we arrive at the following equation for the bound electrons:

$$-\frac{1}{2}(R_{nl}^j)'' + \left[-V_j(r) + \frac{l(l+1)}{2r^2}\right]R_{nl}^j(r) = E_{nl}^j R_{nl}^j(r), \quad (2)$$

where the wave functions satisfy the normalization condition

$$\int_0^{r_0} [R_{nl}^j(r)]^2 dr = 1. \quad (3)$$

The boundary conditions required to determine the eigenfunctions $R_{nl}^j(r)$ and the eigenvalues E_{nl}^j of the energy can be imposed as follows:

$$R_{nl}^j(0) = 0, \quad R_{nl}^j(r_0) = 0. \quad (4)$$

The potential $V_j(r)$ is written as

$$V_j(r) = V_1^j(r) + V_2^j(r). \quad (5)$$

Here,

$$V_1^j(r) = \frac{Z}{r} - \frac{4\pi}{r}\int_0^r r_1^2 \rho_j(r_1) dr_1 - 4\pi\int_r^{r_0} r_1 \rho_j(r_1), \quad (6)$$

$$V_2^j(r) = \frac{\pi\rho_j(r)}{\Theta}\left[1 + 6\frac{\rho_j(r)}{\Theta^{3/2}} + \frac{\pi^4}{3}\left(\frac{\rho_j(r)}{\Theta^{3/2}}\right)^2\right]^{-1/3}, \quad (7)$$

where $V_1^j(r)$ is the Coulomb interaction potential and $V_2^j(r)$ is the potential introduced artificially in order to approximately take into account the exchange interaction. The potential $V_2^j(r)$ can be described by different approximate formulas that have been proposed earlier. For our analysis, we chose the approximate expression that was proposed by Nikiforov and Uvarov [9]:

The electron density is represented as

$$\rho_j(r) = \rho_1^j(r) + \rho_2^j(r). \quad (8)$$

Here, the density of the bound electrons is equal to

$$\rho_1^j(r) = \frac{1}{4\pi r^2}\sum_{n,l} N_{nl}^j (R_{nl}^j(r))^2, \quad (9)$$

and the density of the unbound electrons is described in the quasiclassical approximation:

$$\rho_2^j(r) = \frac{\sqrt{2}\Theta^{3/2}}{\pi^2}\int_A \sqrt{y}\left\{1 + \exp\left[y - \frac{V_j(r)}{\Theta} - \frac{\mu}{\Theta}\right]\right\}^{-1} dy, \quad A: y > \frac{V_j(r)}{\Theta}. \quad (10)$$

The chemical potential μ can be deduced from the electroneutrality condition, $\sum_j W_j N_j = Z$, where $N_j = \sum_{nl} N_{nl}^j + 4\pi\int_0^{r_0} \rho_2^j(r) r^2 dr$ is the total number of electrons in the jth subsystem and W_j is the Gibbs distribution,

$$W_j = C g_j \exp\left\{-\frac{E_j - \mu N_j}{\Theta}\right\}, \quad (11)$$

with E_j being the total energy and $g_j = \prod_{nl} C_{2(2l+1)}^{N_{nl}^j}$ being the statistical weight.

The set of equations (2)–(11) describes the state of the statistical ensemble of plasma ions. Obviously, the groups of equations describing the states of subsystems denoted by subscripts $j = 1, 2$, etc., are coupled through the electroneutrality condition. Such equations are impossible to solve for all plasma ions even with the most advanced computers. However, these equations can be solved for the subsystem of main (or "reference") ions, which have the highest densities W_j. Having solved Eqs. (2)–(11) solely for this ion subsystem, we can apply the perturbation theory in order to determine the quantum parameters of the remaining plasma ions with lower densities.

3. METHOD FOR INCORPORATING THE STARK BROADENING AND SHIFT OF THE SPECTRAL LINES IN A NONIDEAL PLASMA

In order to calculate the shape of the spectral line corresponding to the transition between the sublevels $\alpha = nlm$ and $\beta = n'l'm'$ of the levels $a = n$, l and $b = n'l'$, respectively, Golosnoĭ [4] proposed the following approximate formula, which is a linear combination of the dispersion formula and the Gauss distribution:

$$I_{\alpha\beta}(\omega) = f(\Gamma)\frac{\gamma_{\alpha\beta}}{2\pi}\frac{1}{(\omega - \omega_0 - \omega_{\alpha\beta})^2 + \left(\frac{1}{2}\gamma_{\alpha\beta}\right)^2} + (1 - f(\Gamma))\frac{1}{\sqrt{\pi}\delta_{\alpha\beta}}\exp\left[-\left(\frac{\omega - \omega_0 - \omega_{\alpha\beta}}{\delta_{\alpha\beta}}\right)^2\right], \quad (12)$$

where ω_0 is the transition rate, $\Gamma = \frac{1}{r_0\Theta}$, and $f(\Gamma) = \exp\left(-\frac{1}{3}Z_0 Z_A \Gamma\right)$. The charges Z_0 and Z_A will be defined below. As Γ increases, the function $f(\Gamma)$ tends to zero. Since we simulated a strongly nonideal plasma, we set $f(\Gamma) = 0$ and described the spectral-line shape by the formula

$$I_{\alpha\beta}(\omega) = \frac{1}{\sqrt{\pi}\delta_{\alpha\beta}}\exp\left[-\left(\frac{\omega - \omega_0 - \omega_{\alpha\beta}}{\delta_{\alpha\beta}}\right)^2\right]. \quad (13)$$

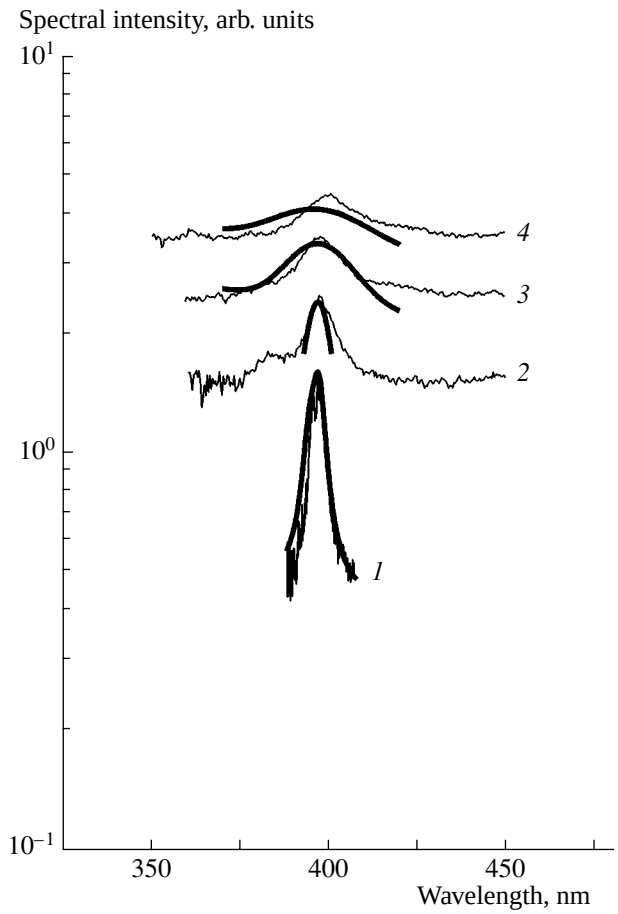

Fig. 1. Experimentally measured spectral intensities of radiation from a xenon plasma with an admixture of aluminum at different temperatures and different densities (light curves) and shapes of the AlI $3p\ ^2P^0_{1/2}$–$4s\ ^2S_{1/2}$ and AlI $3p\ ^2P^0_{3/2}$–$4s\ ^2S_{1/2}$ spectral lines calculated here for the same conditions (heavy curves). The computations were carried out for the following plasma mass densities: ρ = (*1*) 1.24×10^{-3}, (*2*) 3.02×10^{-3}, (*3*) 5.9×10^{-3}, and (*4*) 8.8×10^{-3} g/cm^3.

Here, $\delta_{\alpha\beta} = 2.5 C_{\alpha\beta}\zeta_{\max}$ is the dispersion and $\omega_{\alpha\beta} = C_{\alpha\beta}\zeta_{\max}$ is the expression for the most probable frequency shift, in which

$$C_{\alpha\beta} = \sum_{n_1 l_1}{}' \left[\frac{|\langle n'l'm'|z|n_1 l_1 m\rangle|^2}{E_{n'l'} - E_{n_1 l_1}} - \frac{|\langle nlm|z|n_1 l_1 m\rangle|^2}{E_{nl} - E_{n_1 l_1}} \right]. \quad (14)$$

Golosnoĭ [4] proposed the following formula for calculating the most probable value of the squared microfield $\zeta_{\max}$:

$$\zeta_{\max} = \frac{Z_A^2 \zeta_0}{\left[0.8\left(\frac{Z_A}{Z_B}\right)^4 + 4\frac{Z_A^4}{Z_B^5} Z_0 Z_C \Gamma + (Z_0 Z_A \Gamma)^2 \right]^{1/2}}, \quad (15)$$

where $\zeta_0 = \frac{1}{r_0^4}$, $Z_A = \sum_k Z_k X_k$, $Z_B = [\sum_k Z_k^{3/2} X_k]^{2/3}$, $Z_C = \sum_k Z_k^2 X_k$, $X_k = \frac{N_k}{N}$, N_k is the density of the ions with charge Z_k, N [1/cm^3] is the nucleus density, and Z_0 is the charge of the emitting ion.

Of course, in our calculations, we took into account the effect of both the natural broadening and the Doppler broadening. This effect was found to be insignificant as compared to the Stark effect.

4. COMPARISON BETWEEN THE CALCULATED RESULTS AND EXPERIMENTAL DATA

The results of measurements of the spectral intensities of radiation from a xenon plasma with an admixture of aluminum at different temperatures and different densities are illustrated by the light curves in Fig. 1 [10]. The objective of the experiments was to investigate the behavior of the spectral lines AlI $3p\ ^2P^0_{1/2}$–$4s\ ^2S_{1/2}$ and AlI $3p\ ^2P^0_{3/2}$–$4s\ ^2S_{1/2}$.

The experimental conditions were as follows:

(i) $T = 21700$ K and $\rho = 1.24 \times 10^{-3}$ g/cm^3, the density of unbound electrons being $N_e = 5.85 \times 10^{18}$ cm^{-3};

(ii) $T = 22900$ K and $\rho = 3.02 \times 10^{-3}$ g/cm^3, the density of unbound electrons being $N_e = 1.39 \times 10^{19}$ cm^{-3};

(iii) $T = 23900$ K and $\rho = 5.9 \times 10^{-3}$ g/cm^3, the density of unbound electrons being $N_e = 2.67 \times 10^{19}$ cm^{-3}; and

(iv) $T = 24500$ K and $\rho = 8.8 \times 10^{-3}$ g/cm^3, the density of unbound electrons being $N_e = 3.9 \times 10^{19}$ cm^{-3}.

The heavy curves in Fig. 1 show the shapes of the AlI $3p\ ^2P^0_{1/2}$–$4s\ ^2S_{1/2}$ and AlI $3p\ ^2P^0_{3/2}$–$4s\ ^2S_{1/2}$ spectral lines that were calculated for the temperatures and densities indicated in items (i)–(iv) by the method described above. It should be noted that, in our calculations, the Hartree–Fock equation was solved by applying one of the most exact among the presently known methods [8]. However, even with this method, the positions of the spectral lines were found to deviate from the experimentally measured positions by about 20%. Because of this, the calculated positions were refined by using the experimental data of [11]. Note also that, in simulations, we ignored the influence of the Stark effect on the populations of the electronic levels.

Figure 2 shows the shifts of the spectral lines versus the plasma density. As is seen, the experimentally observed spectral line shifts differ markedly from those obtained using the theory developed by H.R. Griem. On the other hand, the method proposed here provides a fairly exact agreement with experiment.

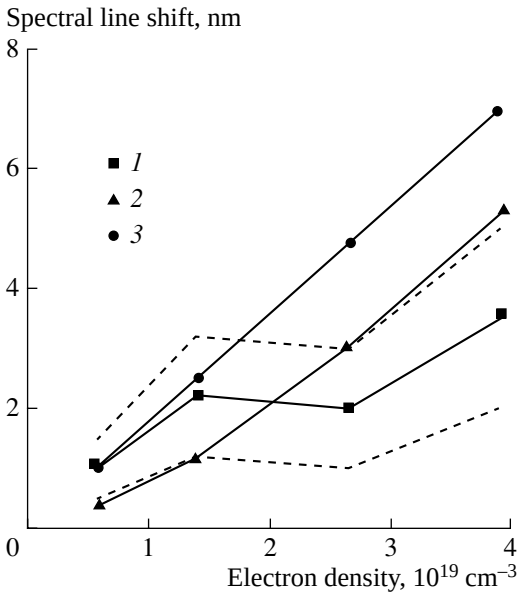

Fig. 2. Shift of the AlI $3p\ ^2P^0_{1/2}$–$4s\ ^2S_{1/2}$ and AlI $3p\ ^2P^0_{3/2}$–$4s\ ^2S_{1/2}$ spectral lines vs. electron density N_e: (*1*) experimental data (the dashed lines indicate the limits of experimental error), (*2*) results of calculations by the ion plasma model, and (*3*) results of calculations by the Griem theory.

5. CONCLUSIONS

A comparison between the calculated results described above and the experimental data obtained in [10] allows one to conclude that, for a correct theoretical description of the mechanism for the broadening and shift of spectral lines in a strongly nonideal plasma, it is necessary to fairly accurately account for the effects associated with the nonideal nature of the plasma. In the present study, which is based on the ion plasma model, the nonideal plasma nature is taken into account in solving the set of equations for the self-consistent field. This approach is found to yield good agreement between the theoretical results and experimental data. We have considered only one mechanism for the broadening and shift of the spectral lines. It can be hoped that calculations of other mechanisms with allowance for the nonideal character of the plasma will lead to a closer agreement with experiment.

REFERENCES

1. V. E. Fortov and I. T. Yakubov, *Physics of Nonideal Plasma* (Hemispere, New York, 1990).
2. M. Kulish, V. Gryaznov, A. Mezhipa, *et al.*, in *Proceedings of the International Conference on Physics of Strongly Coupled Plasmas, Binz, 1995*, p. 337.
3. O. B. Denisov, N. Yu. Orlov, V. E. Fortov, *et al.*, Fiz. Plazmy **27**, 1081 (2001) [Plasma Phys. Rep. **27**, 1021 (2001)].
4. I. O. Golosnoĭ, Preprint No. 38 (All-Russia Center of Mathematical Modeling, USSR Academy of Sciences, Moscow, 1991).
5. N. Y. Orlov, Laser Part. Beams **15**, 627 (1997).
6. N. Y. Orlov and V. E. Fortov, in *Proceedings of the 3rd International Conference on Intense Ion Beam Interaction with Matter, Moscow, 2000*, p. 268.
7. N. Yu. Orlov and V. E. Fortov, Fiz. Plazmy **27**, 45 (2001) [Plasma Phys. Rep. **27**, 44 (2001)].
8. C. Froese Fischer, T. Brage, and P. Joensson, *Computational Atomic Structure: An MCHF Approach* (Institute of Physics Publishing, Bristol, 1997).
9. A. F. Nikiforov and V. B. Uvarov, *Numerical Methods of Continuum Mechanics* (1973), Vol. 4, p. 114.
10. M. Kulish, V. Gryaznov, A. Mezhipa, *et al.*, in *Proceedings of the 23rd International Conference on Phenomena in Ionized Gases, Toulouse, 1997*, p. I-212.
11. C. E. Moore, *Atomic Energy Levels*, Circular of the National Bureau of Standards, No. 467 (Natl. Bur. Stand., Washington, 1949).

Translated by O.E. Khadin

Plasma Physics Reports, Vol. 30, No. 10, 2004, pp. 882–893. Translated from Fizika Plazmy, Vol. 30, No. 10, 2004, pp. 948–960.

LOW-TEMPERATURE PLASMA

Diagnostics of Heterogeneous Processes with the Participation of Radicals by Time-Resolved Actinometry

D. V. Lopaev and A. V. Smirnov

Skobeltsyn Institute of Nuclear Physics, Moscow State University, Vorob'evy gory, Moscow, 119899 Russia

Received November 17, 2003; in final form, February 4, 2004

Abstract—A method is proposed for measuring the probabilities of the heterogeneous loss of radicals in a gas-discharge plasma. The method is based on the time-resolved modulation actinometry. It is shown that this method is applicable for O, H, F, and CF_2 radicals. The probabilities of the loss of these radicals on the discharge tube wall are measured in a dc glow discharge. It is shown that the measurement results do not depend on which radical's emission line is used. The measurement results are only slightly affected by the dissociative excitation of the radical's emitting states and the background emission from the plasma. It is shown that the technique proposed is similar to the method of laser-induced fluorescence and provides a fairly high accuracy when measuring the probabilities (up to $\gamma_R \sim 10^{-2}$–10^{-1}) of the surface loss of radicals in a gas-discharge plasma. In contrast to the LIF method, this technique allows one to acquire a large amount of experimental data over a reasonable time interval (up to one thousand of γ_R measurements per hour). This feature is an important and necessary condition for a thorough study of the surface reactions and the complicated many-parametrical mechanism for the heterogeneous loss of radicals. © *2004 MAIK "Nauka/Interperiodica".*

1. INTRODUCTION

At present, plasma–surface interactions are attracting great attention of researchers because of the wide use of plasma technologies in various fields of industry and good prospects for developing new materials with unique properties, as well as different structures on their base. First of all, these studies are important for nanotechnology, which is a very rapidly developing field of applied physics. Here, the processes of plasma–surface interaction are of key significance. The capabilities and prospects of nanotechnology are related to knowledge of the surface processes at atomic level and the ability to control them. However, in spite of the obvious success in plasma nanotechnology and the great number of scientific publications in this field, there is still very little fundamental information (which is to be based on the large number of reliable experimental data) on the elementary processes of the plasma–surface interaction. The current knowledge is mainly related to the investigators' concepts of the processes occurring on the surface, rather than to reliable experimental data. These concepts often appear to be self-contradictory and to disagree with the data on the well-known processes in the plasma volume.

Radicals are the most active particles that play an important role in the formation and growth of the surface structures. Available models of the interaction between radicals and surface often employ constant heterogeneous loss probabilities γ_R or take into account only the dependence of γ_R on such integral parameters as the surface temperature (if there are such experimental data). In fact, the loss probability γ_R is a function not only of the large number of parameters related to the state of the surface (which is determined by the properties of active surface sites; species and concentrations of the adsorbed particles, including the radicals themselves; species and energies of the ions; etc.) at a given time, but also of the plasma parameters (the gas composition, the electron and ion energy distribution functions, the concentrations of active particles, etc.). Hence, the heterogeneous loss probability itself is actually a "model" of the surface processes. Obviously, such a situation gives rise to a vicious circle of "fitting" the experimental data to the "desired" conception instead of verifying the conception itself. Attempts to break this vicious circle using the experimental data on the surface processes in an ultra-high vacuum [1] (with the help of tunnel, atomic force, electron, and ion microscopy; the ion- and laser-induced desorption and fluorescence; etc.), as well as the great capabilities of the modern methods for modeling molecular dynamics and many-particle interaction, though casting light on the physical nature of a number of phenomena, have been mainly restricted to the narrow field of atomically clean surfaces. Under actual technological conditions, mechanisms for the surface processes can be more complicated and the processes themselves can proceed in somewhat different ways. Therefore, to acquire the necessary experimental data on these mechanisms, one needs simultaneous *in situ* diagnostics of the processes both on the surface and in the plasma volume.

It is the measurements of the probabilities of the heterogeneous loss of radicals under various experimental conditions that may serve as one of the means for such diagnostics. A schematic of this approach is shown in

1063-780X/04/3010-0882$26.00

Fig. 1. Here, the model of the surface processes with the participation of R radicals is represented by an operator that maps a multi-parametrical function $\gamma_R(M_i)$ (where M_i are macroparameters such as the gas composition, the concentrations of radicals and charged particles, the ion energy, the surface temperature, etc.) into a function $\gamma_R(m_i)$ (where m_i are microparameters such as the adsorption energy of active particles, the activation energies of the surface reactions, the density of the active surface sites, etc.). To enable a unique mapping and, accordingly, the development of a non-self-contradictory model of the surface processes, it is necessary to adjust the numbers of micro- and macroparameters to one another. The more sophisticated the mechanism for surface processes, the larger the number of microparameters that are required to describe them; an equally large number of measurements should be performed to obtain more or less reliable data on the values of these microparameters. For example, for ten microparameters, about 10^7 measurements are necessary to obtain the experimental representation of $\gamma_R(M_i)$ over each parameter by at least five experimental points. The use of *a priori* information about any process on the surface or in the plasma volume may reduce the number of the necessary parameters; however, in view of the very essence of the problem, this reduction is not large. Otherwise, it makes no sense to carry out experiments whose results are known in advance. Thus, the degree of detalization and accuracy of the model developed, as well as its predicting ability, are functions of the number and accuracy of the measurements, i.e., of the capabilities of *in situ* diagnostics. Taking into account available experimental data on the probabilities of the heterogeneous loss of different radicals, one can assert that $\gamma_R(m_i)$ are functions of no less than four to eight parameters; consequently, about 10^4–10^5 measurements are required to enable good agreement between the model and experiment. Thus, *in situ* diagnostics of the surface processes imposes rather strict requirements to the experimental technique and apparatus. Besides such obvious requirements as the apparatus sensitivity and resolution, these are also requirements to the rates of acquiring and processing the experimental data. No less than ten to one hundred measurements per hour are required to ensure a reasonable duration (one to two months) of the experiment.

Radicals with unpaired valent electrons generally show a great many intense transitions in different spectral ranges; this property is often used to diagnose them. At present, the most precise methods for the diagnostics of atoms and radicals in plasma are laser ones, such as laser-induced fluorescence (LIF) [2, 3], intracavity laser spectroscopy [4], laser diode spectroscopy [5], etc. The LIF method, which provides not only the high sensitivity but also the high spatial and time resolution, is used most frequently. However, the excitation energies of most of the atoms and molecules that are of interest for technology (H, O, N, C, F, Cl, Si, CH_x, CF_x, SiH_x (x = 1–3), etc.) lie in the UV and VUV ranges. In many cases, this calls for the employment of the two-photon LIF, which is a complicated and rather expensive technique. To perform a single measurement of the probability of the heterogeneous loss of radicals under given conditions, one has to measure either the density of radicals near the surface or the time behavior of their concentration when the plasmochemical equilibrium in the discharge volume is violated due to the loss of radicals in the kinetic regime (i.e., when the main loss mechanism is the loss of radicals on the surface). In both cases, to obtain one γ_R value, it is necessary to perform a series of LIF measurements consisting of hundreds spatial and time points. Taking into account the scheme of LIF measurements, it can be seen that only a very narrow range of the parameters M_i can be studied. Certainly, the data on the $\gamma_R(M_i)$ thus obtained are very important; however, they are often insufficient for an unambiguous interpretation of the experimental results and the development of a model of the surface processes.

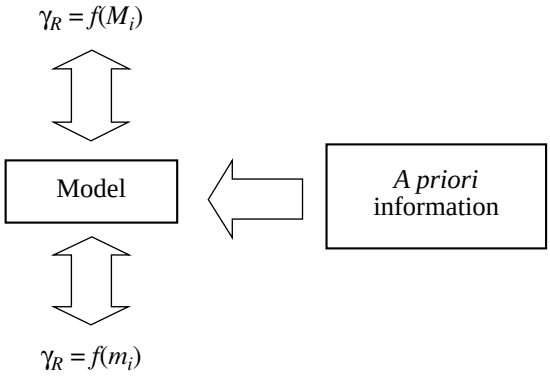

Fig. 1. Probability γ_R of the heterogeneous loss of radicals as a many-parametrical function of micro- (m_i) and macro- (M_i) parameters (see text).

In this paper, a new and very simple method is proposed that provides results similar to those obtained by the LIF method, but does not require so cumbersome apparatus. In contrast to the LIF method, it enables a few thousands of measurements of $\gamma_R(M_i)$ within a few hours. As was noted above, this is a necessary condition for studying the mechanisms for the interaction of atoms and radicals with actual surfaces. Of course, this method is not free of drawbacks, which will be discussed below.

2. EXPERIMENTAL TECHNIQUE

It is obvious that surface processes with the participation of radicals significantly affect their density in the plasma volume only when the heterogeneous loss of radicals is the main loss mechanism. If such a system is somehow disturbed from an equilibrium condition, then the concentration of radicals will come to equilib-

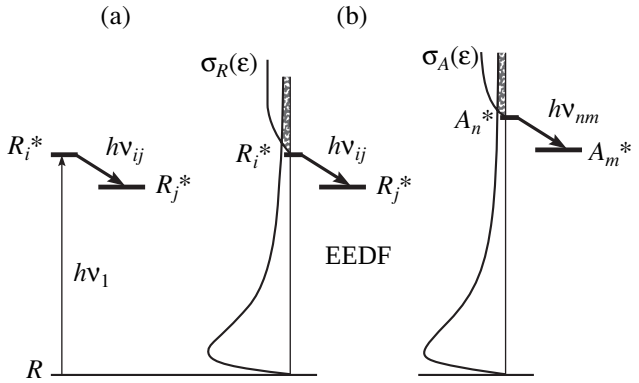

Fig. 2. Scheme of the detection of radicals in the ground state by the (a) LIF and (b) actinometry methods. *R* and *A* stand for the radicals and actinometer atoms, and $h\nu_l$ is the laser radiation photon (see text).

rium with the characteristic time of a heterogeneous process; from this time, one can deduce the corresponding value of $\gamma_R(M_i)$. This process can be monitored using the LIF technique, in which the laser power does not vary over time. Here, we propose a method in which, in contrast to the LIF technique, the upper emitting level is excited by the plasma electrons, which serve as an incoherent excitation source (see Fig. 2), rather than by photons. Evidently, if the discharge power remained constant during the evolution of the radical concentration, then the method of plasma-induced fluorescence of radicals would be identical to the LIF method. To provide such conditions, the time evolution of the atomic and radical densities is recorded by the method of time-resolved actinometry. In this case, the useful signal is the ratio between the line emission intensities of the radical and actinometer—an admixture (most often, of noble gas atoms) that does not participate in chemical reactions and whose cross section for the electron-impact excitation of the emitting level is similar in shape to that of the radical [6, 7]. The latter requirement is almost always satisfied, and there is no need for the excited levels of the actinometer and the radical to be close to one another. The processes affecting the populations of the excited states and, consequently, the line emission intensities of the radical *R* and actinometer atom *A* are as follows:

$$e + R \xrightarrow{k_e^R} e + R_i^*, \tag{1}$$

$$e + A \xrightarrow{k_e^A} e + A_n^*, \tag{2}$$

$$R_i^* \xrightarrow{A_{ij}} R_j^* + h\nu_{ij}, \tag{3}$$

$$A_n^* \xrightarrow{A_{nm}} A_m^* + h\nu_{nm}, \tag{4}$$

$$e + RX \xrightarrow{k_{de}^R} R_i^* + X + e, \tag{5}$$

$$R_i^* + M_q \xrightarrow{k_q^R} R + M_q, \tag{6}$$

$$A_n^* + M_q \xrightarrow{k_q^A} A + M_q. \tag{7}$$

Here, ν_{ij} and ν_{nm} are the frequencies of the spontaneous radiative transitions of the radical and actinometer atoms, respectively (processes (3) and (4)); A_{ij} and A_{nm} are the corresponding Einstein coefficients; k_e^R and k_e^A are the rate constants for the direct electron-impact excitation of the R_i^* and A_n^* emitting states of the radicals and actinometer atoms, respectively (processes (1) and (2)); k_{de}^R is the rate constant for the production of R_i^* radicals in the dissociative excitation of *RX* molecules (process (5)); and k_q^R and k_q^A are the rate constants for the quenching of the R_i^* and A_n^* emitting states of the radicals and actinometer atoms by the gas particles of the *q*th species (processes (6) and (7)). It follows from expressions (1)–(7) that the radical concentration is related to the ratio between the line emission intensities of the radicals and actinometer atoms by the formula

$$\frac{[R]}{[RX]} = C_R^A \frac{I_R}{I_A} - \frac{k_{de}^R}{k_e^R}, \tag{8}$$

where

$$C_R^A = \frac{[A]}{[RX]} \frac{h\nu_{nm} A_{nm}}{h\nu_{ij} A_{ij}} \frac{k_e^A}{k_e^R} \times \frac{\sum_j A_{ij} + \sum_q k_q^R [M_q]}{\sum_m A_{nm} + \sum_q k_q^A [M_q]}, \tag{9}$$

I_R and I_A are the lines emission intensities of the radicals and actinometer atoms, respectively; $[A]$, $[R]$, $[RX]$, and $[M_q]$ are the concentrations of actinometer atoms, the radicals, the stable molecules from which these radicals are produced, and the gas particles of the *q*th species.

The actinometry method always employs the short-lived upper states of both the radical and actinometer (R_i^* and A_n^*, respectively); hence, for most low-pressure plasma systems, the rate of the radiative decay of these states is higher than the rate of their collisional quenching. It can be seen from formula (8) that the actinometric signal (the ratio I_R/I_A of the line intensities) follows the dynamics of the radical concentration (as is in the LIF method) only if the coefficient C_R^A, the ratio k_{de}^R/k_e^R, and the concentration of *RX* molecules remain constant during the evolution of $[R]$. It was shown in

[6–8] that the ratio between the excitation rate constants changes only slightly within a wide range of the reduced electric fields and is almost independent of the effects related to the nonlocal character of the electron energy spectrum. For small variations in the plasma electric field (on the order of 10%), this ratio remains constant with an accuracy of no worse than ~0.1%. The degree of gas dissociation in the discharge plasma is almost always much less than unity; as a result, we have $[R] \ll [RX]$. Hence, small variations in the radical concentration $[\delta R]$ ($[\delta R] \ll [R]$) that are caused by a slight deviation of the system from the equilibrium state have almost no effect on the RX concentration.

To disturb the equilibrium, one can modulate the discharge current by rectangular pulses with a modulation depth of ≤10–15%. In this case, the line emission intensities of the radical and actinometer change in a jumplike manner because of the rapid change in the discharge parameters. The radiative lifetimes of the emitting levels and the characteristic relaxation times of the electron distribution function and the concentrations of charged particles are much shorter than the characteristic loss time of radicals. For this reason, when the plasma parameters have already reached their new stationary values after a rapid change in the discharge current, the concentration of radicals $[\delta R]$ may continue to either increase (an additional production of radicals) or decrease (the loss of radicals). Thus, the time evolution of the actinometric signal will closely follow the time evolution of $[\delta R]$ over a quite long time interval after a jump in the discharge current. From this time evolution, the value of $\gamma_R(M_i)$) can be derived. Slight variations in the discharge parameters during the evolution of $[\delta R]$ (in the plasma of electronegative gases, these variations are caused by the associative detachment of electrons from negative ions in reactions with radicals) can be traced by recording the emission from the actinometer atoms and, thus, do not affect the measurement results. Note that the characteristic rise and decay times of the radical concentrations should be close to one another if the discharge modulation does not affect the processes with the participation of radicals. This is a good applicability criterion for the method proposed.

The response of radicals on the discharge modulation is most adequately represented by the time evolution of the relative variations in their concentrations. When both the dissociative excitation of the R_i^* state and the background plasma emission at the wavelengths of radical emission can be ignored, the relative variation in the radical density in a modulated discharge is

$$1 + \frac{[\delta R](t)}{[R]} = \frac{1 + \delta I_R(t)/I_R}{1 + \delta I_A(t)/I_A}. \quad (10)$$

To adequately represent the time evolution of the relative variation in the radical density, it is necessary to normalize the radical line emission intensity to the line emission intensity of the actinometer (the normalization coefficient is $c = I_R/I_A$). If the dissociative excitation of the R_i^* state or the background plasma emission (which is generally the emission from the short-lived allowed molecular transitions of the main or a buffer gas, e.g., H_2, N_2, O_2, or CF_4) gives a significant contribution to the emission intensity at the wavelengths of radical emission, then expression (10) fails to hold. Actually, this lead to a renormalization of the right-hand side of expression (10); as a result, the modulation depth of the actinometric signal is no longer equal to the modulation depth of the radical density $[\delta R]/[R]$. We note, however, that such a renormalization does not change the time behavior of the actinometric signal; i.e., it does not affect the measurements of the characteristic loss time of radicals. This opens great prospects for using the method proposed to study the heterogeneous reactions of radicals in the plasma of polyatomic gases, whose emission spectrum is rather complicated, so that it is hardly possible to avoid overlapping between the emission lines of different particles.

This paper is devoted to studying the capabilities and applicability criteria of the method proposed. The method is shown to be applicable to studying the mechanism for the surface recombination of O and H atoms on a chemically inert surface (e.g., quartz or glass) under discharge conditions. It is also demonstrated that the method can be used to investigate the processes with the participation of F atoms and CF_2 radicals in a fluorocarbon plasma.

3. EXPERIMENT

The experiments were performed with a conventional glow discharge in a long cylindrical tube. It is well known that, in such a discharge, the electron energy distribution function (EEDF) and the electron density n_e are almost constant along the positive column. A schematic of the experiment is shown in Fig. 3. We carried out experiments with O_2, H_2, N_2, and CF_4 at pressures of 0.1–3 torr and discharge current densities of 0.2–25 mA/cm^2. As discharge tubes, we used a quartz tube with an inner diameter of 14 mm and two molybdenum-glass tubes with inner diameters of 12 and 18 mm. The use of different tubes allowed us to determine the sensitivity of our method for measuring the probabilities of the heterogeneous loss of atoms and radicals to the type of the tube material and to the manufacturing conditions and "life history" of a given material. The distance between the electrodes was no less than 500 mm. The electrodes were placed in special sockets, as is done in laser tubes (see Fig. 3). It can be seen that the schematic of the experiment is quite simple (especially in comparison to the LIF scheme). A 1–3% argon admixture to the gases under study was used as an actinometer. Such a small percentage of argon has almost no effect on the EEDF and the discharge parameters.

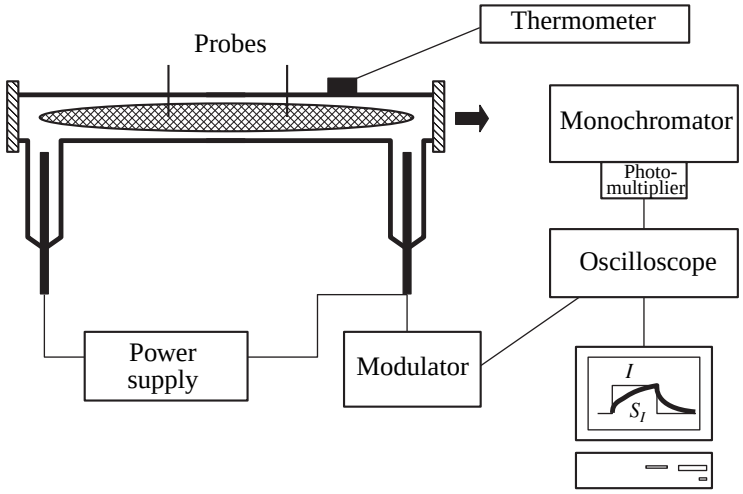

Fig. 3. Schematic of the experimental facility.

The emission from the positive column was spectrally selected by a monochromator and then recorded by a photomultiplier. The photomultiplier signal was applied to the first channel of a digital oscilloscope. The discharge current signal was applied to the second channel. In some experiments, when the emission lines of the radical and actinometer were widely separated in spectrum and the operating spectral range of the photomultiplier no longer provided the required signal-to-noise ratio, we used two optical recording channels (two monochromators and two photomultipliers). In this case, the signal from the other photomultiplier was applied to the second channel of the oscilloscope.

The discharge current was modulated by rectangular pulses. Both the modulation frequency and the modulation depth could be varied within very wide ranges, from a fraction of hertz to 10 kHz and from 1 to 60%, respectively. The temperature of the discharge tube wall was measured with a calibrated thermocouple sensor. The temperatures of the inner and outer surfaces of the discharge tube were assumed to be the same; this assumption is quite reasonable because, in our experiments, the temperature drop across the tube wall was no more than 1–2 K.

The glow discharge geometry ensured the constancy of the actinometric signal along the tube. This allowed us not only to use the results of integral measurements of the radical and atomic emission from the ends of the discharge tube (this option significantly increases the signal-to-noise ratio) but also to determine directly the probability of the heterogeneous loss of radicals γ_R via the characteristic time of the experimentally measured variations in the radical concentration $[\delta R]$. When the radicals are lost on the wall of a long cylindrical tube, we have

$$\frac{d[\delta R]}{dt} = -\frac{[\delta R]}{\tau_{exp}} = -\gamma_R \frac{[\delta R_w] v_T}{4} \frac{S}{V}. \qquad (11)$$

Here, τ_{exp} is the radical loss time determined from an exponential fitting of the experimentally measured evolution of the actinometric signal, γ_R is the probability of radical recombination on the tube wall, $v_T = \sqrt{8k_B T_w/\pi M_R}$ is the thermal velocity of radicals near the wall, T_w is the wall temperature, k_B is the Boltzmann constant, M_R is the mass of a radical, $S/V = 2/r$ is a geometrical factor (where r is the tube radius), and $[\delta R_w]$ is the radical concentration near the wall. When the loss of radicals is not limited by diffusion, we have $[\delta R_w] \approx [\delta R]$ and

$$\gamma_R = \frac{2r}{v_T \tau_{exp}}. \qquad (12)$$

Under typical glow discharge conditions ($pd \le 1$ torr cm), expression (12) is applicable at $\gamma_R < 10^{-1}$. Otherwise, Eq. (11) becomes invalid and the problem becomes much more complicated because, in a general case, one needs to take into account the nonuniform and nonstationary transport of radicals.

In each experiment, the modulation frequency and modulation depth were chosen such that, on the one hand, the accuracy in measuring τ_{exp} was no worse than 5–10% (the measurement accuracy increases with modulation depth) but, on the other, the kinetics of radicals changed insignificantly (obviously, the less the modulation depth, the smaller the effect of modulation on the measurements of τ_{exp}). To determine the effect of discharge modulation on the processes with the participation of radicals, the following criterion was used: the modulation effect was ignored when the measured characteristic times τ_{exp} corresponding to the rise and decay phases of $[\delta R]$ coincided within the measurement accuracy.

4. EXPERIMENTAL RESULTS AND DISCUSSION

First of all, we recorded the emission spectra from discharges in O_2, H_2, N_2, and CF_4 with small admixtures of Ar in wide ranges of pressures and discharge currents. We identified the emission lines of Ar, O, H, N, and F atoms, as well as the emission bands of O_2, H_2, N_2, and CF_4 molecules, including the molecular bands of CF and CF_2 radicals present in CF_4. The results are as follows:

The Ar 750.3-nm emission line, corresponding to the $2p_1 \longrightarrow 1s_2$ transition, was one of the most intense lines in the emission spectrum of argon in all of the gases used. Note that this transition is most often used in actinometry. We also used this transition in our measurements.

In pure O_2, the most intense emission lines were the 844- and 777-nm lines corresponding to the $O(3p^3P_{0,1,2} \longrightarrow 3p^3S_1^0)$ and $O(3p^5P_{1,2,3} \longrightarrow 3p^5S_2^0)$ transitions, respectively. These lines, as well as the Ar 750.3-nm line, were well resolved and did not overlap with the emission spectrum of O_2. This allowed us to use the actinometry of oxygen atoms by argon atoms under almost all discharge conditions. The resolution of the monochromator employed in our experiments allowed us to resolve the fine structure of the $O(3p^3P_{0,1,2} \longrightarrow 3p^3S_1^0)$ and $O(3p^5P_{1,2,3} \longrightarrow 3p^5S_2^0)$ transitions. We verified the method in question for each component of the fine structure. The time evolution of all the fine structure components in a modulated discharge was always identical; for this reason, we will say of these transitions as 844- and 777-nm emission lines of atomic oxygen. Figure 4a shows, as an example, the time evolution of the emission intensities of the 844- and 777-nm lines of atomic oxygen and the 750.3-nm line of argon in the O_2 : Ar = 98 : 2 mixture at a pressure of 2 torr in a discharge with a current density of 15 mA/cm^2 and current modulation depth of ~23%. It can be seen that, when the discharge current undergoes a jump, the intensities of all the emission lines change very rapidly (almost in a jumplike manner on the time scale of Fig. 4a). After a new steady-state discharge regime is established (in about a few tens of microseconds), the line emission intensities change more slowly. As was expected, slow variations in the line emission intensity of atomic oxygen are mainly caused by variations in the atomic concentration. Slight variations in the emission intensity of Ar atoms after a steady-state discharge regime is established are related to slow variations in the plasma electric field and the electron density due to the associative detachment of electrons from negative oxygen ions [9, 10].

Figure 4b shows the evolution of the discharge current density $S_J = 1 + \delta J_d/J_d$ and the actinometric signals

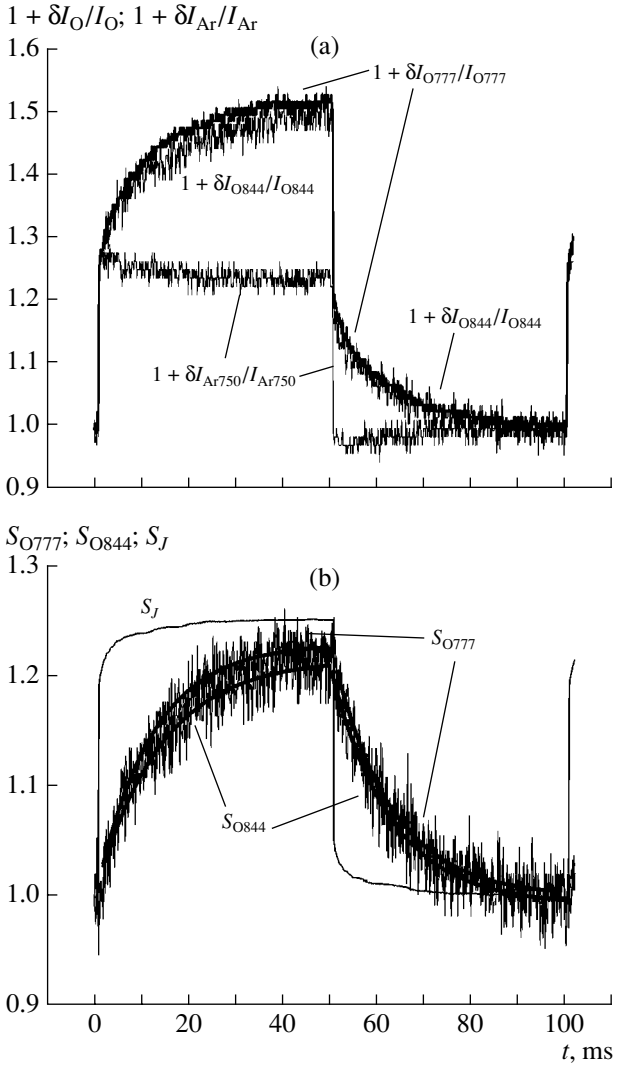

Fig. 4. (a) Time evolution of the emission intensities of the 844- and 777-nm lines of atomic oxygen and the 750.3-nm line of argon in a modulated discharge in the O_2 : Ar = 98 : 2 mixture at p = 2 torr and J_d = 15 mA/cm^2. (b) Waveforms of the normalized discharge current density $S_J = 1 + \delta J_d/J_d$ and the actinometric signals $S_{O777} = \dfrac{1 + \delta I_{O777}/I_{O777}}{1 + \delta I_{Ar750}/I_{Ar750}}$ and $S_{O844} = \dfrac{1 + \delta I_{O844}/I_{O844}}{1 + \delta I_{Ar750}/I_{Ar750}}$ for the 777- and 844-nm lines of atomic oxygen, respectively. The heavy lines show the exponential approximations of the rise and decay segments of the S_{O777} and S_{O844} signals.

$$S_{O777} = \frac{1 + \delta I_{O777}/I_{O777}}{1 + \delta I_{Ar750}/I_{Ar750}} \text{ and } S_{O844} = \frac{1 + \delta I_{O844}/I_{O844}}{1 + \delta I_{Ar750}/I_{Ar750}}$$

for the 777- and 844-nm lines of atomic oxygen, respectively. The S_{O777} and S_{O844} actinometric signals are absolutely identical (to distinguish between them, we slightly reduced one of them in Fig. 4b). This result agrees well with formula (10), in deriving which the

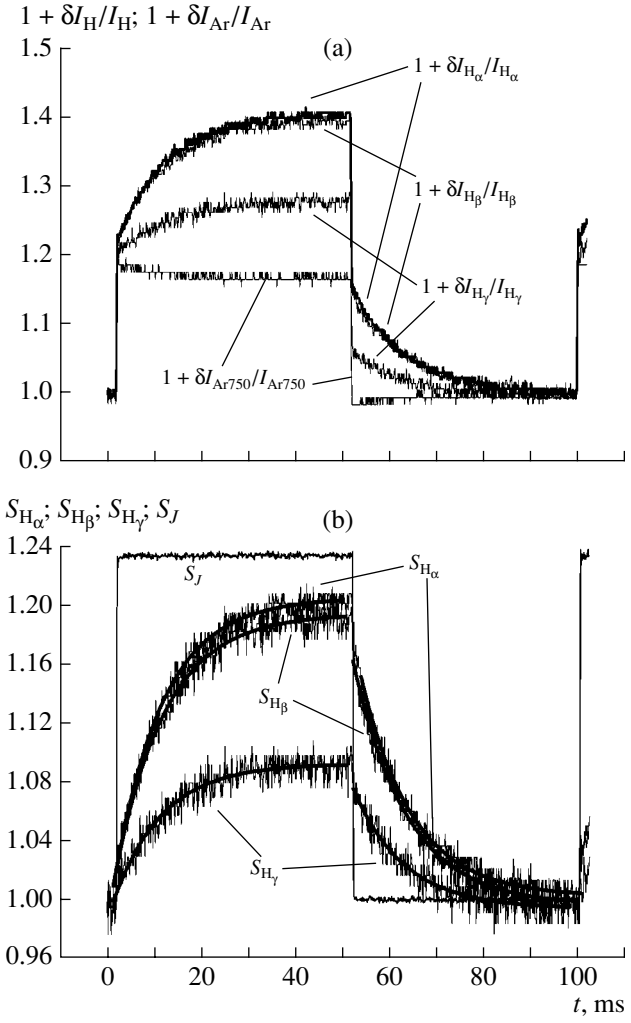

Fig. 5. (a) Time evolution of the emission intensities of the H_α 656.3-nm, H_β 486.1-nm, and H_γ 434.0-nm lines of the hydrogen Balmer series and the 750.3-nm line of argon in a modulated discharge in the H_2 : Ar = 98 : 2 mixture at p = 2 torr and J_d = 10 mA/cm^2. (b) Waveforms of the normalized discharge current density $S_J = 1 + \delta J_d/J_d$ and the actinometric signals $S_{H_\alpha} = \frac{1 + \delta I_{H656}/I_{H656}}{1 + \delta I_{Ar750}/I_{Ar750}}$, $S_{H_\beta} = \frac{1 + \delta I_{H486}/I_{H486}}{1 + \delta I_{Ar750}/I_{Ar750}}$, and $S_{H_\gamma} = \frac{1 + \delta I_{H434}/I_{H434}}{1 + \delta I_{Ar750}/I_{Ar750}}$ for the H_α, H_β, and H_γ hydrogen lines, respectively. The heavy lines show the exponential approximations of the rise and decay segments of the S_{H_α}, S_{H_β}, and S_{H_γ} signals.

dissociative excitation of the upper emitting states and the background emission at the wavelengths under study were ignored. The heavy lines show the exponential approximations for the rise and decay segments of the S_{O777} and S_{O844} signals, from which the corresponding characteristic time τ_{exp} of oxygen atom loss was derived. For the S_{O777} and S_{O844} signals, these times are the same, which confirms the validity of the method. The quantity $\gamma_O = (2.05 \pm 0.07) \times 10^{-3}$ (the relative error is as low as 3%), which was determined by formula (12), is rather small; therefore, the applicability of the formula (12) to calculating γ_O is quite justified. The γ_O value thus obtained is in good agreement with the data of [8, 11–14] on the probability of the heterogeneous loss of $O(^3P)$ atoms on a glass surface under discharge conditions. Note that, after a discharge is switched into a new regime, the time during which a new steady-state discharge current is established is rather long. This indicates the presence of electron production processes other than direct electron-impact ionization. This is typical of discharges in electronegative gases. In these discharges, the density of negative ions is often comparable to or even significantly higher than the electron density. Consequently, the reactions of associative electron detachment on active particles (which are generally radicals) that are present in the discharge volume contribute significantly to the charge balance. In this case, the time during which the charge balance is established is determined by the lifetime of active particles. In a molecular oxygen plasma, such long-lived particles are $O(^3P)$ atoms and $O_2(a^1\Delta_g)$ metastable molecules. For example, the characteristic time during which the $O_2(a^1\Delta_g)$ concentration is established may be as long as hundreds of milliseconds. Apparently, such nonsteady behavior of the plasma affects many processes, including the excitation of the emitting states of neutral particles. The use of the actinometry technique allows one to take into account the nonsteady behavior of excitation by using the emission from the short-lived allowed transitions of actinometer atoms (in our case, Ar atoms) (see Fig. 4a).

Three lines of the Balmer series of atomic hydrogen, namely, H_α (λ 656.3-nm, H_β 486.1-nm, and H_γ 434.0-nm lines, corresponding to the $H(n = 3, 4, 5 \longrightarrow n = 2)$ transitions, were clearly seen in the emission spectrum of pure H_2. Throughout the entire 200- to 850-nm spectral range under study, there were also the emission bands of molecular hydrogen. The intensities of H_α, H_β, and Ar 750.3-nm lines greatly exceeded the intensities of the emission bands of H_2, and only the intensity of the H_γ line was comparable to them at low discharge currents. To illustrate, Fig. 5a shows the time evolution of the line emission intensities of the Balmer series of atomic hydrogen and the 750.3-nm line of argon in a modulated discharge in the H_2 : Ar = 98 : 2 mixture at a pressure of 2 torr, current density of 10 mA/cm^2, and current modulation depth of ~23%. It can be seen that, after a jump in the discharge current, the relative variation in the intensity of the H_γ line is much lower than that of the H_α and H_β lines. This testifies to a significant contribution to the intensity of the H_γ line from the emission that is not related to hydrogen atoms. After switching the discharge into a new state, the emission intensity of Ar atoms changes to a lower

extent than in oxygen, and the emission intensity relaxes to its new steady value much faster.

Figure 5b shows the waveforms of the normalized discharge current density $S_J = 1 + \delta J_d/J_d$ and the actinometric signals for the H_α, H_β, and H_γ lines of atomic hydrogen: $S_{H_\alpha} = \frac{1 + \delta I_{H656}/I_{H656}}{1 + \delta I_{Ar750}/I_{Ar750}}$; $S_{H_\beta} = \frac{1 + \delta I_{H486}/I_{H486}}{1 + \delta I_{Ar750}/I_{Ar750}}$, and $S_{H_\gamma} = \frac{1 + \delta I_{H434}/I_{H434}}{1 + \delta I_{Ar750}/I_{Ar750}}$, respectively. It can be seen from Fig. 5b that the modulation depth of the S_{H_α} and S_{H_β} actinometric signals and especially of the S_{H_γ} signal is smaller than modulation depth of the discharge current. This fact indicates that the concentration of hydrogen atoms is so low that the contribution of dissociative excitation becomes significant. This contribution increases with increasing level number n due to the corresponding decrease in the cross section for the direct electron-impact excitation of the $H(n)$ level. Since the time evolution of the concentration of stable H_2 molecules is similar to that of Ar atoms, the time evolution of the emission from $H(n = 3, 4, 5)$ atoms produced via dissociative excitation is similar to that of the 750-nm line. In other words, any contribution to the intensity of the H_α, H_β, and H_γ emission lines of H_2 molecules is equivalent to the contribution from Ar actinometer; i.e., this contribution leads only to the renormalization of the relative variation in the actinometric signal (see above). We recall that, in principle, any neutral atoms or molecules that have appropriate levels and whose density varies slightly can act as actinometers. The intense emission of H_2 molecules at a wavelength of 434 nm leads to a further decrease in the modulation depth of the S_{H_γ} signal. However, as was noted above, such a renormalization does not affect the measurement of γ_H. Heavy lines in Fig. 5b show the exponential approximations of the rise and decay segments of the S_{H_α}, S_{H_β}, and S_{H_γ} signals, from which we determined the probabilities γ_H of the heterogeneous loss of hydrogen atoms: $\gamma_{H_\alpha} = (6.98 \pm 0.04) \times 10^{-4}$, $\gamma_{H_\beta} = (7.02 \pm 0.11) \times 10^{-4}$, and $\gamma_{H_\gamma} = (7.01 \pm 0.17) \times 10^{-4}$. The average value is $\gamma_H = (7 \pm 0.11) \times 10^{-4}$, the relative measurement error being 1.5%. The experiments performed within wide ranges of currents and pressures showed that the relative measurement error of γ_H was always no larger than 5%. The measured loss probability of hydrogen atoms on a quartz surface is in good agreement with the available literature data [11, 15–18]. It can be seen from Fig. 5b that the discharge current changes very rapidly when switching into a new steady state. This indicates that the rate of electron production via the associative recombination of negative H^- ions on hydrogen atoms is low compared to the rate of electron-impact ionization. This is quite understandable because, in contrast to a discharge in oxygen, the concentration of negative ions in the plasma of molecular hydrogen is much lower than the electron density, $[H^-/n_e] \ll 1$.

The most intense components in the emission spectrum of a discharge in pure N_2 are the molecular bands of the 2^+ and 1^+ nitrogen systems corresponding to the $N_2(C^3\Pi_u \longrightarrow A^3\Sigma_u^+)$ and $N_2(B^3\Pi_g \longrightarrow A^3\Sigma_u^+)$ transitions, respectively. It is well known that, within visible and infrared spectral regions, the intense $N(3p^4S^0_{3/2} \longrightarrow 3s^4P_{1/2, 3/2, 5/2})$ transitions with wavelengths of 742.4, 744.2, and 746.8 nm are the most appropriate for actinometry of nitrogen atoms. Unfortunately, only at high discharge currents and low pressures (of <0.5 torr) were we able to detect the most intense of these lines (namely, the 746.8-nm line) against the background of very intense emission of the 1^+ nitrogen system. Obviously, this indicates the possibility of using the actinometry method to record nitrogen atoms, however, only if their concentration is sufficiently high. For example, the actinometry technique was successfully used in the case of a surface-wave discharge excited in a surfatron microwave cavity. The degree of dissociation of N_2 molecules in this discharge was larger than 1% [19, 20]. We studied the VUV emission spectrum of a glow discharge in N_2 using a vacuum monochromator and visible-blind FEU-142 photomultiplier with a MgF_2 entrance window. As in the visible spectral region, the discharge emission was mainly concentrated in molecular nitrogen bands, namely, in the Ogawa–Tanaka–Wilkinson–Mulliken bands $N_2(a'^1\Sigma_u^- \longrightarrow X^1\Sigma_g^+)$ and the Lyman–Birge–Hopfield bands $N_2(a^1\Pi_g^- \longrightarrow X^1\Sigma_g^+)$. Although we used rather thin (~0.5-mm-thick) MgF_2 windows at the tube ends, the 120-nm resonance emission line (the $N(3s^4P_{1/2, 3/2, 5/2} \longrightarrow 2p^4S^0_{3/2})$ transition of nitrogen atoms) could hardly be observed (almost at a level corresponding to photon counting) because of its strong absorption in MgF_2. For this reason, we abandoned the wide-range test of the method proposed as applied to N atoms. However, the above results can be useful when carrying out actinometric studies in a nitrogen plasma.

In the plasma of pure CF_4, the emission bands of CF_4 molecules and CF_2 radicals were the most intense throughout the entire 120- to 850-nm spectral range under study. Unfortunately, in all the discharges, the emission intensity of the UV bands of CF radicals ($CF(B^2\Delta, v' \longrightarrow X^2\Pi, v'')$ transitions with $\lambda \approx 195$–210 nm and $CF(A^2\Sigma^+, v' \longrightarrow X^2\Pi, v'')$ transitions with $\lambda \approx 209$–234 nm [21, 22]) was so low that we were not able to unambiguously detect them against the intense background emission of CF_4 and CF_2 molecules. As for the emission of CF_3 radicals, the low-intensity broad

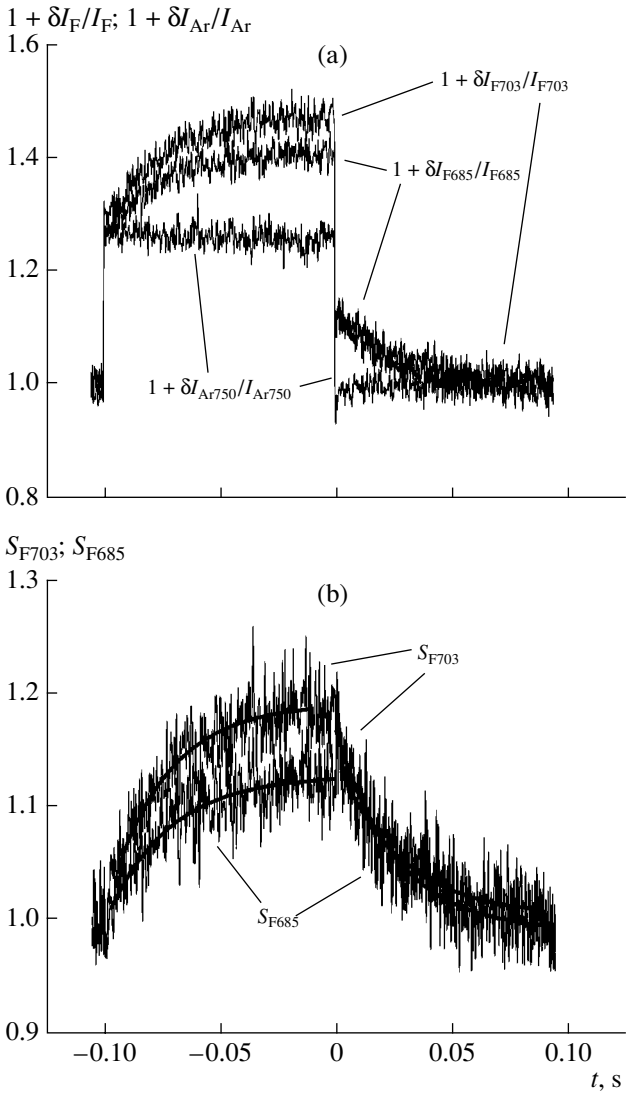

Fig. 6. (a) Waveforms of the normalized emission intensities of the 703.8- and 686.6-nm lines of atomic fluorine and the 750.3-nm line of argon in a modulated discharge in the CF_4 : Ar = 98 : 2 mixture at p = 1 torr and J_d = 10 mA/cm^2; (b) actinometric signals $S_{F703} = \frac{1 + \delta I_{F703}/I_{F703}}{1 + \delta I_{Ar750}/I_{Ar750}}$ and $S_{F685} = \frac{1 + \delta I_{F685}/I_{F685}}{1 + \delta I_{Ar750}/I_{Ar750}}$ for the 703.8- and 686.6-nm lines of atomic fluorine, respectively. The heavy lines show the exponential approximations of the rise and decay segments of the S_{F703} and S_{F685} signals.

bands corresponding to the $CF_3(\tilde{E}(2^2A_1') \longrightarrow \tilde{\chi}(1^2A_2''))$ transitions with $\lambda \approx 200$–270 nm and $CF_3(\tilde{B}(2^2A_2'') \longrightarrow \tilde{A}(1^2A_1'))$ transitions with $\lambda \approx 450$–750 nm [23–27] were clearly observed only at pressures higher than ~1 torr. However, the known emission bands of CF_2 radicals $CF_2(^1B_1 \longrightarrow {}^1A_1)$ with $\lambda \approx 240$–350 nm and $CF_2(^3B_1 \longrightarrow {}^1A_1)$ with $\lambda \approx 350$–720 nm [23, 24, 28–30]) turned out to be rather intense within wide ranges of currents and CF_4 pressures. Studies of the time evolution of the intensities of the CF_2 emission bands in a modulated discharge as a function of the discharge parameters showed that only the UV emission corresponding to the $CF_2(^1B_1 \longrightarrow {}^1A_1)$ band is caused by the electron-impact excitation from the ground state of the radical (process (1)). The emission of CF_2 radicals within a wide $CF_2(^3B_1 \longrightarrow {}^1A_1)$ band is almost completely related to the dissociative excitation of C_xF_y (x = 2, 3, …; y = 2, 3, …) polyatomic polymer molecules, which are produced in the discharge volume in the processes of the plasma polymerization of fluorocarbons [31, 32] (process (7)). For C_xF_y molecules, the threshold for dissociative excitation is quite low. This is of great interest because this emission can be used for the actinometric detection of polymer fluorocarbon molecules in a gas-discharge plasma. In this study, we used only the $CF_2(^1B_1 \longrightarrow {}^1A_1)$ emission band and investigated the feasibility of applying the proposed method to study the loss of CF_2 radicals under the conditions of the intense polymerization of fluorocarbons in the plasma volume and on the tube wall.

The emission intensity of fluorine and argon atoms in a CF_4 plasma was significantly lower than that of CF_2 radicals. However, the spectral lines of F and Ar atoms were located apart from the most intense $CF_2(^3B_1 \longrightarrow {}^1A_1)$ emission band and, thus, could easily be resolved. As before, the Ar ($2p_1 \longrightarrow 1s_2$) transition with λ = 750.3 nm was the most appropriate for our purposes. To record F atoms, we used two transitions from upper levels with different multiplicity, namely, $F(3p^2P^0_{3/2} \longrightarrow 3s^2P_{3/2})$ and $F(3p^4D^0_{7/2} \longrightarrow 3s^4P_{5/2})$. These transitions correspond to the most intense emission lines of F atom with λ = 703.8 and 685.6 nm, respectively.

Figure 6a shows the time evolution of the relative emission intensities of the 703.8- and 686.6-nm lines of fluorine atoms and the 750.3-nm line of argon in a modulated discharge in the CF_4 : Ar = 98 : 2 mixture at a pressure of 1 torr, current density of 10 mA/cm^2, and current modulation depth of ~30%. It can be seen that the time behavior of the emission intensities of F and Ar atoms is similar to that observed in pure O_2 and H_2 for oxygen and hydrogen atoms; however, the characteristic time scale here is twice as long. When the discharge is switched into a new quasi-steady state, the relative change in the emission intensity of the F 685.6-nm line is smaller than for the F 703.8-nm line. This points to the presence of another 685.6-nm emission source that is not related to fluorine atoms. Figure 6b shows the waveforms of the actinometric signals $S_{F703} = \frac{1 + \delta I_{F703}/I_{F703}}{1 + \delta I_{Ar750}/I_{Ar750}}$ and $S_{F685} = \frac{1 + \delta I_{F685}/I_{F685}}{1 + \delta I_{Ar750}/I_{Ar750}}$, corresponding to the 703.8- and 685.6-nm lines of fluorine

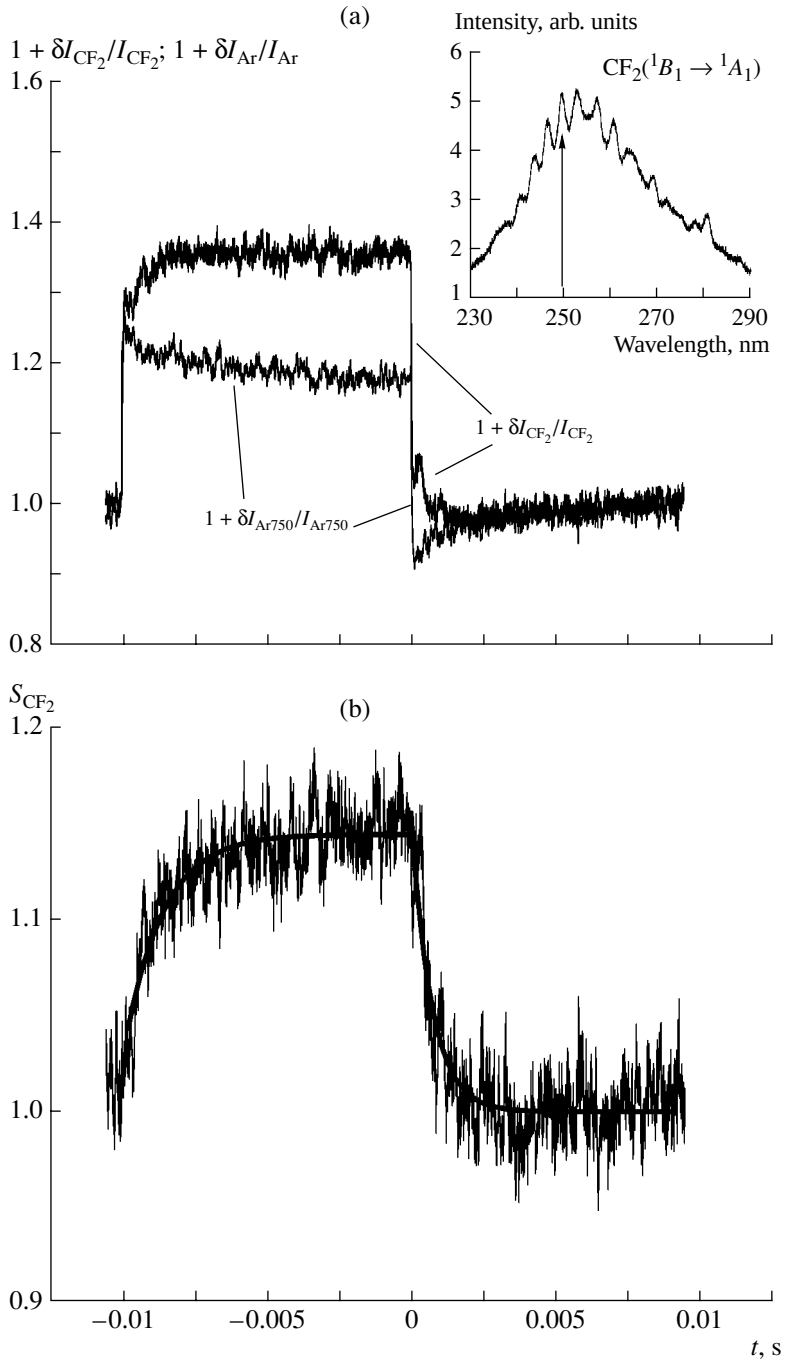

Fig. 7. (a) Waveforms of the normalized emission intensities of the 750.3-nm line of argon and 248.5-nm line (the $CF_2(^1B_1, 060 \longrightarrow {}^1A_1, 000)$ transition) of CF_2 radicals in a modulated discharge in the CF_4 : Ar = 98 : 2 mixture at p = 1 torr and J_d = 10 mA/cm^2. (b) Actinometric signal $S_{CF_2} = \dfrac{1 + \delta I_{CF_2}/I_{CF_2}}{1 + \delta I_{Ar750}/I_{Ar750}}$. The heavy lines show the exponential approximations of the rise and decay segments of the S_{CF_2} signal.

atoms. The modulation depth of the S_{F703} and S_{F685} actinometric signals is smaller than the modulation depth of the discharge current, which is equal to ~30%. This is related to the contribution from the $CF_2(^3B_1 \longrightarrow {}^1A_1)$ transition to the intensity of the 703.8-nm and 686.6-nm emission lines. However, since the production of radicals in the $CF_2(^3B_1)$ state proceeds mainly via the dissociative excitation of stable polymer mole-

cules C_xF_y, which are the products of fluorocarbon polymerization, the time evolution of the $CF_2(^3B_1 \longrightarrow {}^1A_1)$ band emission should be similar to that of the actinometer signal. This was verified by comparing the time evolution of the emission lines corresponding to the $CF_2(^3B_1 \longrightarrow {}^1A_1)$ transition to that of the Ar 750-nm line in a modulated discharge. On the characteristic time scale of variations in the concentration of fluorine atoms, these time evolutions were similar to one another with good accuracy. Therefore, the effect of the $CF_2(^3B_1 \longrightarrow {}^1A_1)$ band on the emission intensity of the 703.8- and 685.6-nm lines reduces to a decrease in the modulation depth of the S_{F703} and S_{F685} actinometric signals. However, as with hydrogen atoms, this does affect the measurements of the probability of the heterogeneous loss of F atoms. The heavy lines in Fig. 6b show the exponential approximations for the rise and decay segments of the S_{F703} and S_{F685} actinometric signals. Using these approximations and formula (12), we obtain $\gamma_F = (9.7 \pm 0.05) \times 10^{-4}$ (the relative error is ~5%).

Figure 7a shows the time evolution of the relative emission intensities of the 750-nm line of argon and the 248.5-nm line (the $CF_2(^1B_1, 060 \longrightarrow {}^1A_1, 000)$ transition) of CF_2 radicals in a modulated discharge in the $CF_4 : Ar = 98 : 2$ mixture at a pressure of 1 torr, current density of 10 mA/cm^2, and current modulation depth of ~30%. The inset in Fig. 7a shows the emission spectrum corresponding to the $CF_2(^1B_1 \longrightarrow {}^1A_1)$ UV band; the arrow indicates the emission line whose time evolution was monitored. Figure 7b shows the waveform of the actinometric signal $S_{CF_2} = \dfrac{1 + \delta I_{CF_2}/I_{CF_2}}{1 + \delta I_{Ar750}/I_{Ar750}}$. The heavy lines show the exponential approximations for the rise and decay segments of the S_{CF_2} signal. The obtained characteristic loss time of CF_2 radicals is ~1 ms, which is in good agreement with the time measured in a similar discharge by the time-resolved LIF method [31, 32]. This time is much shorter than the characteristic loss time of fluorine atoms; this indirectly points to the presence of chemical reactions with the participation of CF_2 radicals. The probability of the heterogeneous loss of CF_2 radicals calculated by formula (12) is $\gamma_{CF_2} = (5.1 \pm 1) \times 10^{-2}$. This value is in good agreement with the probability of the heterogeneous loss of CF_2 molecules in plasmochemical etching reactors in which fluorocarbons are used as a working gas [33–35].

5. CONCLUSIONS

A new method has been proposed for measuring the probabilities of the heterogeneous loss of radicals in a gas-discharge plasma. The method is based on the time-resolved modulation actinometry and is easy to implement in experiments. The method has been shown to be applicable to O, H, F, and CF_2 radicals in a dc glow discharge. It has been shown that the method proposed is similar to the LIF technique and ensures high accuracy (up to ~0.1) in measuring the probabilities of the surface loss of radicals under gas-discharge conditions. The method is much more efficient than the LIF method, especially when applied to the plasma of molecular gases, where the number of the parameters determining the surface loss of radicals can be very large. The method allows one to acquire a large amount of experimental data over a reasonable time (a few thousand experimental points in a few weeks). This is of great importance, since these experimental data allow one to study in detail the mechanism for the heterogeneous loss of radicals. This, in turn, makes it possible to determine the microparameters of elementary surface processes with the participation of radicals.

ACKNOWLEDGMENTS

This study was supported by the Russian Foundation for Basic Research, project nos. 00-15-96554 and 03-02-16925.

REFERENCES

1. D. P. Woodruff and T. A. Delchar, *Modern Techniques of Surface Science* (Cambridge Univ. Press, 1986; Mir, Moscow, 1989).
2. J. Amorim, G. Baravian, and J. Jolly, J. Phys. D **33**, R51 (2000).
3. H. F. Dobele, U. Czarnetzki, and A. Goehlich, Plasma Sources Sci. Technol. **9**, 477 (2000).
4. M. D. Wheeler, S. M. Newman, A. J. Orr-Ewing, and M. N. R. Ashfold, J. Chem. Soc., Faraday Trans. **94**, 337 (1998).
5. M. Haverlag, E. Stoffels, W. W. Stoffels, *et al.*, Sci. Technol. A **12**, 3102 (1994).
6. V. V. Ivanov, K. S. Klopovskiĭ, D. V. Lopaev, *et al.*, Fiz. Plazmy **26**, 1046 (2000) [Plasma Phys. Rep. **26**, 980 (2000)].
7. V. V. Ivanov, K. S. Klopovskiĭ, D. V. Lopaev, *et al.*, Fiz. Plazmy **26**, 1038 (2000) [Plasma Phys. Rep. **26**, 972 (2000)].
8. D. Pagnon, J. Amorim, J. Nahorny, *et al.*, J. Phys. D **28**, 1856 (1995).
9. V. V. Ivanov, K. S. Klopovskiy, D. V. Lopaev, *et al.*, IEEE Trans. Plasma Sci. **27**, 1279 (1999).
10. V. A. Feoktistov, V. V. Ivanov, A. M. Popov, *et al.*, J. Phys. D **30**, 423 (1997).
11. Y. C. Kimm and M. Boudart, Langmuir **7**, 2999 (1991).
12. L. Magne, H. Coitout, G. Cernogora, and G. Gousset, J. Phys. III France **3**, 1871 (1993).
13. G. Cartry, L. Magne, and G. Cernogora, J. Phys. D **32**, L53 (1999).
14. G. Cartry, L. Magne, and G. Cernogora, J. Phys. D **33**, 1303 (2000).
15. A. Rousseau, G. Cartry, and X. Duten, J. Appl. Phys. **89**, 2074 (2001).

16. J. Amorim, J. Loureiro, G. Baravian, and M. Touzeau, J. Appl. Phys. **82**, 2795 (1997).
17. A. D. Tserepi and T. A. Miller, J. Appl. Phys. **75**, 7231 (1994).
18. B. Gordiets, C. M. Ferrera, M. J. Pinheiro, and A. Ricard, Plasma Sources Sci. Technol. **7**, 379 (1998).
19. C. M. Ferreira, E. Tatarova, V. Guerra, *et al.*, in *Selected Research Papers on Spectroscopy of Nonequilibrium Plasma at Elevated Pressures*, Ed. by V. N. Ochkin (SPIE, Washington, 2002), p. 99.
20. J. Henriques, E. Tatarova, F. M. Dias, and C. M. Ferreira, J. Appl. Phys. **91**, 5632 (2002).
21. J. Luque, E. A. Hudson, and J.-P. Booth, J. Chem. Phys. **118**, 622 (2003).
22. J. Luque, E. A. Hudson, J.-P. Booth, and I. D. Petsalakis, J. Chem. Phys. **118**, 1206 (2003).
23. M. Suto and N. Washida, J. Chem. Phys. **78**, 1007 (1983).
24. M. Suto and N. Washida, J. Chem. Phys. **78**, 1012 (1983).
25. M. Suto, M. Washida, H. Akimoto, and M. Nakamura, J. Chem. Phys. **78**, 1019 (1983).
26. N. Washida, M. Suto, S. Nagase, *et al.*, J. Chem. Phys. **78**, 1025 (1983).
27. C. Larrieu, M. Chaillet, and A. Dargelos, J. Chem. Phys. **96**, 3732 (1992).
28. S. Koda, Chem. Phys. Lett. **55**, 353 (1978).
29. Z.-L. Cai, J. Phys. Chem. **97**, 8399 (1993).
30. Q.-T. Trung, G. Durocher, P. Sauvagear, and C. Sandorfy, Chem. Phys. Lett. **47**, 404 (1977).
31. V. V. Ivanov, K. S. Klopovskiĭ, D. V. Lopaev, *et al.*, Fiz. Plazmy **28**, 257 (2002) [Plasma Phys. Rep. **28**, 229 (2002)].
32. V. V. Ivanov, K. S. Klopovskiĭ, D. V. Lopaev, *et al.*, Fiz. Plazmy **28**, 272 (2002) [Plasma Phys. Rep. **28**, 243 (2002)].
33. A. D. Tserepi, J. Derouard, J.-P. Booth, and N. Sadeghi, J. Appl. Phys. **81**, 2124 (1997).
34. T. Arai, M. Goto, K. Horikoshi, *et al.*, Jpn. J. Appl. Phys. **38**, 4377 (1999).
35. C. Suzuki, K. Sasaki, and K. Kadota, Jpn. J. Appl. Phys. **36**, L824 (1997).

Translated by N.N. Ustinovskiĭ